THÈSE

Pour obtenir le grade de

DOCTEUR DE L'UNIVERSITÉ GRENOBLE ALPES

École doctorale : EEATS - Electronique, Electrotechnique, Automatique, Traitement du Signal
Spécialité : Nano électronique et Nano technologies
Unité de recherche : Laboratoire des Technologies de la Microélectronique

Typage de l'espèce Escherichia coli par piégeage optique de cellule unique sur puce optofluidique

Single-cell optical trapping for the typing of Escherichia coli using an optofluidic chip

Présentée par :

Khouloud ARFAOUI

Direction de thèse :

Marc ZELSMANN DIRECTEUR DE RECHERCHE, CNRS délégation Alpes	Directeur de thèse
Valérie STAMBOULI CHARGEE DE RECHERCHE HDR, CNRS	Co-directrice de thèse
Pierre MARCOUX INGENIEUR HDR, CEA CENTRE DE GRENOBLE	Co-directeur de thèse
Emmanuel PICARD INGENIEUR CHERCHEUR, CEA CENTRE DE GRENOBLE	Co-encadrant de thèse

Rapporteurs :

Taha BENYATTOU
DIRECTEUR DE RECHERCHE, CNRS délégation Rhône Auvergne

Isabelle LEDOUX-RAK
PROFESSEURE DES UNIVERSITES, ENS Paris Saclay

Thèse soutenue publiquement le **24 juin 2026**, devant le jury composé de :

Ahmad BSIESY, PROFESSEUR DES UNIVERSITES, Université Grenoble Alpes	Président
Marc ZELSMANN, DIRECTEUR DE RECHERCHE, CNRS délégation Alpes	Directeur de thèse
Pierre MARCOUX, INGENIEUR HDR, CEA Centre de Grenoble	Co-directeur de thèse
Taha BENYATTOU, DIRECTEUR DE RECHERCHE, CNRS délégation Rhône Auvergne	Rapporteur
Isabelle LEDOUX-RAK, PROFESSEURE DES UNIVERSITES, ENS Paris Saclay	Rapporteure
Sigolène LECUYER, CHARGEE DE RECHERCHE, CNRS délégation Rhône Auvergne	Examinatrice

Invités :

Emmanuel PICARD
INGENIEUR, CEA IRIG - Laboratoire PHotonique ELectronique et Ingénierie QuantiqueS

Valérie STAMBOULI-SENE
CHARGE DE RECHERCHE HDR, Laboratoire des Matériaux et du Génie Physique (LMGP)

لن أعود كما ذهبت،
ولن أعود... ولو لـمامًا !

– مَحمُود دَرْوِيْش

“ I will not return as I once left,
and I will not return… not even briefly. ”

— Mahmoud Darwish

Abstract

The rise of antimicrobial resistance has transformed the treatment of bacterial infections into a race against time, as it is predicted to become a leading cause of mortality worldwide by 2050. This situation is driven in part by the widespread use of broad-spectrum antibiotics, which remain necessary in the absence of precise diagnostic alternatives capable of guiding therapeutic strategies. Addressing this challenge requires a deeper investigation of bacterial populations at the single-cell level, not only to understand their behaviour, but also to anticipate the emergence of phenotypic shifts and resistance-associated changes.

Conventional microbiological methods rely predominantly on population-averaged measurements, which provide robust and standardized information but fail to capture the heterogeneity that may exist within bacterial populations. As a result, rare or transient behaviours expressed by a small fraction of cells may remain undetected, despite their potential role in the development of resistance or in the response to environmental stress. Detecting these early signs requires experimental approaches capable of isolating and probing individual cells with sufficient sensitivity and reproducibility.

Optical methods offer a promising framework to address these limitations. The interaction of light with microscopic objects enables both the manipulation and the characterization of single cells in a non-invasive manner. In particular, photonic structures allow strong confinement of light, enhancing sensitivity to minute variations in cellular properties. When combined with microfluidic systems, these approaches provide precise control over the cellular environment while enabling continuous and non-invasive measurements.

In this manuscript, we present the development of optofluidic chips based on SOI photonic crystal optical resonators for the trapping and analysis of individual *Escherichia coli* bacterial cells. Particular attention was given to the design and integration of the microfluidic circuit, enabling controlled delivery and positioning of cells within the optical structures. These devices integrate optical manipulation and sensitive detection within a microfluidic platform, allowing controlled investigations of cell-surface interactions, and optical responses at the single-cell level.

The results demonstrate the ability of this approach to trap individual bacterial cells and to probe their physical interactions with the surrounding environment, including transient behaviours that were investigated and controlled through adjustments of the experimental conditions. Statistical analysis confirms the reproducibility of the optical measurements and the ability to extract consistent single-cell signatures. These observations highlight the variability of bacterial responses and indicate that discrimination between *Escherichia coli* strains remains challenging under the current experimental conditions. Finally, the measured optical responses were used to estimate the refractive index of each bacterial strain in the infrared.

Overall, this work contributes to the development of optical tools for single-cell microbiology and outlines perspectives for more precise diagnostic approaches.

Keywords : photonic crystals, optical trapping, optofluidics, microfluidics, single-cell analysis, *Escherichia coli*, bacterial typing, cell-surface interactions, measurement reproducibility

Résumé

L'émergence de la résistance aux antimicrobiens a transformé le traitement des infections bactériennes en une course contre la montre et devrait devenir l'une des principales causes de mortalité dans le monde d'ici 2050. Cette situation s'explique en partie par l'utilisation généralisée d'antibiotiques à large spectre, qui restent nécessaires en l'absence d'outils diagnostiques suffisamment précis pour orienter les stratégies thérapeutiques. Répondre à cet enjeu nécessite une étude plus approfondie des populations bactériennes à l'échelle de la cellule unique, afin non seulement de comprendre leur comportement, mais aussi d'anticiper l'émergence de variations phénotypiques et de mécanismes de résistance.

Les méthodes microbiologiques conventionnelles reposent majoritairement sur des mesures moyennées à l'échelle de la population, qui fournissent des informations robustes et standardisées mais ne permettent pas de saisir l'hétérogénéité intrinsèque des populations bactériennes. En conséquence, des comportements rares ou transitoires, portés par une faible fraction de cellules, peuvent passer inaperçus malgré leur rôle potentiel dans l'apparition de résistances ou dans la réponse à des contraintes environnementales. La détection de ces comportements précoces requiert des approches expérimentales capables d'isoler et de sonder des cellules individuelles avec une sensibilité et une reproductibilité suffisantes.

Les approches optiques constituent une voie particulièrement prometteuse pour dépasser ces limitations. L'interaction de la lumière avec des objets microscopiques permet à la fois la manipulation et la caractérisation de cellules individuelles de manière non invasive. En particulier, les structures photoniques permettent un fort confinement de la lumière, ce qui accroît la sensibilité aux variations fines des propriétés cellulaires. Couplées à des systèmes microfluidiques, ces approches offrent un contrôle précis de l'environnement cellulaire tout en permettant des mesures continues et non-invasives.

Dans ce manuscrit, nous présentons le développement de puces optofluidiques basées sur des résonateurs optiques à cristaux photoniques pour le piégeage et l'analyse de cellules bactériennes individuelles d'*Escherichia coli*. Une attention particulière a été portée à la conception et à l'intégration du circuit microfluidique, permettant un positionnement et une distribution contrôlés des cellules au sein des structures optiques. Ces dispositifs combinent des fonctions de manipulation optique et de détection sensible au sein d'une plateforme microfluidique, permettant des investigations contrôlées des interactions cellule-surface et des réponses optiques à l'échelle de la cellule unique.

Les résultats démontrent la capacité de cette approche à piéger des cellules bactériennes individuelles et à sonder leurs interactions physiques avec l'environnement, y compris les comportements transitoires, qui ont été étudiés et maîtrisés grâce à l'ajustement des conditions expérimentales. L'analyse statistique confirme la reproductibilité des mesures optiques et l'extraction de signatures optiques cohérentes à l'échelle de la cellule unique. Ces observations mettent en évidence la variabilité des réponses bactériennes et indiquent que la discrimination entre souches d'*Escherichia coli* reste limitée dans les conditions expérimentales actuelles. Enfin, les réponses optiques mesurées ont permis d'estimer l'indice de réfraction de chaque souche dans l'infrarouge.

Dans l'ensemble, ce travail contribue au développement d'outils optiques pour la microbiologie à l'échelle de la cellule unique et ouvre des perspectives vers des approches diagnostiques plus précises.

Mots-clés : Cristaux photoniques, piégeage optique, microfluidique, analyse à cellule unique, *Escherichia coli*, typage bactérien, interactions cellule-surface, reproductibilité des mesures

Acknowledgments

Sitting at the start of the manuscript, this section was written last, almost two months after the defense itself. I am still having a hard time realising this PhD adventure is over, and that I am now indeed, and finally, a Doctor. However, this sudden excess of free time gave me the chance to reflect on the journey itself that led to this achievement, and above all, on the people who made it possible in one way or another.

This journey started by a group of researchers who saw potential in a student they barely knew from an adjacent Master's internship. They trusted I had, perhaps not all the skills needed, but enough ambition to get an experimental project out of a technical slump it was experiencing for years. For this, I will never thank enough, first and foremost, my PhD director Marc who was the biggest and best support I've had on all levels. He gave me the freedom and autonomy needed for curious exploration, while rightfully steering the wheel whenever that same curiosity threatened to carry me too far off shore. I am also very thankful for all my supervision team, namely Manu, and especially Pierre and Valérie who both followed along from afar but always replied present whenever I reached out to them. Finally, I want to extend my gratitude to all the researchers and engineers who assisted me to various degrees with filling knowledge gaps, solving technical matters and answering my stupid questions. So, in no particular order, thank you to the SiNaps/IRIG team particularly Emmanuel Hadji, thank you to professors from LMGP namely Marianne Weidenhaupt, and thank you to various people from the LTM lab especially Sebastien Labau, David Fuard and Alice Nicolas.

While backed-up with a good team of supervisors, the success of this journey was also a fruit of the collaboration it generated with fellow young researchers to whom I am infinitely grateful as well. The MVP here is Simon Glicenstein, who would have been mentioned alongside my supervisors had he not been a PhD candidate himself at the time. Thank you also to Dylan and Clément for all the glasses you had to pierce and the tubes you had to glue. Thank you to Thibault, Sacha and all the LTM students with whom I spent endless afternoons troubleshooting one specific machine that almost made us all go loose. Thank you to Louis, who came along later but helped round up my work and advance the experiment to the next level.

Last but certainly not least on the list of collaborators, as this PhD was part of a franco-swiss project, I want to insist on expressing my gratitude to all the team members from Lausanne for each person's unique contributions and fresh points of view that helped advance the project in general and each of our personal understandings of the various domains implicated in it. I want to particularly thank Enrico and Nicolas who welcomed me for a week in their lab at EPFL.

On top of work itself, many friends at the lab helped make the journey worthwhile. Thank you to the gossip group, Aída, Andrea and my officemate Gianluca for all the moments we shared yapping, eating and repeating. The trip we shared in *Andalucía* was a dream I am glad I got to realise along side you. Thank you to Rémy Tribout for the funny shenanigans, to Jonathan for the musical breaks, to Thomas for the political debates, to Yasmine for the smiley presence, and to all those who these lines will not suffice to include.

I would like to thank the friends outside of work who have not necessarily understood my work, but were always present to support the ambition I had for it. Thank you to the *Phear* group, my friends from engineering school who have made my life abroad fun from since I first arrived

in Grenoble. Thank you to Hajer and Samar, for the valuable deep friendships that survived the hardships of distance and time.

I owe a big part of my success to my family who taught me the value of hard work and perseverance since day one. With both my parents being teachers, their biggest focus was always around education and I am glad to be honoring their efforts, as well as Granma's memory, through this doctorate. I also owe a big part of who I am to my sisters who are the constants in my life and the dearest to my heart. Thank you for everything. I am the eldest but I am not leading the path as much as you are paving it by your care and support. This joy is ours and not just mine.

I would like to finish by thanking the person that my heart chose, my partner and my best friend, Valentin. For more than six years, you have been the sunshine that makes my sad days happy and my happy days happier. Doing our PhDs simultaneously has challenged us but also made us closer and I am eager for all the adventures that life still holds for us together. Thank you, and to your family who opened their arms wide open to me and made my homesickness easier to bare.

Lastly, thank you to anyone reading these words, whether you looked closely through the manuscript or skimmed it. I hope it leaves you with a renewed curiosity for making cool science.

Grenoble, 12 August 2026.

Contents

Abstract (English/Français) i

Acknowledgments iv

Table of contents vii

List of Figures x

Introduction **1**

1 Optical Forces & Applications **3**

1.1 Light-Matter Interactions 4

1.1.1 Absorption and Transmission 4

1.1.2 Reflection and Refraction 4

1.1.3 Scattering 5

1.2 Optical Forces 6

1.3 Optical Trapping 8

1.4 Devices for Optical Trapping 9

1.4.1 Free-space Optical Trapping 10

1.4.2 On-Chip Optical Trapping 13

1.5 Conclusions 19

2 Our Setup **21**

2.1 Photonic Traps: Structure Selection 22

2.2 Photonic Traps: Chip Realisation 23

2.2.1 Design Tuning 23

2.2.2 Fabrication 26

2.2.3 Effect of SOI thickness 30

2.2.4 Light Coupling & Mode Adaptors 35

2.3 Microfluidic Integration 42

2.3.1 Static Fluidic Pool 42

2.3.2 On-chip Fluidic System: Designing 43

2.3.3 On-chip Fluidic System: Fabrication 44

2.4 Optical Bench 47

2.5 Conclusions & Perspectives 50

3 Microbiology & Bacteria **53**

3.1 Introduction 54

3.1.1 Bacteria as Micro-Organisms 54

3.1.2 Bacterial Classification 55

3.1.3 Importance of Bacterial Detection & Identification 60

3.2 Bacterial Identification: Classical Methods 60

3.2.1 Culture-based and Biochemical Bethods 60

3.2.2 Serotyping and Immunological Methods 63

3.2.3 Molecular and Sequencing-based Methods . . . 66
3.2.4 Mass spectrometry-based methods . . . 69
3.3 Bacterial Identification: Optical Methods . . . 71
3.3.1 Fluorescence and Scattering detection . . . 71
3.3.2 Vibrational Spectroscopies . . . 74
3.3.3 Plasmonic and Photonic Sensors . . . 76
3.4 Prior Work within the Research Group . . . 76
3.5 Motivations & Biological Framework of the Present Work . . . 81
3.6 Conclusions . . . 82

4 SOI-Bacteria Interactions **85**
4.1 Introduction . . . 86
4.2 Experimental observations . . . 86
4.3 Force Analysis at the SOI-Bacteria Interface . . . 89
4.3.1 Decomposition . . . 89
4.3.2 Analysis . . . 89
4.3.3 Summary . . . 92
4.4 Surface Charges . . . 92
4.4.1 Zeta Potential: Theory . . . 93
4.4.2 Zeta Potential: Experimental Protocol . . . 95
4.4.3 Bacterial Surface Charges . . . 97
4.4.4 SOI Surface Charges . . . 98
4.4.5 Electrostatic Interaction at the SOI–Bacteria Interface . . . 98
4.5 SOI Surface Treatment . . . 99
4.5.1 SOI Surface Treatment: Methods . . . 100
4.5.2 SOI Surface Treatment: Results . . . 101
4.5.3 Limitations of BSA functionalization. . . . 102
4.6 Modification of the Suspension Medium . . . 103
4.6.1 Choice of Suspension Medium . . . 103
4.6.2 Effects of Suspension Medium Change . . . 105
4.7 Conclusions and Perspectives . . . 107

5 Optical Signals Analysis **110**
5.1 Introduction . . . 111
5.2 Data Collection . . . 111
5.2.1 Experimental Protocol . . . 111
5.2.2 Technical Considerations & Limitations . . . 113
5.2.3 Cavity State Changes . . . 113
5.2.4 Optofluidic Chip Cleaning . . . 115
5.3 Signal Pre-Processing Methodology . . . 119
5.4 Data Analysis: Methods . . . 123
5.4.1 Statistical Representation . . . 123
5.4.2 Reproducibility Scores . . . 125
5.4.3 Supervised Classification Framework . . . 127
5.5 Signal Analysis: Results . . . 128
5.5.1 Intra-Strain Variability . . . 128
5.5.2 Inter-Strain Discrimination . . . 132
5.6 Optical Determination of Strain Refractive Index . . . 135
5.7 Genomic Correlation . . . 140
5.8 Conclusions and Perspectives . . . 141

Conclusion & perspectives **144**

Bibliography **I**

A Appendix 1 : Additional Microbiology Methods and Practices **XVIII**
A.1 Sample Preparation XVIII
A.2 Extended Culture-Based and Biochemical Methods XIX

B Appendix 2 : Trapping Signals **XXII**

List of Figures

1.1 Illustration of some types of light-matter interactions . . . 5
1.2 Illustration of light scattering . . . 6
1.3 Illustration of Optical Forces . . . 7
1.4 Optical Tweezers . . . 10
1.5 Examples of Advanced Optical Tweezers . . . 12
1.6 Waveguides . . . 14
1.7 Optical Ring Resonators Geometries . . . 15
1.8 Examples of Plasmonic Nanostructures Geometries . . . 16
1.9 Illustration of Photonic Crystal Cavities . . . 17
1.10 Resonance Spectrum of a 1D Photonic Crystal Cavity . . . 18

2.1 SNOM image of a 1D PhC cavity in resonance. . . . 22
2.2 Illustration of a 1D PhC cavity design . . . 24
2.3 Spectral Characterisation of CMT3,4&5 . . . 25
2.4 Illustration of internal reflections within a CMT3 . . . 26
2.5 Characteristic dimensions of CMT3 cavities . . . 27
2.6 Illustration of the layered structure of SOI wafers . . . 27
2.7 Photolithography Steps . . . 29
2.8 SEM image of a CMT3 . . . 29
2.9 SEM image of 2D PhC resonators . . . 29
2.10 Electric field distribution simulations . . . 31
2.11 Evanescent electric field extent simulations . . . 32
2.12 Spectra of CMT3 structures with different SOI layer thickness and comparison of their characteristic parameters . . . 34
2.13 Pointed fiber tip aligned to SI waveguide for injection. . . . 36
2.14 Illustration of CMT3 tapered waveguides . . . 36
2.15 SEM image of funnel and inverted tapers fabricated on the same chip . . . 37
2.16 SEM image of an SU-8 mode adapter overlaid on an inverted SOI taper . . . 37
2.17 Exposure dose tests . . . 38
2.18 Image of fabricated SU-8 mode adapters . . . 39
2.19 Spectra of cavities with different types of tapers . . . 40
2.20 Comparison of the centering of inverted tapers overlaid with SU-8 mode adapters 41
2.21 Steps of static fluidics pool installation . . . 42
2.22 Design of the fluidic channel . . . 44
2.23 Microfluidic chip inlet and outlet connectors. . . . 46
2.24 SU-8 mode adapters next to the SU-8 block containing the microfluidic channel . 47
2.25 Summary of fabrication step of the optofluidic chip . . . 48
2.26 Illustration of the optical bench components . . . 49
2.27 Image of the optical bench with annotations indicating the main components . . . 50

3.1 Diagram of a bacterial cell showing structural parts . . . 54
3.2 Diagram of bacterial morphology . . . 57

3.3 Cell wall structure of Gram-positive and Gram-negative bacteria 58
3.4 Electron microscopy image showing bacterial surface appendages 59
3.5 Microscopic image of Gram-stained mixed preparation. 61
3.6 Examples of API 20E strip results. 62
3.7 Presentation of the VITEK and BACTEC platforms and consumables. 63
3.8 Examples of agglutination test results. 64
3.9 Illustration of the sandwich ELISA steps 65
3.10 Illustration of the double-strand DNA genome structure. 67
3.11 MALDI-TOF set-up and example of results. 70
3.12 Fluorescence microscopy images of bacterial cells labeled with fluorescent dyes. 73
3.13 Results of species differentiation experiments. 78
3.14 Comparison of the optical characteristics of 1D and 2D photonic crystals. 79
3.15 Comparison of transmitted signal characteristics for bacteria of different Gram types. 80
3.16 Assessment of the effect of T4 phages using photonic chips and classical assays. . 82

4.1 Example of transmitted signal during a transient trapping event. 87
4.2 Illustration of zeta potential and slipping plane 94
4.3 Zeta potential measurement setup. 95
4.4 Zeta potential measurements for bacterial cells in deionized water. 98
4.5 Example of transmitted signal after BSA treatment. 102
4.6 Zeta potential measurements for bacterial cells in deionized water and in PBS. . . 105
4.7 Example of transmitted signal after BSA treatment and suspension medium change. 106

5.1 Experimental protocol used for data collection. 113
5.2 Evolution of the characteristic values of the CMT3 optical trap 114
5.3 Images of PBS crystallization in fluidic canals. 117
5.4 Optical cavity before and after bacterial clump accumulation. 118
5.5 Example of a typical trapping signal. 120
5.6 Illustrative example of the drop-detection procedure. 121
5.7 Expression of the transmission signal as resonance wavelength shifts. 122
5.8 Example of a histogram fitted with a skew-normal distribution. 124
5.9 $(\mu - \sigma)$ parameters distribution for all trapped bacterial strains. 129
5.10 Coefficient of variance per strain. 131
5.11 Distribution of fitting parameters for all strains. 132
5.12 Confusion matrices of the bacterial strain predictions. 134
5.13 λ_0=f(n)obtained from FDTD simulations. 136
5.14 Resonance spectra of CMT3 cavities in air and in deionized water. 137

A.1 Examples of differential and selective properties of different growth media. . . . XX
A.2 Examples of enzymatic assays results. XXI

B.1 Distribution of $(\mu - \sigma)$ parameters for ***EC11*** optical signatures. XXIII
B.2 Distribution of $(\mu - \sigma)$ parameters for ***EC225*** optical signatures. XXIII
B.3 Distribution of $(\mu - \sigma)$ parameters for ***EcB*** optical signatures. XXIV
B.4 Distribution of $(\mu - \sigma)$ parameters for ***Eco0124*** optical signatures. XXIV
B.5 Distribution of $(\mu - \sigma)$ parameters for ***Eco0126*** optical signatures. XXV
B.6 Distribution of $(\mu - \sigma)$ parameters for ***Eco0127*** optical signatures. XXV
B.7 Distribution of $(\mu - \sigma)$ parameters for ***Eco0128*** optical signatures. XXVI
B.8 Distribution of $(\mu - \sigma)$ parameters for ***Eco0129*** optical signatures. XXVI
B.9 Distribution of $(\mu - \sigma)$ parameters for ***Eco0130*** optical signatures. XXVII
B.10 Distribution of $(\mu - \sigma)$ parameters for ***Eco0131*** optical signatures. XXVII

Introduction

In clinical environments, time and information shape every decision. Yet when a patient arrives with a suspected bacterial infection, what can be readily measured tells only part of the story needed for a full, precise diagnosis. Most diagnostic methods still rely on growing bacterial cultures that take days to weeks to reveal both the identity of the pathogen and its response profile. As a result, treatment is frequently initiated in the absence of clear information. Clinicians must estimate based on symptoms and administer broad-spectrum mixes of antimicrobial agents that cover a variety of common or possible infections.

The predominantly used antimicrobial agents in the prevention and treatment of infectious diseases are antibiotics. They are drugs that can kill or inhibit the growth of microorganisms such as bacteria. The discovery of antibiotics, starting with penicillin in the early 20th century, was a revolutionary breakthrough that transformed modern medicine. Their impact is undeniable, extending the average human lifespan by more than two decades [1]. However, we have seen in recent years the consequence of broad-spectrum treatments that often expose patients and their bacterial flora to more antibiotic molecules than needed for the specific pathogen to be treated. This results, over time, in an over-exposure to antibiotics and consequently leads to antimicrobial resistance (AMR). AMR appears when bacteria evolve or mutate to acquire traits that reduce their susceptibility to drugs. Clinically, AMR translates to longer illness, more complicated treatment regimens, and a higher risk of treatment failure.

Resistance to antimicrobials can spread widely within bacterial populations in humans and animals, and consequently be transmitted between healthy and infected individuals, and from human consumption of animal products containing resistant bacteria. This accelerating spread has led the World Health Organization (WHO) in 2010 to declare AMR as a fundamental health threat and to estimate it, if not controlled, to become the first cause of mortality in the world by 2050 [2]. Addressing this challenge requires more in-depth investigations of bacterial populations to study their behaviour and predict any trend changes or mutations.

However, studying bacterial pathogens has long depended on clinical tools that mostly capture population-level behaviours. These routine diagnostic methods have improved over the years, yet the vast majority still delivers only an average response from a sample. Rare or unusual behaviours expressed only by a few cells within the population can disappear into the background and remain unnoticed when everything is blended into a single readout. In a clinical context, detecting these early signals before they spread within the flora can change therapeutic decisions and improve patient outcomes.

These limitations underscore the need for approaches that observe how individual bacterial cells behave, rather than relying solely on population averages. Although single-cell techniques have advanced considerably, many still face challenges that limit their applicability for routine measurements. Some methods require extensive preparation or specialized equipment, while others lack the sensitivity necessary to capture the earliest changes in a bacterium's physical or biochemical state. As a result, behaviours that begin in only a small fraction of cells may remain hidden, leaving gaps in our understanding of early cellular responses.

Optical approaches offer a promising alternative. Light interacts with microscopic structures in a precise and controllable manner, allowing both manipulation of individual cells and sensitive detection of their properties. Because these interactions occur without direct physical contact, optical methods can monitor cells gently and continuously, making them well suited for detecting subtle or transient behaviours. Photonic structures, in particular, can confine light in volumes smaller than the cell itself, amplifying the sensitivity of these measurements.

In this manuscript, we present the fabrication and use of optofluidic chips based on photonic crystal optical resonators in order to capture individual bacterial cells and probe their membranes. These chips combine the functions of optical traps and highly sensitive sensors with the efficiency of microfluidic structures for precise sample control. The work builds on a long-standing collaboration between different laboratories on the CEA campus in Grenoble: LTM *(Laboratoire des Technologies de la Microélectronique)* from CNRS, SiNaps *(Silicium, Nanoélectronique, Photonique et Structure)* from CEA/IRIG and L4IV *(Laboratoire Instrumentation optique et Traitement de l'Information pour l'Imagerie In Vitro)* from CEA/Leti. Additionally, a project funded by the ANR *(Agence Nationale de la Recherche)* extended this collaboration to a mixed team from EPFL *(École Polytechnique Fédérale de Lausanne)* and CHUV *(Centre Hospitalier Universitaire Vaudois)* in Lausanne, Switzerland. All results presented in this manuscript are my own unless explicitly stated to involve collaborators, which is clearly noted in the text or figures.

The manuscript is organized into five thematic chapters:

- Chapter 1 introduces the physical principles underlying optical trapping. It presents the main mechanisms governing light-matter interactions at the microscale, with a particular focus on optical forces and their implementation for the manipulation of microscopic objects. Existing optical trapping techniques are reviewed, highlighting their capabilities and limitations when applied to biological systems.

- Chapter 2 describes how these optical forces are harnessed in practice to trap biological objects using photonic crystal resonators. It details the design, fabrication, and experimental implementation of the optofluidic chip developed in this work, including the integration of coupling structures and the fluidic circuit. The performance of the device, enabling simultaneous trapping and sensing, is characterized in terms of its optical properties and operational constraints.

- Chapter 3 focuses on the biological system investigated in this work, namely bacterial cells. It provides an overview of commonly used microbiological techniques, with an emphasis on methods relevant to the characterization of physical and physiological properties at both the single-cell and population levels. This chapter positions the optical approach developed here within the broader landscape of existing experimental tools.

- Chapter 4 investigates the interactions between bacterial cells and the surface of the silicon-on-insulator (SOI) photonic chip. In particular, electrostatic effects at the interface are examined through zeta potential measurements of both the surface and the bacteria. Strategies to mitigate repulsive interactions, including surface functionalization and modification of trapping conditions, are implemented and evaluated in terms of their impact on trapping behaviour.

- Chapter 5 focuses on the collection and the analysis of the optical signals obtained during bacterial trapping. Practical aspects related to the operation and long-term use of optofluidic chips are discussed. The reproducibility of the measurements is assessed, and the potential of the device for discriminating between different *E. coli* strains is explored. In addition, the optical response of trapped cells is used to extract quantitative information on their effective refractive index in the infrared range, providing insight into intrinsic cellular properties that are not readily accessible through conventional techniques.

1 Optical Forces & Applications

This chapter introduces the optical concepts and phenomena used in our device to achieve an optical trapping of single particles. It first discusses the fundamental physics of light propagation and optical forces, then presents various optical applications utilizing these forces.

Contents

1.1 Light-Matter Interactions 4
1.1.1 Absorption and Transmission 4
1.1.2 Reflection and Refraction 4
1.1.3 Scattering 5
1.2 Optical Forces 6
1.3 Optical Trapping 8
1.4 Devices for Optical Trapping 9
1.4.1 Free-space Optical Trapping 10
1.4.2 On-Chip Optical Trapping 13
1.5 Conclusions 19

1.1 Light-Matter Interactions

Light, in its many forms, is at the heart of our understanding of the physical world. It serves as a fundamental tool both in our daily lives to illuminate our surroundings, and for science where it is used to probe these same surroundings. First revealed through classical interference phenomena and later formalized in quantum theory, light exhibits a unique dual nature behaving both as a wave and as a particle. This duality is the origin of light's sensitive responses and reactions to the properties of its environment; whether it's propagating through vacuum or interacting with complex media.

In this section, we will explore the various types of light-matter interactions, the principles that govern them, and some of the applications that exploit these interactions.

1.1.1 Absorption and Transmission

When light propagates through a homogeneous material or environment of a constant refractive index, its behaviour is governed by the possible electronic or vibrational transitions that photons may induce in the medium. These interactions dictate whether light is absorbed or transmitted. If the energy of the incoming photons matches the discrete energy gaps between electronic or vibrational states of the material, some or most of them transition to higher energy levels and are thus removed from the forward-propagating beam. In this case, the photon are said to be optically absorbed by the material, leading to partial or complete loss of the incident beam's intensity. This optical attenuation is quantified via the Beer-Bouguer-Lambert law:

$$I(l) = I_0 \cdot e^{-\mu_a(\lambda)\cdot l} \tag{1.1}$$

where I_0 is the initial intensity of light, $\mu_a(\lambda)$ is the wavelength-dependent absorption coefficient of the medium, and l the light path length.
In spectral regions where the absorption is negligible ($\alpha \approx 0$) , light is not absorbed, but rather transmitted. The intensity of the incident beam remains constant (aside from the phenomena that will be presented in the following sections). However, its phase, which represents the wave's oscillation timing, can be altered by the medium, which manifests as a propagation delay.

Together, these complementary phenomena of transmission and absorption (illustrated in figure 1.1) of light form the foundation of multiple optical techniques used for imaging, sensing and material characterization. Their spectral dependence on the intrinsic electronic structure of materials allows light to serve as a highly sensitive probe of composition. Therefore, applications range from absorbance-based measurement tools like optical filters, to advanced spectroscopic methods such as infrared (IR), ultraviolet (UV) and visible spectroscopy. Such techniques are central to both fundamental research and applied technologies in multiple domains of science.

1.1.2 Reflection and Refraction

As light travels, it can encounter interfaces between different materials or inhomogeneous regions where the refractive indices change. The refractive index is a fundamental property of a material that quantifies how much light slows down relative to its speed in vacuum. It not only governs the speed of propagation but also determines how strongly light is bent or refracted when entering a new medium. At these interfaces, and due to its dual nature, light behaves as an electromagnetic wave that responds to the abrupt variations in the optical properties of its surroundings. Therefore, its propagation direction and distribution of energy change. Following Maxwell's boundary conditions, which require continuity of the tangential components of the electric and magnetic fields, part of the incident beam is reflected back into the first medium, while

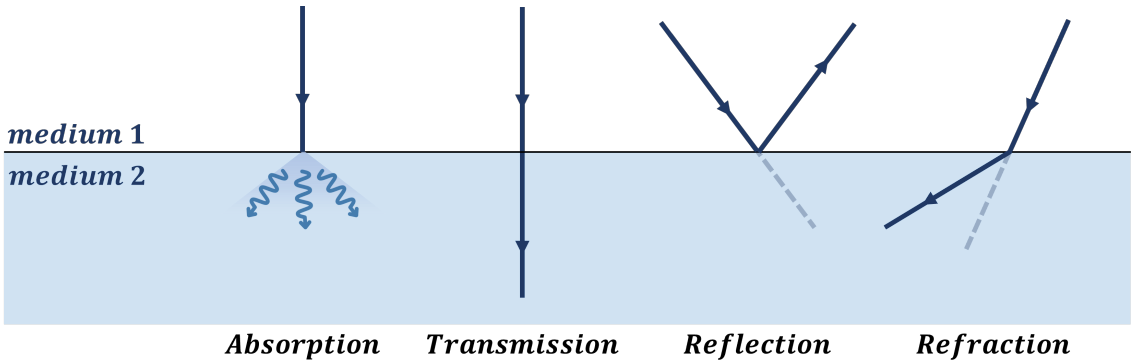

Figure 1.1: Illustration of some types of light-matter interactions

the remainder is transmitted into the second medium along a refracted trajectory. The direction of the transmitted portion is determined by Snell's law:

$$n_1 \cdot sin\theta_i = n_2 \cdot sin\theta_t \tag{1.2}$$

where n_1 and n_2 are the refractive indices of the two media, and θ_i and θ_t are the incident and transmitted beam angle, respectively. Reflection and refraction thus coexist as a redistribution of electromagnetic energy, through changes in the wave's direction, phase velocity, and amplitude. Importantly, these processes involve no intrinsic loss of energy, as the total electromagnetic power is conserved and divided between the refracted and reflected waves.

Together, these complementary phenomena (also illustrated in figure 1.1) explain a broad range of light behaviours at boundaries. Their predictability, rooted in the deterministic nature of reflection and refraction, enables numerous optical and photonic applications, from conventional imaging and lens design to advanced technologies where precise control of light paths is essential. Among the most important applications in modern optics are optical fibers, which allow high-rate transmission of light over long distances through repeated total internal reflection.

1.1.3 Scattering

The previous section describes reflection and refraction: the phenomena occurring when a light beam encounters a planar, linear interface between two regions or mediums. However, in non-ideal mediums, interfaces might be irregular, presenting small-scale inhomogeneities due to numerous factors like microscopic variations in refractive index, local discontinuities, surface roughness or density fluctuations to cite a few. When passing through such localized irregularities, light is deviated at every micro-interface from the path predicted by the law of reflection, scattering it in multiple new directions, as illustrated in figure 1.2.

At the microscopic level, these localized irregularities turn into oscillating dipoles induced within particles by the incident field. These dipoles act like secondary light sources, re-radiating electromagnetic energy in directions determined by their geometry and optical properties like polarizability. Scattering can thus be viewed as a redistribution of electromagnetic energy caused by the local disruptions in the propagation medium.

Three primary scattering regimes are distinguished by comparing the order of magnitudes of the incident light's wavelength and the characteristic dimension of the irregularity it encounters a:

- If $\lambda \gg a$: scattering is described by Rayleigh's theory. In this regime, intensity scales as $I(\theta) \propto I_0 \cdot \lambda^{-4} \cdot (1 + cos^2\theta)$, thus giving this emission a strong wavelength dependence.

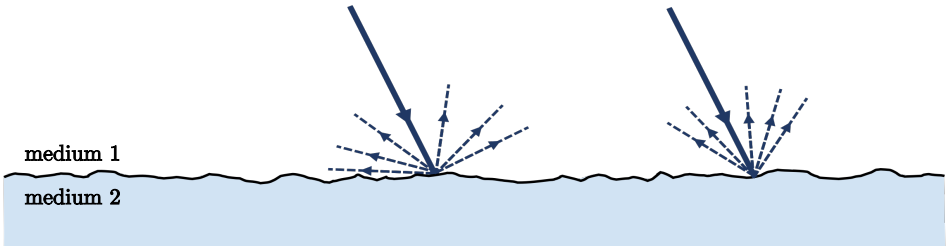

Figure 1.2: Illustration of the scattering of incident light beams (full line) into multiple scattered rays (dashed lines) depending on interface irregularities.

- If $\lambda \sim a$: the interaction between them falls within the Mie regime. Contrary to the Rayleigh regime, the intensity here is only proportional to λ^{-1} making the scattering less sensitive to the incident wavelength.

- If $\lambda \ll a$: we approximate that, locally, conditions are ideal and that light propagation follows the reflection/refraction law of classic geometrical optics.

Scattering, being the most common light–matter interaction in natural and engineered systems, serves as the basis for a wide range of scientific and technological applications for sensing, biomedical imaging, materials characterization and optical manipulation. In the context of this work, scattering plays a key role in the optical manipulation of microscopic biological particles, where the momentum exchanged during photon deflection gives rise to forces capable of trapping, moving, or sorting matter without physical contact.

1.2 Optical Forces

While the previous section focused on the exchanges of energy and momentum that occur when light interacts with matter, this section examines how these exchanges translate into mechanical effects known as optical forces in the Rayleigh regime when particles are much smaller than the incident wavelength.

In fact, these exchanges happen because photons, despite being massless, carry both energy given by $E = h\nu$ and momentum given by $p = E/c = h/\lambda$ where ν is the light frequency, h is Planck's constant, λ is the wavelength, and c is the speed of light in a vacuum. When a photon is absorbed, reflected, or refracted by a particle, its momentum is changed. According to Newton's third law, this change in the photon's momentum must be balanced by an equal and opposite change in the momentum of the particle.

As a simple example, let's consider a photon striking a perfect mirror at normal incidence and reflecting straight back. Its momentum vector changes from $+\vec{n}p$ (where $\vec{n}$ is the normal vector) to $-\vec{n}p$, causing a net change of $\Delta(p) = (-p\vec{n}) - (+p\vec{n}) = -2p\vec{n}$. Therefore, by conservation of momentum, the mirror gains +2p per reflected photon.

At the scale of the entire light beam, these individual momentum transfers between matter and individual photons accumulate, resulting in a net mechanical force know as the radiation-pressure force or the scattering force. Although it is typically on the order of magnitude of $\mu N/m^2$, this scattering force pushes matter along the beam's propagation direction. It is expressed as [3]:

$$\vec{F}_{scatt} = \frac{k}{c} \cdot \varepsilon_0 \varepsilon_m \cdot Im(\alpha) \cdot \|E_0\|^2 \cdot \vec{n} \tag{1.3}$$

where $k = 2\pi/\lambda$ is the wave number, α is the complex polarizability of the object, E_0 is the amplitude of the electric field and $\vec{n}$ is the unit vector in the direction of light propagation. The complex polarizability α characterizes how the particle responds to the applied electric field. In this equation, $\mathrm{Im}(\alpha)$ can be seen as a microscopic analogue of absorption, quantifying how the particle removes energy from the incident light, either through scattering or true absorption. The complete expression of α as well as a detailed explanation of this parameter are given later in this section.

The idea of radiation pressure was first proposed by Kepler in the 17th century, later formalized by Maxwell, and eventually confirmed experimentally in the late 19th century. Nearly a century afterward, Ashkin experimentally identified and reported the detection of another component of optical force known as the gradient force [4].

Gradient forces occur when the electric field around a particle is spatially non-uniform; which could be intrinsic to the structure of the incident beam, or a result of another type of light-matter interaction like scattering. Gradient forces describes how, following a momentum exchange, induced dipoles within the particle interact with the local variations of light intensity around it. Its movements become governed by the gradient of the energy landscape. The particle is pulled toward regions of higher field intensity in order to minimize its own potential energy. This can be analogous, from an energy perspective, to a mass rolling downhill in a gravitational potential. It is given by [3]:

$$\vec{F}_{grad} = \frac{1}{4} \cdot \varepsilon_0 \varepsilon_m \cdot Re(\alpha) \cdot \vec{\nabla} \|E_0\|^2 \tag{1.4}$$

Therefore, the total optical force perceived by an object interacting with light, represented in fig. 1.3, is a sum of both contributions:

$$\vec{F}_{op} = \vec{F}_{scatt} + \vec{F}_{grad} \tag{1.5}$$

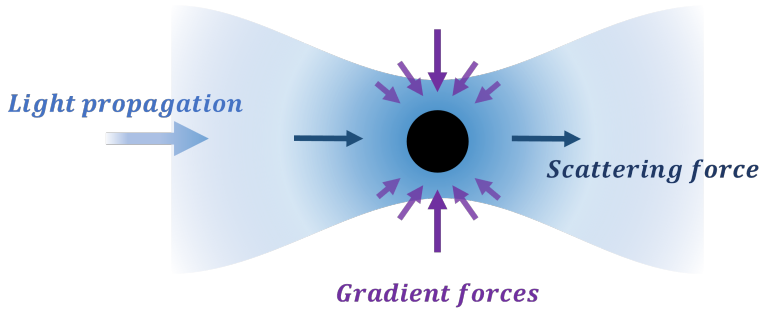

Figure 1.3: Illustration of optical forces applied to a particle by a focused beam. The scattering force pushes the particle in the direction of propagation of light. The gradient force pulls the particle towards the beam waist.

It is important to note that the object's polarizability, included in the expressions of optical forces, is a reflection of how easily the electron cloud surrounding a particle is displaced by an electric field. The complex polarizability, α, characterizes this response: its real part, $\mathrm{Re}(\alpha)$, determines the strength of the induced dipole and governs the gradient force that pulls the particle toward regions of higher field intensity, while its imaginary part, $\mathrm{Im}(\alpha)$, represents the component that dissipates energy and contributes to momentum transfer along the propagation direction (scattering force). It is quantitatively expressed as:

$$\alpha = Re(\alpha) + i \cdot Im(\alpha) \tag{1.6}$$

$$Re(\alpha) = 4\pi \cdot a^3 \cdot \frac{\rho^2 - 1}{\rho^2 + 2} \tag{1.7}$$

$$Im(\alpha) = \frac{k^3}{6\pi} \cdot Re(\alpha)^2 \tag{1.8}$$

Where ε_0 and ε_m are respectively the vacuum's and the medium's permittivity, a is the size of the particle and ρ is the ratio of the index of refraction of the particle to the index of the medium (n_p/n_m). These equations show that the polarizability, and therefore the optical forces, depend strongly on both the particle size and the refractive index contrast. Since $\vec{F}_{op} \propto a^3$, larger particles experience substantially stronger forces along the beam propagation direction and, simultaneously, toward regions of higher field intensity, making them easier to manipulate using the same optical setup. Conversely, smaller particles experience weaker forces, which can pose challenges for stable trapping but also allows selective manipulation of different-sized particles in mixed samples.

Additionally, the refractive index contrast, ρ, plays a critical role: particles with a higher refractive index relative to the surrounding medium have larger polarizabilities and therefore experience stronger forces, while particles closer in refractive index to the medium interact more weakly with the field. This interplay between size and refractive index is crucial when designing experiments, as it dictates both the efficiency of trapping and the choice of particle types or mediums for optimal manipulation.

1.3 Optical Trapping

Since the unveiling of the components of optical forces by Ashkin in 1970 [4], numerous applications have emerged that take advantage of this behaviour of light. The scope of these phenomena covers a wide range of fields, from the manipulation of single inert objects and biological specimens, to their stable optical trapping.

Optical trapping was in fact among the first experimental demonstrations of the mechanical action of light on small objects. It was first reported by Ashkin et al. [5] shortly after his initial studies of gradient and scattering forces, and has since become a benchmark technique for both illustrating and exploiting optical forces.

Optical trapping refers to the ability of a light beam to spatially confine, in three dimensions, an object of microscopic or nanoscopic size. Early demonstrations of optical trapping were achieved using two counter-propagating laser beams [4]. In this configuration, axial confinement arises from the balance of radiation pressure forces exerted by the two beams, preventing the particle from being continuously driven along the propagation axis and allowing a stable equilibrium position to be established.

Later, Ashkin demonstrated that trapping can also be achieved using a single tightly focused light beam, such as the one previously represented in fig. 1.3. In this case, the highest light intensity occurs near a focal spot, referred to as the beam waist. The size of the beam waist depends on the numerical aperture (NA) of the lens used to focus the laser beam. The numerical aperture is a dimensionless parameter that characterizes the range of angles over which a lens can collect and emit light. High-numerical-aperture objectives typically have NA values ranging from about 0.8

for air objectives up to 1.4 for oil-immersion objectives, with higher NA corresponding to tighter focusing. Under these conditions, the intensity gradient near the waist is sufficiently steep that the gradient force can dominate over the forward-directed scattering force. In this regime, a particle is drawn toward the focus and held in a stable equilibrium position.

The effectiveness of optical trapping depends critically on both the size of the object and its optical properties, in particular its refractive index, as discussed previously through the mathematical expressions of optical forces. The size of the object determines whether its interaction with the beam falls within the Rayleigh or Mie regime.

For particles much smaller than the wavelength (Rayleigh regime, $a \ll \lambda$), the particle behaves as an induced dipole interacting with the field gradient. Trapping is efficient when the particle has a refractive index sufficiently higher than that of the surrounding medium, such that the gradient force can overcome scattering forces and thermal fluctuations due to Brownian motion.

For particles comparable to or larger than the wavelength (Mie regime, $a \gtrsim \lambda$), the simple dipole approximation no longer holds, and the optical forces must be treated using full scattering theory. In this regime, the stability of confinement is largely determined by the balance between gradient and scattering forces: the gradient force pulls the particle toward regions of high intensity, while scattering pushes it along the beam propagation direction. Achieving stable trapping therefore requires that the gradient force be sufficiently strong relative to scattering, which depends on both particle size and refractive index contrast.

In both the Rayleigh and Mie regimes, if the refractive index contrast ($\rho = n_p/n_m$, see equations (1.3) to (1.8)) is too low, optical forces become insufficient to confine the particle effectively. Consequently, in the near-infrared (NIR, $0.7 - 1.4\ \mu m$) and short-wave infrared (SWIR, $1.4 - 3\ \mu m$) spectral regions, dielectric particles ranging from submicron to several microns, with moderate refractive index contrast relative to the surrounding medium, constitute the most suitable candidates for stable optical trapping. This parameter range defines the practical working conditions for most optical manipulation experiments and guides the selection of both target particles and beam parameters.

In the specific context of biological optical manipulation, these considerations are furthermore relevant, as the characteristic sizes of the objects of interest span both interaction regimes. Viral particles, with typical radii on the order of 10–50 nm, interact with near-infrared trapping beams at telecommunication wavelengths (around 1550 nm) well within the Rayleigh regime ($a \ll \lambda$). In contrast, larger biological objects such as bacteria, which upcoming chapters will focus on, whose characteristic dimensions are typically of the order of 0.5–2 μm, have sizes comparable to the wavelength and are therefore more appropriately described within the Mie regime ($a \sim \lambda$).

This distinction between Rayleigh and Mie regimes underlies the selection of appropriate trapping configurations and device parameters, as it dictates the relevant force models and sets requirements on beam shaping and numerical aperture.

1.4 Devices for Optical Trapping

This section presents a non-exhaustive list of free-space and on-chip devices used for optical trapping, together with examples of their applications. For brevity, these examples will be limited here to biological uses. However, it is important to note that optical traps are widely studied and employed in multiple other domain like quantum photonics [6–9], semiconductor research [9–12], and material assembly [13–16].

1.4.1 Free-space Optical Trapping

Optical Tweezers

The term "optical tweezers" has in recent years become, in the scientific field, an umbrella term that encompasses a broad set of methods for optical trapping. However, it originally referred specifically to the single-beam optical tweezers, also known as “single-beam gradient force traps”, which was the first device used for optical trapping demonstrations [17–19]. This device has since become the most commonly used technique for this purpose among researchers, due to its simplicity. In fact, to create a single-beam optical tweezers setup, one simply needs to pass a laser beam through a high numerical aperture microscope objective. This produces a tightly focused beam with a steep intensity gradient around the beam waist, toward which objects are pulled and trapped, as illustrated in fig. 1.4.

Optical tweezers most commonly use near-infrared lasers ($\lambda \sim 1064$ nm), although telecommunication wavelength lasers ($\lambda \sim 1550$ nm) can also be employed in specialized setups. Focused through high-NA objectives (NA ~ 1.2), the diffraction-limited beam waist is on the order of a few hundred nanometers, depending on wavelength (smaller wavelengths produce tighter waists), input beam size, and residual aberrations [20]; providing the steep gradient required for stable trapping. The system can be tuned to the target particle by adjusting laser wavelength and power [19], and the trapping force can be quantified using established calibration methods (*e.g.*, drag force or power spectrum) [21]. Furthermore, for manipulations that require to move objects within a stationary sample, the direction of optical tweezers can be steered using, for example, a beam steering mirror set-up [22, 23] or spatial modulators [24]. Such small beam waists are particularly important when manipulating submicron biological objects, where the gradient force must dominate over scattering to achieve stable confinement.

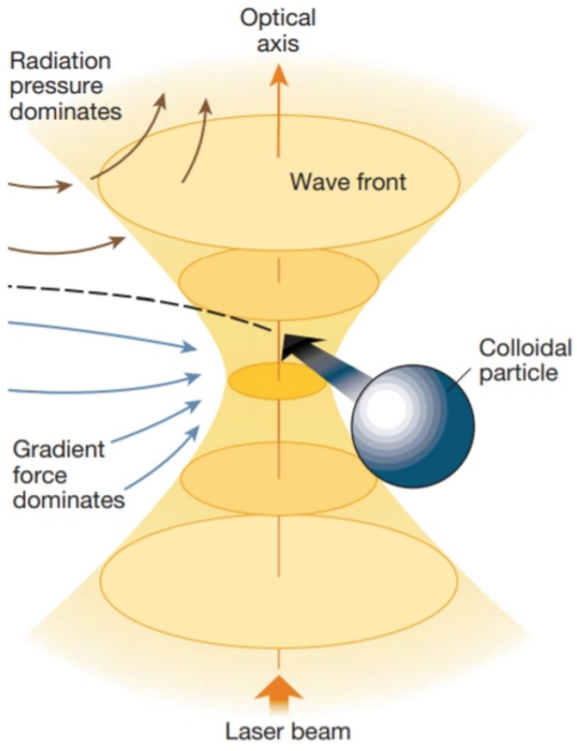

Figure 1.4: Optical tweezers. The balance between gradient forces, which pull particles toward the focus, and radiation pressure, which pushes them along the beam axis, enables stable three-dimensional trapping. Reprinted from [25].

Although conceptually simple, single-beam optical tweezers remain a powerful tool, widely used to manipulate biological objects and investigate biophysical processes. Their ability to capture single cells in a contact-free, non-invasive, and reversible manner enables highly precise studies. For example, Pang et al. employed optical tweezers as a tool for virometry, i.e. the measurement of viruses in a sample. They studied the heterogeneity within a population of HIV-1 viruses in terms of size. This was achieved by optically trapping individual HIV-1 virions (particles of about $100 - 150$ nm containing the viral genome and protein coat), in culture fluid, and quantifying the deflection (deviation) of the laser beam [26]. Another application of cell probing is found in the work of N'guessan et al. related to the use of optical trapping to compare the mechanical properties of healthy and infected red blood cells. In this study, silica (SiO_2) beads were held in the optical trap and brought into contact with red blood cells suspended in biological fluid. The bead's displacement within the trap, following its attachement to the cell, reflected the cell's mechanical resistance, providing a measure of its elasticity [27]. Beyond single-cell studies in vitro, optical tweezers have also been applied in vivo; meaning in or on whole living organisms, as opposed to dead organisms or extracted biological samples. For instance, optical tweezers have been shown to manipulate red blood cells directly within capillary microvessels in order to control cellular flow, rotation, and orientation. Such demonstrations were performed in zebrafish tails [28] and in mouse ears [29], illustrating the potential of optical tweezers for probing living systems at the microscale.

Advanced Optical Tweezers

Depending on the application, it is possible to further advance the basic optical tweezers (OTs) set-up by combining it with other techniques or by generating multiple traps simultaneously. For instance, some studies may require the simultaneous manipulation of more than one object or multiple positions of the same sample, thus requiring multiple traps. This can be achieved using a single-beam source either by splitting the beam or by steering it rapidly between positions [22, 24, 30]. A versatile approach to this is the use of holographic optical tweezers (HOT). This technique uses a computer generated hologram that is applied to the wavefront of the single-beam source, creating multiple, configurable optical traps, each capable of holding and manipulating a microscopic particle with high spatial resolution [31], as illustrated in fig. 1.5(a) [32]. For example, Kemper et al. demonstrated the use of HOTs to manipulate individual bacteria in 3D and align them with potential host cells to observe infectious mechanisms [33].

Alternatively, multiple traps can also be generated in a straightforward way by employing several independent single-beam tweezers. This method is less flexible and scalable than HOTs, for example, but can serve as a simple option when flexibility is not required. In one case, Abbondanzieri et al. demonstrated the use of a dual-trap using two independent optical tweezers to form a "dumbbell" arrangement in order to study DNA mechanisms. In this experiment, each tweezers trapped a polystyrene bead; one bead was tethered to a DNA template and the other to a molecule of RNA polymerase; as illustrated in fig. 1.5(b). These are the two reactants required for transcription in living cells; a sequential chain reaction in which RNA polymerase synthesizes new RNA strands from a DNA template. This setup allowed to extrapolate the size of steps taken by the RNA molecule during the transcription from the movement of the polystyrene bead within the trap, in an Å-scale resolution [34].

Moreover, optical tweezers can be combined with classical imaging and spectroscopic techniques when there is interest not only in the physical properties of trapped microscopic objects, but also their chemical ones. Multiple optical methods can be combined with optical tweezers [31, 35, 36], among them Raman spectroscopy. Raman is commonly used in chemistry to identify molecules via their characteristic vibrational fingerprint by measuring their vibrational modes. Typically, Raman measurements are performed by focusing a laser into a sample (for example,

a solution) and collecting the inelastically scattered light; the resulting spectrum is an ensemble average of all individual molecules within the probe volume. The simultaneous use of a second, independent beam as an optical tweezers creates an arrangement known as “Raman tweezers" and enables Raman studies of single trapped objects at the molecular level [35], as illustrated in fig. 1.5(c) [37]. A specific biological application of this setup is presented in the works of Shuyun et al., who identified liver cancer cells by scanning them with Raman tweezers and classifying the spectra using machine learning [38]. Other techniques, not covered in this manuscript, that can be combined with optical tweezers to create hybrid setups are fluorescence resonance energy transfer spectroscopy (FRET) [39] and surface-enhanced Raman spectroscopy (SERS) [40].

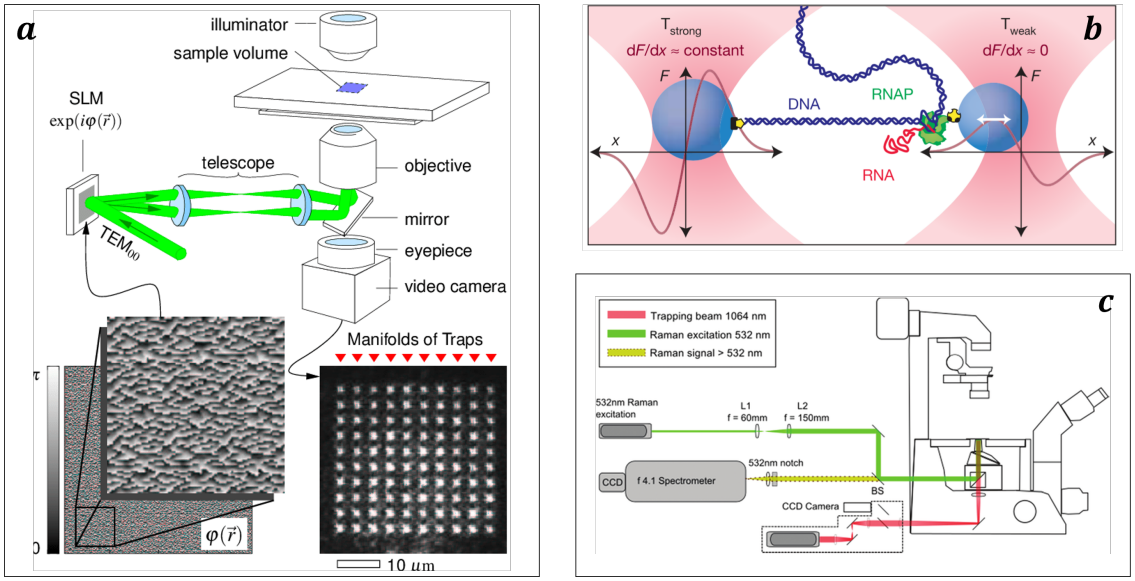

Figure 1.5: Examples of Advanced Optical Tweezers. ***(a)*** *Holographic Optical Tweezers (HOT). A source beam is diffracted by a Spatial Light Modulator (SLM) into multiple beams, which are relayed into an objective lens that focuses each into an individual optical trap. Reprinted from [32].* ***(b)*** *illustration of the dual-beam dumbbell geometry with two trapped beads (blue) where one is tethered to an active RNA polymerase (RNAP, green) molecule and the other to a DNA template (dark blue). To synthesize new RNA (bright red), RNAP first needs to locally open the double-stranded DNA, causing its elongation, and thus the beads move apart. The relative displacement is measured using force–position curves (dark red). Reprinted from [34].* ***(c)*** *An example of Raman tweezers. An optical trap (red) holds cells in position for alignment with the optical setup. Backscattered Raman light from the individual cells, excited by a Raman laser at 532nm, pass through a beam-splitted (BS) and a 532nm "notch" filter both aligned with the spectrometer. Reprinted from [37].*

Drawbacks & Limitations

Advanced optical trapping systems, particularly when combined with complementary optical techniques as presented in the previous section, typically demand conceptually simple yet experimentally elaborate arrangements that rely on bulky objectives and alignment-sensitive free-space components. These requirements introduce several limitations. The physical footprint of the setup increases, making parallelization of experiments more difficult, since each additional trap often implies the use of further optical hardware. Moreover, the long-term stability of free-space tweezers can be compromised by mechanical drift or misalignment of optical elements, leading to fluctuations in trapping performance and reducing the reproducibility of measurements.

Beyond these technical considerations, a more fundamental challenge arises from the application of classical free-space OTs specifically for trapping biological objects, which can be restricted by the potential for laser-induced damage. In fact, stable trapping usually requires high light intensities, but these can impose stress on living systems in two principal ways: photodamage and thermal damage [41]. Photodamage arises when photon absorption by biomolecules leads to electronic excitation. This phenomenon is primarily a linear process. Therefore, elevated laser powers accelerate molecular excitation, which in turn accelerates cellular damage. This was clearly illustrated in early experiments in the field of optical trapping, conducted by Ashkin and Dziedzic, where a bacterium remained intact for 10 minutes under a low-power beam of $\sim$ 5mW but was killed within about a minute, losing much of its intracellular content, when the power was raised to $\sim$ 100mW [19].

The choice of the trapping wavelength strongly influences the extent of such effects. In fact, ultraviolet (320-400 nm) and visible (400-700 nm) wavelengths are efficiently absorbed by biomolecules [41], making them particularly damaging and therefore largely unsuitable for long-term manipulation [42]. Consequently, such wavelengths have been largely avoided since the earliest optical trapping studies. Indeed, Ashkin and Dziedzic initially employed a visible laser at 514.5nm in the previously mentioned experiment [19], but in a subsequent work published the same year, Ashkin et al. focused their work on a near-infrared (NIR) laser (1064nm) to reduce absorption by biological material and improve cell viability [5].

The move to infrared light, now widely adopted for optical trapping of biological objects, represented a crucial step in establishing OTs as a practical tool for biology. However, it introduces another consideration: thermal effects. While heating can in principle occur at any wavelength if sufficient energy is absorbed, in the NIR the dominant contribution arises from weak but non-negligible absorption by water, the main component of biological samples. This localized heating near the beam focus can lead to cell stress and thermal damage, which has been documented in bacteria [5, 41, 43], red blood cells [44], and single living cells such as Chinese hamster ovary cells and human sperm cells [45].

Therefore, while infrared lasers lower the risk of of photodamage to optically trapped objects, the trade-off is a higher risk of thermal damages to biological samples. The choice of an optical trap's exact configuration for biological applications thus represents a delicate balance between trapping stability and sample integrity.

1.4.2 On-Chip Optical Trapping

Waveguides

A waveguide, or optical guide, is a simple physical structure that directs light waves injected into it along a specific path defined by the guide's geometry. Optical fibers are a well-known example of such guides. When light propagates inside a waveguide, an evanescent component of the electromagnetic field extends from the core into the surrounding medium. This evanescent field, illustrated in fig. 1.6b, does not propagate freely in space, but rather decays exponentially away from the waveguide. The exponential decay of the evanescent field creates a steep intensity gradient in the surrounding medium. This gradient gives rise to optical gradient forces that can attract and trap particles near the waveguide surface, making it possible to manipulate nanoscale objects with precision. Because the evanescent field stays within the nearby environment, guides can be exploited for applications such as optical trapping. For this purpose, both fiber-based technologies and on-chip lithographically fabricated guides are commonly used.

Although fiber-based technologies are presented here in the on-chip traps section within the context of evanescent trapping, it is important to note that, in literature, they often stand as their own separate category: they are not free-space traps since light is confined and delivered via the

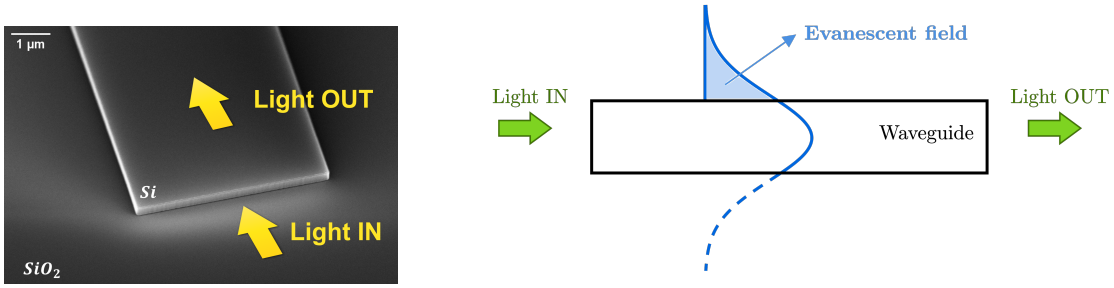

(a) *(b)*

Figure 1.6: Waveguides. (a) SEM image of a Silicone (Si) waveguide. (b) Illustration of electric field and its evanescent part when light travels through a waveguide.

physical guide (the fiber) in contrast to focusing the beam via lenses in open space, nor are they strictly on-chip technologies since they are not fabricated and integrated on a planar structures. Independently of their exact classification, optical fibers are versatile optical tools since their geometry can be changed to make, for example, micro- or nano- fibers with sub-wavelength diameters. The evanescent field present in the surroundings of such nanofibers when light propagates within them can be used to trap and manipulated particles, including various bacterial species [46–48].

The same trapping principle applies to classical optical guides fabricated on planar chips, such as the example shown in fig. 1.6a. The choice of waveguide material primarily depends on its refractive index and transparency at the trapping wavelength. In addition, the effectiveness of trapping is influenced by the refractive index of the surrounding medium and the objects to be trapped. The literature contains many examples of materials used for fabricating waveguide traps such as polymers [49, 50], or dielectric and semiconductor materials [51, 52]. For example, Gaugiran et al. demonstrated trapping and propulsion of red blood cells and yeast cells along a silicon nitride Si_3N_4 waveguide [52], which is transparent in the visible spectrum, unlike silicon Si.

Optical Ring Resonators

An optical ring resonator is a closed-loop waveguide, typically at the micrometer scale, that traps light by repeatedly circulating it around the loop. Resonance occurs when the round-trip optical path length is an integer multiple of the wavelength, allowing the circulating light to constructively interfere with itself and form a standing wave. Under this condition, light builds up inside the ring, enhancing the optical field both within the core and in its evanescent tail, which can then be used for optical trapping. However, micro-rings do not work as a stand-alone device. They most typically rely on evanescent coupling from adjacent linear waveguides for excitation.

In order to monitor any changes to the their resonance field, such as those induced by trapped objects, the transmitted light is collected either through the input guide, or a second adjacent one dedicated as an output. The resonator geometry can vary as long as it forms a closed loop, including circular, oval, or spiral shapes, as illustrated in fig. 1.7. Each closed-loop structure constitutes an independent ring resonator, evanescently coupled to a nearby linear waveguide for excitation and readout. Choice of the exact geometry can depend on many factors such as footprint constraints or field enhancement. For example, spiral layouts increase the optical path length within a compact area, enhancing the circulating field and strengthening the evanescent tail used for trapping. In some designs, neighboring resonators may be placed close to one another, but unless specifically engineered for coupling, each ring acts as an independent resonant cavity addressed through its own access waveguide.

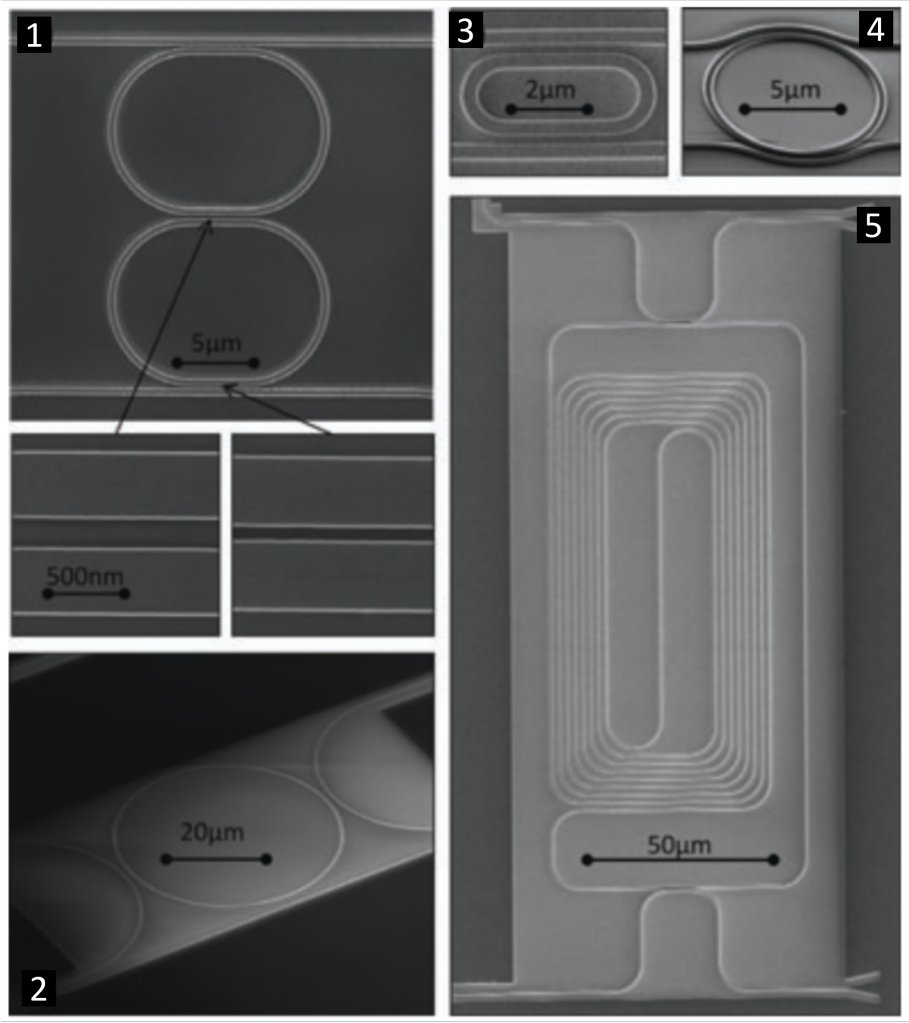

Figure 1.7: Examples of silicon ring resonator geometries. Reprinted from [53]

Like their linear counterparts, ring resonators can also serve as biosensors to trap and manipulate biological objects. In this context, the presence of target analytes is typically inferred from shifts in the resonance field as particles or molecules interact with the evanescent wave surrounding the ring. Several studies highlight this capability: Abul Kalam Ajad et al. demonstrated the detection and quantification of hemoglobin molecules directly in whole blood [54], while Ali et al. reported highly sensitive identification of different cancer cell types in clinical specimens [55].

Plasmonic tweezers

Plasmonic tweezers are a class of optical trapping devices that rely on conducting metallic nanostructures, most commonly fabricated from gold (Au) or silver (Ag), patterned on or integrated within a supporting surface. When such nanostructures are illuminated by a laser, the incident photons couple to the collective oscillations of the excited electrons at the metal–dielectric interface between the plasmonic structure and the medium surrounding it. This coupling gives rise to localized resonances called surface plasmon resonances. As a result, electromagnetic energy is strongly concentrated near the surface into nanoscale volumes far below the diffraction limit, producing highly confined “hot spots” with extremely steep spatial intensity gradients. These gradients generate strong optical forces, which can be exploited to trap and manipulate nanoscale objects in the immediate vicinity of the plasmonic structure.

Additionally, the geometry of plasmonic nanostructures can be tailored to the intended application and to the characteristic size of the objects under study. These structures may be fabricated as embossed features above the conducting surface (*cf. fig. 1.8(a-c)*) or as hollow apertures within it (*cf. fig. 1.8(e-f)*). Each configuration produces distinct patterns of field confinement: localized at protruding tips in the embossed structures and enhanced around aperture edges in the hollow ones.

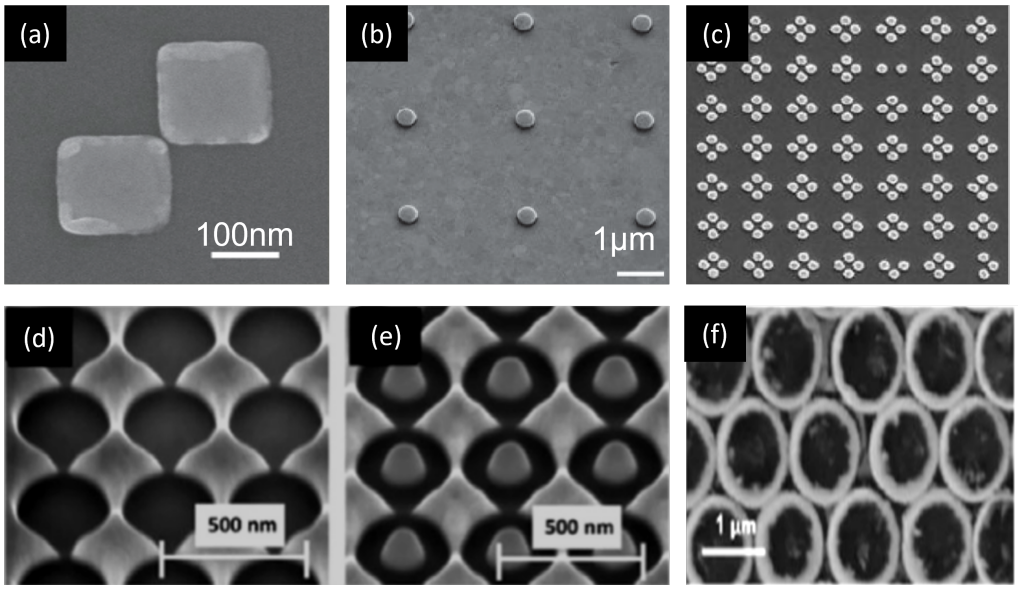

Figure 1.8: Examples of Plasmonic Nanostructures Geometries.
***(a-c)** Embossed patterns. **(d-f)** Hollow apertures.*
Reprinted from: (a) [56], (b) [57], (c) [58], (d-f) [59].

Excitation of plasmonic tweezers is commonly achieved by coupling light into integrated photonic elements such as linear waveguides. Depending on the configuration, coupling can occur either through direct transmission, when the waveguide is aligned with the plasmonic site, or through evanescent fields, when the waveguide runs adjacent to it. Changes in the plasmonic resonance are then detected by monitoring variations in the transmitted light, collected via the input or a dedicated output waveguide.

This ability to integrate plasmonic tweezers with on-chip photonic components makes them particularly suitable for biological studies, in particular in complex liquid environments. For instance, Kee et al. demonstrated real-time monitoring of bacterial growth directly in culture medium [60], while Syal et al. applied plasmonic tweezers to antibiotic susceptibility testing by correlating bacterial motility with metabolic activity under antibiotic stress [61].

Photonic Crystals

Photonic crystals (PhC) are optical devices based on a periodic arrangement of dielectric materials with contrasting refractive indices (RI), in one, two or three dimensions. When illuminated, this periodicity creates a spatial modulation of the electromagnetic environment that reveals frequency intervals, called bands, in which light propagation through the structure is allowed or forbidden. The ranges of these bands depend of the comparison between a the periodicity of the structure, and λ_m the wavelength of light inside the material (not the free-space wavelength in vacuum).

For a given direction within the photonic crystal, if λ_m is much bigger than a, the structure appears homogeneous to the wave, allowing light to propagate almost as in a bulk medium. These

wavelengths are called modes. However, if λ_m is comparable to a, light in repeatedly scattered at each interface between low and high RI regions, resulting in interference between the waves where their intensities and displacements are combined. If the resulting waves have higher amplitudes, the interference is constructive and the wavelengths become allowed modes. On the contrary, if it results in lower amplitude waves, the interference is destructive and these wavelengths, called bandgaps, are forbidden from propagating through the structure.

Photonic crystals can become resonating cavities when their perfect symmetry is disrupted by introducing a defect in a region of high or low RI. In this case, a single mode, that would otherwise fall within a forbidden band, becomes localized within the defect and concentrated in it thanks to the internal reflection between the periodic regions on either sides of the defect that act like mirrors, similar to a Fabry-Pérot system. This creates an evanescent field above the defect, often referred to as cavity, that can be used for optical trapping. Figure 1.9 is an illustration of three types of PhC cavities in one-, two-, and three-dimensional structures. The taper zone shown in fig. 1.9(a) is introduced to gradually adapt the refractive index along the propagation direction and to enhance the concentration of light within the cavity.

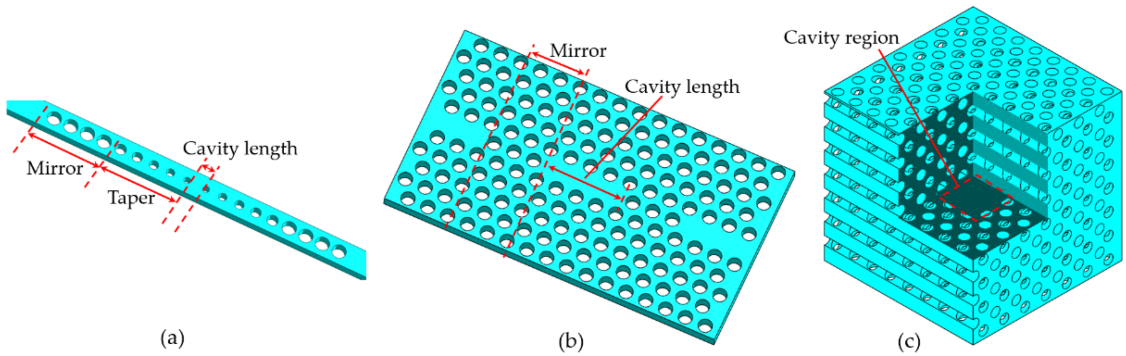

*Figure 1.9: **(a)** 1D, **(b)** 2D, and **(c)** 3D photonic crystal (PhC) cavities. Reprinted from [62].*

When exciting a PhC cavity, typically through a linear waveguide as in the previously described devices, the transmitted spectrum reveals a single mode within its forbidden band, appearing as a peak at the resonance wavelength, as show in fig. 1.10. This wavelength, λ_0, together with the quality factor $Q = \lambda_0/\Delta\lambda$, where $\Delta\lambda$ is the full width at half-maximum (FWHM) of the resonance peak, are unique to each cavity. These parameters are primarily determined by the architecture and dimensions of the structure and can be set through appropriate design choices prior to fabrication. In typical photonic crystal cavities, quality factors range from a few thousand to several tens of thousands. The resonance wavelength, while fixed by design, also remains sensitive to the optical properties of the surrounding medium. Consequently, when the optical forces of the evanescent field attract an object toward the cavity surface, it results modification of the local refractive index (RI), thereby shifting the established resonance. The changes in the transmitted signal following this disruption allows to detect the trapping event.

Photonic crystals are highly scalable, as their architecture can be engineered to obtain specific characteristic values, enabling precise adjustment of the resonance wavelength to the intended study. This makes PhC cavities particularly suitable for experiments involving biological objects. Several studies in the literature report the use of PhC cavities not only as trapping tools but also as biosensors to probe different properties and phenomena. For example, Tardif et al. demonstrated the use of 1D PhCs to study the effect of thermal stress on bacterial viability[63], while Tartari et al. employed 2D PhCs to monitor the lysis (death) of a single bacterium infected with bacteriophages (viruses) [64].

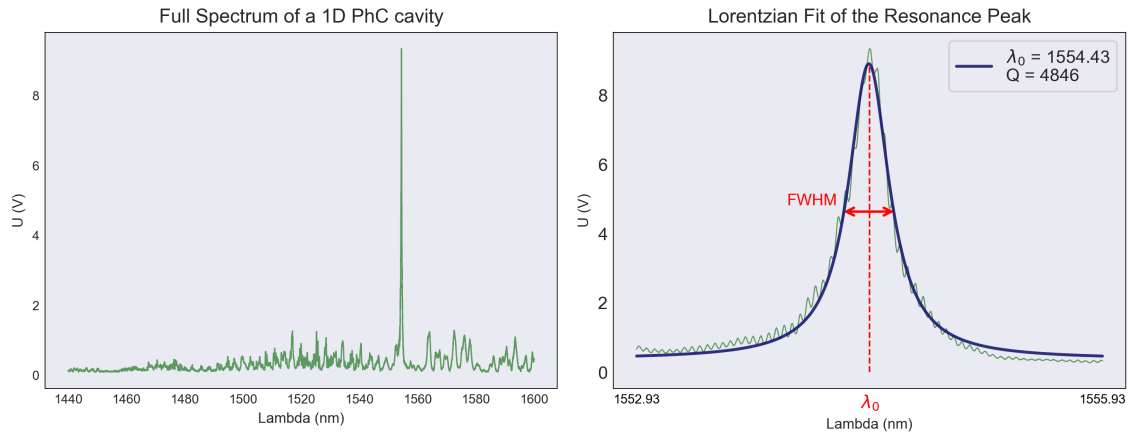

Figure 1.10: Resonance Spectrum of a 1D Photonic Crystal Cavity. ***Left:*** *Original spectrum covering the full spectral range of the source laser (1440-1640 nm), showing the cavity's bandgap and resonance peak. This signal was acquired on a chip fabricated in our lab, with the cavity surrounded by pure water and an input laser power of* 10 mW. ***Right:*** *Zoom on the resonance peak, fitted with a Lorentzian function to determine its characteristic values λ_0 the resonance wavelength, $\Delta\lambda$ (FWHM: FUll-width at half maximum), and Q the quality factor.*

Opto-fluidic devices

The planarity of the on-chip optical devices presented in the previous sections makes them easy to integrate with other on-chip technologies that are fabricated, aligned or packaged using similar or standard processes. In particular, planar photonic elements can be embedded in microfluidic chips, producing compact "opto-fluidic" devices that can steer, hold and channel microscopic objects directly toward on-chip photonic structures with high spatial accuracy.

In such a configuration, the microfluidic channels provide controlled sample delivery, small reaction volumes and clean, isolated chambers, while the optical trap structures ensure non-contact, highly localized manipulation. Therefore, it is possible to position and stabilize individual particles, droplets or cells inside tiny reagent volumes without physical contact or cross-contamination, and to monitor them in real time.

Moreover, since trapping is achieved optically even with low light powers, handling remains non-invasive and label-free, preserving fragile samples while enabling precise operations. The small spatial footprint of these devices also allows parallelization, enabling multiple channels to simultaneously deliver different objects to different embedded traps or to mix reagents efficiently.

All these capabilities make optofluidic systems particularly attractive for single-cell biology, diagnostics, and small-scale automated workflows where precision, cleanliness and integration are critical and crucial requirements.

Advantages & Interests

Building on these integration capabilities, it is useful to highlight the general advantages of on-chip optical tweezers, as they address many of the practical and fundamental limitations of free-space devices presented previously, while giving more opportunities for scalability and multi-functional integration.

By confining optical fields within nano-structures fabricated directly onto photonic chips, the physical footprint of the device is largely reduced. While some classic optical components might still be required for light injection and collection, into and from the waveguides transporting light

to the photonic structures, they can be very minimal and mutualized between multiple traps on the same chip. Indeed, planar integration of such devices enables large-scale parallelism, allowing hundreds to thousands of photonic structures to be integrated on a single chip with lateral dimensions of a few hundred millimeters. Because they are often fabricated using standard semiconductor processes, such devices additionally benefit from the possibility of large-scale, cost-effective mass production.

Beyond these mechanical advantages, on-chip approaches also alleviate several biocompatibility issues that limit free-space optical tweezers. Evanescent-field traps generated by integrated waveguides or resonant structures confine strong optical gradients within the immediate vicinity of the surface and therefore typically require lower input powers than free-space optical tweezers to achieve comparable trapping forces [65]. In practice, such on-chip traps can operate with input optical powers on the order of a few milliwatts while generating optical forces in the piconewton range. The exact force magnitude depends strongly on the size of the trapped object and on the refractive-index contrast between the particle and the surrounding medium, consistent with the optical force expressions introduced earlier. As a result, the reduced optical power requirements significantly decrease both direct optical excitation and heat-induced damage experienced by biomolecules compared to conventional free-space tweezers.

Moreover, resonant enhancement within these structures can further amplify the local optical field for a given input power, thereby improving trapping efficiency. In photonic crystals, for example, this is achieved by tuning the geometry of the holes and the cavity to increase the quality factor (Q). Consequently, biological specimens can often be stably confined using lower light intensities, minimizing both photodamage and thermal stress and enabling longer, non-destructive manipulations. However, Q factors that are too high may actually hinder trapping, as the cavity becomes excessively sensitive to small changes caused by the trapped object, which can reduce the light intensity available for trapping and make confinement less stable. These phenomena, the consequent trade-offs in resonator design, and their implications for optical trapping performance, will be discussed in more detail in the next chapter.

1.5 Conclusions

In this chapter, we presented the main types of light-matter interactions, with a particular emphasis on the use of optical forces to trap and manipulate microscopic objects. Different types of photonic devices can be applied as optical traps, in free-space using simple optical components as well as on-chip with various photonic structures. We discussed the advantages of on-chip photonic structures in comparison to the free-space alternative, as they are compact, more tunable and easy to combine with other on-chip technologies. This chapter lays out part of the theoretical concepts on which the work presented in this manuscript relies, where opto-fluidic on-chip devices based on one-dimensional photonic crystals are used to investigate not only the trapping but also the optical sensing of biological samples, particularly bacteria.

2
Our Setup

In this chapter, we will present the experimental set-up used in this PhD to achieve optical trapping of biological objects, as well as the toolbox of methods and processes applied to fabricate certain components of this set-up.

Contents

2.1 Photonic Traps: Structure Selection 22
2.2 Photonic Traps: Chip Realisation 23
2.2.1 Design Tuning 23
2.2.2 Fabrication 26
2.2.3 Effect of SOI thickness 30
2.2.4 Light Coupling & Mode Adaptors 35
2.3 Microfluidic Integration 42
2.3.1 Static Fluidic Pool 42
2.3.2 On-chip Fluidic System: Designing 43
2.3.3 On-chip Fluidic System: Fabrication 44
2.4 Optical Bench 47
2.5 Conclusions & Perspectives 50

2.1 Photonic Traps: Structure Selection

As this work centers on the optical trapping of bacteria, we selected photonic crystals as our trapping device, rather than alternative on-chip trapping schemes such as ring resonators or plasmonic devices. This choice was guided by several practical and functional considerations that balance optical performance, fabrication feasibility, and biological compatibility.

Architecturally, one- and two-dimensional PhCs provide strong field localization at the surface of their cavities while maintaining relatively low fabrication complexity. The structure's periodicity enables robust light confinement and avoids the strict fabrication sensitivities associated with resonant ring traps [66, 67]. Although resonating PhCs are not entirely immune to imperfections, the spatially extended evanescent field of their cavity modes tends to average out the impact of localized fabrication defects, making their optical response comparatively less sensitive to such errors. When such PhC structures are in resonance, they localize light around their cavity region, but this resonance is not confined to a single point; it "leaks" into several nearby photonic crystal unit cells, creating multiple small overlapping maxima around the cavity, as shown in fig. 2.1. This energy distribution across several lattice sites implies that the effect of a single geometric imperfection in one of these sites is diluted compared to a single-spot resonance, leading to a smaller change in the intensity profile. Therefore, gradient forces in photonic crystal cavities are comparatively less affected by fabrication imperfections, especially in 1D PhCs in comparison to 2D or 3D ones as the design simplicity lowers the statistical risk of errors [68].

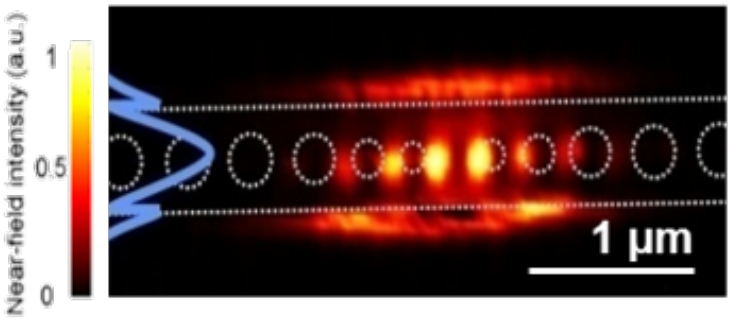

Figure 2.1: SNOM (scanning near-field optical microscopy) image of an excited 1D photonic crystal cavity at resonance. SNOM enables direct observation of evanescent fields in nanostructures. The image reveals that the evanescent field is localized in the defect region while extending into the neighboring unit cells. The exact dimensions of the cavity used for this measurement are unknown. Image credits go to Kevin FOUBERT (CEA/SiNaPS, 2010) [69].

Moreover, while plasmonic traps are also capable of generating strong near-field confinement, the conductive nature of their metallic surfaces introduces significant absorption losses and localized heating problems [70, 71], which are typically undesirable when manipulating biological samples, such as bacteria, to avoid the risk of photodamage and thermal stress. In contrast, photonic crystals made of dielectrics or semiconductor materials embedded in dielectric media are far less prone to ohmic losses and thermal effects [72], making them more compatible for delicate biological applications. This thermal stability not only preserves sample viability but also ensures that optical forces remain the dominant mechanism influencing sample dynamics.

Finally, as mentioned earlier, the planar and compact geometry of photonic crystal resonators allows for seamless parallelization of trapping sites. Therefore, although all the experiments presented in this manuscript were conducted primarily on 1D PhCs, we fabricated and used chips that actually contain both 1D and 2D photonic crystals as a part of our collaboration with researchers from EPFL in Switzerland, who focus their research on 2D PhCs. In our current design, each of these different structures is excited by its own waveguide so they are used independently of

one another. This layout results in chips holding 120 waveguides distributed over less than one third of their length, corresponding to $\approx$ 1cm, and covering the full width of the chip. The remaining area along the length is deliberately left empty to allow manual handling with laboratory tweezers without damaging the photonic structures. These numbers indicate that the chip could accommodate far more devices if the full surface was utilized. This joint chip therefore showcases the advantages of the on-chip architectures presented in the previous chapter, where compactness facilitates multi-integration. Accordingly, in this chapter we present the exact architecture of these chips, their incorporation into a microfluidic system, as well as the technical considerations and procedures followed for their fabrication.

2.2 Photonic Traps: Chip Realisation

2.2.1 Design Tuning

Before the actual fabrication of a photonic crystal cavity, a design phase is required to determine the precise dimensions of the structure. This step is essential, as the optical properties of a 1D PhC cavity, such as its characteristic parameters λ_0 and Q, referring respectively to the resonance wavelength and quality factor, are highly sensitive to geometrical parameters including lattice period, hole radius, and cavity length. Careful tuning of these parameters ensures that the final structure meets the spectral and functional requirements of the intended experiment, while remaining compatible with fabrication tolerances.

The general design of our resonating cavity is illustrated in fig. 2.2. It is made of two symmetrical series of periodic holes separated by a gap that constitutes the defect of this photonic crystal. The number, arrangement and dimensions of these holes all influence the optical properties of the structure. The holes in this cavity fall into four regions: two mirror regions and two taper zones. The mirror regions are formed by a constant repetition of identical holes whose equal diameters and strictly periodic arrangement create a photonic bandgap. Wavelengths lying within this band are strongly reflected by the mirrors, so they cannot propagate through the periodic lattice. However, a small portion of the field penetrates into the mirror regions as an evanescent tail. This evanescent component plays two essential roles. First, when an incident field is reflected by the mirrors, its weak evanescent penetration can reach the defect region, and if its frequency matches the defect mode, it excites the cavity and produces resonance. It is important to note that, in the context of guided waves, a “mode” refers to the spatial distribution of the electromagnetic field and not to its optical frequency. Second, once the cavity is resonating, the high reflectivity of the mirror regions confines the field between the two mirrors while still allowing it to extend slightly into the mirror regions. This leakage enlarges the near-field volume above the surface that can be exploited for optical trapping by expanding the effective trapping spot, and it also allows a fraction of the light to couple out of the cavity and propagate through the waveguide to be collected. The SNOM images shown previously in fig. 2.1 illustrate this penetration of the resonant field into the mirror regions.

While the mirrors govern the reflection and confinement of the cavity mode, the taper regions determine how efficiently energy is exchanged between the defect mode and the surrounding mirror regions. The taper regions lie immediately adjacent to the defect, where the hole size increases progressively with distance from the center, as seen in fig. 2.2. Without these tapers, the abrupt boundary between the defect and the periodic mirror lattice would introduce a strong impedance mismatch that causes scattering and reduces the cavity quality factor. By gradually modulating the local effective refractive index, the tapers create a spatially varying photonic bandgap, thus

offering an adiabatic spatial transition from the highly confined defect mode to the evanescent modes supported by the periodic mirror regions. This gradual transformation improves spatial mode overlap and increases the efficiency with which energy is coupled into and out of the defect. It also reduces undesired back-reflection and scattering at the interfaces between the mirrors and the waveguides[73, 74]. As a result, the tapers significantly enhance both the Q factor and the usability of the cavity mode for practical coupling and optical manipulation.

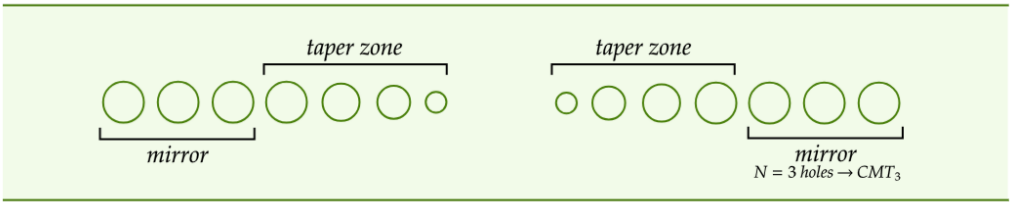

Figure 2.2: Illustration of a 1D PhC cavity design

It is important to note that while the theory behind the role of mirror and taper zones is presented in this manuscript, their geometry and design (number, diameter and spacing of holes) were chosen and optimized in previous studies within our research group. Modifying the design of either part of the cavity goes beyond the objectives of this PhD. The current work presented here focuses on experiments using photonic chips that were fabricated in our labs, either prior to or concurrently with this PhD, mainly by Marc ZELSMANN, the PhD director. All other measurements or results presented (such as characterization spectra, microfluidic integration, and so on) were obtained by me, unless clearly stated.

Moreover, in these previous studies the 1D PhC cavities were named CMTx for brevity: CMT stands for coupled-mode theory, as a representation of how these resonators are excited, while x is the number of holes per mirror. For instance, the design presented in fig. 2.2 is a CMT3, as this resonator has three holes per mirror. This nomenclature will be kept throughout this manuscript.

In fact, the number of repeated holes plays a critical role. Long mirrors contain a larger number of identical periodic holes. While increasing the number of periods does not change the photonic bandgap itself, it increases the mirror reflectivity because evanescent modes decay more strongly as they extend through a longer mirror. As a result, the resonant field becomes more tightly confined around the defect, which leads to higher quality factors Q. Conversely, shorter mirrors contain fewer holes, so the evanescent field decays less before reaching the output waveguide. This weaker attenuation allows more efficient in- and out-coupling, which increases the transmission amplitude of the resonance peak, as observed experimentally. However, the reduced mirror reflectivity also decreases the degree of confinement.

This trade-off is illustrated in fig. 2.3, where we compare the spectra of three resonators: CMT3, CMT4 and CMT5. In these structures, the cavity length as well as the taper and mirror hole dimensions are identical, so the only variable is the number of mirror holes. Additionally, all spectra where measured under the same conditions in water, with the same laser power input $P_{in} = 10mW$. The results show that increasing the number of mirror holes leads to higher quality factors Q, consistent with stronger confinement of light in the cavity. At the same time, we experimentally observe that reducing the mirror length leads to a higher transmission amplitude of the resonance peak, indicating more efficient coupling of light from the cavity into the output waveguide.

In addition, we observe on these spectra from fig. 2.3 a slight, non-linear blueshift of the resonant wavelength as the number of mirror holes increases. This shift results from the change of the effective refractive index between the three structures CMT3, CMT4 and CMT5. The effective RI n_{eff} represents the refractive index that the mode "feels" as it propagates through the structure.

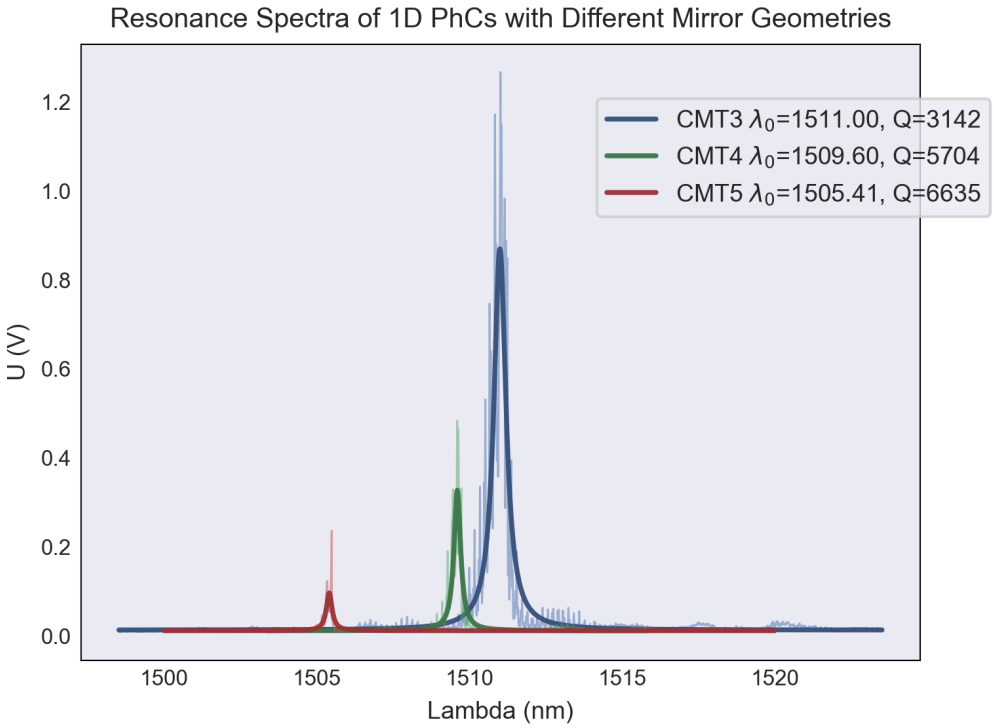

Figure 2.3: Comparison of spectral characterization of 1D PhCs with different mirror lengths (number of identical holes): CMT3, CMT4 & CMT5. These resonance spectra were acquired on structures fabricated in our lab, with the cavity surrounded by pure water and an input laser power of 10 mW.

In fact, since the resonating mode penetrates partially into the mirrors (cf. fig. 2.1), extending the mirror modifies the penetration depth and thus extending the refractive index variation experienced by the mode as it overlaps with regions of different materials. According to the resonance condition defined as

$$\lambda \approx \frac{2n_{eff}L}{m} \tag{2.1}$$

where L is the cavity length and m is an integer, a reduction in n_{eff} leads to shorter resonance wavelength. This indicates that in structures with longer mirrors, such as CMT5, the resonant field penetrates less into the mirror regions, resulting in a lower effective refractive index and explaining the observed blueshift.

Lastly, the spectra presented throughout this manuscript, such as figs. 1.10 and 2.3, are fitted with a Lorentzian distribution to suppress undesired interferences within the device. These interferences result from the strong effective refractive index mismatch between the cavity regions and the input and output waveguides, as well as between the waveguides and the surrounding medium (air, water,... etc), which causes internal reflections illustrated in fig. 2.4 (red and gray loops). These reflections manifest as sinusoidal modulations superimposed on the resonance peaks and can therefore distort the spectral response and signal quality. Beyond its mathematical convenience, the Lorentzian lineshape has a physical origin, as it corresponds to the spectral response of a single resonant mode undergoing exponential energy decay in time [75]. To obtain a more reliable estimation of the cavity's characteristic parameters, a Lorentzian fit is applied using `Python`. The fitting routine relies on the analytical expression of the Lorentzian function:

$$L(\lambda) = A + \frac{B}{1+4\left(\frac{\lambda-\lambda_0}{\gamma}\right)^2} \tag{2.2}$$

where λ_0 is the resonance wavelength, γ is the full width at half maximum (FWHM), A represents the baseline offset, and B corresponds to the amplitude related to the peak intensity. The optimization is performed iteratively through nonlinear least-squares regression and carried out in two successive steps. A preliminary fit using a simplified Lorentzian provides initial estimates of λ_0 and γ, which are then refined in a second fit including amplitude and offset parameters. This two-step approach improves numerical stability and ensures consistent extraction of the resonance wavelength and quality factor, $Q = \lambda_0/\gamma$, while effectively filtering out parasitic oscillations caused by internal reflections.

It should be noted that, although undesirable for cavity characterization, these additional spectral components can, via Fourier transform analysis, provide broader information about the device; such as the lengths of the waveguides between its facets or between each facet and the cavity. These aspects, however, are beyond the scope of the present work and are not addressed in this manuscript.

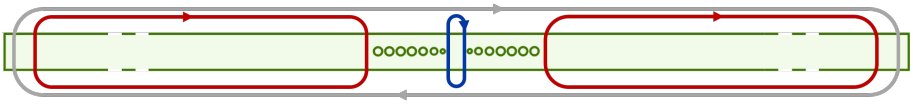

Figure 2.4: Illustration of internal reflections within a CMT3. Blue indicates resonance in the central cavity, red shows reflections between the input/output facets and the cavity, and gray represents reflections between the outer facets. Arrows are drawn outside the waveguide for clarity, although the reflections occur within its bulk, highlighted in light green.

Taking all these design considerations into account, the structures chosen for our optical trapping experiments are CMT3. The exact architecture of the resonating cavities, i.e. the cavity's length and the holes' dimensions, was inspired by previous works in this project by Manon TARDIF [76] for a 250 nm-thick photonic layer, and subsequently finetuned via `Lumerical` simulations by Dylan DAVID for samples with a 220 nm-thick layer. These dimensions are presented in fig. 2.5, and the choices regarding the sample thickness values mentioned here will be discussed later within this chip realisation section.

2.2.2 Fabrication

After designing and validating these photonic structures, the next step is their physical realization through fabrication. This is typically carried out on a semiconductor wafer based on silicon-on-insulator (SOI) technology, which consists of three distinct layers, as illustrated in fig. 2.6 (not to scale). The bottom layer, a thick silicon Si substrate of about $750\mu m$, provides mechanical stability to the wafer. Referred to as the support layer or the handle layer, it increases the wafer's overall rigidity and minimizes the risk of breakage during processing. Above it lies the buried oxide (BOX) layer, an embedded SiO_2 film of $2\mu m$, which acts as an electrical insulator and optically separates the top device layer from the substrate, thereby reducing optical leakage. Finally, the topmost layer is a thin film of monocrystalline silicon, typically a few hundred nanometers thick. This layer is often referred to as the device layer or the active layer, as this is where the functional structures are patterned and etched, enabling the definition of electronic circuits or, in our case, nanophotonic components; it was also referred to as the photonic layer in the previous section. It is this top layer that gives SOI wafers their name Silicon-on-insulator, but also their versatility, making them the platform of choice for integrated photonics. At infrared wavelengths

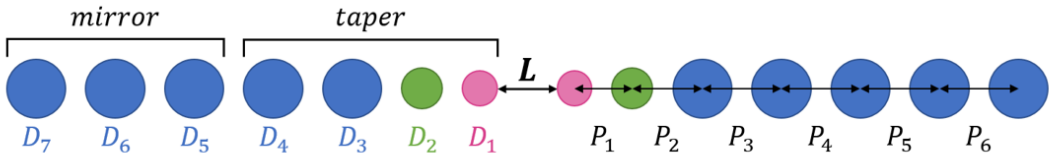

hole diameters (nm)	
D_1	170
D_2	200
D_3	230
D_4	230
D_5	230
D_6	230
D_7	230

Cavity length (nm)	
L	424

hole periodicity (nm)	
P_1	339
P_2	362
P_3	364
P_4	390
P_5	415
P_6	415

Figure 2.5: Characteristic dimensions of CMT3 cavities optimized through optical simulations for samples with a photonic layer of 220 nm thickness. The periodicity is defined as the distance between the centers of consecutive holes, while the cavity length is measured between the edges of the innermost holes.

($\sim$ 1550 nm), the refractive index of silicon is approximately 3.48, while that of silicon dioxide is about 1.44 [77]. This provides strong vertical optical confinement in the device layer, as light is largely confined within the high-index silicon by total internal reflection at the interface with the lower-index oxide and at the upper interface with the surrounding medium, minimizing leakage into the substrate. This medium is typically air or an aqueous solution. As a result, even before any patterning, the device layer behaves as a planar slab waveguide, and it is this intrinsic guiding property that makes SOI particularly suited for nanophotonic design.

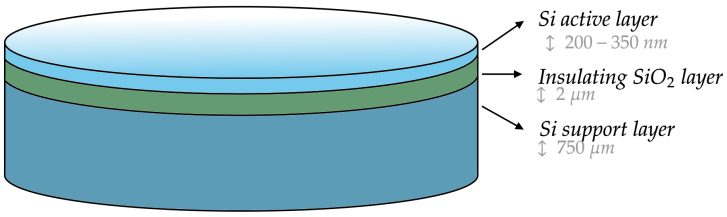

Figure 2.6: Illustration of the layered structure of the SOI wafers used in this work. At the bottom, the Si handle layer is 750µm thick and provides mechanical support for wafer rigidity. In the middle, the SiO_2 buried oxide layer is 2µm thick and electrically insulates the device layer. At the top, the Si device layer, a few hundred nanometers thick, is where the electronic and photonic structures are fabricated.

The process of going from a native SOI wafer, where the active layer is still intact, to a wafer with fabricated structures includes two main steps: lithography followed by etching. This process, conducted in strict clean rooms conditions, typically requires three key products: a wafer, a mask and a photoresist. The SOI wafers used are standard 8-inch ($\approx$ 20.3 cm) disks, large enough to accommodate multiple iterations of our 1×3 cm^2 chip design, so up to 25 or more chips per wafer. The mask, also known as a photomask or reticle, is a glass plate coated with chrome to block light, while specific regions are left transparent to let light pass through. These transparent regions define the pattern of the structures to be fabricated.

The photoresist (PR) is a liquid material, made from a mixture of resin and solvent, in addition to some optional photosensitive compounds. Once applied to the wafer, the PR is exposed to light through the mask, and then treated with a developer, which is a chemical solution that selectively dissolves either the exposed or unexposed regions of the photoresist, depending on its polarity. In fact, photoresists are classified as either positive or negative tone, depending on how they respond to light. A positive PR is initially insoluble in its developer, but exposure to light makes it soluble. In contrast, a negative PR is initially soluble in its developer, but light exposure corss-links (hardens) it, making it insoluble.

After development, the next step is pattern transfer, where the created PR pattern is used as a mask to define regions of the wafer for material removal or modification. This is achieved through etching, which can be done either by chemical (wet etching) or plasma-based (dry etching) processes. In this step, the unprotected areas of the wafer are removed, while the areas covered by cross-linked photoresist remain intact.

Once the designed pattern has been transferred into the active layer of the wafer, the remaining photoresist is no longer needed. It is removed in a step called stripping, usually performed with chemical solvents or plasma ashing. Stripping leaves behind only the etched wafer structures, clean and ready for the next cycle of fabrication.

These steps are illustrated and summarized in fig. 2.7. For our structures, the photoresist used is NEB22 which has a negative polarity, so the obtained chip surfaces are predominantly SiO_2 with nanometric silicon photonic structures above it. Moreover, the exposure was done using electron beam (e-beam) irradiation instead of conventional light sources. Although figuratively represented in fig. 2.7 with a physical mask, e-beam lithography is in fact a maskless process. In this technique, a focused beam of electrons is scanned directly across the photoresist to draw the desired pattern, unlike optical lithography, which relies on a physical mask to project the pattern.

The main advantage of e-beam lithography, as demonstrated with the `Vistec SB254` system we use in the CEA cleanrooms, is its extremely high resolution. Since electrons have much shorter wavelengths than visible or UV light, they can define features at the nanometer scale, far beyond the diffraction limit of optical systems. For example, at a typical accelerating voltage of 50 keV, the electron wavelength is about 0.007 nm, compared to roughly 350 nm for UV light.

This enormous difference makes e-beam particularly useful for fabricating very small or complex structures that cannot be achieved with standard photolithography. Another benefit is flexibility: since no mask is required, design changes can be implemented quickly by simply updating the pattern file, which is especially valuable for prototyping and research applications. While e-beam systems themselves are costly and relatively slow compared to optical methods, the absence of expensive masks and the ease of rapid design iteration make the technique cost-effective in settings where the need for precision and flexibility outweigh the need for speed and throughput.

After fabrication, even though intermediary verification protocols are implemented by CEA cleanroom technicians to reduce the likelihood of errors, it is important to confirm that the final structures match the theoretical design specifications. This post-fabrication verification was carried out by the users rather than by the cleanroom technicians; in this work, I performed this verification using a scanning electron microscope (SEM), which provides high-resolution images of the structures' topography and allows precise dimensional measurement. For this purpose, one chip from the wafer is "sacrificed" for metallization, a sample preparation step required when the surface is insufficiently conducting. Without this treatment, the SEM electron beam would cause charge accumulation, leading to image distortion and signal degradation, therefore making our dimensional verification inaccurate. In practice, this metallization step consists of coating the chip surface with an ultra-thin conductive film ($2-10$nm), typically a gold/palladium (Au/Pd) alloy.

Figures 2.8 and 2.9 are examples of such SEM images both taken with an electron beam voltage of $1.50kV$. A CMT3 cavity is represented in fig. 2.8, while fig. 2.9 shows a 2D photonic

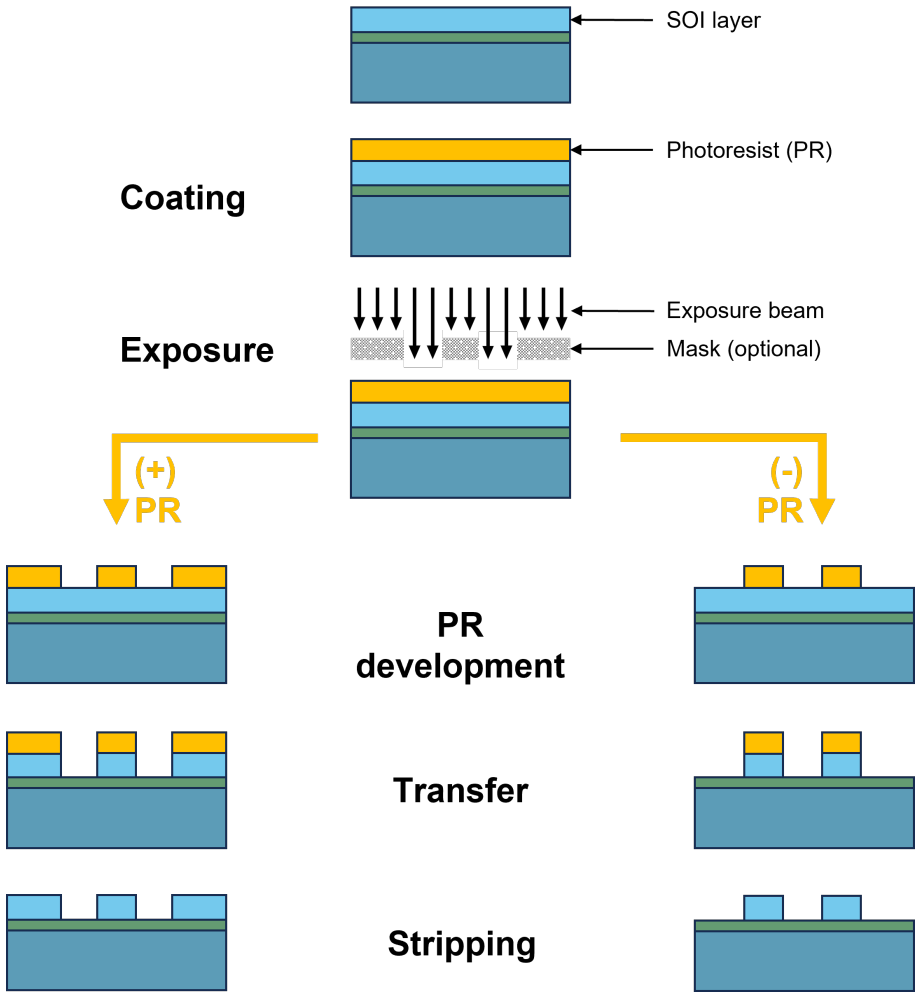

Figure 2.7: Photolithography Steps

crystal with two defect regions, a big circular hole a few lines above the central waveguide and a rectangular slot a few lines below it. This particular geometry results in two resonators, each having its own characteristic parameters λ_0 and Q. The latter device is fabricated on our chips but only exploited by our collaborators in EPFL, Switzerland. As already mentioned, the work presented in this manuscript focuses on the former structure, the CMT3.

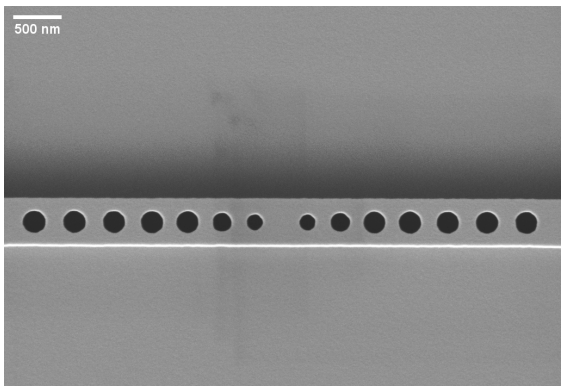

Figure 2.8: SEM image of a CMT3

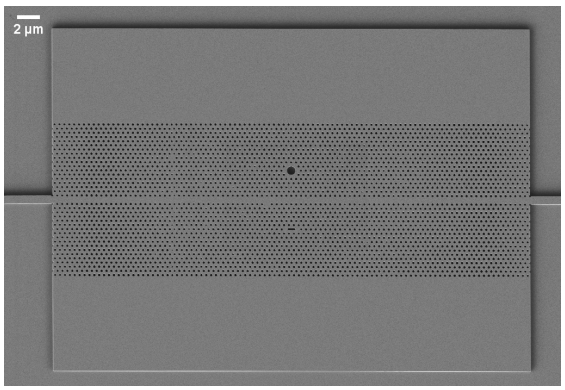

Figure 2.9: SEM image of 2D PhC resonators

2.2.3 Effect of SOI thickness

In photonic crystal traps, the optical forces responsible for trapping arise from the evanescent field present above the resonating cavity. When resonance occurs, the electromagnetic field is primarily confined within the silicon active layer, while the evanescent component corresponds to the fraction of this field that extends into the surrounding medium. Consequently, the thickness of the silicon layer plays a key role in determining the extent of the evanescent field above the surface and, therefore, how strongly the guided mode interacts with its environment. A thinner silicon core weakens the vertical confinement of the optical mode, allowing a larger fraction of the field to extend above the surface, whereas a thicker core enhances confinement but reduces the accessible evanescent component.

Earlier fabrication runs within the project mainly explored two SOI thicknesses, 340 nm and 250 nm. However, experimental observations showed that these values were not optimal for stable trapping of the studied micro-objects, whether dielectric or biological, as reproducible trapping protocols remained difficult to achieve. In order to better understand the influence of the silicon slab thickness on the spatial distribution of the optical field, numerical simulations were performed during this PhD using the finite-difference time-domain (FDTD) method implemented in the software `Lumerical`. To reproduce the experimental trapping conditions, the simulations considered water as the surrounding medium and were used to quantify how the confinement of the resonant mode within the silicon slab affects the amplitude and spatial extent of the evanescent field above the photonic crystal surface.

Field distributions were first simulated in order to visualize the spatial organization of the resonant mode within the structure. The reference coordinate system used for the simulations is illustrated in fig. 2.10(a), where x corresponds to the propagation axis of the waveguide, y to the transverse direction within the plane of the slab, and z to the vertical direction perpendicular to the SOI surface. The electric field distribution obtained at resonance is shown in fig. 2.10(b) for the central xz plane of the cavity. Several intensity maxima are visible along the cavity axis, symmetrically distributed around its centre. This spatial distribution is consistent with previously reported SNOM measurements on similar devices (see fig. 2.1 [69]), indicating that the simulations reproduce the expected modal profile. Additionally, the corresponding yz cross-section taken at the position of one of the most intense hotspots along the cavity (denoted $x_{\max}$) is shown in fig. 2.10(c). This plane highlights the vertical confinement of the optical mode within the silicon layer and the evanescent field extending above the waveguide surface.

In addition to the central intensity maximum within the waveguide, smaller lateral maxima are observed near the waveguide edges (around $y = \pm 400\,\text{nm}$). Although weaker than the central peak, these side lobes may lead to lateral optical forces that could be experienced by very small objects, such as viruses or sub-100 nm nanoparticles. While this effect has not been explored in the present study and remains relatively under-investigated in the literature, one relevant work by Lin et al. examined the potential for lateral trapping in photonic crystal waveguides through numerical simulation. In that study, the authors introduced a local waveguide waist near the cavity to enhance spatial exploration of the lateral evanescent field and calculated the optical forces present within this region [78]. However, no experimental realization of this design was reported. These observations suggest that the lateral structure of the evanescent field in our cavity could have subtle effects on particle interactions, though the dominant contribution for the bacterial cells studied here remains the central, vertically confined mode.

To quantify the vertical reach of the evanescent component, the electric field amplitude was extracted along the z axis above the cavity surface at a representative hotspot (region of maximum field amplitude), located at $(x = x_{\max}, y = 0)$. Due to the symmetry of the cavity, an equivalent hotspot exists on the opposite side of the cavity centre at $(x = -x_{\max}, y = 0)$, exhibiting the same vertical field behaviour; but only one representative position is considered for the analysis. The

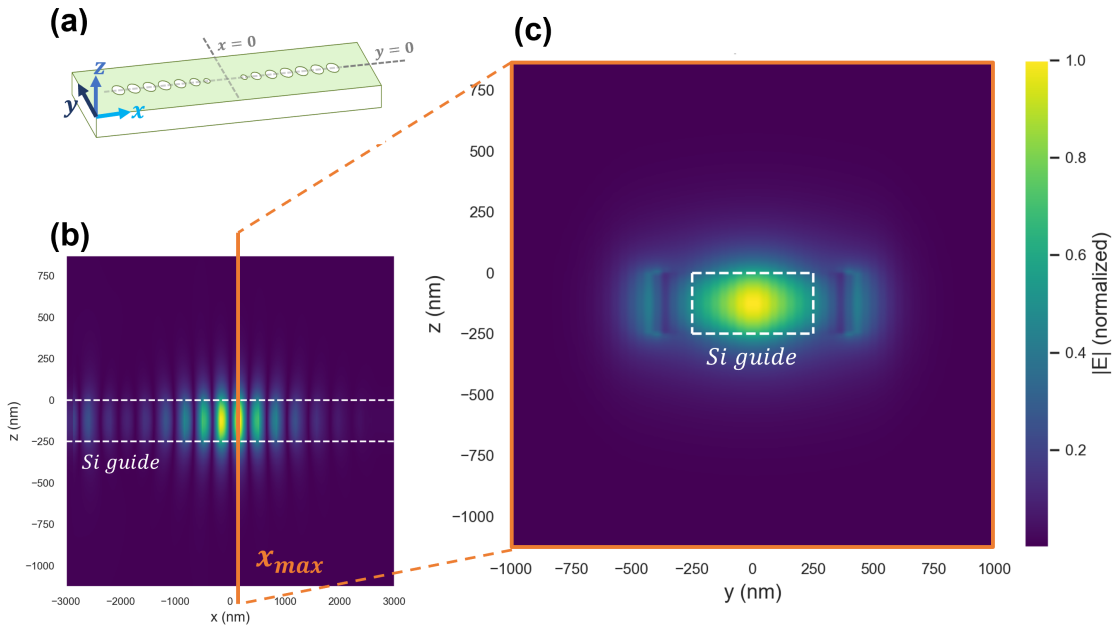

Figure 2.10: FDTD simulations of the electric field distribution at resonance for a CMT3 cavity. (a) Reference axes used in the simulations with respect to the photonic structure. (x: propagation, y: transverse in-plane, z: vertical). (b) Field intensity map in the central xz plane showing the longitudinal distribution of the resonant mode and the multiple symmetric hotspots characteristic of the CMT3 geometry. (c) yz cross-section taken at one representative hotspot position along the cavity ($x = x_{\max}$), showing the vertical confinement within the silicon slab and the evanescent tail above the surface.

resulting profiles are presented in fig. 2.11(a) for SOI thicknesses between 200 and 250 nm. In this representation, all curves are aligned so that $z = 0$ corresponds to the waveguide surface, independantly of the slab thickness. A zoom near the surface is given in fig. 2.11(b). Discrete values of the normalized electric field at selected heights above the surface are collected in fig. 2.11(c).

The simulations show a clear trend: thinner SOI slabs yield larger evanescent field amplitudes at the same height above the surface. Quantitatively, comparing the 200 nm and 250 nm slabs shows that the normalized electric field amplitude $|E|$ increases systematically as the silicon layer becomes thinner. For instance, as shown in fig. 2.11(c), at $z = 100$ nm above the surface, the normalized field amplitude increases from approximately $0.221\,V$ (250 nm slab) to $0.245\,V$ (200 nm slab), corresponding to an amplitude enhancement of about 11%. Similar differences are observed throughout the investigated vertical range, with amplitude increases between the two thicknesses varying from approximately 10% to 14% for distances between 50 and 200 nm above the surface. In fact, previous studies have shown that, for stable optical trapping, the trapped object should ideally be located about $80 - 110$ nm above the CMT resonator surface [76]. This region coincides with the near-surface range highlighted in fig. 2.11, where the simulated field enhancement between different SOI thicknesses is already clearly visible.

Furthermore, it is important to note that optical trapping forces are related to the optical intensity, which scales with the square of the electric field amplitude ($F_{opt} \propto |E|^2$, *cf.* equation (1.4)). As a result, even moderate increases in $|E|$ lead to larger relative increases in optical intensity. In the present case, the amplitude enhancements of $10 - 14\%$ correspond to intensity increases of approximately $21 - 29\%$. Therefore, these increases indicate that thinner SOI layers can provide noticeably stronger trapping conditions for the same launched optical power.

Based on these considerations, several photonic chips were fabricated within the project using

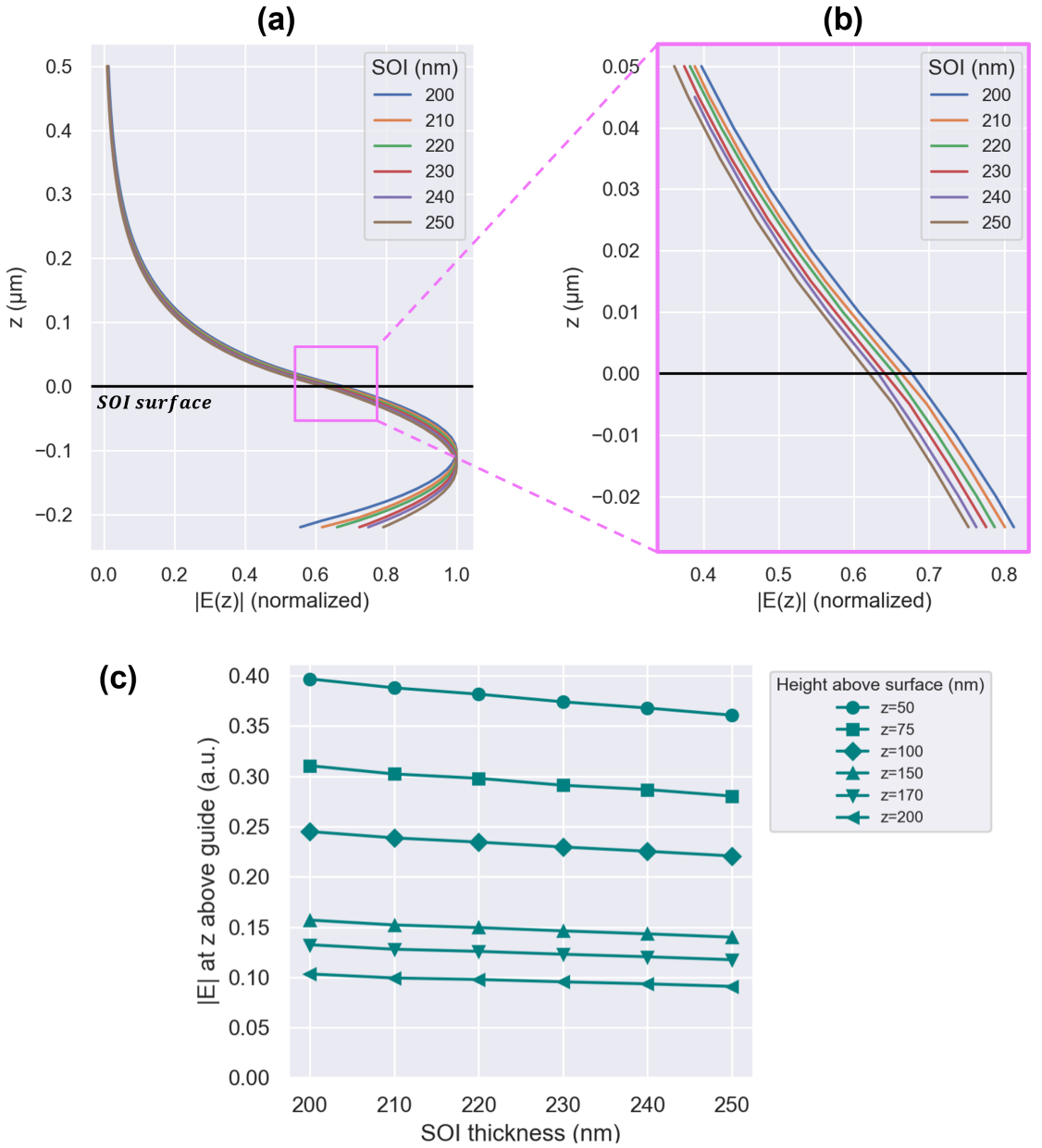

Figure 2.11: Vertical profiles of the normalized evanescent electric field amplitude above the photonic crystal cavity at resonance, obtained from FDTD simulations for different SOI thicknesses. (a) Normalized electric field amplitude $E(z)$ extracted at a representative hotspot position $(x = x_{\max}, y = 0)$ for SOI slabs with thicknesses between 200 and 250 nm. (b) Zoom of the near-surface region where optical trapping typically occurs. (c) Normalized field amplitudes extracted at discrete heights above the surface for each simulated SOI thickness.

thinner SOI layers in order to experimentally investigate this regime. However, it is important to note that although multiple thicknesses were fabricated, the cavity geometry itself (hole diameters, periods, and taper design) was not re-optimized for each thickness. The same parameters previously optimized for a 250 nm silicon slab [76] were reused for the fabrication, and thus also for the simulations. Consequently, the simulated structures presented here do not correspond to geometries individually optimized for each SOI thickness, but rather to a fixed cavity design evaluated for different slab thicknesses. A dedicated re-optimization of the CMT3 cavity geometry (hole radii, cavity length, taper zones... etc) for each SOI thickness would likely further enhance

the evanescent field extent and the associated trapping efficiency.

To experimentally probe this predicted enhancement in optical performance, photonic chips were fabricated using thinner SOI layers. Four nominal thicknesses were selected (200, 210, 220 and 230 nm), corresponding to the region where the simulations predict the strongest variation in vertical confinement. The optical characterization of these chips constituted my first practical experiment within this PhD project. The fabrication process itself was carried out by cleanroom technicians. Upon receiving the samples, spectroscopic ellipsometry was used to verify the actual SOI thickness, as small deviations can occur between the commissioned and fabricated values. The comparison, presented in table 2.1, shows that while the measured values are not perfectly identical, the deviations remain minimal and are thus considered sufficiently accurate.

SOI thickness (nm)				
Commissioned	200	210	220	230
Measured	200.0	208.6	218.9	227.7

Table 2.1: SOI thickness ellipsometry measurements: comparison between commissioned values and measured sample thickness after fabrication.

For the experimental investigation of the effect of changing SOI thickness, we did not have access to tools capable of directly probing the evanescent field, such as SNOM imaging (cf. fig. 2.1). Consequently, the analysis relied on the optical characterization of identical CMT3 resonant cavities fabricated on each wafer. By comparing the spectral response of these structures, it is possible to indirectly evaluate how the slab thickness affects the optical confinement and resonance properties of the cavities.

Figure 2.12(a) shows the measured resonance spectra for these samples, all obtained under identical experimental conditions. Signal amplitudes were normalized to remove variations due to coupling alignement variations, which will be discussed in the next section. As they are independent from SOI thickness, this amplitude normalization does not affect this analysis. Thus, our comparison of the different SOI thicknesses focuses on the resonance wavelength and quality factor, which more directly reflect changes in effective index and field confinement within the PhC. They are shown in fig. 2.12(b-c).

These experimental results confirm the correlation between SOI thickness and the optical performance of the CMT3 cavities. As the silicon slab becomes thicker, the resonance wavelength progressively shifts towards longer wavelengths, from approximately 1449 nm for the 200 nm sample to about 1524 nm for the 230 nm sample. This behaviour is consistent with the expected increase in the effective refractive index of the guided mode when the slab thickness increases, which leads to a red-shift of the cavity resonance.

The evolution of the quality factor reveals a different trend: the thinnest sample (200 nm) exhibits a significantly larger measured Q than the other structures. This trend is not reproduced in the numerical simulations, which instead predict Q values within the same order of magnitude for slabs between 200 and 250 nm, varying respectively between 2400 and 2700. In addition, the transmission signal measured for the 200 nm cavity was noticeably noisier than for the other samples. Unfortunately, the chip was damaged before additional measurements could be performed, preventing further investigation of this behaviour.

Nevertheless, these discrepancies in the 200 nm sample, both in quality factor value and in signal noisiness, could potentially be explained by several experimental factors that may contribute to it. Thinner slabs are more susceptible to fabrication-induced variations because small deviations in hole shape or surface roughness represent a larger proportion of the slab thickness, thereby influencing the resonance linewidth more strongly than in thicker slabs. Such deviations can alter

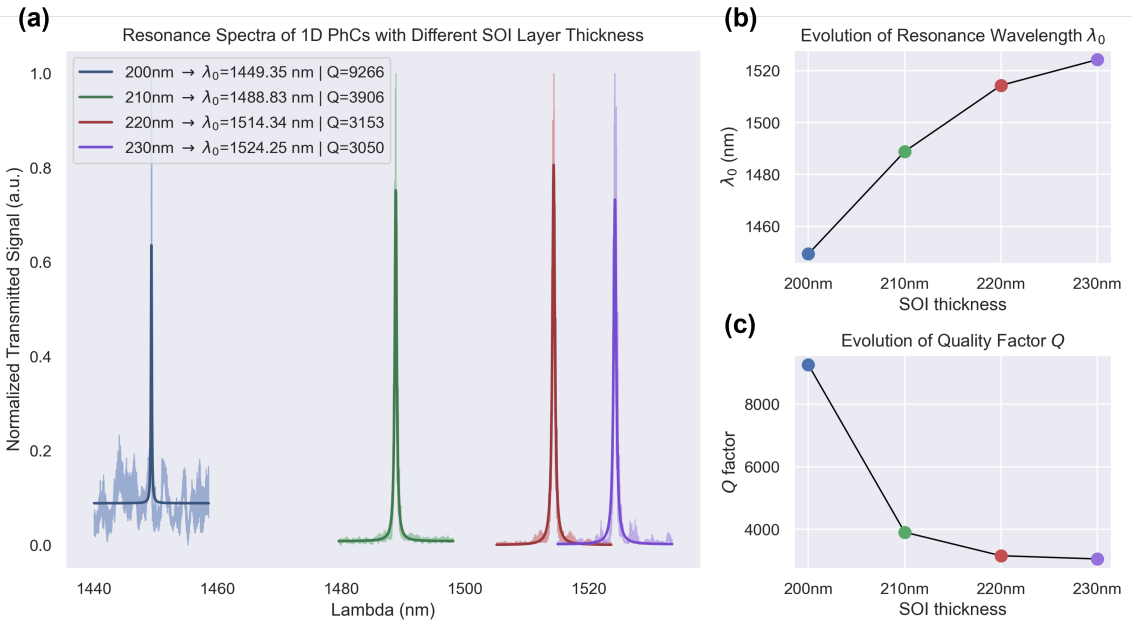

Figure 2.12: (a) Spectra of identical CMT3 structures with different SOI layer thickness. Raw signals are fitted with a Lorentzian fit. (b-c) Evolution of, respectively, the resonance wavelength λ_0 and the quality factor Q as a function of sample SOI thickness.

the resonance linewidth compared to idealized simulations. The reduced cross-section dimensions may also lead to less stable fiber-chip coupling conditions during measurement, which could explain the larger fluctuations observed in the transmission signal. Finally, the presence of noise in the measured spectra may itself affect the Lorentzian fitting procedure used to extract the resonance linewidth, potentially biasing the extracted Q value. For these reasons, the exceptionally large quality factor measured for the 200 nm sample should be interpreted with caution.

Even if this large quality factor were representative of the cavity behaviour, it would not necessarily be desirable for the optical trapping experiments considered in this work. These experiments are in fact performed while continuously injecting light at the cavity's characteristic wavelength λ_0 in order to maintain its resonance. When an object is trapped, it perturbs the cavity environment, causing a slight shift in the resonance wavelength. Because the injected laser wavelength remains fixed in our protocol, if the shift becomes too large compared to the resonance bandwidth, the cavity becomes completely detuned: the injected light no longer overlaps with the "effective" resonance of the perturbed cavity. This detuning results in loss of optical feedback and prevents stable trapping. Consequently, from an application point of view, excessively high quality factors can be detrimental, since they make the trapped state highly sensitive to small perturbations. It is possible to implement additional experimental steps, either manual or automated, to re-adjust the injected wavelength each time an object is trapped so that it matches the new cavity resonance. This was however not implemented in either of the experiments discussed in this manuscript to avoid adding more complexity to the optical bench, whose complete set-up will be presented at the end of this chapter.

It is important to re-emphasize that the observations discussed in this section reflect the behaviour of cavities whose in-plane geometry was originally optimized for a 250 nm slab and not re-designed for each SOI thickness. The differences in optical performance therefore result from both the change in slab thickness and the fact that the geometry is not strictly adapted to these new effective indices. As a result, the trends observed here provide comparative indications rather than an absolute optimization of the thickness. A full optimization would therefore require re-simulating and re-fabricating the cavity geometry for each thickness and, ideally, performing

direct near-field measurements to confirm the evanescent-field extent.

Taking these elements into account and within the range of sample thicknesses available in this study, the cavity fabricated on the 220 nm SOI wafer offered the most practical compromise for subsequent trapping experiments. This thickness provides a balance between maintaining a sufficiently strong evanescent field while preserving robust optical coupling and stable spectral behaviour. It exhibited a moderate quality factor of approximately 3000, which is sufficient to maintain strong optical field confinement within the cavity while remaining tolerant to small perturbations. Moreover, its resonance wavelength, around 1514 nm, lies near the center of the operating range of our tunable laser source ($1440-1640$ nm), where both the output power and spectral stability are typically highest. Operating near this region ensures more efficient excitation of the cavity mode and reduces sensitivity to spectral drifts of the laser. These practical and optical criteria make 220 nm the most reliable choice for the systematic trapping experiments reported here, while recognizing that re-optimization of the cavity geometry could identify different thicknesses as optimal from a purely design perspective. Therefore, unless otherwise specified, all measurements and experiments presented in the following sections and chapters of this manuscript were conducted on photonic chips with an SOI thickness of 220 nm, re-designed with updated hole diameters, lattice period and taper dimensions as given in fig. 2.5.

2.2.4 Light Coupling & Mode Adaptors

Light injection into resonating cavities, as well as collection of transmitted light from them, is achieved via waveguides that transport light within their bulk to and from the cavities. Light is supplied to the waveguide via an optical fiber coupled to its side facet. As is typical in photonics, we used single-mode optical fibers (SMFs), which support only a single spatial mode whose transverse field profile is approximately Gaussian. This property ensures that the electromagnetic field is well confined within the fiber core and can be efficiently coupled into nanoscale photonic structures such as waveguides or cavities. Modes that are poorly confined or carry higher-order spatial components would result in inefficient injection and reduced coupling efficiency.

Optical fibers typically consist of a glass core, through which the light propagates, surrounded by one or more layers of cladding with lower optical indexes that protect the core, provide mechanical flexibility, and facilitate handling. The dimensions of these parts vary depending on the application. For single-mode fibers, which are widely used in the fields of photonics and telecommunication, the fiber core diameter is around $8-9\mu m$. In contrast, the cross-sectional area of the 1D photonic crystal waveguide used here is only $0.22\mu m \times 0.5\mu m \approx 0.11\mu m^2$, compared to the $\simeq 64\,\mu m^2$ area of the fiber core, resulting in a surface overlap of less than 0.2% (fig. 2.13), which explains the significant coupling losses. To minimize this effect, we employed two strategies. First, we used SMFs with tapered, pointed ends rather than straight cleaves. These fibers concentrate the optical field into a smaller spot size, improving mode matching to the nanoscale photonic crystal waveguide and thereby reducing coupling losses.

Second, we modified the geometry of the waveguides that transport light into the photonic crystal, by introducing tapers at both the input and output facets. Tapering gradually transforms the effective refractive index and the mode profile along the propagation direction, thereby enhancing the spatial overlap with the fiber mode. Two types of tapers were employed in this work, as shown schematically in fig. 2.14 and in a scanning electron microscope (SEM) image of an actual sample in fig. 2.15. The first are conventional tapers, where the waveguide width expands outward in a funnel-like geometry from $0.5\mu m$ width to $5\mu m$, facilitating the transition from the larger fiber mode to the narrow cavity mode at the input, and vice versa at the output. To avoid confusion, we will refer to these tapers in this manuscript as funnel tapers.

The second type are inverted tapers, in which the waveguide narrows to a pointed thin tip facing outward. In this case, the overlap between the waveguide's input facet and the SMF is even

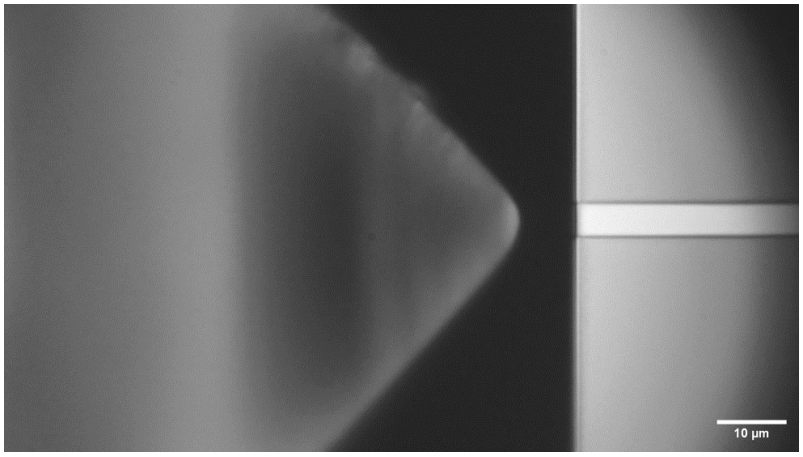

Figure 2.13: Microscope image showing the tapered tip of a single-mode optical fiber precisely aligned with the edge of a waveguide. The fiber injects light into the waveguide to excite the resonating cavity.

smaller. To address this, we applied an additional mode adapter overlaid on these inverted tapers. This adapter consists of a polymer cladding made of SU-8 resin. Its cross-section is designed to be around $6 \times 8\mu m^2$, as shown in fig. 2.16, closely matching that of the input optical fiber to minimize coupling losses. The refractive index contrast ensures that light is first guided into the resin (RI $\approx$ 1.57 at 1550 nm) and then gradually transferred into the silicon inverted taper (RI $\approx$ 3.48 at 1550 nm). This combined configuration effectively enlarges the mode field diameter and provides a smoother transition into the resonant cavity, thereby improving the overall coupling efficiency.

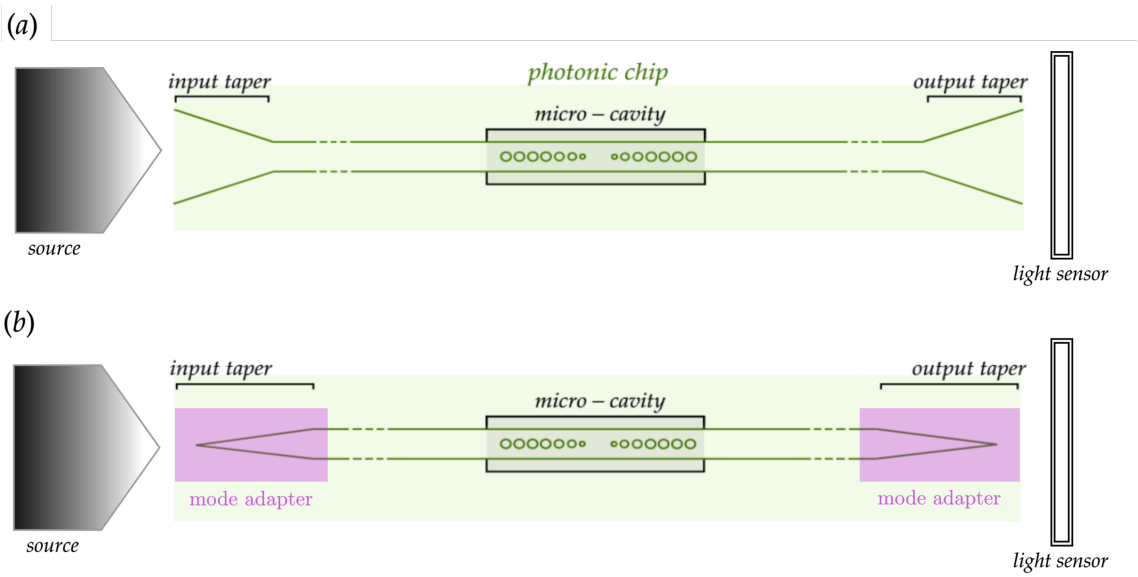

Figure 2.14: Illustration of CMT3 waveguides with (a) funnel tapers and (b) inverted tapers overlayed with SU-8 mode adapters. Both waveguides are aligned with a pointed single-mode fiber as a light source at the input and a light sensor for collection of transmitted signal at the output.

Both taper types were included on the chip for practical and collaborative reasons. The funnel tapers are traditionally used in our research group, while the inverted tapers are the standard choice of our collaborators in EPFL. By incorporating both geometries on a single chip, we created a device that can be used by both groups, while also providing an opportunity to directly compare

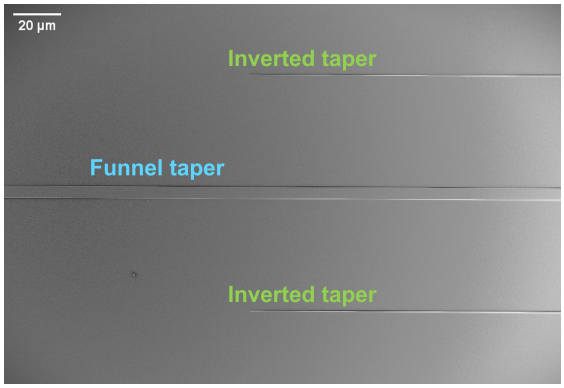

Figure 2.15: SEM image (top view) of funnel and inverted tapers fabricated on the same chip. The tapers consist of patterned Si defined on top of a uniform SiO_2 layer.

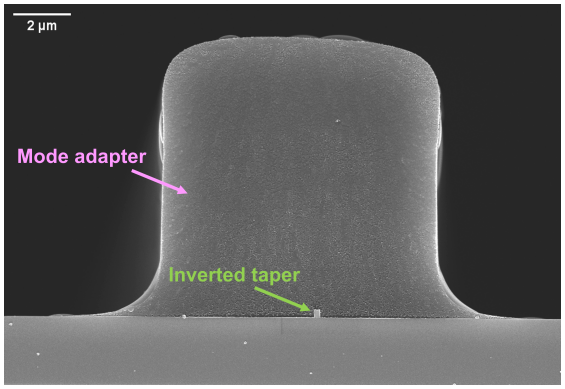

Figure 2.16: SEM image (cross section) of an SU-8 mode adapter overlaid on an inverted SOI taper. The dark region in the image corresponds to the SEM chamber behind the sample.

their performance.

It is important to emphasize that these tapers are positioned approximately $5-6$ mm away from the photonic crystal region, at both facets of its access waveguide. The PhC itself extends only about 5μm in length when all structural elements (holes and defect) are taken into account. Consequently, the presence of the tapers does not directly affect the immediate coupling of light into the cavity. Instead, their primary role is to optimize light injection into the input waveguide, which then acts as a conduit for the optical mode toward the photonic crystal. The same reasoning applies to the output tapers: their influence on the resonator is indirect, mediated through the waveguide that carries the transmitted signal to the output, rather than through direct interaction with the cavity field.

Polymer Mode Adaptors Fabrication

Mode adaptors were fabricated using a maskless ultraviolet (UV) lithography equipment called `Smart Print UV (SPUV)` [79]. This system is based on a digital micromirror device (DMD), which consists of a two-dimensional array of microscopic mirrors, each of which can be individually actuated. By tilting the mirrors to either reflect or deflect incident UV light, the DMD enables dynamic generation of illumination patterns following a given digital design, like a video projector. Therefore, the need for conventional physical photomasks is completely eliminated. The SPUV system provides multiple writing resolutions through different interchangeable optical objectives ($1\times$, $2.5\times$, $5\times$, $10\times$) used for light projection on the sample, and can achieve features as small as $1.5\mu m$. Although less resolute than e-beam or classic UV lithography, this maskless UV lithography technique offers multiple advantages in terms of cost, rapid prototyping and system compactness.

Multiple settings can be adjusted on the SPUV. First, the power of the ultraviolet lamp (UV, $\lambda = 385nm$) used for exposure can be adjusted between $13mW$ and $30mW$. Second, the exposure time can be modified to the centisecond. Together, these parameters define the total exposure dose (dose = power $\times$ time), which can be critical for the precision of the patterning. If the dose is too low or too high, features may either fail to appear or become distorted. To ensure proper definition of the pattern according to the intended design, the exposure dose should be referenced from the datasheet of the specific photoresist. In addition, the SPUV objective can be changed, as mentioned previously, to offer multiple field of view (FOV) sizes, which changes the pixel size of the projected pattern and therefore the precision of the patterning and the UV fluence (energy per unit area delivered to the photoresist). Smaller FOVs offer better precision, but the trade-off is

longer patterning times, as the overall design must be divided into stitches (sub-images) to match the FOV size, with each stitch exposed individually. The transition between stitches is handled automatically by the machine.

In our application, we aimed to fabricate mode adapters that are $8\mu m$ thick, $6\mu m$ large, and $3mm$ long, using SU-8-2010 as a photoresist. Thickness was primarily determined by the spin-coating speed and acceleration of the PR, which were precisely chosen according to its datasheet, and verified after fabrication using a profilometer. The other dimensions were determined on the digital design, therefore their accurate execution depended on the exposure parameters. While the datasheet provides precise instructions for spin-coating speed, the recommended exposure dose covers a broad range of thicknesses ($6-15\mu m$). Therefore, multiple $\langle$exposure time, LED power$\rangle$ combinations were tested to identify the optimal patterning conditions. Figure 2.17 shows some of these trial-and-error experiment results on experimental features of the same critical dimensions as our target. Eventually, we opted for an exposure time of $12.5s$ and LED power of $\approx 13mW$. Finally, we selected a $5\times$ objective with a FOV of $2.1 \times 1.2mm^2$ and a pixel size of $1.1\mu m$, which provided the best trade-off between total exposure time and feature precision.

An example of the obtained results is shown in fig. 2.18, corresponding to a photonic chip with multiple waveguides, some fabricated with funnel tapers and others with inverted tapers. The two types can be distinguished visually, as the funnel tapers are wider. Mode adapters are also visible in light- or dark-field microscope images, overlaid on the outer ends of the inverted tapers.

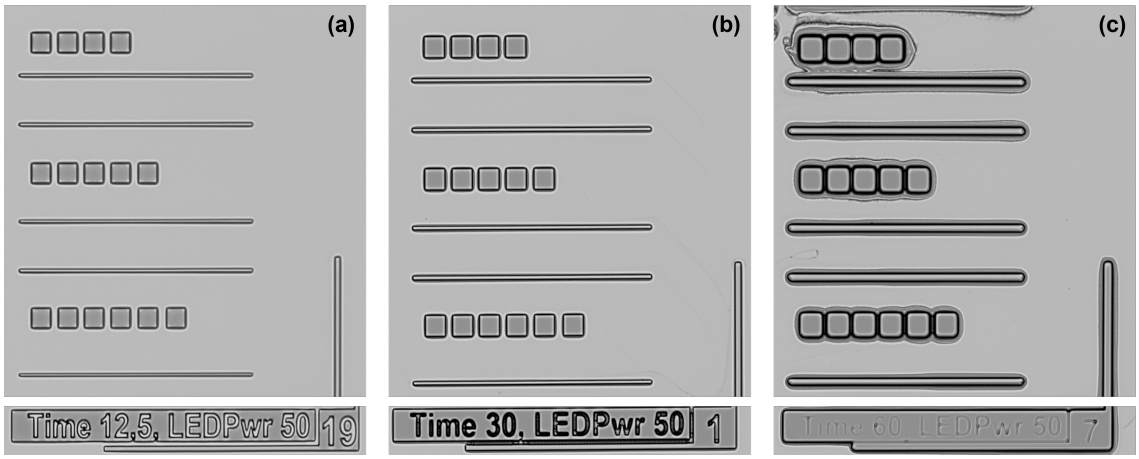

Figure 2.17: Optical microscope (objective $\times 10$) images of exposure dose tests done at LED power 50% ($\approx 13mW$) and exposure time (a) $12.5s$, (b) $30s$, and (c) $60s$. At higher doses, features are thicker because the photoresist is over-exposed making the UV beam diffuse into surrounding regions that were not intended to be exposed.

Tapers Comparison

To compare the coupling efficiency of these two types of tapers, we fabricated on the same chip pairs of identical CMT3 cavities (same microresonator geometry), but with waveguides tapered differently: either funnel tapers on both ends, or inverted tapers with SU-8 mode adapters on both ends as well. The pairs themselves had small architectural differences from one pair to the other that were used for validating the design simulations mentioned previously. This validation aspect is not within the scope of this section.

Figure 2.19 shows some examples of the comparison spectra obtained, while table 2.2 presents all the obtained comparison data. We observe few differences between the CMT3 guides with funnel tapers (blue) and those with inverted tapers and mode adapters (purple). For brevity, in the

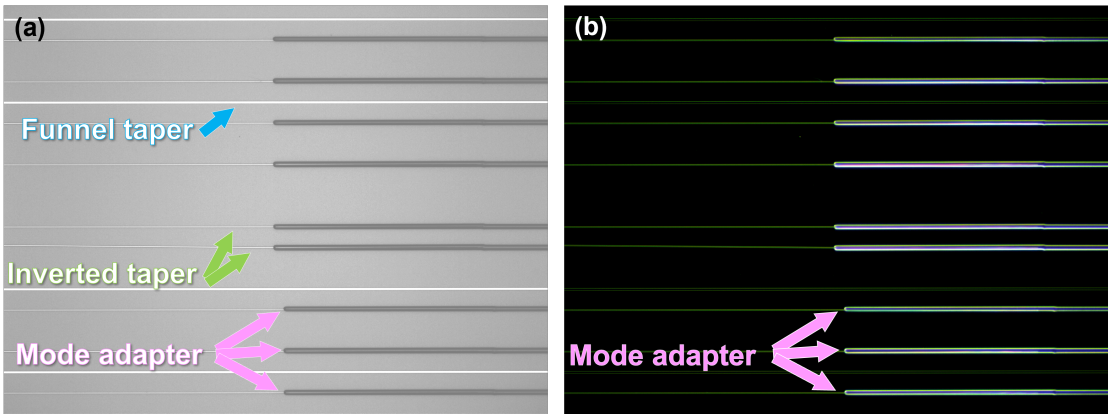

Figure 2.18: Optical microscope images in (a) bright field and (b) dark field of SU-8 mode adapters overlaid on inverted tapers on an SOI chip containing multiple parallel waveguides. In this figure, the mode adapters appear on the output tapers; equivalent adapters are implemented on the input side as well.

rest of this section we refer to the combination of inverted tapers plus adapters simply as "inverted tapers". The principal, and expected, difference is a systematic change in the amplitude of the transmitted signal: inverted tapers consistently yield higher transmitted peaks at resonance. We quantify the relative increase in transmitted amplitude as $\Delta U = 100 \times (U_{max}^{inv.} - U_{max}^{fun.})/U_{max}^{inv}$, where $fun.$ and $inv.$ respectively denote funnel and inverted tapers, and U_{max} in the maximum of the raw transmitted signal (not its Lorentzian fit). On average the transmitted peak amplitude increased by 52%, with a best-case improvement of about 78%. However, these values presented a significant dispersion with a standard deviation (STD) of $\approx 22\%$. This variability can be attributed primarily to technical factors associated with light injection into the tapers.

We also observe that the spectra obtained with inverted tapers exhibit fewer parasitic oscillations. This can be explained by reduced back-reflections at the waveguide facets: in the absence of adapters, the strong refractive index contrast between silicon ($n \approx 3.48$) and air ($n \approx 1.00$) leads to significant reflections, whereas the SU-8 layer ($n \approx 1.57$) provides a more gradual index transition. Combined with the mode expansion provided by the inverted taper, this reduces undesired reflections and thus suppresses these oscillations, resulting in smoother spectra. This in turn improves the robustness of the Lorentzian fitting of the resonance peaks and enables a more accurate characterization of the cavity quality factor.

In fact, the chip used for this comparison contains a total of 60 waveguides with various cavities, arranged into 10 groups across the chip surface. Each group included, among other devices, a pair of identical CMT3 that differ only by their taper geometry, which we use for the comparison. When fabricating the SU-8 mode adapters on the `Smart Print UV` as presented previously, the waveguide tapers were aligned to the projected design and exposed group by group, prior to developing everything together. This group-by-group exposure strategy was chosen to mitigate small spatial drift of the SPUV system, which is comparable to the lateral dimensions of the SU-8 mode adapters and can therefore lead to significant misalignment.

Nevertheless, exact centering of the SOI tip inside the SU-8 adapter remains difficult to guarantee, because the SPUV camera resolution limits the reproducibility of this manual alignment. In addition, performing the design alignment separately for each taper group introduces further variability in the centering across the chip. For example, fig. 2.20 shows SEM cross-sections of three mode adapters fabricated on different inverted tapers from the same photonic chip. We clearly observe that the SOI tips can be displaced relatively to the adapter centers and that this offset from the center differs from taper to taper. It is important to note that the SEM images in fig. 2.20 are

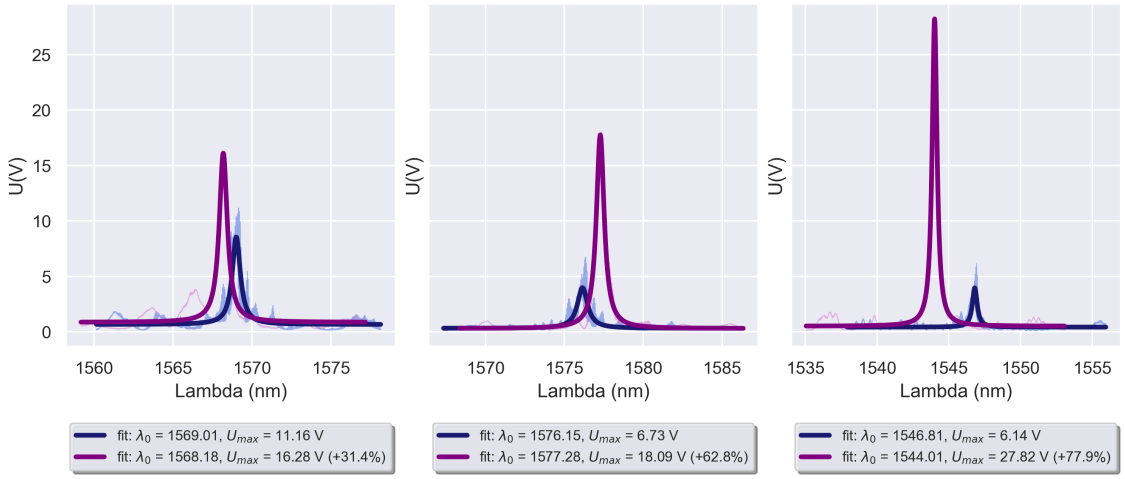

Figure 2.19: Spectra of pairs of identical CMT3 cavities with different types of tapers on the waveguides' edges: funnel tapers (blue) or inverted tapers with SU-8 modes adapters (purple). All spectra are acquired in water, with a laser power $P_{in} = 10mW$.

Funnel taper		**Inv. taper + SU-8**		**Comparison (inv-funnel)**		
$\lambda(nm)$	$U_{max}(V)$	$\lambda(nm)$	$U_{max}(V)$	λ shift	$\Delta\lambda(nm)$	ΔU
1555.68	4.95	1557.52	17.07	Red	+1.84	+ 71.0 %
1546.81	6.14	1544.01	27.82	Blue	-2.80	+ 77.9 %
1569.01	11.16	1568.18	16.28	Blue	-0.82	+ 31.4 %
1547.60	6.85	1548.23	23.09	Red	+0.63	+ 70.3 %
1576.15	6.73	1577.28	18.09	Red	+1.13	+ 62.8 %
1555.91	5.59	1554.66	10.26	Blue	-1.24	+ 45.5 %
1562.37	6.88	1562.43	8.99	Red	+0.05	+ 23.5 %
				Average	*≈ -0.51*	*≈ 52 %*
				STD	*≈ 1.4*	*≈ 22%*

Table 2.2: Tapers comparison: characteristic data obtained from CMT3 spectra with funnel tapers or inverted tapers overlaid with SU-8 mode adapters.

illustrative and do not correspond to the exact guides used for the taper-efficiency comparison reported in table 2.2, because that specific chip was subsequently used in trapping experiments and therefore could not be sacrificed (metalized) for SEM imaging.

This centering variability directly impacts the amplitude of the resonance peak. In particular, a lateral offset of the SOI tip inside the SU-8 adapter degrades the modal overlap at the adapter-taper interface. As a result, the coupling efficiency into the guided mode is reduced, which in turn lowers the transmitted peak. In addition, this misalignment also affects the practical optimization of the fiber-to-chip coupling. Although aligning the optical fiber with the apparent center of the SU-8 adapter would, in principle, provide optimal injection, we observed experimentally that the maximum transmitted signal does not always occur at this nominal position. Instead, a slight intentional horizontal offset can improve the coupling efficiency. This behavior likely reflects the fact that the tapered SOI tip is not perfectly centered within the adapter, so the fiber couples more efficiently when it is positioned closer to the actual location of the waveguide rather than to the

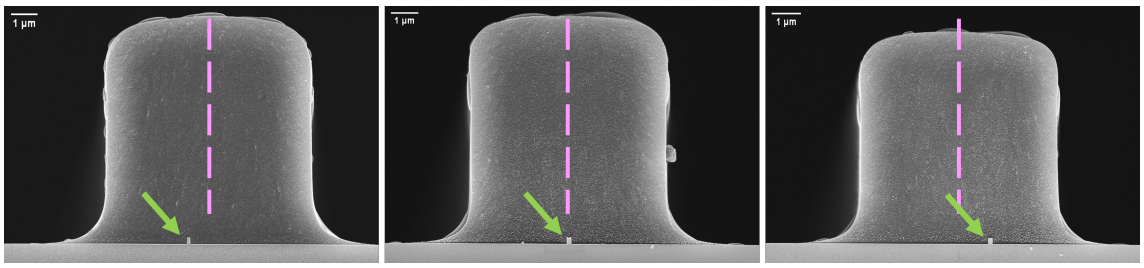

Figure 2.20: Comparison of the centering of inverted tapers overlaid with SU-8 mode adapters. On these SEM images, the pink dotted lines indicated the center of the mode adapter, while the green arrow points to the tip of the inverted taper.

visible center of the adapter. However, this interpretation cannot be verified directly, as the camera used for alignment does not provide sufficient resolution or depth of field to resolve the tapered SOI tip through the adapter.

These two mechanisms are complementary and likely both contribute to the large standard deviation ($\approx 22\%$) of the amplitude increase. Nevertheless, despite this variability, the average increase in amplitude signal ($\approx 52\%$) suggests a clear performance advantage for inverted tapers with SU-8 adapters, despite the fabrication complexities associated with the mode adapters. This supports the conclusion that coupling CMT3 cavities via inverted tapers (with adapters) is preferable to using funnel tapers. However, confirming this conclusion rigorously would benefit from more statistical tests and further controlled coupling experiments and simulations.

The second difference observed in the comparison data, which was less expected than the increase in amplitude, is the small shifts in resonance wavelength between each pair of supposedly identical CMT3 cavities. As the architectural design of these structure are the same, we would in theory obtain fully identical resonance wavelengths, which does not correspond to our results where cavities differ by an average absolute shift of $\approx 0.51nm$ with a standard deviation of $1.4nm$. A few theories could explain these shifts. First, tiny architectural imperfections from the e-beam lithography or the plasma etching could affect either one or more hole diameters, hole circularity, or surface roughness. Second, resin residues could locally linger on the resonating cavity either from the e-beam process or the later SU-8 fabrication of mode adapters. In either case, the local refractive index around the cavity is altered. Third, the characterizations of these cavities were all performed in water. This means that the medium surrounding the photonic crystal is pure deionized water (DIW). However, if this medium does not uniformly fill all the holes of the PhC at the time of measurement, the effective refractive-index periodicity of the structure changes and thus shifts the resonance wavelength.

Confirming the fabrication related theories requires very thorough checks to be conducted on every cavity of every chip, which often implies sacrificing the chip for scanning electrom microscopy (SEM) or atomic force microscopy (AFM). In contrast, there is currently no straightforward experimental method to control or monitor the third theory regarding how PhC holes are filled with any liquid mediums surrounding it, even if we were to use surface treatments to promote surface wettability. A practical solution would have been to acquire the resonance spectra in air, prior to wetting the chip. Either way, these wavelength shifts are independent of the taper type, since the tapers only affect light injection and transmission at the waveguide ends, a few millimetres away from the cavity.

2.3 Microfluidic Integration

Optical trapping using photonic crystal resonators relies on a delicate interplay between the localized resonance field and the spatial positioning of the microscopic samples to be trapped. Establishing a stable interaction between the optical forces and the specimen requires bringing the target into the immediate space above the resonator's cavity, where the resonant evanescent field lies. Consequently, to hold these samples in suspension above the surface, they are typically maintained in aqueous mediums where they can undergo Brownian motion and, in the case of biological objects, remain viable and in a physiologically stable state.

However, introducing a liquid medium above the photonic chip must be carefully controlled. If left uncontrolled, the medium presents two main risks. On one hand, allowing it to sit freely exposes the experimental area to contamination (dust, spores, bacteria) and leads to rapid evaporation of the air-exposed liquid. This significantly limits the experiment duration and exposes the SOI surface to the risk of sample residues or biofilm formation that are difficult to remove. On the other hand, simply placing the liquid sample on the chip does not guarantee that it will remain over the photonic regions of interest. During handling or over time, the liquid can shift or spread, and suspended particles may move away from the areas where efficient optical coupling is required.

2.3.1 Static Fluidic Pool

To mitigate these issues, a static pool configuration was previously used in our project to confine the liquid medium directly on the chip surface. The installation steps for this setup are shown in fig. 2.21. The pool was made out of a polydimethylsiloxane (PDMS) rectangular frame, about 100-150 μm in thickness, manually cut and positioned on the chip. It was then covered with a thin glass coverslip ($\approx 150\,\mu$m), which weakly adhered to the PDMS through van der Waals interactions and surface tension effects, thereby creating a temporary airtight seal that reduced evaporation and sample drying. Since this adherence was incomplete, air bubbles would eventually form within the pool, typically appearing anywhere from a few minutes to several hours after assembly.

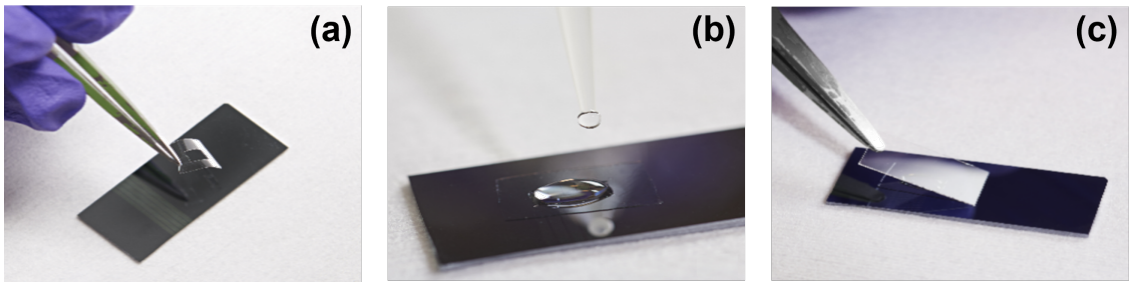

Figure 2.21: Steps of static fluidics pool installation. (a) Manual placement of a PDMS frame on the photonic chip, ensuring the resonators are centered within the frame. (b) Deposition of liquid medium. (c) Manual covering of the pool with a glass coverslip. Credits to Manon TARDIF.

This approach, tested for several months in the beginning of this PhD, offered the advantage of being very simple to fabricate, install and remove, allowing easy replacement of either the pool itself or just the medium within it, and facilitating the cleaning of the chip surface. However, it also presented several drawbacks. First, PDMS is mechanically fragile and prone to deformation during handling, which can compromise the pool geometry and sealing. Second, because the seal between the frame and the glass cover is not fully airtight, gradual leakage and evaporation of the liquid can occur at variable rates, reducing the reproducibility of the experiments.

Moreover, when the pool's contents evaporate, replacing the pool or the medium requires removing the photonic chip from the optical bench (which will be presented in the next section), handling it, and then realigning it with the rest of the optical components. This not only increases the risk of damaging the fragile photonic structures on the chip through excessive handling, but is also time-consuming and introduces significant alignment and coupling variability between different measurements. Lastly, the static pool offers no hydrodynamic control over the motion of suspended particles, which drift randomly due to Brownian motion.

To compensate for this lack of flow control, we relied on highly concentrated suspensions of specimens (on the order of $10^9 - 10^{10}$ cells/mL when using bacteria, corresponding to the resuspension of approximately $5 - 10$ colonies in 1 mL of liquid medium) to maximize the statistical likelihood of a particle passing sufficiently close to the cavity's evanescent field to be optically trapped. While this concentration-based strategy was sufficient for our experiments, it can be very limiting when working with dilute samples (i.e., a low volumetric concentration of biomass) or expensive biological materials.

These limitations motivated the development of a more controlled and reliable configuration for handling and controlling liquid media during optical trapping experiments. Therefore, a microfluidic system was designed and integrated directly onto the photonic chip to ensure precise confinement and renewal of the liquid medium without the need to remove or realign the chip between experiments. This configuration allows multiple experiments to be performed consecutively under stable and reproducible conditions.

More importantly, this integration provides a means to regulate the flow of suspended particles, enabling better spatial control over their trajectories and significantly improving the probability of bringing objects into the vicinity of the resonant field for optical trapping. The airtight nature of the integrated microfluidic channel suppresses evaporation and maintains stable experimental conditions, while also opening perspectives for quantitative studies such as the estimation of optical trapping forces under well-defined hydrodynamic conditions.

2.3.2 On-chip Fluidic System: Designing

This section details the design and implementation of the on-chip microfluidic system developed for optical trapping experiments. The system is designed to maintain a controlled liquid environment above the photonic crystal resonators, deliver suspended samples to the resonant regions, and enable precise control of liquid input, output, and flow through external valves without direct manipulation of the chip. The on-chip system is composed of three main components: a fluidic channel, a glass coverslip used to seal it, and two tubes attached to holes within the glass coverslip that allow liquid to flow in and out.

The fluidic channel architecture itself, presented in fig. 2.22, was designed collaboratively by our project colleagues Nicolas Villa and Clément Bernard. During the design process, several geometric and practical considerations were implemented based on observations from previous iterations. First, sharp angles were deliberately avoided, since earlier designs revealed that they tend to trap air bubbles, which can obstruct fluid flow or retain particles from past experiments. Such residues may later diffuse into new sample suspensions, complicating the interpretation of trapping results. Sharp corners can also shied these residues from being flushed out of the cavity, which builds up overtime, clogging the channel. Second, to ensure proper access of optical forces to the suspended particles passing through the microfluidic system, alignment markers were introduced to precisely match the channel with the photonic resonator layout, guaranteeing that the cavities remain centered beneath the flow path as pointed out in fig. 2.22. Lastly, a checkerboard design was implemented around the channel region, whose utility will be explained when presenting the fabrication process of this system.

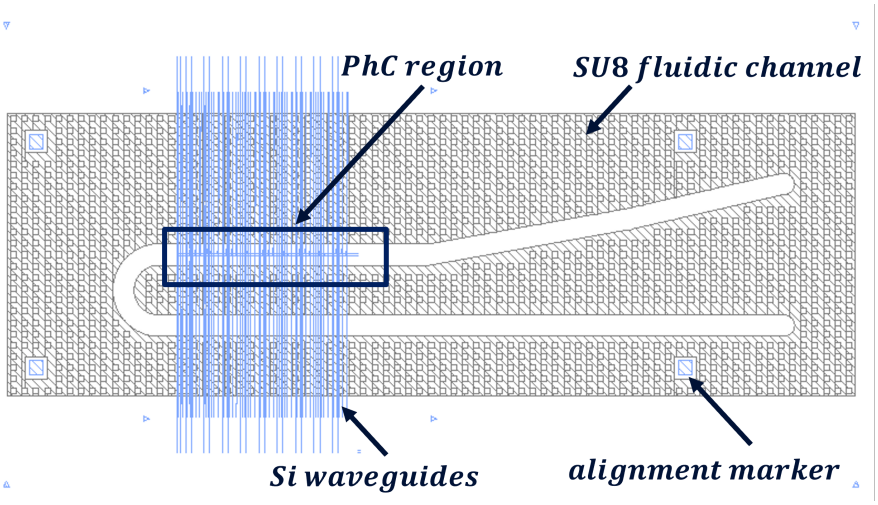

Figure 2.22: Design of the fluidic channel architecture (black) overlaid with the design of the photonic waveguides structure layout (blue). Alignment markers serve as references during fabrication of the SU-8 fluidic system to ensure that the resonant cavities lie within the channel, allowing particles to pass directly above them.

2.3.3 On-chip Fluidic System: Fabrication

Fluidic Channels

The fluidic channel was fabricated using the photoresist SU-8 for its biocompatibility [80], which was an essential factor of choice for this region that is in direct contact with the specimen. Fabrication was carried out on the `SmartPrintUV` machine, using a 2.5× objective (FOV: $4200 \times 2400\,\mu m$, resolution $6\mu m$). Each stitch of the design was exposed at an LED power of $\approx$ 13mW for a duration of 30s, leading to a total exposure time of about 20 minutes (39 stitches). In fact, the overall design dimensions are 3×1,cm, and its smallest features include the channel width ($750\mu m$) and the lattice of alignment squares ($800\mu m$). In hindsight, a 1× objective (FOV: $10560 \times 5940\,\mu m$, resolution $15\mu m$) would have provided sufficient resolution while significantly reducing the total exposure time due to its larger field of view.

Chamber Sealing

Once the SU-8 microchannel was patterned and fully cured, the next step was to seal it and create a closed fluidic environment. This was achieved using a thin glass coverslip ($\approx 300\mu m$ thick) with two drilled holes to allow liquid inlet and outlet. The preparation of these holes was conducted by Dylan DAVID, through a process of machining with a fine dental drill to pierce the glass. Once retrieved, the glass is cleaned first with acetone and then with isopropanol (IPA) in an ultrasonic bath to remove any dust and debries that might have resulted from the drilling. Next, an approximately $3\mu m$ thin layer of UV-curable glue (Reference: Norland Optical Adhesives 68) was spin-coated on its surface. The coverslip was then manually positioned using tweezers and pressed onto the SU-8 fluidic structure.

Precise alignment of the holes in the glass coverslip with the ends of the channels is critical to prevent the formation of "dead zones", where air bubbles or sample residues could become trapped. The checkerboard pattern that was incorporated around the SU-8 canal region in the design (cf. fig. 2.22) plays an important role in this sealing step since it acts as a buffer zone for any excess glue that may spread during manual placement, thereby preventing accidental clogging of the microchannels. If such clogging is observed before the UV curing of the glue, the ensemble can be immersed in acetone for a few minutes to dissolve the adhesive, allowing retrieval of both

the chip and coverslip to repeat the process. The glue is cured with a UV light flood exposure using the MJB4, a mask aligner machine typically used in photolithography used for both exposure and contact alignment. Once cured, the glue hardens which permanently seals the microfluidic chamber.

This manual attachment approach, while appearing rudimentary, was chosen after multiple rounds of trial and error to develop a more reliable sealing process. Several alternative attachment strategies were tested. One involved a custom-built mechanism with a suction pen to hold the glue-coated coverslip upside-down, and lower it onto the fixed chip using a handle, before releasing the glass from the suction. Another approach reversed the setup: the glass coverslip was fixed in place, and the chip was raised to contact it using the MJB4 mask aligner, typically employed for photolithography. In this case, the glue-coated coverslip was temporarily held in place with low-adhesion PDMS strips on a transparent mask, while the chip, mounted on the upward-moving stage, was brought into contact from below.

In both cases, achieving perfect alignment between the glass holes and the SU-8 channels proved very difficult for two main reasons. First, there was a big lack of direct perpendicular visibility during both processes due to the various parts of the used machines, especially in the case of the MJB4 whose microscope sits above the samples and is too highly magnified to view the holes properly, as it is designed for smaller features. Second, and most importantly, ensuring uniform pressure at the moment of contact between the fixed and moving parts proved very challenging, often causing lateral slippage due to the viscosity of the uncured UV glue. These issues often resulted in partial or complete misalignment and, consequently, blockage of the fluidic channels and/or the inlet and outlet holes.

All described processes were initially tested with a different thicknesses of SU-8 spin-coated on the glass slides, in multiple attempts to achieve a resin-resin bond, but were unsuccessful. Later discussions with colleagues led us to suspect that the issue was related to the specific formulation of the SU-8 photoresist we were using which was SU-8 2010 (Kayaku Advanced Materials). Tests of different versions, such as SU-8 GM1040 (Gersteltec Engineering Solutions), were planned but never executed due to delivery delays which led us to look for alternative accessible options, like the UV-curable glue.

Inlet & Outlet

Finally, to complete the chip, two stainless steel tubes are attached to the drilled glass holes to provide an inlet and outlet for fluids within the channels. Fluid circulation is achieved via flexible silicone tubing, that subsequently connects the metal tubes to a sample container on one side and a discard vessel on the other. The flow is controlled using a compact, tabletop, pressure-based microfluidic controller (Flow EZ ™, Fluigent). Both stainless steel and silicone were chosen for the biocompatibility of these materials.

The metal tubes were fixed to the glass holes using Torr Seal epoxy (Agilent Technologies). This two-component vacuum-grade adhesive was selected for its strong bonding properties, high viscosity and excellent chemical resistance, which are essential for maintaining leak-free operation in fluidic systems. In addition, although Torr Seal has a crosslinking temperature of 170°C, it can still be cured at room temperature, avoiding exposure of the photonic chip to excessive heat that could compromise the SU-8 structures fabricated on its surface. Moreover, the adhesive's high viscosity, appearing as a thick, non-flowing paste, makes it easier to handle in a controlled way compared to other adhesives we briefly tested, such as various viscosities of UV-curable glues.

The attachment procedure is, however, particularly delicate. Each tube must be kept strictly vertical during adhesive curing to ensure proper alignment and to prevent the epoxy from seeping beneath the tubes and clogging the channels. This is typically achieved by inserting thin alignment

pins inside the steel tubes and securing them to a support block to maintain stability. Because Torr Seal is opaque once mixed, any undesired spreading beneath the tube cannot be visually detected. Therefore, there is unfortunately no intermediate verification step during this attachment procedure. One must wait until full curing and subsequently test the device. In the case of any obstructed channel, the entire chip is rendered unusable. An example of the final result obtained after tube attachment is shown in fig. 2.23(a).

An alternative approach was also explored, in which a small PDMS connector block (approximately 1 cm high) was fabricated, punched to create through-holes, and plasma-bonded to the glass surface. An example of this is shown in fig. 2.23(b) tested on a dummy chip, i.e. a microfluidic channel fabricated on a Silicon wafer sample with no photonic structures. In practice, this PDMS connector method proved unreliable: plasma activation was inconsistent, possibly due to surface roughness introduced by the glass drilling, and inserting the tubes afterward frequently caused cracking of the PDMS or leakage from beneath it.

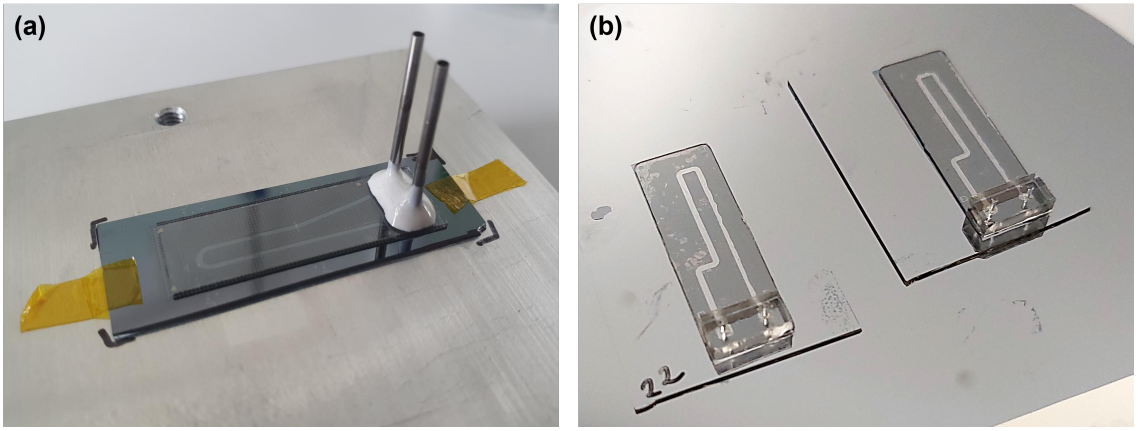

Figure 2.23: Microfluidic chip inlet and outlet connectors. (a) Stainless steel tubes glued with Torr Seal adherent. The chip is fixed to a sample holder using yellow tape. (b) Pierced PDMS connector blocks attached on dummy microfluidic chips.

The Torr Seal approach proved highly inefficient, as nine out of ten chips fabricated using this method suffered from clogging, rendering them unusable. Nonetheless, it remained the most practical solution at the time, given the human resource and time constraints that limited further optimization of this specific step in the microfluidic chip fabrication process. After several months devoted to refining the complete fabrication workflow, from mode adapters to fluidic integration, a couple of functional photonic–microfluidic chips were successfully realized. Subsequently, efforts shifted toward optical trapping experiments using this chip, which constitute the primary objective of this PhD project. Building upon this work, new studies have recently been initiated in our laboratory to develop a more reliable and efficient microfluidic system compatible with our photonic chips. This new approach relies on a polymer known as off-stoichiometry thiol-ene (OSTEMER), which undergoes a double-curing process: after the first cure, it remains soft and malleable, allowing manipulation and integration steps, while the second cure renders it fully rigid and strongly bonded to silicon. This property enables the inlet and outlet tubing to be embedded directly within the microchannels prior to final curing, thereby eliminating the connection issues encountered with Torr Seal.

Integration with Mode Adapters

It is important to note that the fabrication of mode adapters for inverted tapers, as presented in previous sections, is carried out prior to the fabrication of the microfluidic channel. Although these

structures are made from the same material, they do not intersect: the fluidic channel is centered with respect to the input and output mode adapters, with no overlap, as can be seen in fig. 2.24.

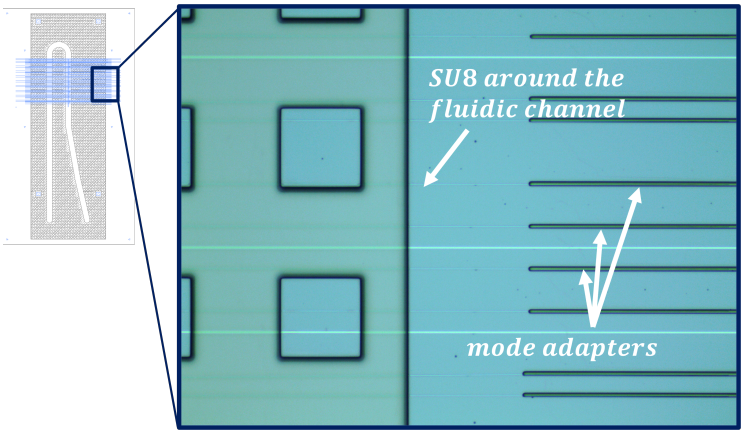

Figure 2.24: Microscope image zooming in on the fabricated SU-8 mode adapters, positioned next to the edge of the SU-8 block that contains the microfluidic channel, surrounded by a checkerboard pattern. The two SU-8 structure types are separate and do not overlap.

Moreover, the SU-8 structures differ in height. The mode adapters are $8\mu m$ thick to match the dimensions of the input optical fiber, whereas the microfluidic walls have to be higher in thickness to accommodate the volume of liquid passing through the channel. This thickness is primarily controlled by adjusting the spin-coating speed of the SU-8 photoresist during deposition and plays a crucial role in determining the flow rate within the channel.

During this PhD, two channel thicknesses were used: $14\mu m$ and $30\mu m$. Although no precise flow rate measurements were conducted on these chips, narrower channels were experimentally observed to significantly hinder fluid motion within the $750\mu m$-wide structure. However, narrower channels also increase the probability that particles travel close to the chip surface, where they have more probability of being trapped by the optical forces generated by the resonating cavities, rather than moving far above it. This can be a big advantage when only small sample volumes are available. The optimal balance between these competing factors remains to be investigated in future work.

Finally, fig. 2.25 summarizes all fabrication steps of this hybrid optofluidic chip: from the e-beam lithography of the photonic structures, to the fabrication of the SU-8 mode adapters, followed by the definition of the SU-8 fluidic channel. A subsequent but necessary step is the cleaving of the chip's edges to provide lateral access to the waveguides for optical coupling. Then, once the microfluidic chip is sealed with the glass coverslip and the metal tubes are connected, the optofluidic chip is ready to be integrated within the optical bench described in the next section.

2.4 Optical Bench

The optofluidic chip does not operate as a standalone device. Instead, it forms the central component of a broader experimental setup, shown schematically in fig. 2.26 and in its experimental implementation in fig. 2.27. This setup enables both excitation and observation of the device's optical response, while also allowing liquid samples to be handled within the microfluidic circuit. It combines several complementary subsystems that can be grouped into four functional categories:

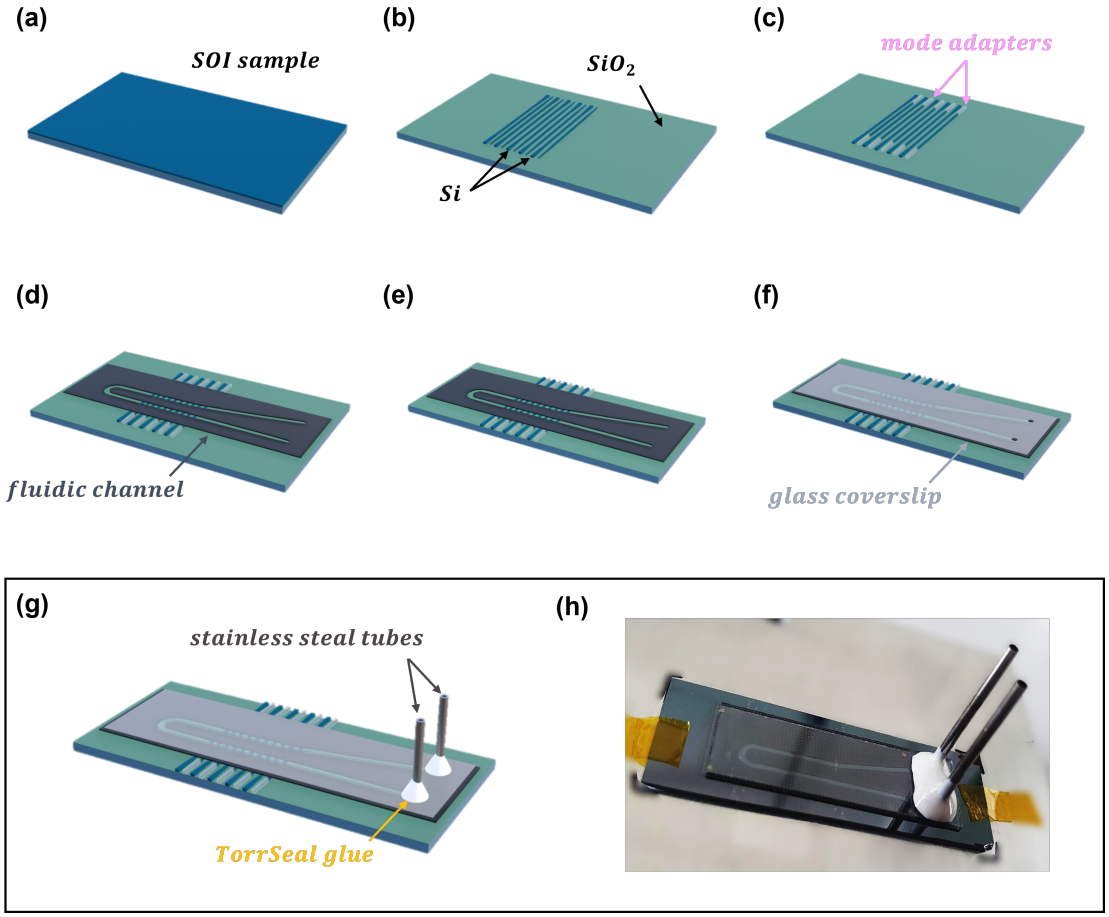

Figure 2.25: Summary of fabrication step of the optofluidic chip. (a) SOI sample before e-beam lithography. (b) SOI photonic chip after e-beam lithography, where only photonic structures are left from the SOI active layer. (c) Fabrication of SU-8 mode adapters. (d) Fabrication of the SU-8 microfluidic channel. (e) Chip edges cleaving for lateral coupling of the waveguides. (f) Sealing the microfluidic channel using a glass cover slip with two drilled holes. (g-h) Final result after connecting stainless steel tubes using Torr Seal as adherent.

microfluidic control, light delivery, transmitted signal monitoring, and optical cavity visualization. Together, these elements ensure the stable operation, optical coupling, and precise characterization of the photonic chip.

The microfluidic control system, as described in a previous section, includes silicone tubing connected to the chip and a tabletop microfluidic flow controller (Fluigent EZ). This controller, in combination with optional manual valves, provides precise regulation of flow rates and pressures. The input pressure can be adjusted from 0 to 1000 mbar, with 0.1 mbar precision. The system is powered by the laboratory's pressurized air line, ensuring stable and reproducible conditions for fluid delivery. Delivery times through the circuit, from the tube holding the sample to the actual microfluidic channel on top of the photonic chip, depend not only on the pressure set on the flow controller, but also on the thickness of the channel. Thicker channels allow larger volumes to flow with lower hydrodynamic resistance, while thinner channels increase resistance and slow the flow. At a pressure of 100mbar and a total tube length of approximately 15cm, we observed that it takes a couple of minutes for the 14μm channel to fill, while the 30μm channel typically fills in under a minute. Further optimization of flow control will be necessary, especially after updating the inlet and outlet connection protocol, since the current Torr Seal–based attachment prevents direct inspection of the channel entrance and may lead to chip-to-chip variations in effective flow

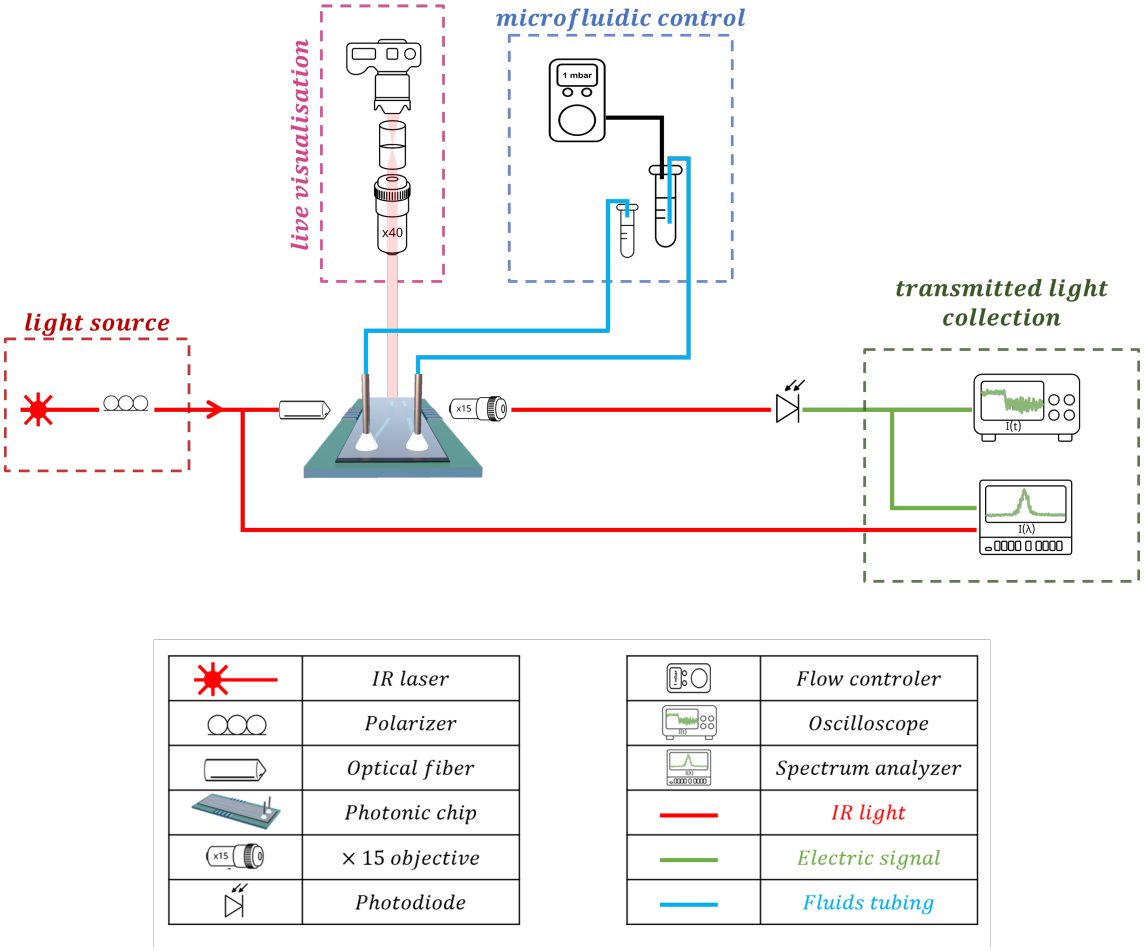

Figure 2.26: Illustration of the optical bench components

resistance as explained previously. Such optimization will eventually ensure reproducible and efficient delivery in future experiments.

The light source is delivered through a single-mode optical fiber with a tapered tip, previously described. It is powered by a tunable infrared laser (1440–1640 nm), allowing precise adjustment of both wavelength and injected optical power. Lefèvre loops placed between the laser and the fiber ensure proper polarization control of the light entering the photonic waveguides. This control is particularly important when coupling light into photonic crystal cavities, because the resonant modes exist only for a specific polarization. In our devices, the cavities are designed to support only transverse electric (TE) modes, with the electric field oriented in-plane relative to the chip. Matching the input light polarization to that of the cavity maximizes coupling into the resonator, enhances the strength of the resonant field, and allows selective probing of mode-dependent optical behavior.

The light transmitted through the chip is collected at the output of the waveguides using a 15× objective, which focuses the beam onto a photodiode. The photodiode converts the optical signal into an electrical one, which is then amplified by a preamplifier to increase the signal strength and inverted by an inverter to match the oscilloscope input requirements, before being recorded in real time by the oscilloscope. Both the photodiode and the input laser are also connected to a CT400 spectrum analyzer, enabling spectral characterization of the optical cavities over the full spectral range of the source. For alignment procedures, a gold mirror mounted on a rotatable holder can be inserted after the collection objective to redirect the transmitted beam toward an infrared camera,

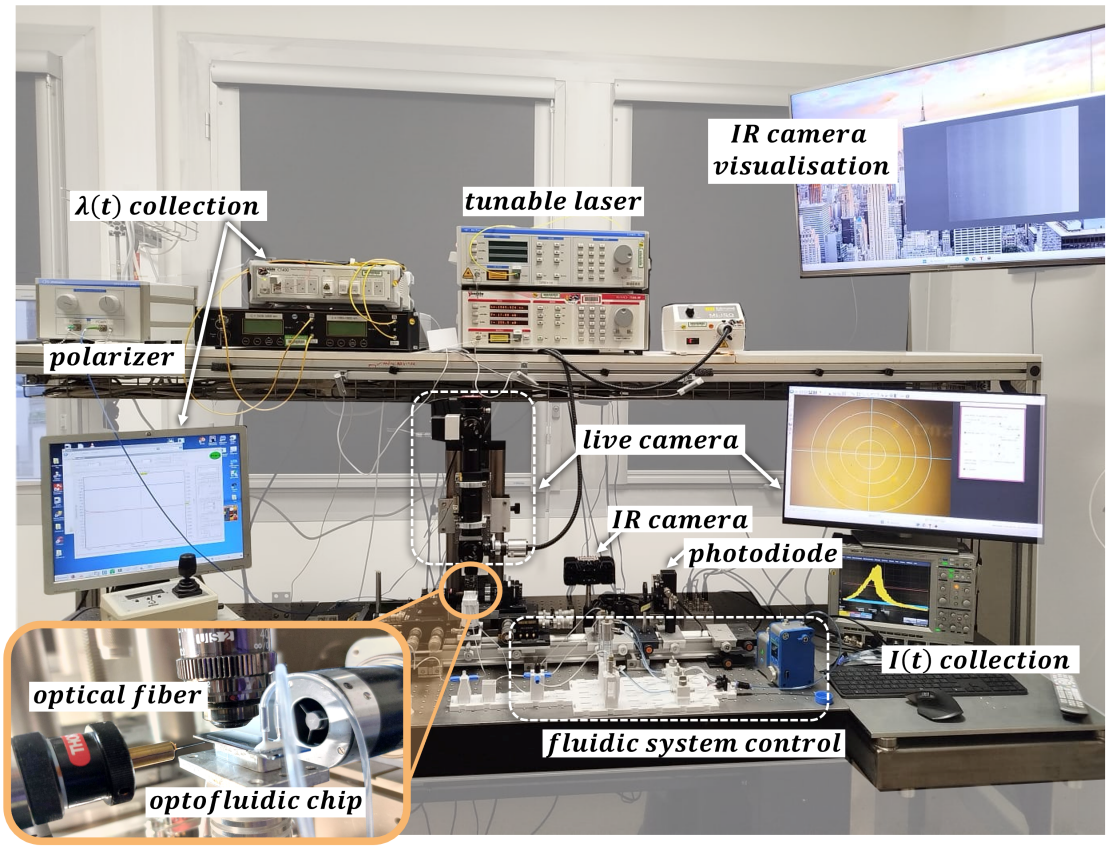

Figure 2.27: Image of the optical bench with annotations indicating the main components

providing direct visual feedback of the output facet during setup adjustments.

Finally, a visualization system mounted above the chip enables direct observation of the microfluidic region and resonant cavities during operation. It consists of a Sony CCD camera with a large high-resolution sensor, coupled to a standard 40× microscope objective fixed on a vertical column. This configuration allows live imaging or video recording of the optical cavities, providing an essential visual complement to the optical and electrical measurements obtained from the other subsystems.

2.5 Conclusions & Perspectives

In this chapter, we presented the technical toolbox developed and implemented throughout this work. The fabrication of the photonic chips constitutes the foundation of our project and relies on careful design and optimization of the photonic structures' architecture. The introduction of inverted tapers combined with SU-8 mode adapters represented a significant improvement in the optical efficiency of our chip. Furthermore, integrating a microfluidic system directly onto the chip greatly enhanced the overall usability of the device, making experiments both faster to perform and, more importantly, more reproducible than in previous setups.

Several avenues for improvement can still be envisioned for this platform, some of which were already discussed throughout the chapter. The microfluidic system, in particular, could ben-

efit from refinements such as improving the attachment procedure for inlet and outlet connectors, optimizing the channel height to accelerate sample delivery, and adjusting the channel width to achieve a more controlled flow rate in the immediate vicinity of the resonating cavities. In future designs, multiplexing the optical waveguides and microfluidic channels could also be considered to allow several independent photonic crystal cavities to be simultaneously excited. This configuration would make it possible to deliver either different or identical samples to each cavity, thereby enabling parallel measurements and increasing the overall experimental throughput.

Another important direction concerns the optical and mechanical packaging of the device. Ongoing work in our group aims to develop permanent and reproducible connections between optical fibers and on-chip waveguides by directly bonding the fibers to the chip edges. Such an approach would not only improve coupling efficiency and long-term stability but also represent a crucial step toward compact, portable photonic platforms. In the same spirit, further developments could focus on automating the optical alignment and fluidic control processes through computer-assisted feedback systems. This would reduce the need for manual adjustments, improve reproducibility across experiments, and pave the way for high-throughput operation.

In a longer-term perspective, the overall footprint of the optical bench could be progressively reduced to bring the system closer to a genuine lab-on-chip platform. While certain components, such as the infrared laser, will remain essential, the live visualization setup in particular could eventually be removed once sufficient data have been collected to study optical trapping exclusively through the transmitted signals of the photonic structures.

The next chapter introduces the second major component of this PhD work: the biological specimens investigated using the platform developed here. We will describe their intrinsic characteristics and the classical biological tools typically used to study them. Later chapters will explore the advantages of combining these objects with the hybrid chip and discuss the results obtained through this approach.

3

Microbiology & Bacteria

In this chapter, we will present the specific biological objects of interest in this PhD and their characteristics. We will discuss how they are typically studied in the microbiology world and compare these classical methods to the photonic alternative we developed.

Contents

3.1 Introduction 54
3.1.1 Bacteria as Micro-Organisms 54
3.1.2 Bacterial Classification 55
3.1.3 Importance of Bacterial Detection & Identification 60
3.2 Bacterial Identification: Classical Methods 60
3.2.1 Culture-based and Biochemical Bethods 60
3.2.2 Serotyping and Immunological Methods 63
3.2.3 Molecular and Sequencing-based Methods 66
3.2.4 Mass spectrometry-based methods 69
3.3 Bacterial Identification: Optical Methods 71
3.3.1 Fluorescence and Scattering detection 71
3.3.2 Vibrational Spectroscopies 74
3.3.3 Plasmonic and Photonic Sensors 76
3.4 Prior Work within the Research Group 76
3.5 Motivations & Biological Framework of the Present Work 81
3.6 Conclusions 82

3.1 Introduction

3.1.1 Bacteria as Micro-Organisms

Bacteria are among the simplest and most fascinating forms of life on Earth. They are ubiquitous, existing as part of virtually every ecosystem and inhabiting environments that range from oceanic depths to human skin [81]. These unicellular prokaryotes are characterized by the absence of a nucleus and other complex organelles such as mitochondria. Instead, their genetic material is organized into a single circular DNA molecule located in a region called the nucleoid, which floats freely within the cell. Many bacteria also contain small, additional DNA circles known as plasmids, which carry extra genes that can provide useful traits, such as antibiotic resistance [82]. These components are indicated on fig. 3.1 where the structure of a bacterial cell is represented.

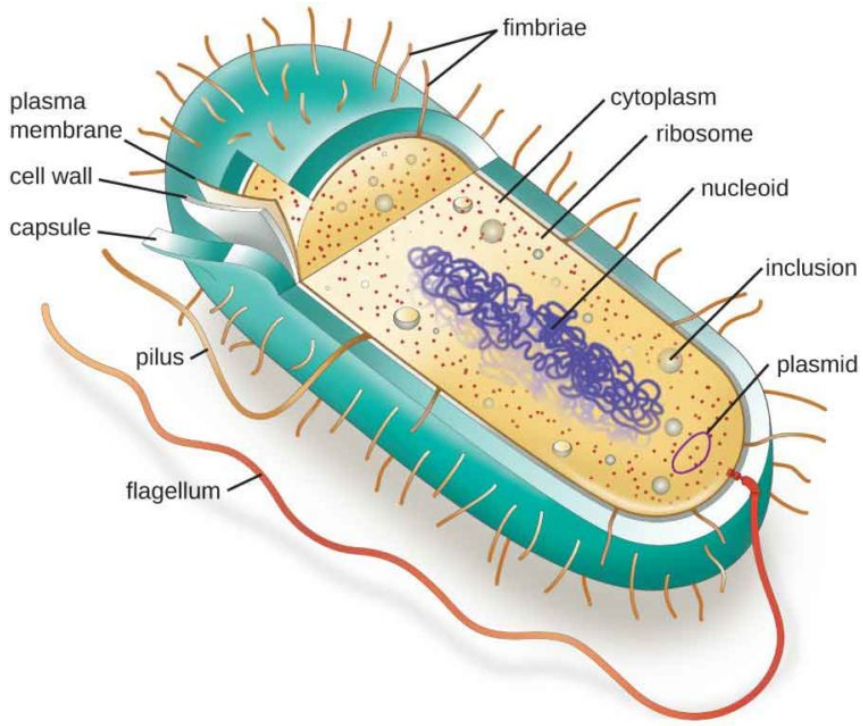

Figure 3.1: Diagram of a bacterial cell showing structural parts. (Copyright-free image from Wikimedia Commons)

Typically measuring between 0.5 and 5 μm, bacterial cells are enclosed by a rigid cell wall that maintains their shape and provides mechanical protection. The interior of the cell, known as the cytoplasm, hosts all metabolic processes and contains the essential biomolecules required for survival and replication. Most bacteria reproduce through binary fission, a rapid and highly efficient process that, under optimal growth conditions, can produce population doubling times as short as $20 - 30$ minutes in fast-growing species [81, 83].

Bacteria display remarkable metabolic versatility, enabling them to thrive in virtually every environment on Earth [84]. Many bacteria perform essential ecological and physiological roles. For example, some bacteria aid with digestion in the human intestines [85, 86], others clean-up pollutants such as heavy metals in soil and water [87, 88], and certain strains are employed in food production through fermentation [89, 90]. However, while many bacteria contribute positively to multiple biological and industrial processes, their effects can be strongly context-dependent [91, 92]. Under specific genetic or environmental conditions, some species may become pathogenic through the expression of virulence factors. In other cases, such traits are not acquired but are

already encoded in the genome yet only expressed under particular conditions. Either way, once expressed, these virulence factors enable host invasion and tissue damage, giving rise to **a range of infections in humans and animals, from localized forms such as those affecting the skin or respiratory tract to severe systemic diseases like sepsis or meningitis. Pathogenic bacteria can also spread from infected to healthy hosts through various routes. Transmission methods include person-to-person contact or droplets, animal contact or consumption of contaminated meat, eggs, or dairy, and even through plants via improperly washed or handled produce [92].

In this context, understanding the structural and physiological characteristics of bacteria is essential not only for advancing microbiological knowledge but also for enabling the development of rapid detection technologies, ranging from improved implementations of classical approaches such as rapid antibiograms [93] to more recent methods based on microfluidics and optical interrogation [94]. This chapter will describe how bacteria are classified and characterized using both classical microbiological methods and more recent approaches based on optical techniques. We will therefore present bacterial features that are relevant for the on-chip manipulation of single cells within the optofluidic platform introduced earlier. In particular, we will emphasize the properties governing bacterial interactions with both the chip surface and the optical fields above it, as well as impacting the resulting optical signatures. This chapter therefore forms the basis of the analysis presented in the rest of the manuscript. Additional methodological details related to microbiological practices, including sample preparation and extended culture-based techniques, are provided in chapter A for completeness.

3.1.2 Bacterial Classification

Bacteria represent an exceptionally diverse domain of life, encompassing countless species that differ in structure, physiology, and ecological function. To manage this diversity, microbiologists employ classification systems that organize bacteria into defined categories based on shared characteristics, physiological traits, and genetic relatedness. These categories provide a framework for identifying and comparing bacterial species, as well as for predicting their behavior in different environments. Here, we present a non-exhaustive list of key bacterial classification categories.

Taxonomy

Taxonomy is the formal discipline that governs the organization, naming, and hierarchical arrangement of any living organisms like animals or plants, but also bacteria. It establishes a universal language that enables scientists worldwide to accurately identify and compare microbes (microorganisms) [95].

The taxonomic hierarchy begins with the broadest category, the domain, and becomes progressively more specific through the following ranks: phylum, class, order, family, genus, and species. Each rank groups organisms based on shared characteristics, with species representing the most specific rank. For example, the bacterium *Staphylococcus aureus* belongs to the domain *Bacteria*, phylum *Firmicutes*, class *Bacilli*, order *Bacillales*, family *Staphylococcaceae*, genus *Staphylococcus*, and species *S. aureus*. Another widely studied example is the bacterium *Escherichia coli*, which belongs to the domain *Bacteria*, phylum *Proteobacteria*, class *Gammaproteobacteria*, order *Enterobacterales*, genus *Escherichia*, and species *E. coli*. The names assigned to each bacterium follow specific international conventions, reflecting their taxonomic relationships and facilitating consistent communication among scientists [82].

Within a single species, bacteria may exist as distinct strains or subtypes, which are genetically or phenotypically distinct populations. These strains are often designated with additional identifiers appended to the species name, for example, *E. coli* O157:H7, *E. coli* K12, or laboratory-specific labels such as *E. coli* 123 and *E. coli* 456. Strain-level identification is crucial in microbi-

ology, as different strains can vary significantly in pathogenicity, metabolic capabilities, or other functional traits [82].

However, in many physics- and photonics-related applications, researchers typically focus on the species level without distinguishing among strains. In the majority of cases, species-level identification is sufficient for experimental purposes. Strain-level typing becomes particularly important in contexts such as epidemiology, where fine distinctions between closely related variants are required. Nevertheless, overlooking strain-level variability may mask important functional differences that can influence behaviours such as microbial interactions or responses to environmental conditions [81].

Biosafety and Risk Groups

Pathogenic bacteria do not all represent the same risk. In fact, they vary widely in their potential to cause disease and are, therefore, classified in biosafety groups that include other pathogenic organisms such as viruses. The categories depend on the degree of hazard, the routes of transmission and the availability of effective treatment or preventative measures. These categories are called risk groups and range from Risk Group 1 (inoffensive) to Risk Group 4 (highly dangerous). They are closely associated with biosafety levels (BSL-1 to BSL-4), which define the corresponding laboratory safety practices and containment requirements for handling bacterial samples.

This classification can be illustrated through representative examples across different risk groups. For instance, certain attenuated laboratory strains of *Escherichia coli* (e.g. K-12) fall within Risk Group 1. In contrast, many other strains of *E. coli* are classified in Risk Group 2 due to their pathogenic potential, for example in gastrointestinal infections. At higher risk levels, highly virulent agents such as *Yersinia pestis* (responsible for plague) are classified in Risk Group 3. Risk Group 4 includes extremely hazardous pathogens for which no effective treatment is available, such as certain extensively drug-resistant, highly contagious and deadly strains of *Mycobacterium tuberculosis*. This hierarchical system is essential for ensuring safe microbiological research and for mitigating risks associated with the handling of infectious agents. It is important to emphasize that different strains from the same bacterial species may be classified in different biosafety levels.

Morphology

Bacterial morphology is the description of its external shape and structural features that characterize and distinguish one bacterial species from another. Bacteria display multiple types of shapes and arrangements, as represented in fig. 3.2. The most common morphologies are *cocci* (spherical) and *bacilli* (rod-shaped). Multiple other shapes exist like *spirilla* (spiral), *vibrios* (comma-shaped), and even uncasual ones like star-shaped bacteria have been described [96]. For every one of these shapes, numerous variations and intermediate forms exist. Some bacteria are even pleomorphic, such as *Mycoplasma* species, which lack a cell wall and can therefore display significant variability in shape and size. This wide variety of morphological traits is generally defined by the cell wall and influences many bacterial processes including moving through their environment, interacting with surroundings and even acquiring nutrition [82, 97].

Motility

Motility is the definition of a bacterium's ability to actively navigate through a medium, whether liquid or semi-solid. It is a defining feature of many bacterial species, acquired by specialized features of their outer membrane. The main structure that enables bacteria to swim and propel their bodies are the tail-like appendages called *flagella* (about 20 nanometres in diameter and up to 20 micrometres in length, represented in fig. 3.1), which is a helical protein structure that

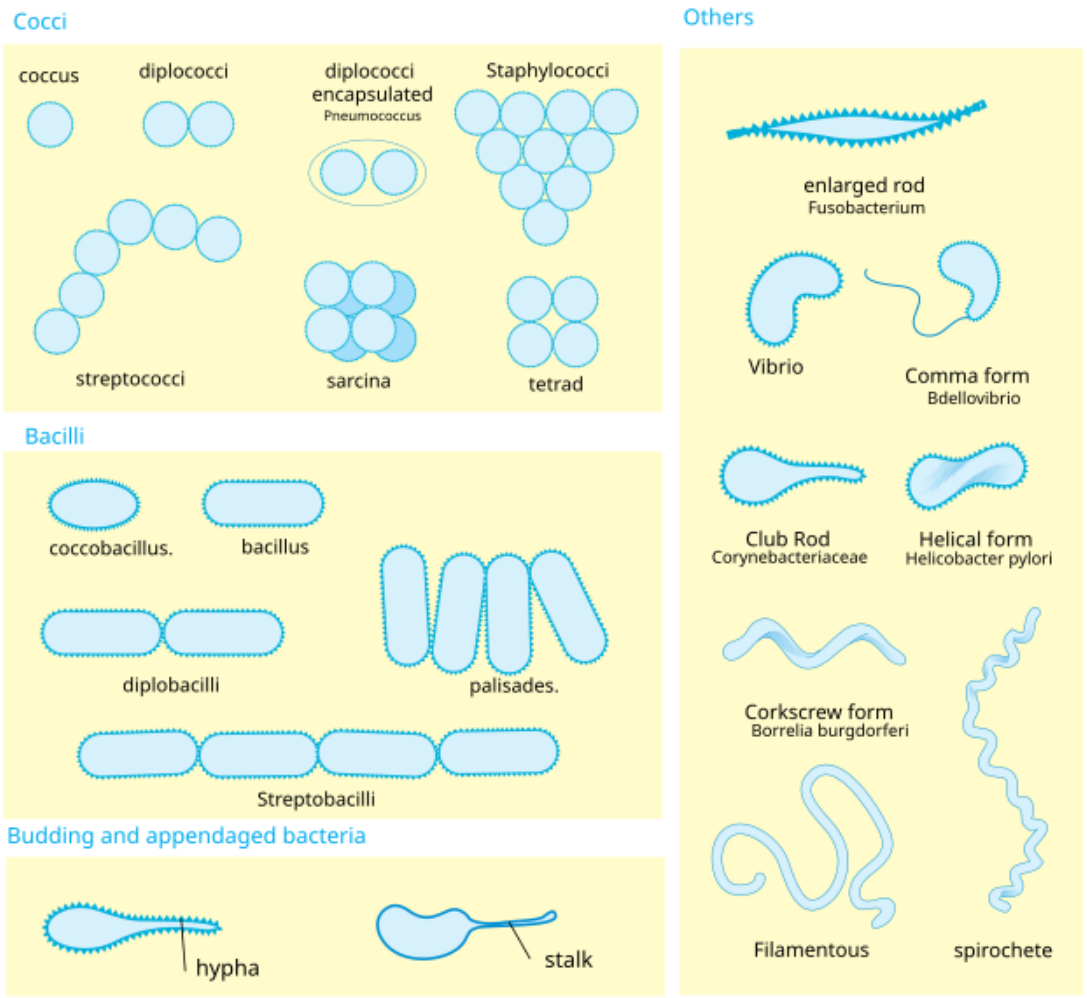

Figure 3.2: Diagram of bacterial morphology. (Copyright-free image from Wikimedia Commons)

generates propulsive forces through rotational motion. Some bacteria, however, exhibit gliding or twitching motility driven by surface structures like *pili* which are fine filaments of protein ($2-10$ nanometres in diameter and up to several micrometres in length, also represented in fig. 3.1) distributed over the surface of the cell, or by secretion-based mechanisms. The presence, number, and arrangement of these appendages can vary widely among taxa (taxonomy groups). Motility not only aids in nutrient acquisition and colonization but also plays a critical role in biofilm development, cells sticking to each other and often also to a surface, and pathogenesis, the development of diseases caused by pathogenic bacteria [82, 97].

Cell Wall Composition

The bacterial cell envelope is a complex structure that defines many physiological but also immunological properties. Based on their cell wall composition, bacteria are broadly classified as Gram-positive or Gram-negative according to the results of a coloration technique known as Gram staining. This coloration reflects differences in the structure of the cell envelope surrounding the cytoplasmic membrane. In the case of Gram-positive bacteria, the cell envelope is a thick peptidoglycan layer that retains crystal violet dye. On the other hand, Gram-negative bacteria have a thinner peptidoglycan wall with an additional outer membrane containing lipopolysaccharides (LPS) that does not retain the violet dye, resulting in a pink coloration after counterstaining with

safranin [82, 97]. These membrane structures are represented in fig. 3.3.

In Gram-negative bacteria, lipopolysaccharides (LPS) are the dominant components of the outer membrane and can occupy up to 75% of the cell surface, thereby playing a major role in interactions with the surrounding environment and with solid interfaces [97, 98]. The structure of LPS is organized into three main regions: lipid A, which anchors the molecule in the membrane; a core oligosaccharide; and a distal O-polysaccharide chain (O-antigen), which is strain-specific [99]. This outermost O-antigen is the most exposed and variable component, composed of repeating oligosaccharide units that can extend several tens of nanometers into the surrounding medium.

Because of their hydrophilic nature and conformational flexibility, these polysaccharide chains form an extended layer at the bacterial surface that directly interacts with the external environment. This layer can influence bacterial adhesion and interactions with nearby structures, as it introduces steric and energetic barriers to surface contact [98]. Such effects are particularly relevant in the context of optical trapping near surfaces, where the evanescent field primarily probes these outer membrane components.

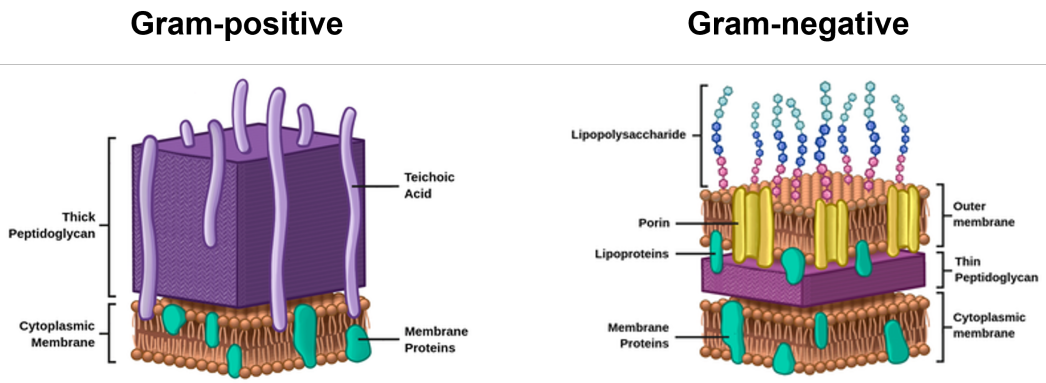

Figure 3.3: Visual summary of cell envelope organization in Gram-positive (left) and Gram-negative (right) bacteria, representing the relative thickness of the peptidoglycan layer and the presence of an outer membrane. (Copyright-free image from Labster)

It should be noted that such schematic representations provide a simplified view of the bacterial envelope. In reality, the cell surface is far more complex and dynamic, with numerous external structures extending into the surrounding medium, as illustrated in fig. 3.1. These include lipopolysaccharides (LPS), capsular or extracellular polysaccharides (EPS), which form a hydrated matrix surrounding the cell, as well as fibrillar proteins such as fimbriae or pili, which are thin, hair-like appendages that mediate adhesion to surfaces and other cells. Depending on the species and environmental conditions, these surface structures can extend from a few tens of nanometers up to several hundreds of nanometers, or even approach micrometer scales in the case of long fimbriae as shown in fig. 3.4 [100, 101].

As a result, bacterial cells should not be considered as rigid objects with well-defined boundaries, but rather as "soft" and extended interfaces. This has important implications for optical trapping near surfaces, since the evanescent field primarily interacts with these outermost and highly variable structures rather than with the cell envelope core.

Serotype

A serotype refers to a distinct variation within a bacterial species that is defined by differences in the molecular structures of specific surface molecules called antigens. Antigens vary in chemical structure and may occur in several forms, including proteins, peptides (amino acid chains),

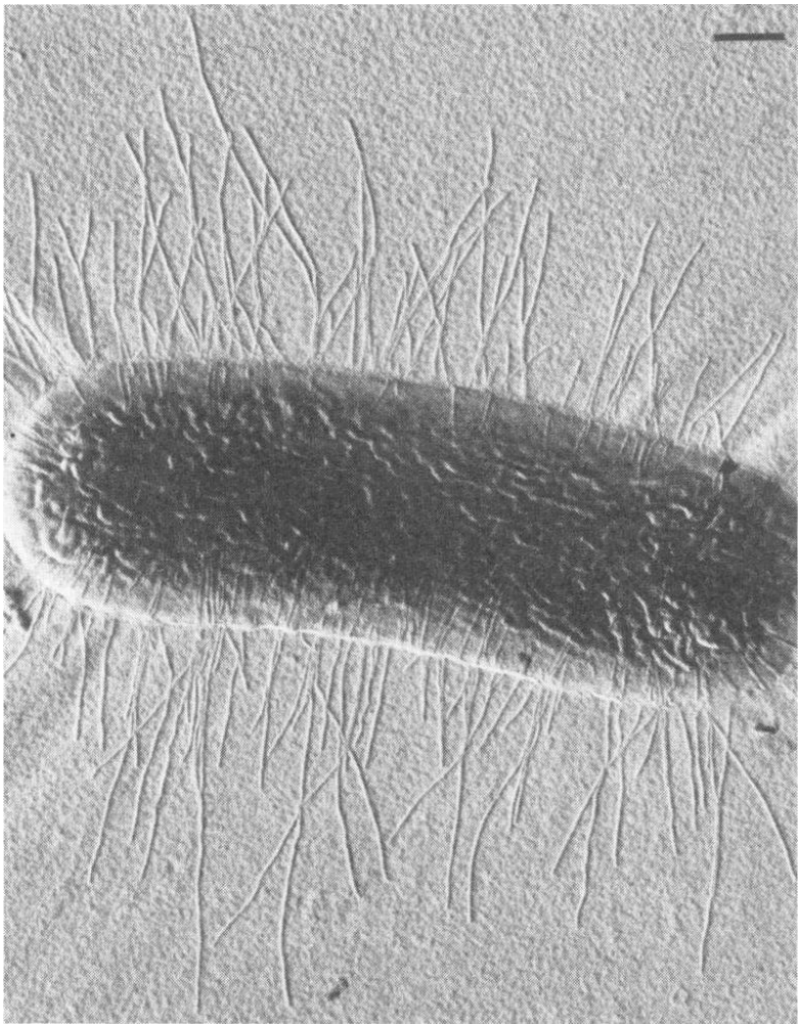

Figure 3.4: Electron microscopy image of the Gram-negative bacterium Escherichia coli (strain 469-3) illustrating numerous thin fibrillar surface appendages, such as fimbriae or pili, extending from the cell envelope. These long, filamentous structures can reach several hundreds of nanometers or more in length and contribute to the extended, "soft" nature of the bacterial surface beyond the core membrane. The scalebar corresponds to $0.2\mu m$*. Reprinted from [100].*

or polysaccharides (chains of simple sugars). These antigenic markers trigger specific immune responses and are used to distinguish closely related bacterial strains that may otherwise appear identical under the microscope or share similar genetic backgrounds. The most common types are the O-antigen present in the lipopolysaccharides attached to the membrane of Gram-negative cells, the H-antigen present on the flagella of motile species, and the K-antigen associated with the bacterial capsule when present. In practice, serotyping often focuses on O and H antigens because they are highly immunogenic, relatively stable, and widely distributed among species such as *Escherichia coli*. Each antigen type can exist in multiple variants, producing combinations like the well-known highly virulent *E. coli* O157:H7, where O157 designates the specific O-antigen and H7 the flagellar antigen. Serotyping is important because antigenic variation often determines a bacterium's virulence, host specificity, and ability to evade immune detection. Since serotypes are typically stable within bacterial populations, they serve as reliable markers for tracing infection sources, monitoring outbreaks, and informing vaccine development. However, with the rapid decrease in the cost of sequencing technologies in recent years, which will be presented later, serotyping is increasingly complemented, and in some cases replaced, by genomic approaches that provide higher-resolution characterization.

3.1.3 Importance of Bacterial Detection & Identification

Detection

Bacterial detection refers to the process of determining whether microorganisms are present in a given sample. In industrial and environmental contexts, it serves as a preventive measure to ensure product safety and quality in sectors such as food processing, pharmaceuticals, and cosmetology. Routine monitoring typically targeted and standardized to confirm the absence of known bacterial species of concern, in order to confirm sterility or acceptable microbial levels. Therefore, these detection procedures help maintain compliance with regulatory standards and safeguard public health.

In clinical settings, bacterial detection takes on a diagnostic role. The goal is to determine whether pathogenic bacteria are present in specimens collected from patients. Sample types vary according to observed symptoms and may include blood, urine, feces, sputum (cough mucus), or tissue biopsies. Because the underlying cause of infection is often unknown at this stage, detection assays are designed to screen for a broad range of potential pathogens. Furthermore, detection techniques are selected in adaption to the biological nature of the sample and the urgency of diagnosis. Reliable detection in this context is critical for timely medical intervention, as it informs subsequent identification and susceptibility testing that guide clinical decision-making.

Identification

Once bacterial presence has been confirmed, identification focuses on determining the specific species, strain, or serotype involved. This step is fundamental to microbiology, as it enables classification of the bacteria into the categories mentioned beforehand. In clinical practice, accurate identification supports therapeutic decisions and infection control, while in industrial and environmental contexts it helps trace sources of contamination and design targeted mitigation strategies.

Over time, bacterial identification methods have evolved to include multiple approaches commonly used in biology studies, each offering a distinct balance between specificity, speed, and experimental complexity. Classical biochemical tests and culture-based methods remain fundamental, but they are increasingly complemented by molecular and spectroscopic approaches capable of providing faster and more precise results. Beyond speed, these developments also aim at improving the level of detail at which bacteria can be characterized, in particular by enabling analysis at the single-cell level, where population heterogeneity can be resolved.

The following sections present an overview of these established strategies and their limitations, before introducing emerging optical techniques that enable label-free bacterial recognition at the single-cell scale. These approaches form the conceptual foundation for the optical trapping-based manipulation and sensing methods explored in this manuscript.

3.2 Bacterial Identification: Classical Methods

3.2.1 Culture-based and Biochemical Bethods

Traditional microbiology relies mainly on culture-based phenotyping, which consists of determining observable and biochemical characteristics of bacterial isolates to distinguish their features and attributes. In this section, we present the main techniques that remain relevant today, while additional classical approaches (including selective media and extended biochemical assays) are provided in chapter A for completeness.

Colony Morphology & Staining

Staining methods are widely used in microbiology to improve contrast and observe cellular structure. The most common among them is Gram staining, previously mentioned, which differentiates bacteria into Gram-positive or Gram-negative classes based on how cell walls retain or lose dye. First developed in 1884, the protocol proceeds as follows: a bacterial smear is first stained with crystal violet (also known as hexamethyl pararosaniline chloride), then treated with iodine, which acts as a mordant to fix the dye to the cell wall. A decolorizing solvent (typically ethanol, acetone, or a mixture thereof) is applied to wash out the dye from cells that cannot retain it, and finally a counterstain such as safranin (red dye) is added to color decolorized cells [102].

In Gram-positive bacteria, with their thick peptidoglycan layer, the crystal violet-iodine complex resists removal, leading to a purple appearance. In Gram-negative bacteria, whose thin peptidoglycan and outer membrane allow the complex to be washed out during decolorization, the subsequent safranin counterstain results in pink or red coloring. [102] Under light microscopy, the contrasting colors and cell morphologies (cocci, rods, chains, clusters) are revealed, as shown in fig. 3.5.

Gram staining, which can be performed manually or through automated systems for greater efficiency [103], remains an important and rapid preliminary assay in both clinical and research settings. It provides a broad classification of bacteria based on cell wall type and morphology, helping clinicians initiate empiric therapy and guiding their choices of full culture identification tests. Its short turnaround time and low cost make it especially valuable in urgent or resource-limited contexts. This rapidity is possible because Gram staining is not always dependent on prior culture, which can take from several hours to weeks to complete. Instead, direct Gram staining can be performed immediately on specimens with sufficient bacterial load, such as sterile body fluids (blood, urine) or mucosal secretions like vaginal discharge [104]. However, in cases with small volumes or low bacterial density, culture amplification before staining generally improves detection sensitivity and interpretability.

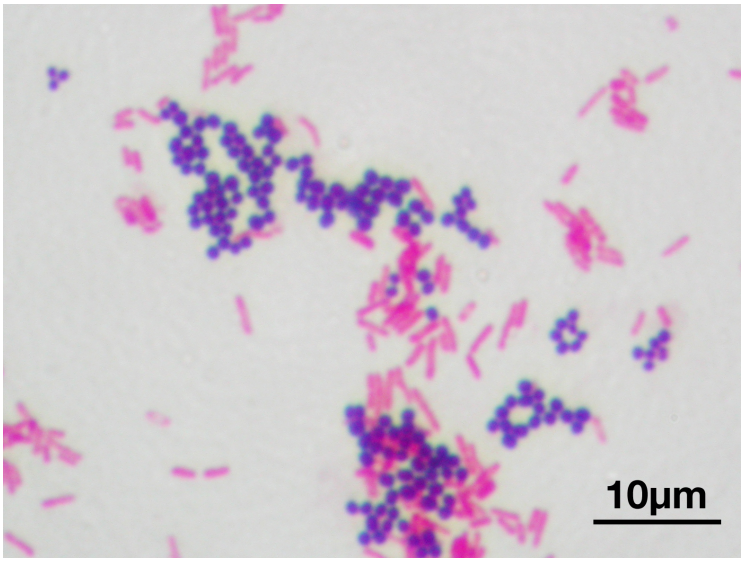

Figure 3.5: Microscopic image of Gram-stained mixed preparation showing Staphylococcus aureus (ATCC 25923; purple, Gram-positive cocci) and Escherichia coli (ATCC 11775; red, Gram-negative bacilli), both commonly used as reference organisms in Gram staining. (Source: Y tambe, 2010, Creative Commons license: CC BY-SA 3.0)

Automated and Miniature Systems

While classical biochemical assays remain foundational in microbiology, particularly in the field of research, their sequential and labor-intensive nature has prompted the development of test kits and automated platforms that enable faster and more standardized bacterial detection and identification, especially in clinical environments where rapidity is often required.

Among the earliest and most influential miniature systems developed to consolidate multiple biochemical tests is the Analytical Profile Index (API). Each API strip is designed to streamline bacterial identification through an array of small wells preloaded with dehydrated substrates corresponding to distinct biochemical reactions. When inoculated with a standardized bacterial suspension (typically adjusted to 0.5 McFarland), these substrates are rehydrated and, after incubation, produce color changes that reflect specific metabolic activities. Figure 3.6 illustrates representative positive (a) and negative (b) reactions obtained with an API 20E strip (bioMérieux), a format developed for $18-24$-hour identification of *Enterobacterales* and other non-fastidious Gram-negative bacteria [105]. In fact, different API versions incorporate tailored sets of reagents to target particular bacterial groups or characteristics. The resulting pattern of positive and negative reactions is compared with established databases to generate a rapid tentative identification. The API system thus consolidates numerous conventional biochemical assays into a single, standardized format, reducing the use of consumables, hands-on time, and inter-test variability.

However, this approach requires a priori selection of the appropriate test gallery, which is typically guided by preliminary phenotypic assays such as Gram staining and, when relevant, catalase or oxidase tests. In addition, the system relies on manual inoculation and visual interpretation, and its performance is inherently limited by the scope of the reference database, which can reduce accuracy for atypical isolates or emerging taxa.



Figure 3.6: Examples of API 20E strip results after incubation showing examples of (a) all positive and (b) all negative results for the included tests. Bacterial species used for these demonstrations are unknown. Figure reprinted and adapted from [106].

The limitations of semi-manual kits such as the API have driven the development of platforms that build upon the same biochemical testing principles while introducing fully automated procedures. Systems such as the VITEK2 (bioMérieux) and BD Phoenix (Becton Dickinson) platforms integrate miniaturized biochemical testing within sealed disposable cards that are automatically inoculated, incubated, and optically monitored. Multiple cards can be processed simultaneously, each containing several wells $(64-136)$ with different combinations of reagents, as shown in fig. 3.7(a-b), enabling extensive parallel testing. In these systems, metabolic changes are detected through turbidimetric or fluorometric signals in each well. These signals are continuously analyzed by embedded software that compares reaction kinetics to extensive reference databases to provide species-level identification and antimicrobial susceptibility profiles. Such automation significantly reduces manual handling, shortens turnaround time, and enhances standardization

in high-throughput clinical laboratories. However, these systems rely on proprietary databases each maintained by the different manufacturers, which are not fully shared across platforms. This not only limits comparability between systems, but can also introduce variability and potential misidentification when taxa are missing or under-represented [107].

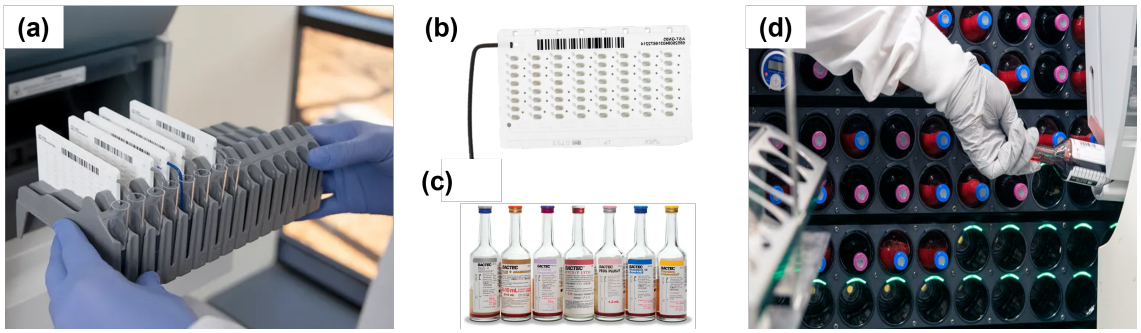

Figure 3.7: Presentation of the VITEK and BACTEC platforms and associated consumables. ***(a)*** *Cassette loader inside a VITEK instrument holding up to 15 identification cards, each connected to a tube containing the bacterial suspension to be analyzed (Source: bioMérieux).* ***(b)*** *Example of an unused VITEK card showing the array of biochemical reagent wells and a barcode for automated data entry (Source: bioMérieux).* ***(c)*** *Selection of BACTEC culture bottles designed for different standardized growth conditions (aerobic, anaerobic, pediatric, mycobacterial), each labeled with a barcode for sample tracking (Source: Becton Dickinson).* ***(d)*** *Interior of a BACTEC instrument showing the incubator racks accommodating multiple culture bottles for parallel testing (Source: Becton Dickinson).*

The systems presented in this section represent only a subset of the automated culture and monitoring technologies that have transformed clinical microbiology. By integrating incubation, detection, and in many cases preliminary identification into compact, high-throughput workflows, these platforms substantially reduce manual workload, shorten detection times, and improve the reproducibility of biochemical assay results. Nevertheless, their reliance on database-driven interpretation and their limited ability to identify unusual, mixed, or slow-growing organisms mean that additional confirmatory testing often remains necessary. Furthermore, the high cost of instrumentation and ongoing maintenance can restrict their implementation in resource-limited laboratories. Beyond these examples focused on culture-based and biochemical assays, other automated systems that rely on alternative principles are increasingly incorporated into diagnostic workflows and will be discussed in subsequent sections of this manuscript.

3.2.2 Serotyping and Immunological Methods

Serotyping refers to the classification of bacterial strains based on their serotypes; a cell wall categorization presented in previous sections. As this characteristic is related to surface antigens, traditional serotyping methods rely on immunological reactions between these bacterial antigens and antibodies. In this section, we introduce the classical methods of conducting such tests and visualizing their results.

Agglutination Assays

Agglutination assays are among the oldest and most widely applied immunological tools for bacterial serotyping. They rely on the formation of visible clumps when specific antibodies bind to their corresponding antigens on the bacterial surface. This method can be used both for identifying

bacterial isolates and for detecting bacterial-specific antibodies in patient samples, which indicates previous exposure to a pathogen.

In its simplest form, a bacterial suspension is mixed with a drop of specific antiserum on a glass slide, in a small well or in a tube. The formation of visible clumps within seconds to minutes, as shown in fig. 3.8, indicates a positive reaction. Slide and well assays provide rapid qualitative results, while tube-based formats enable semi-quantitative analysis through serial dilution [108]. Variants using antibody-coated particles, such as latex beads, can further enhance sensitivity and facilitate detection of weakly expressed or soluble antigens [108].

Agglutination assays are widely used for the identification of clinically relevant bacteria such as *Escherichia coli*, *Pseudomonas aeruginosa*, *Salmonella group B*, and many more [109–112]. Moreover, it can be combined with automated image analysis to improve throughput and objectivity [112]. However, these methods may suffer from cross-reactivity, subjective interpretation, and reduced specificity compared with molecular approaches. Despite these limitations, their simplicity and rapid readout make them valuable tools in routine diagnostics.

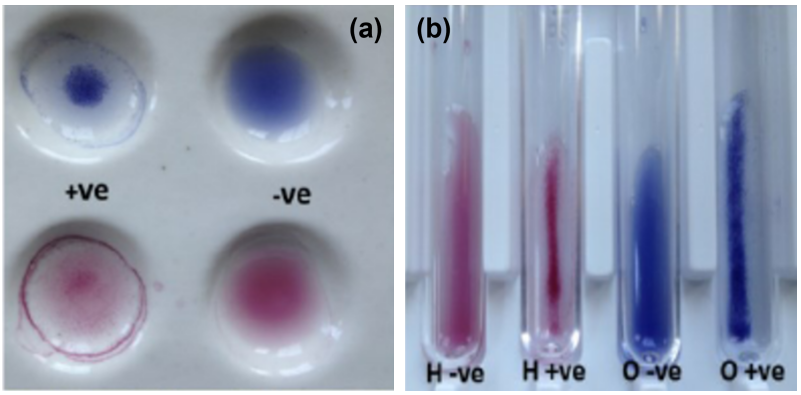

Figure 3.8: Examples of agglutination test results in wells (a) and in tubes (b). In negative tests (−ve), particles remain freely suspended in the liquid medium, whereas in positive tests (+ve), visible clumps are formed. Reprinted and adapted from [113].

Enzyme-Linked Immunosorbent Assay (ELISA)

Another method for determining bacterial serotypes is the enzyme-linked immunosorbent assay (ELISA), which relies on enzyme-labeled antibodies to convert antigen-antibody recognition into an amplified and easily detectable signal. Among the different formats, the sandwich ELISA is the most widely used due to its high specificity and sensitivity.

In this configuration, a capture antibody is first immobilized on a solid surface, either by the user or, in many commercial kits, by the manufacturer. When a bacterial sample is introduced, target antigens present on the surface of the cells bind specifically to these antibodies. A secondary enzyme-labeled antibody is then added, forming an antibody-antigen-antibody “sandwich”. Finally, upon addition of a suitable substrate, the enzyme generates an amplified signal that can be detected through various transduction modes, including colorimetric, fluorescent, luminescent, or electrochemical readouts. A simplified illustration of this process is presentedin fig. 3.9.

This assay offers not only qualitative information related to the detection of bacterial presence, but also quantitative results used for classification. These results are obtained by analyzing the appearance and intensity of this color therefore indicate the presence as well as the relative amount of the target antigen in the studied sample. Measurements are typically performed using microplate readers and standard 96-well formats, allowing high-throughput screening and simultaneous automated analysis of multiple samples or antigens [115]. ELISA has been widely applied to the

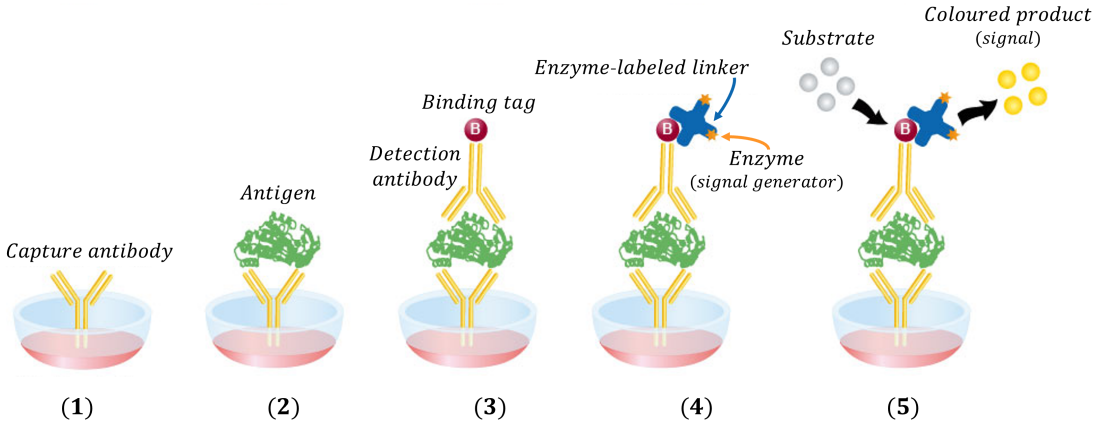

Figure 3.9: Schematic representation of the sandwich ELISA workflow. $(1-3)$ *Formation of the antibody-antigen-antibody complex, including a labeled detection antibody.* (4) *Binding of an enzyme-linked conjugate via the detection label.* (5) *Enzymatic conversion of the substrate into a detectable signal. Reprinted and adapted from [114].*

detection and serotyping of bacteria such as *Escherichia coli*, *Vibrio cholerae*, *Bacillus cereus*, and *Salmonella* [115–120]. Its high sensitivity, specificity, and capacity for quantitative analysis make it valuable for both diagnostic and epidemiological surveillance purposes.

However, ELISA requires high-quality antibodies to ensure specificity, and cross-reactivity between related serotypes may occur. The method also involves multiple sample preparation steps and specific equipment (microplate redears), leading to longer processing times compared with rapid agglutination assays and potentially limiting its field applicability.

Limitations of Classical Serotyping Assays

Despite their historical importance and continued use in diagnostic and surveillance laboratories, classical serotyping assays such as agglutination and ELISA present several limitations that restrict their accuracy and applicability. Cross-reactions between closely related serotypes represent one of the most common issues, and it can lead to ambiguous or false-positive results due to structural similarities among bacterial surface antigens. In addition, assay performance depends strongly on the quality and consistency of antibodies, which can vary between batches or suppliers [121–123].

Another limitation lies in their dependence on subjective interpretation and labor-intensive workflows. Slide agglutination is attractive because results can often be read directly by eye, making it suitable for rapid or point-of-care applications. In contrast, ELISA requires multiple incubation and washing steps, increasing assay time and potential variability [124]. Furthermore, bacterial strains may alter or lose surface antigens under certain conditions, leading to incomplete or inaccurate serotyping [125]. A related, but generally more subtle constraint is reliance on reference materials and curated databases of well-characterized reference strains. Gaps or inconsistencies in these databases can affect interpretation [126], although routine curation and confirmatory testing typically mitigate this risk.

Because of these constraints, there has been a progressive shift toward molecular and genomic approaches that directly target the genetic determinants of antigenic variation. These methods provide higher resolution and reduce the ambiguity associated with immunological assays, and will be discussed in the following sections.

3.2.3 Molecular and Sequencing-based Methods

Molecular and sequencing-based methods for bacterial identification and classification rely on the analysis of the genetic material of bacteria rather than their antigenic or phenotypic traits. Genetic material refers to the nucleic acids inside a cell, which are bio-molecules that carry the hereditary information defining each living organism. In most bacteria this material is DNA (deoxyribonucleic acid), a long, double-stranded molecule composed of four chemical bases arranged in a specific sequence. Sections of this sequence, known as genes, act as instructions for particular characteristics, such as the production of surface proteins or enzymes that determine virulence or antibiotic resistance. Subtle variations in gene sequences or in gene content are what molecular methods detect to distinguish species, serotypes, and strains.

Investigating this unique genetic fingerprint allows for precise identification even amongst closely related isolates, with high specificity and resolution. These molecular methods have therefore become indispensable in both clinical and public health laboratories, complementing or replacing classical serological and biochemical assays. The following subsections present a non-exhaustive selection of commonly used molecular techniques that illustrate the diversity and versatility of these approaches.

Whole genome sequencing (WGS)

Whole genome sequencing (WGS) is one of the most advanced and comprehensive approaches for bacterial characterization. It enables the complete determination of a microorganism's genetic code, offering the highest possible level of detail about its genetic composition. The process is usually performed by first extracting and purifying the bacterial DNA, which is then fragmented into short pieces. These fragments are subsequently processed by sequencing instruments that determine the exact order of the four chemical bases that constitute DNA: adenine (A), thymine (T), guanine (G) and cytosine (C), as shown in fig. 3.10. The millions of resulting short sequences are then computationally reassembled into a complete digital representation of the genome using advanced bioinformatic algorithms.

Once the genome sequence is obtained, it can be compared with public databases or previously sequenced strains. This enables identification of the bacterium at species or even strain level, and allows the detection of genetic features associated with serotype, antibiotic resistance, virulence or metabolic functions. Because the entire genome is analyzed, WGS can also reveal relationships between isolates and their evolutionary background from emergence to spread, supporting the tracing of infection sources during outbreaks and the monitoring of resistant clones in hospitals and communities. For these reasons, it has become the reference method for bacterial outbreak investigation, strain typing and classification, and large-scale genomic surveillance [127].

To perform WGS, several sequencing technologies are currently available, differing mainly in the length of DNA fragments they can read [128, 129]. Short-read sequencing platforms, such as Illumina or Ion Torrent, generate millions of highly accurate reads typically 100-300 bases long. These systems are widely used for routine bacterial genomics because they provide high throughput, low cost per base, and excellent sequence quality, although they may have difficulty resolving repetitive or highly variable regions. In contrast, long-read technologies, such as Oxford Nanopore and Pacific Biosciences (PacBio), produce reads that can exceed tens of thousands of bases, facilitating complete genome assembly, plasmid reconstruction, and detection of structural variants. While long-read platforms generally show higher error rates, their continuous improvement and the use of hybrid assembly strategies combining both short and long reads now allow near-complete genome reconstruction with high accuracy.

Recent advances in sequencing chemistry, rapid library-preparation methods and real-time data analysis have greatly reduced the cost and turnaround time of WGS. In optimized workflows,

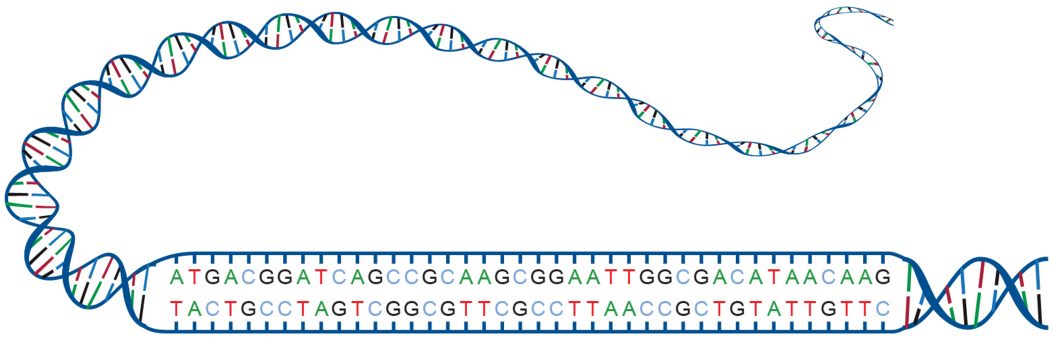

Figure 3.10: Illustration of the double-strand DNA genome structure made of 4 complementary chemical bases: adenine (A) couples with thymine (T), while cytosine (C) couples with guanine (G) (Image source: NIH).

particularly with nanopore-based systems, sample-to-answer times of only a few hours have been demonstrated [128, 130]. In most laboratories, high-quality genome sequences from cultured isolates are typically obtained within a few days to a few weeks [129]. Despite these improvements, direct WGS or metagenomic detection from clinical samples with low bacterial load remains limited by sensitivity, often requiring culture or enrichment. Although WGS has become increasingly accessible, it still demands specialized equipment, dedicated bioinformatics pipelines and substantial computational resources. Consequently, the technique is mainly implemented in reference laboratories and surveillance centers with established expertise and infrastructure. As sequencing platforms become more compact and analysis tools more automated, whole genome sequencing continues to advance toward routine use in bacterial identification, typing and public health monitoring [131].

Polymerase chain reaction (PCR)

Polymerase chain reaction (PCR) is one of the most widely used molecular techniques for bacterial detection. It allows the exponential amplification of a defined DNA fragment from minute amounts of genetic material, enabling rapid and sensitive identification. Because of its ability to selectively amplify specific regions of DNA, PCR is not only used as a standalone diagnostic tool, but also constitutes a fundamental step in many sequencing workflows, including whole genome sequencing, where sufficient genetic material must be generated prior to analysis.

The assay is often performed on bacteria by first breaking down the cells thermally to release their DNA (for example by heat or chemical lysis). The extracted DNA is mixed with multiple reagents: primer sequences (short synthetic DNA fragments that define the target region), nucleotides (DNA building blocks), a buffer (maintains optimal chemical conditions for the reaction) and a heat-stable DNA polymerase (the enzyme that copies DNA). The mixture is then subjected to repeated cycles of heating and cooling to separate the DNA strands, allow primers to bind, and enable the polymerase to extend new strands. At each cycle, the number of target molecules approximately doubles, hence the term chain reaction. Typical assays run for about 25-50 cycles, and may take from under an hour to several hours depending on the protocol and the instrument [132].

Numerous variations of PCR exist, each tailored to specific applications [133–136]. For instance, conventional PCR is commonly used to confirm the presence of a target DNA sequence. In modern workflows, detection is most often achieved through real-time PCR or quantitative PCR (qPCR), rather than post-amplification analysis. In this technique, the accumulation of amplified DNA is monitored in real time using fluorescent dyes or probes that emit light as the product increases in quantity. The cycle threshold (Ct) corresponds to the number of cycles required for this fluorescence signal to exceed a defined detection threshold. Modern qPCR assays are typically programmed to run for about 35–45 cycles and complete within one to two hours. If the detection threshold is not reached within the set number of cycles, the test is considered negative. This approach is thus widely used in clinical diagnostics because it combines speed and sensitivity with reduced cross-contamination risks, since amplification and signal detection occur within a closed system without any post-PCR sample handling [134, 137]. Another variation, called multiplex PCR, extends this principle by including several primer sets in a single reaction that allows simultaneous detection of multiple target genes to identify species, serotypes or virulence markers. While efficient for screening, multiplexing requires careful primer design to avoid cross-reactivity and unintended interactions between reagents, and can reduce sensitivity for some targets [135].

Beyond these direct variations, several molecular typing methods also make indirect use of PCR to obtain genetic information for bacterial classification. One notable example is multilocus sequence typing (MLST), which relies on amplifying and sequencing a small set of conserved housekeeping genes. Each distinct combination of gene variants, called alleles, defines a unique sequence type (ST) that can be compared across laboratories through standardized databases. This approach enables the identification of strains and the study of their genetic relatedness. More recent adaptations, such as core-genome MLST (cgMLST), extend this concept to genome-wide data obtained from whole genome sequencing, offering higher resolution for strain differentiation [138, 139].

Limitations common to PCR-based methods are primarily practical. Tests rely on the recognition of specific DNA regions, so mutations in target sequences can lead to missed detections. Because PCR reactions are highly sensitive, they require very pure DNA templates, as residual substances from clinical samples can inhibit amplification. In addition, non-specific amplification and background signals may appear at high cycle numbers, which is why assays are limited to a predefined number of cycles and interpreted using appropriate controls. Moreover, the required extraction and purification steps increase both time and labor. Another important limitation is cost: PCR reagents, consumables, and instrument maintenance can represent a substantial expense, particularly in resource-limited settings where reagent storage conditions may also be challenging. Furthermore, conventional thermocycler-based instruments typically process one run at a time, limiting throughput and making continuous, around-the-clock testing difficult.

Despite these caveats, PCR and its variants remain rapid, flexible and powerful tools for rapid diagnosis and molecular epidemiology [140].

Advantages and limitations

WGS and PCR are examples of, respectively, broad and specific molecular methods for studying and classifying bacteria. Altogether, this group of techniques provides highly specific and sensitive tools for bacterial identification and characterization. They offer an unmatched capacity to resolve genetic relationships, track evolutionary lineages, and detect resistance or virulence markers directly from the genome. However, their implementation often requires cultured isolates, advanced laboratory infrastructure for DNA extraction and amplification, and skilled personnel for sequence analysis. In many diagnostic settings where rapid, low-cost, and culture-independent identification is desirable, researchers and clinicians turned to alternative analytical strategies. Among these, mass spectrometry-based methods have emerged as robust and efficient tools capa-

ble of providing complementary information derived from bacterial proteins rather than nucleic acids. The following section presents the main principles and applications of these approaches.

3.2.4 Mass spectrometry-based methods

Mass spectrometry (MS) is an analytical technique that identifies and characterizes microorganisms based on the mass-to-charge ratio of their molecular components. In contrast to molecular methods, which examine nucleic acids, MS techniques analyze the protein composition of cells, providing a distinct yet complementary view of their biological identity. In microorganisms, proteins reflect both the genetic content and the physiological state of the cells, therefore revealing a specific phenotypic fingerprint that can be used for the identification and classification of different bacterial species and strains, even with no preliminary knowledge of the isolates to be typed [139].

MALDI-TOF mass spectrometry

MALDI-TOF stands for matrix-assisted laser desorption/ionization time-of-flight, which is the most widely used mass spectrometry technique in bacterial identification. This method works by ionizing bacterial proteins using short laser pulses, then accelerating the generated ions in an electric field to travel through a flight tube of known length. Their time-of-flight in this tube reflects the mass-to-charge ratio of the molecules, as lighter molecules travel faster than heavier ones. This time is measured, creating a unique mass spectrum used for identifying the molecules through comparison to reference databases containing characteristic patterns from known species, which consist of experimentally acquired mass spectra rather than sequence-based data [141]. In practice, commercial platforms such as the Bruker MALDI Biotyper and the bioMérieux VITEK MS have standardized this approach, making MALDI-TOF an integral part of modern clinical microbiology workflows [142]. The general configuration of these platforms is represented in fig. 3.11(a).

The entire process typically requires only a single bacterial colony and minimal sample preparation, making it highly efficient for routine use. For analysis, bacteria from patient specimens are grown as isolated colonies on agar plates, and a small amount of biomass is transferred to a MALDI target plate. Identification can be performed directly from whole cells or after a brief formic acid extraction that lyses the bacteria to avoid contamination, ensure biosafety from pathogenic strains, and, most importantly, to release intracellular proteins that improve spectral quality for certain species. This mild acid extraction is a destructive step, but it enhances reproducibility and allows identification of Gram-positive and encapsulated bacteria that are otherwise difficult to lyse. Finally, the prepared sample is overlaid with a crystallized light-absorbing organic matrix before laser desorption/ionization [141, 143].

Examples of representative MALDI-TOF spectra of different bacterial species are represented in fig. 3.11(b). These profiles are automatically analyzed by dedicated softwares that assign a confidence score based on the similarity between the sample and reference spectra [145]. Through this process, MALDI-TOF has transformed bacterial diagnostics by providing rapid, cost-effective, and reliable species-level identification in clinical laboratories [144]. Its ability to generate reproducible results within minutes has made it particularly valuable for the routine analysis of patient isolates and for the rapid confirmation of outbreaks. As its accuracy and throughput have improved, MALDI-TOF has progressively extended beyond clinical microbiology into environmental and food testing laboratories, where it supports large-scale microbial surveillance and biodiversity assessments.

Despite its broad applicability, several factors still limit the precision and universality of MALDI-TOF identification. The method's robustness is limited mainly by the depth and quality of its reference libraries and by inherent challenges in discriminating extremely closely related species, such as *E. coli* and *Shigella*, or species rarely encountered in laboratories. Commercial

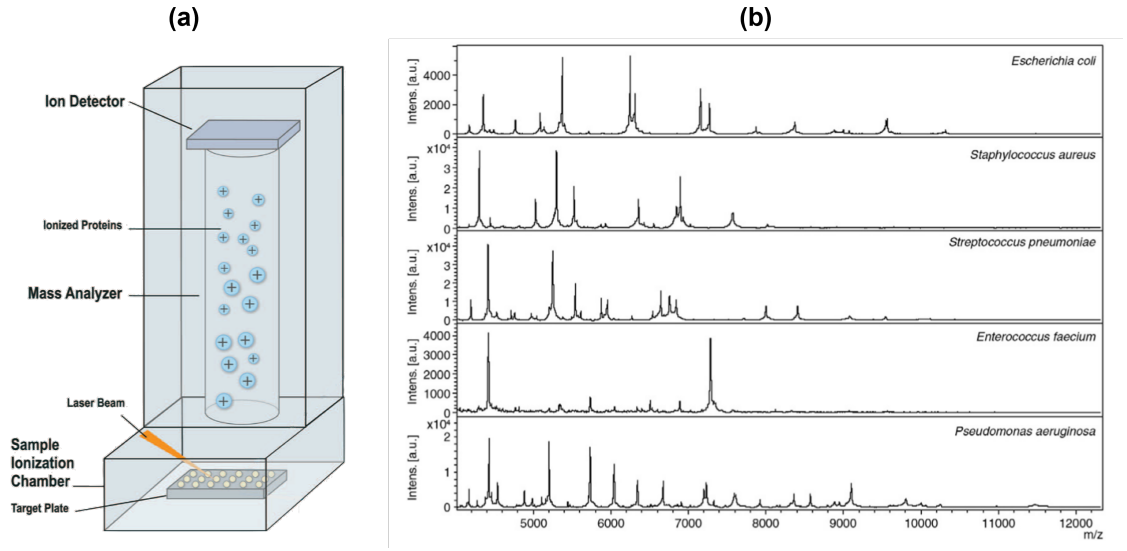

Figure 3.11: MALDI-TOF. ***(a)*** *Illustration of the main components of the MALDI-TOF mass spectrometer. The target plate is irradiated by a nitrogen laser ($\lambda = 337nm$), which ionizes proteins in the sample (typical mass range $1-500$ kDa). Resulting ions are accelerated into the $1-2$ m time-of-flight (TOF) linear tube mass analyzer and detected over time by the ion detector. The platform is typically connected to a computer where the analytical computations are performed. Reprinted and adapted from [143].* ***(b)*** *Examples of spectra obtained from whole bacterial colonies of five different species. The peaks can be specific to genus, species, and even subspecies. Reprinted from [144].*

databases may also be incomplete or overly dependent on user-generated entries [146]. Moreover, reproducible spectra are obtained only when bacteria are grown under identical conditions, as variations in culture medium, growth phase or incubation temperature can alter protein expression and spectral profiles [144, 147]. Beyond these technical limitations, MALDI-TOF remains a phenotypic identification tool that derives its results from the abundant ribosomal and housekeeping proteins of microorganisms rather than specific genetic determinants. Consequently, its ability to detect antibiotic-resistance mechanisms, virulence factors or fine strain-level distinctions remains limited in routine practice [148]. Nevertheless, its principal advantages, which are speed, low consumable cost and minimal preparation, continue to drive its widespread adoption. Recent studies have explored integrating MALDI-TOF data with machine-learning algorithms or complementary genomic analyses to enhance its discriminatory power and extend its diagnostic reach [149].

Other mass spectrometry approaches, such as liquid chromatography coupled to mass spectrometry (LC-MS), enable more detailed proteomic analyses by combining molecular separation with high-resolution detection. While these methods provide deeper insight into protein composition and function, their more complex sample preparation and data analysis currently limit their routine use in clinical microbiology [150–152].

Advantages and limitations

Mass spectrometry-based approaches offer several important advantages for microbial identification. Although some methods involve complex sample preparation, MALDI-TOF in particular requires minimal handling and provides rapid, accurate results with low consumable cost and limited manual intervention. Once isolated colonies are available, analyses can be completed within minutes, making MS-based platforms especially well suited for high-throughput diagnostic workflows. Their automation and scalability have made them indispensable tools in clinical, en-

vironmental, and food microbiology laboratories. Moreover, as mass spectrometric databases and computational tools continue to expand, the resolution and reliability of these methods are steadily improving [142, 153].

However, these techniques also present limitations. They generally require pure bacterial cultures and are less effective when applied directly to polymicrobial or low-biomass specimens. Closely related or taxonomically complex species, such as *Escherichia coli* and *Shigella*, remain difficult to discriminate solely based on spectral profiles. Additionally, because protein mass spectra mainly reflect phenotypic proteins instead of genotypic sequences, these methods do not directly detect genetic determinants such as antibiotic resistance or virulence genes. Furthermore, the accuracy of identification depends strongly on the completeness and quality of reference databases. Despite these constraints, MS-based strategies represent a major advancement in microbial diagnostics. Their continued evolution is expected to further enhance both their discriminatory capacity and their role in comprehensive microbial characterization [146, 153, 154]. In parallel, alternative approaches based on light-matter interactions have emerged to probe complementary properties of bacterial cells, which will be presented in the next section.

3.3 Bacterial Identification: Optical Methods

Optical methods exploit the interaction of light with microbial cells to extract physicochemical information that is characteristic of their biological identity. Unlike the previously described techniques, which probe the phenotypic, genotypic or molecular characteristics of bacterial cells, optical approaches interrogate intrinsic or induced optical signatures arising from cellular structures or metabolic states [155, 156]. These light-matter interactions generate highly specific spectral or photonic fingerprints that allow rapid and often label-free differentiation of bacterial species and strains. Optical methods encompass a broad range of techniques, each offering a complementary perspective on microbial cells. In this section, we will present some of the commonly used optical techniques in microbiology labs, as well as emerging photonic applications.

3.3.1 Fluorescence and Scattering detection

Fluorescence and scattering techniques rely on the emission or redirection of light from microorganisms when illuminated under controlled conditions. These responses arise from intrinsic fluorophores, labeled molecular targets, or structural features that govern how cells interact with incident light, resulting in optical signatures used for discriminating and analysing bacterial cells.

Flow Cytometry

Flow cytometry is a widely used single-cell analytical technique for investigating human cells but also bacterial ones. In this approach, single individuals from bacterial populations are detected and characterized by measuring the optical signals generated as they pass through a focused laser beam within a controlled fluidic stream. This measurement can be performed on whole unmarked cells. In this case, the optical signals collected arise from light scattering on the bacterial cells. The resulting scattered rays, collected mainly in the forward direction (forward scatter, FSC) and at 90° (side scatter, SSC), reveal multiple information about each individual such as its size, texture, or internal complexity. For a more investigative analysis, it is a common practice to label cells using one or more dyes or antibodies that bind to each bacterium's membrane or DNA and to collect, in addition to the scattered rays, the fluorescence emission resulting from the excitation of these

dyes with an adequate laser source. This staining reveals additional cellular properties such as vitality, protein identity and enzymatic activities which improves the discrimination of bacterial populations [157, 158].

By combining scattering signals (FSC and SSC) with fluorescence signals from multiple fluorophores excited by different lasers, flow cytometry provides a multidimensional fingerprint of each event and enables rapid quantification, classification and sorting of bacterial cells, even within heterogeneous populations [159]. In practice, high-sensitivity cytometers equipped with multiple excitation lasers are typically designed for eukaryotic cells, which range in size from about 10 to 100 micrometers in diameter. However, they have been successfully adapted by microbiology laboratories to detect the smaller size and lower scattering cross section of bacteria, which has expanded the use of flow cytometry in clinical and environmental microbiology [160, 161].

Despite its versatility, several factors limit the widespread adoption of flow cytometry for routine bacterial identification. Optical resolution is constrained by the physical size and refractive properties of bacteria. In fact, bacterial cells are small and their refractive index is close to that of the aqueous suspension media used for transporting the cells within the cytometer. These two factors produce weak scattering signals and may overlap with background noise or non-cellular particles present in complex samples [162, 163]. Accurate identification, particularly at the species or serotype level, heavily depends on fluorescent staining using antibodies conjugated to fluorophores. This increases reagent cost, especially since multiple antibodies may be required to cover antigenic variability within a species, and may introduce variability when labeling efficiency differs between conditions. Moreover, instrument calibration, gating strategies and sample preparation must be standardized carefully, since small deviations can alter cytometric profiles and compromise reproducibility. In addition, flow cytometry predominantly provides phenotypic information derived from morphological and physiological characteristics rather than specific genetic determinants [164]. As a result, its ability to discriminate closely related species or to detect antibiotic-resistance mechanisms remains limited without complementary molecular analyses [165]. Nevertheless, its high throughput (typically up to $10^3 - 10^4$ cells per second [166]), combined with single-cell resolution and capacity to interrogate complex communities continue to make flow cytometry a valuable tool in microbial diagnostics and in studies of bacterial ecology and physiology.

Fluorescence Microscopy

Fluorescence microscopy is another central technique used in bacterial research and is frequently applied for species identification and classification. In this approach, cells are labeled with fluorophores that bind to specific cellular targets such as nucleic acids, membrane structures or surface antigens. When excited with an appropriate light source at the corresponding excitation wavelength, these dyes emit characteristic photons that reveal both the presence and spatial distribution of the tagged components. The resulting fluorescence pattern provides information on cellular morphology, physiological state and molecular composition [156, 167]. An example of such a pattern is shown in fig. 3.12, where species-specific fluorescent probes selectively label different bacterial populations.

Compared to flow cytometry, fluorescence microscopy offers the advantage of direct spatial visualization through a microscope equipped with optical filters. The images obtained allow researchers to distinguish bacterial species, since they often differ in staining patterns, cell shape, intracellular organization or expression of specific proteins. Modern set-ups equipped with sensitive detectors and high-resolution objectives enable the detection of low-intensity signals, and advanced modalities such as confocal or structured illumination microscopy further enhance contrast and allow the reconstruction of three-dimensional arrangements. These platforms are also

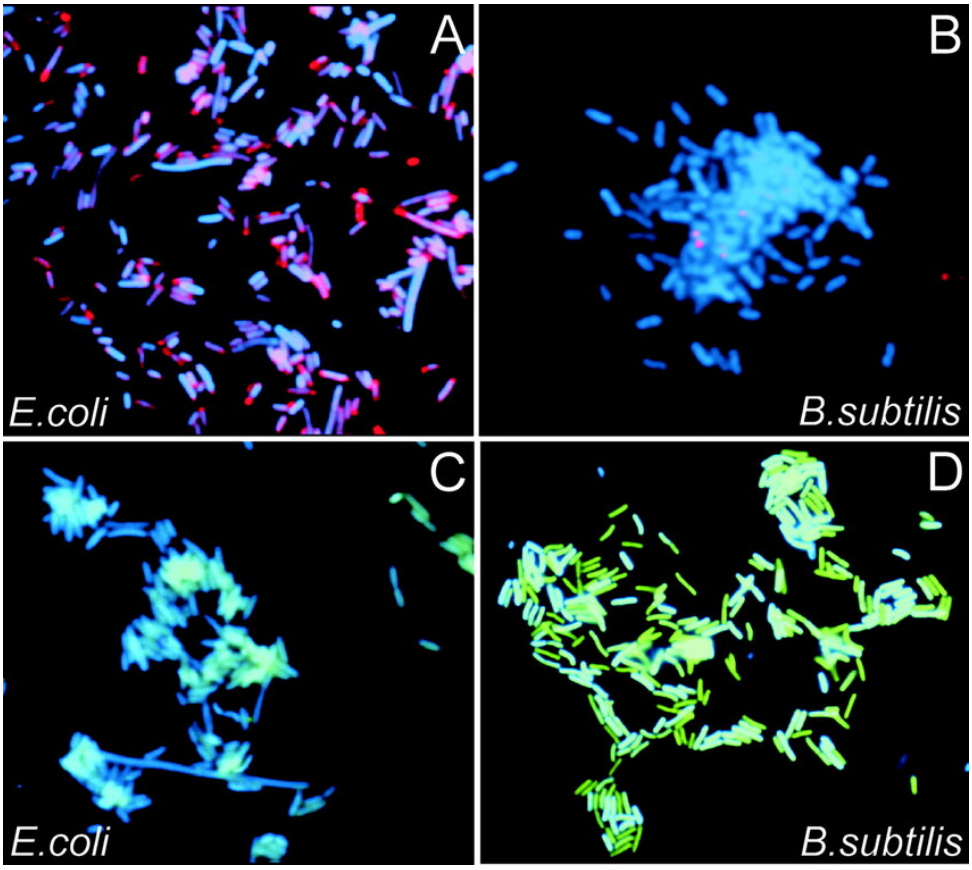

Figure 3.12: Fluorescence microscopy images of Escherichia coli and Bacillus subtilis cells labeled with different fluorescent probes. A non-specific blue DNA stain (such as DAPI) is included for visualization. (A-B) A red fluorescent probe targeting E. coli (based on fluorescence in situ hybridization, FISH) is applied to both populations. Distinct intracellular foci are visible in E. coli, whereas B. subtilis shows no signal. (C-D) A green fluorescent probe targeting B. subtilis is applied to both populations. No signal is observed in E. coli, while B. subtilis is labeled, highlighting its characteristic cellular morphology. Reprinted from [168].

frequently coupled with automated imaging equipment and image processing workflows that provide consistent calibration and reproducible analysis. Together, these features improve the reliable identification of slow-growing or weakly fluorescent bacterial groups [167, 169, 170].

Fluorescence microscopy also allows detection of specific surface antigens when bacteria are labeled with antibodies conjugated to fluorophores, which can support serotyping. For example, indirect immunofluorescence has been used to detect *Escherichia coli* O157:H7 [171]. Despite this, its adoption in routine clinical serotyping remains limited compared to agglutination or molecular methods.

Although the technique provides rich spatial and molecular information, several challenges hinder its use for routine bacterial identification. Since bacteria are small and often weakly fluorescent, relatively high cell concentrations are required to ensure detectable signals, which can be impractical when working with low sample volumes. In addition, these signals can be difficult to interpret in heterogeneous populations or in the presence of intrinsic cellular autofluorescence. Fluorescent staining protocols also require strict optimization, because dye uptake varies with species, growth phase and cell permeability. Prolonged exposure to light excitation can cause photobleaching of the dyes or phototoxic effects on the cells, which gradually degrade signal quality, especially during extended imaging procedures such as three-dimensional scans [156,

172]. Nonetheless, the ability to capture high-resolution spatial information combined with specific molecular labeling continues to make fluorescence microscopy an important tool in bacterial diagnostics and taxonomy.

3.3.2 Vibrational Spectroscopies

Vibrational spectroscopic techniques rely on the characteristic vibrational modes of molecular bonds within bacterial cells. These modes produce highly specific spectral fingerprints that reflect the biochemical composition of the organisms, including nucleic acids, proteins, lipids, and metabolites. In this section, we review the vibrational techniques most commonly studied in the literature.

Raman Spectroscopy

Raman spectroscopy is one of the most widely used vibrational spectroscopic methods in chemistry and in microbiology for bacterial identification and classification. In this approach, label-free cells are illuminated with a monochromatic laser, typically around $532nm$ for bacterial single-cell studies, whose photons interact with molecular vibrations within the bacterium, resulting in energy shifts in a small fraction of the scattered light. This excitation wavelength provides a compromise between signal intensity, which scales with $1/\lambda^4$, and background fluorescence, enabling measurements at the micrometer scale. These Raman shifts produce characteristic spectra that reflect the underlying molecular bonds and biochemical composition of the cell, providing a detailed fingerprint suitable for identification of individual bacteria [173, 174].

Sample preparation for Raman measurements is simple since they are performed on droplets of bacterial suspension deposited onto a glass substrate. The basic technical setup consists of a laser source, a sensitive detector, and standard optical components, making benchtop Raman systems accessible in many research laboratories [175]. However, clinical and industrial environments generally rely on commercial Raman microscopes, which offer stable alignment, automated acquisition routines, and integrated spectral processing [176]. These instruments allow the direct collection of spectra from individual intact cells, producing reproducible patterns that often differ between species due to variations in cell envelope composition, metabolic states, or stress responses. Through comparison with curated spectral databases, spectral differences enable bacterial discrimination and typing, as well as pathogen and drug monitoring [174, 177, 178].

Several variants of Raman spectroscopy have been developed to enhance the sensitivity, resolution, and selectivity of the technique. Surface-enhanced Raman spectroscopy (SERS) can increase signal intensity by placing cells or biomolecules in close proximity to nanostructured metallic substrates that locally amplify the electromagnetic field. However, its performance depends strongly on substrate properties and experimental conditions, which can limit reproducibility compared to optimized label-free Raman measurements [179]. Another example is ultraviolet resonance Raman spectroscopy (UVRR), which selectively enhances specific vibrational modes by tuning the excitation wavelength into the ultraviolet range, where electronic transitions of aromatic amino acids and nucleic acid bases can be probed [180]. These modalities, when combined with automated spectral analysis and machine-learning algorithms, support rapid and reliable bacterial identification and classification [181].

Despite these strengths, several challenges restrict the widespread adoption of Raman spectroscopy in routine diagnostics. The Raman effect is intrinsically weak, as only a minute fraction of scattered photons undergo inelastic scattering. Consequently, high-quality measurements may require acquisition times on the order of a few seconds per cell, in addition to the time needed to accurately focus the laser on the target, or the use of increased laser powers. Such conditions

can introduce photothermal damage and often lead to the destruction of the analyzed cells, particularly in dry samples. In addition, fluorescence from cellular components or culture media can mask Raman features and complicate spectral interpretation. Spectra from mixed or heterogeneous populations may overlap, making analysis difficult without additional advanced approaches. Variations in sample preparation, substrate characteristics, or instrument calibration can also impair reproducibility across platforms [182, 183]. Nonetheless, the ability to obtain label-free molecular fingerprints at the single-cell level continues to make Raman spectroscopy an important tool for bacterial diagnostics and taxonomy.

FTIR Spectroscopy

Fourier-transform infrared (FTIR) spectroscopy is another widely used vibrational spectroscopic method that provides insight into the biochemical makeup of bacterial microorganisms. Similar to Raman spectroscopy, cells are exposed to a light source, and the resulting spectrum (after Fourier-transform and statistical analysis) represents a detailed molecular fingerprint of the studied microorganisms. However, in FTIR the light source is a broadband infrared beam, and the spectra reflect the absorption (and limited emission) of infrared light by molecular bonds in the cell, rather than changes in the scattered light from a laser [184, 185].

In practice, this measurement requires preparing samples in a way that minimizes interference from water, their main component, which strongly absorbs in the mid-infrared region. Bacterial cultures are therefore washed to remove growth medium and dried on infrared-transparent substrates, forming thin, uniform films that enable reproducible transmission measurements [186]. The resulting spectra integrate bulk biochemical signals from lipids, proteins, polysaccharides, and nucleic acids. In fact, FTIR cannot be performed on single bacterial cells because the mid-infrared wavelengths used in the technique limit spatial resolution and the amount of material in a single cell is too small to generate a detectable signal. Nonetheless, the measurements performed on colonies or concentrated cell deposits can be used to distinguish between different microbial species or physiological states [187].

These spectral acquisitions are often performed using commercial FTIR instruments, such as those from Bruker or Thermo Fisher Scientific, which typically cover a wide range of IR wavelengths for broader detection and include automated, sensitive, and rapid acquisition routines with integrated spectral processing to improve reproducibility and throughput [188]. The FTIR workflow can be further adapted by using variants such as attenuated total reflectance (ATR), where cells are pressed directly against a crystal instead of deposited on a flat substrate, helping control bacterial film thickness. In modern implementations, machine-learning algorithms are increasingly integrated to accelerate spectral interpretation and enable bacterial typing at the strain level [189]. Such workflows form the basis of commercial FTIR-based systems for microbial identification, such as the Bruker IR Biotyper, which provides rapid, cost-effective grouping of isolates even if it cannot match the precision of whole-genome sequencing.

A recent variant of vibrational spectroscopy, optical photothermal infrared (O-PTIR) spectroscopy, combines mid-infrared excitation with visible detection, bridging the advantages of FTIR and Raman. This approach allows submicron spatial resolution and the acquisition of infrared spectra from individual bacterial cells, even in the presence of autofluorescence [190, 191]. O-PTIR thus opens new opportunities for label-free, single-cell biochemical analysis while maintaining the molecular specificity of infrared absorption.

Despite these advantages, FTIR spectroscopy presents several practical limitations. Variations in how films dry, or in how thoroughly cells are washed, can lead to noticeable spectral shifts, and even small amounts of residual growth medium may introduce strong absorption features that obscure bacterial signals. Because FTIR is a bulk, destructive approach that does not resolve individual cells and instead reflects averaged contributions from all material in the beam path, mixed

or heterogeneous samples present additional challenges. Moreover, reliable spectra interpretation relies heavily on an accurate design of mathematical analysis algorithms [185, 186]. While these factors limit the technique's diagnostic precision, they do not diminish its utility as a rapid, label-free tool for assessing overall bacterial biochemistry and for classifying different species and strains.

3.3.3 Plasmonic and Photonic Sensors

Finally, the last type of optical techniques for bacterial identification discussed in this section is plasmonic and photonic sensors. These platforms form a distinct class of optical methods that detect microorganisms through their influence on surface-bound electromagnetic modes. The underlying physical principles of these sensors, including field confinement and optical trapping, as well as some broad biological applications, were introduced in the first chapter of this manuscript and will therefore not be detailed here. In this section, we focus specifically on their use as biosensing platforms for bacterial detection, where monitoring the attachment, motion, or proximity of bacteria allows one to detect the resulting modulation of the device's optical response.

Although not yet adopted in standard clinical routines, biosensors based on plasmonic surface resonances or photonic crystals are gaining increasing attention among researchers because they enable label-free monitoring of single-cell interactions and can be integrated with microfluidic or trapping architectures. These systems also benefit from their miniature size, which facilitates straightforward replacement, low-maintenance operation, and potential portability, provided that the measurement environment is equipped with the necessary excitation and detection components such as laser sources for optical coupling and electronic devices for recording the transmitted signal. Furthermore, plasmonic and photonic platforms offer high surface sensitivity and the combined ability to immobilize and interrogate bacteria within the same optical structure, which is particularly advantageous for localized and real-time detection at the single-cell level. Despite these advantages, the technology remains at a relatively early stage of development, and its broader implementation will depend on continued improvements in system robustness, user-friendliness and standardization.

Taken together, these practical and integrational advantages naturally guided the choice of photonic crystals for the investigation of biological objects in the context of my PhD work, as well as in earlier projects conducted in our photonics research group. Their fabrication simplicity, already described in previous chapters, further supported this choice by allowing rapid prototyping and straightforward adaptation of the structures to different experimental needs. The results obtained in these earlier studies will be briefly presented in the next section, as they constitute the main foundation of the work developed in this manuscript and outline the challenges that motivated the investigations carried out during my PhD.

3.4 Prior Work within the Research Group

Interest in photonic crystals in our mixed research group, with contributions from both the LTM and CEA/Sinaps laboratories, goes back about two decades. Early work naturally focused on optimizing the design, fabrication and coupling of photonic crystals [192–194], followed by investigations of the physical phenomena that influence the resonance of these structures and those that emerge from it [195, 196]. The use of these devices as optical trapping platforms then began with the manipulation of inert objects such as polystyrene beads [197, 198]. About ten years after this research effort began, the focus shifted toward exploring the potential of these photonic

structures for studying biological objects. Bacteria were selected as the first target since they are easy to obtain, present low biocontamination risks for strains in risk group 1, and are similar in size (1-2 μm) to the inert beads previously used for proof-of-concept studies. This interest in trapping bacterial cells also led to an academic collaboration with researchers from EPFL, which remains active and has enriched this work. In this section, we present some of the results that emerged from these investigations of bacterial trapping using photonic crystals.

Species Differentiation Based on Behavioural Monitoring

As a transition from inert objects to biological ones, which are more sensitive and demanding, specific efforts were first directed toward carefully tuning the 1D PhC cavity so that its parameters became suitable for trapping living cells. It was essential to establish methods that could monitor bacterial behaviour inside the optical traps with good precision. For this purpose, Manon TARDIF (PhD student at the time) [76, 199] adopted two complementary approaches that were tested on three bacterial species: *Escherichia coli*, *Staphylococcus epidermidis*, and *Bacillus subtilis*.

The first approach focused on characterizing the spatial behaviour of trapped bacteria through microscopic imaging of the photonic structure during operation, followed by image processing that allowed tracking of cell motion. These observations showed that optical trapping confines bacteria within the evanescent resonance field and restricts their Brownian motion, although it does not fully suppress it. Moreover, the image analysis revealed that each species exhibited a distinct spatial signature, as shown in fig. 3.13(a), which can be used to differentiate them.

This result was supported by a second approach based on analysing the optical signals transmitted through the photonic structure during each trapping event, recorded simultaneously with the tracking videos. The histograms of these transmitted signals showed specific shapes and full width at half-maximum (FWHM) values, correlated with optical signatures for each of the three bacterial types, as represented in fig. 3.13(b). Together, these findings demonstrated that 1D photonic crystals can detect distinct optical and spatial behaviours among the three tested bacterial types [76, 199].

While these differences allowed differentiation in this controlled study, it remains uncertain how generalizable this approach is to other strains or species, given potential intra-species variability. Notably, the distinct morphologies of the bacteria tested likely contributed to the observed differences, suggesting that further studies with a broader range of strains will be required to assess the method's species-level specificity.

Gram Type Determination

This investigation was also conducted by Manon TARDIF on 2D PhCs in collaboration with Rita THERISOD from EPFL (also PhD student at the time) [76, 200]. While the previous study centred its signal analysis on oscillations occurring during the trapping event itself, the present work focused on the sudden shift in signal level produced at the exact moment a particle is trapped. As explained in Chapter 1, when a particle enters the evanescent field of a resonator, the optical forces pull it toward the surface to confine it spatially. This alters the local refractive index surrounding the photonic crystal cavity and, as a result, changes the transmitted signal because the injected wavelength is not adjusted to the new virtual resonance wavelength $\lambda_{0,particle}$ of the cavity. The transmission shift corresponds to a redshift of the cavity resonance, which arises because the trapped bacterium locally increases the effective refractive index experienced by the photonic mode. Therefore, during a trapping event, a shift in the transmitted signal appears first, followed by the high-frequency oscillations associated with the Brownian motion described previously. In 1D PhCs this shift appears as a negative transmission drop, while in 2D PhCs it is observed as a

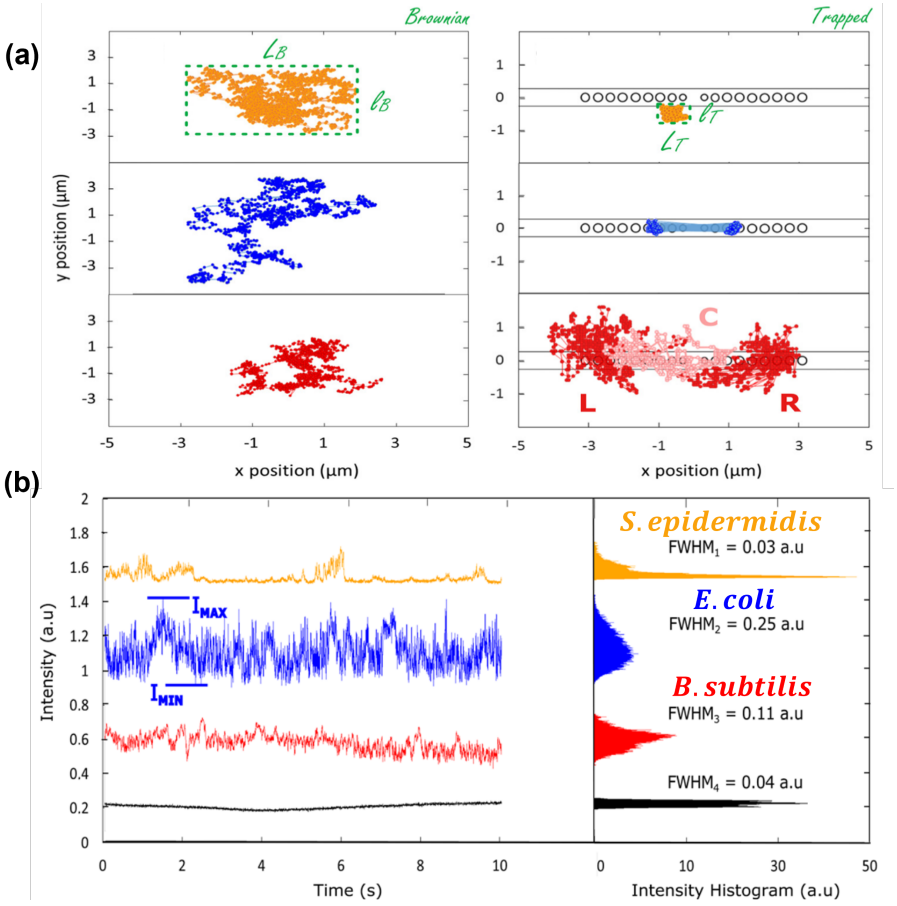

Figure 3.13: Results of species differentiation experiments. The bacteria tested were S. epidermidis, E. coli and B. subtilis, represented respectively in yellow, blue and red. (a) Spatial signatures of bacterial motion tracked over 50s in free suspension on the left, and when trapped in the evanescent field on the right. (b) Examples of the transmitted signal through the resonator during 10s of trapping for each bacterial species, together with the corresponding histograms. The black trace represented the signal of the empty cavity in resonance when no object is trapped.

positive transmission increase as illustrated in fig. 3.14. In both cases, this effect is often treated as an absolute value denoted by ΔT.

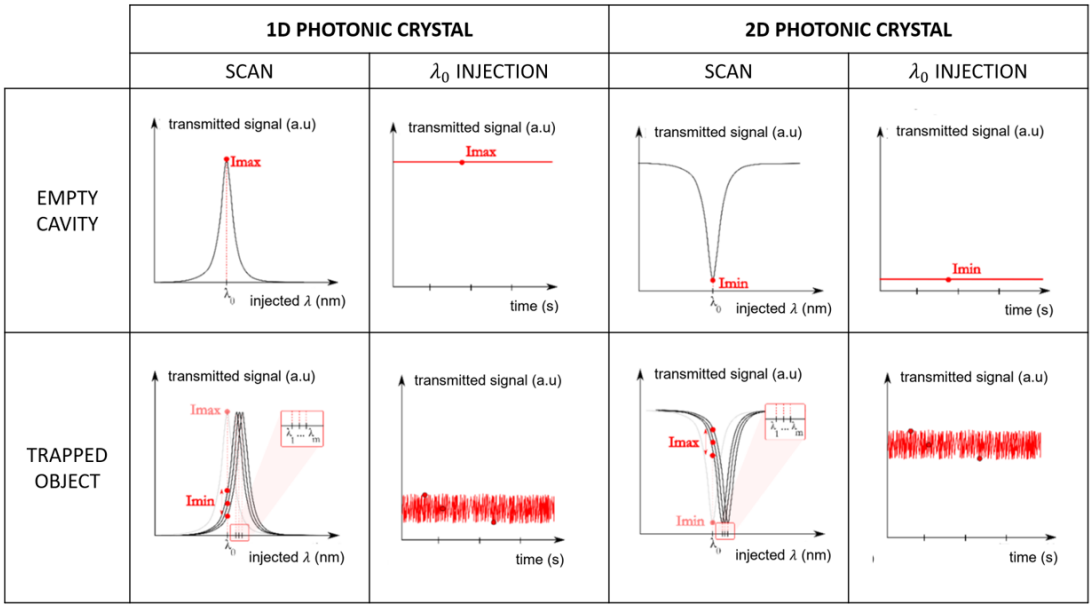

Figure 3.14: Comparison of the optical characteristics of 1D and 2D photonic crystals, using spectral scans and temporal transmitted signals at the injected resonance wavelength, both for empty cavities and for cavities containing a trapped object. These signals are not experimental measurements but illustrate the typical behaviour observed on real structures. Reprinted and adapted from [76].

The students compared the transmission shift associated with the trapping of multiple individuals belonging to seven bacterial species: three rod-shaped Gram-negative species (*Escherichia coli*, *Pseudomonas putida*, *Yersinia ruckeri*), two rod-shaped Gram-positive species (*Listeria innocua*, *Bacillus subtilis*), one coccus-shaped Gram-negative species (*Neisseria sicca*) and one coccus-shaped Gram-positive species (*Staphylococcus epidermidis*). The results, presented in fig. 3.15, reveal a clear distinction between the distributions of ΔT values for these two groups. This demonstrates that photonic crystals can serve as a fast and non-destructive alternative to classical Gram staining assays, provided that a sufficiently broad database is available for comparison when unknown samples are analysed.

Live Bacterial Lysis by Bacteriophages

The most recent result that was demonstrated on photonic crystals is the live detection of bacterial lysis using a 2D photonic crystal [64]. This work emerged from a collaboration between Simon GLICENSTEIN from our research group and both Enrico TARTARI and Nicolas VILLA from EPFL (all PhD students at the time). In this study, the experiments were performed on *E. coli* bacteria using two different bacteriophages, which are viruses that specifically infect bacteria. These prokaryotic viruses are ubiquitous in natural environments and play a major role in regulating bacterial populations. They recognize and bind to specific receptors on the bacterial membrane, inject their genetic material into the host cell, hijack the bacterial machinery to replicate, and ultimately cause the bacterium to lyse and die [201].

Experimentally, the bacterial cultures were first incubated in a liquid medium until a suitable growth phase was reached. The bacteriophages were then introduced into the suspension. Each

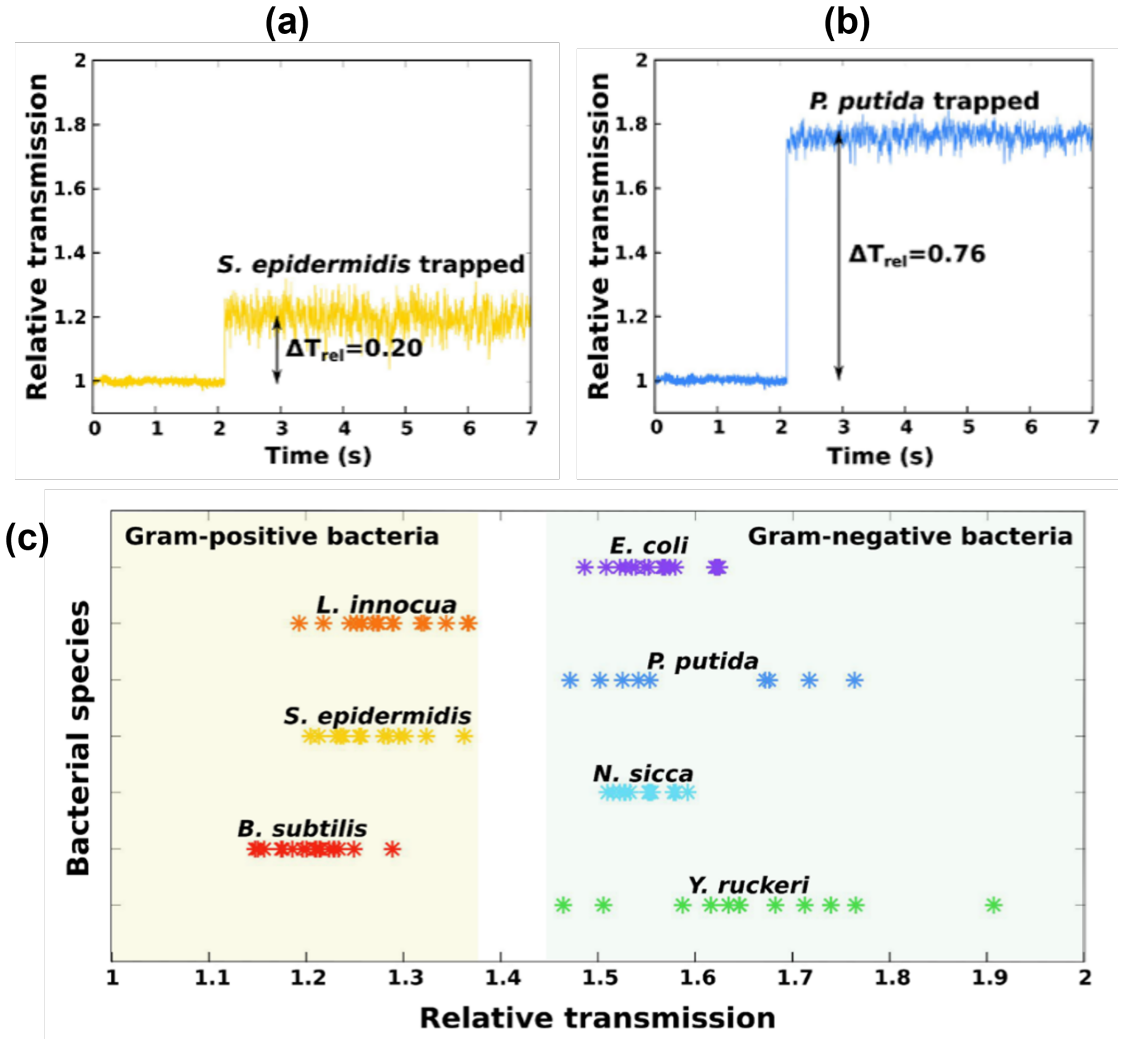

Figure 3.15: Comparison of transmitted signal characteristics for bacteria of different Gram types. (a-b) Examples of normalized transmitted trapping signals illustrating the signal shift associated with the trapping event, denoted by ΔT. (c) Distribution of ΔT values for several bacterial species, revealing a clear distinction between Gram-positive and Gram-negative groups. All figures were reprinted from [200].

phage type, T1 or T4, was tested in a separate preparation in order to isolate its individual effect on the bacteria. The phages were added at concentrations in the range of $10^8 - 10^9\,\mathrm{PFU\,mL^{-1}}$, ensuring efficient infection of the bacterial population prior to injection into the optofluidic chip. Here, PFU refers to plaque-forming units, a standard virological measure of the concentration of infectious viral particles. A preliminary control assay subsequently confirmed that both phage types were actively infecting the *E. coli*. This was verified using turbidity measurements at regular time intervals to monitor the optical density of the suspension, which indicates the concentration of living cells. A decrease in optical density corresponds to a reduction in viable bacteria, which is indeed what the turbidity curves in fig. 3.16(c) revealed.

A portion of the mixture was then injected into a photonic chip equipped with an integrated microfluidic channel, enabling the trapping of individual cells while the infection process was still ongoing. Monitoring the cavity's optical response during trapping revealed sudden shifts in transmission, indicative of cavity detuning resulting either from trapping loss or from a drastic modification of the effective refractive index of the trapped object. Such modifications can stem

from changes in the trapped bacterium's membrane, size, or physiological state [202]. On this basis, the observed shifts were correlated with the occurrence of lysis events, i.e. the moment when the trapped bacterium was effectively killed. Figure 3.16(a) shows an example of the transmission signal recorded for non-infected bacteria, where the transmission level remains stable for the duration of the experiment. In contrast, the signal in fig. 3.16(b), obtained from bacteria infected with T4, clearly displays the sudden drop mentioned above after phases of gradual signal loss associated with the change of the cell's membrane and eventually the decline in its viability. These transmission drops were confirmed to be correlated with lysis events by simultaneous microscopic observations, which showed that the signal decrease occurred at the same time as the physical disruption of the bacterium.

Furthermore, this study demonstrated that infections induced by T1 and T4 produced distinct optical signatures that were characteristic of each phage type. This suggests that our photonic crystal platform could be used not only to monitor lysis in real time, but also to compare the effects of different bacteriophages on individual bacteria, which is of particular interest for applications in phage therapy and antimicrobial susceptibility testing.

3.5 Motivations & Biological Framework of the Present Work

Resonant photonic crystals have allowed our research group to manipulate and sense single bacterial cells with considerable precision, yet a recurring limitation has emerged throughout these studies. Although every bacterial species tested has been successfully trapped on our resonators, this is not always the case for different strains within the same species. Over nearly a decade of work, we consistently encountered strains that simply could not be trapped, even after several design adjustments such as modifying the SOI layer, mentioned earlier, or applying surface functionalization strategies, which will be discussed later. These untrappable strains are not unusual or exotic ones. They are often closely related to strains we routinely manipulate, sharing most of their physical and genetic characteristics. This similarity has been verified by DNA analysis, which will be discussed in a later chapter.

This unexpected observation does not appear in the literature. While many constraints of photonic-crystal-based trapping have been reported, we found no publication explicitly describing differences in trappability at the strain level. It is likely that this behaviour has been noticed elsewhere, but remained unreported, as unsuccessful outcomes rarely appear in scientific articles.

Paradoxically, such a limitation reveals an important strength of our platform. If two very similar individuals produce two different trapping outcomes, it suggests that the device is highly specific to a particular bacterial property that varies from one strain to another. Given that bacterial cells are about 1 to 2 μm, while the evanescent field of a photonic crystal extends only a few hundred nanometers above the surface, only a portion of the cell interacts with the optical field. As a result, the membrane is the main region being probed. Identifying the membrane-related criterion responsible for these differences became the starting motivation of this PhD project.

The present work therefore focuses on the optical and physical interactions between 1D photonic crystal optical traps and several strains of a single bacterial species. We chose to work on *Escherichia coli*, as we had access to the largest number of strains from this species, and because previous studies had shown that some strains are not readily trappable, making it a particularly relevant model to investigate trapping behaviour. The samples we acquired were provided by Pierre MARCOUX from CEA and by Gregory RESCH from CHUV (Lausanne). The complete list of

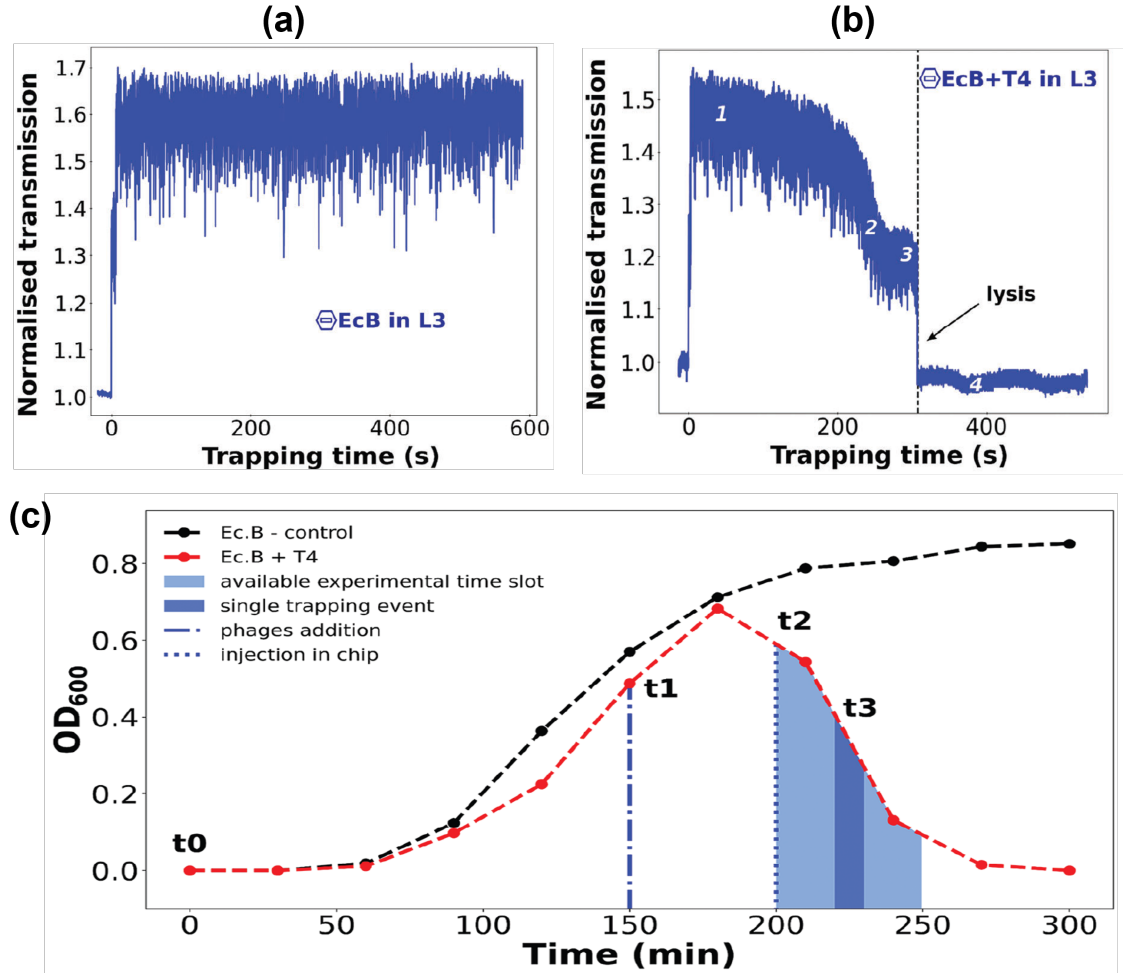

Figure 3.16: Assessment of the effect of T4 phages using photonic chips and classical assays. (a) Transmission signal of an E. coli cell not infected with bacteriophages, trapped on a 2D PhC with an L3 slot-shaped defect. (b) Transmission signal of an E. coli cell infected with T4 phages. The lysis event corresponds to the abrupt decrease in transmission and the return to the level associated with an empty resonating cavity. (c) Turbidity assay comparing the optical density of control bacterial samples over time, shown in black, with the samples where T4 phages were introduced, shown in red. The time window corresponding to the photonic measurement is indicated in blue to highlight its relevance for detecting the lysis event. All figures were reprinted from [64].

strains is given in table 3.1, including their lab-given names as well as their official names that are typically used to reference them in international and commercial microbiology databases.

3.6 Conclusions

In this chapter, we introduced bacteria, the central focus of our biological investigation, completing the picture established in the previous chapters where the technical aspects of our device were presented. With both components now laid out, the biological system and the photonic platform come together to form the basis of our biosensing chips. We outlined the main properties of bacteria and reviewed several widely used methods in academic and clinical environments to

Table 3.1: List of studied E. coli strains.

Lab reference	Official reference	Provider
EC10	ATCC 25922	CEA
EC11	ATCC 8739	CEA
EC21	ATCC 35421	CEA
EC207	ATCC 3521	CEA
EC225	ATCC 43888	CEA
EcB	None (patient strain)	CHUV
Eco0122	IAI13	CHUV
Eco0123	IAI08	CHUV
Eco0124	ECOR-09 / ATCC 35328	CHUV
Eco0125	Nissle 1917	CHUV
Eco0126	DH5α	CHUV
Eco0127	BL21 / ATCC 68338	CHUV
Eco0128	BW25113	CHUV
Eco0129	W3110	CHUV
Eco0130	MC4100	CHUV
Eco0131	MG1655	CHUV

probe them.

This biological overview is essential for understanding the motivations behind our work with the photonic crystal cavity developed in our research group. Although previous members of the group demonstrated several promising applications of these chips, their full potential remains limited by observed variations in the responses of certain bacterial strains. These observations point to a gap in our understanding of the factors that drive the device's strain-dependent behavior.

The next chapters build on this foundation. They present the methods and results of the experiments carried out during my PhD, aimed at understanding the factors that govern this specificity and ultimately improving the performance and reliability of our photonic chips.

4

SOI-Bacteria Interactions

In this chapter, we discuss the near-surface interactions between bacterial cells and the SOI photonic structures that govern the optical trapping experiments, and investigate methods of controlling them.

Contents

4.1 Introduction . . . 86
4.2 Experimental observations . . . 86
4.3 Force Analysis at the SOI-Bacteria Interface . . . 89
4.3.1 Decomposition . . . 89
4.3.2 Analysis . . . 89
4.3.3 Summary . . . 92
4.4 Surface Charges . . . 92
4.4.1 Zeta Potential: Theory . . . 93
4.4.2 Zeta Potential: Experimental Protocol . . . 95
4.4.3 Bacterial Surface Charges . . . 97
4.4.4 SOI Surface Charges . . . 98
4.4.5 Electrostatic Interaction at the SOI–Bacteria Interface . . . 98
4.5 SOI Surface Treatment . . . 99
4.5.1 SOI Surface Treatment: Methods . . . 100
4.5.2 SOI Surface Treatment: Results . . . 101
4.5.3 Limitations of BSA functionalization. . . . 102
4.6 Modification of the Suspension Medium . . . 103
4.6.1 Choice of Suspension Medium . . . 103
4.6.2 Effects of Suspension Medium Change . . . 105
4.7 Conclusions and Perspectives . . . 107

4.1 Introduction

From a photonics standpoint, the spatial confinement of a microscopic object using optical traps is primarily described through light-matter interactions that manifest as optical forces, as presented in the first chapter of this manuscript. Within that framework, the properties of the trapped object taken into account are its size and refractive index contrast with the surrounding medium, as these parameters determine both the magnitude of the optical forces and the stability of the trapping potential.

While this theoretical description applies to any object whose dimensions are compatible with optical trapping, it remains a simplified representation of real systems. In the case of biological objects, and bacteria in particular, intrinsic variability extends beyond these reduced parameters. Variations in morphology, internal composition, and membrane structure can modify both the effective size of the cell and the spatial distribution of its refractive index. In addition, biological objects are not static entities, and their physiological state can evolve over time or in response to their environment, which may further influence their interaction with the optical field. Moreover, such a model does not account for additional mechanisms arising from physicochemical interactions that may occur at interfaces when bacteria are brought in close proximity to a solid surface.

In this chapter, we report the differences observed during experiments conducted with different *E. coli* strains on SOI photonic chips and investigate their possible origins, examining effects that extend beyond purely optical considerations. We also discuss approaches used to control certain effects in order to ensure consistent experimental conditions across all trapping experiments on 1D photonic crystal microresonators.

4.2 Experimental observations

Throughout this PhD, multiple optical trapping experiments were carried out on different SOI photonic chips, with both static and integrated fluidic systems, and using different *E. coli* strains. Across multiple experimental runs, several recurring yet inconsistent behaviours were observed.

Trappability. The most immediate outcome was that trappability itself seemed to be strain dependent. While some strains could be reliably confined within the optical trap, others, although phenotypically similar under standard microscopy, consistently failed to be trapped. In practice, for each strain, a bacterial suspension is introduced within the optofluidic chip and the interactions with the cavity are observed both via the live visualization system and through the transmitted optical signal. The detailed experimental protocol is beyond the scope of this chapter, but will be presented in the following one. To assess trappability, each experimental run for each strain is conducted for at least an hour. First, a bacterial suspension prepared from a small number of colonies (typically $2-3$ colonies) is introduced in the chip, corresponding to a moderate cell concentration. If only a few ($\lesssim 3$) or no optical signatures corresponding to trapping events are observed, the experiment is repeated. The second run is then performed using a significantly higher concentration, obtained by resuspending a larger number of colonies (typically $3-4$ times more) from a fresh culture. This additional verification step allows us to verify that the low event count is not due to sample-specific issues such as reduced viability in the case of zero events, or contamination and experimental artefacts in the case of sporadic events. If the second run is completely negative, the strain is classed as untrappable. Table 4.1 summarizes the resulting classification for all strains tested in this work. The existence of such a binary behaviour among bacteria of the same species already suggests that parameters beyond the simplified optical description may be involved.

Table 4.1: Trappability of tested E. coli strains on SOI photonic chips.

(a) Trappable strains

	Lab ref.	Official reference
✓	EC11	ATCC 8739
✓	EC225	ATCC 43888
✓	EcB	None (patient strain)
✓	Eco0124	ECOR-09 / ATCC 35328
✓	Eco0126	DH5α
✓	Eco0127	BL21 / ATCC 68338
✓	Eco0128	BW25113
✓	Eco0129	W3110
✓	Eco0130	MC4100
✓	Eco0131	MG1655

(b) Untrappable strains

	Lab ref.	Official reference
✗	EC10	ATCC 25922
✗	EC21	ATCC 35421
✗	EC207	ATCC 3521
✗	Eco0122	IAI13
✗	Eco0123	IAI08
✗	Eco0125	Nissle 1917

Transient trapping. Even among strains classified as trappable, the behaviour was not always consistent. In several instances, cells approached the vicinity of the optical cavity, induced a clear trapping signature in the transmitted signal, yet escaped the trap after only a few seconds, as illustrated in fig. 4.1. Under stable conditions, a trapped object is expected to remain confined as long as the laser excitation is maintained, since the optical forces responsible for confinement are still present. However, in multiple cases, cells escaped while the resonance was still established. Importantly, this transient trapping was observed in both dynamic microfluidic circuits and static pools. It therefore cannot be attributed solely to fluid flow or associated drag forces, which are negligible in static configurations. Moreover, this phenomenon appears stochastic, as no clear trend was identified regarding specific strains or characteristic trapping durations. Such behaviour points toward a limited trap stiffness or a shallow trapping potential, potentially resulting from weak refractive index contrast, fluctuations in cellular properties, or additional interactions at the interface with the chip surface.

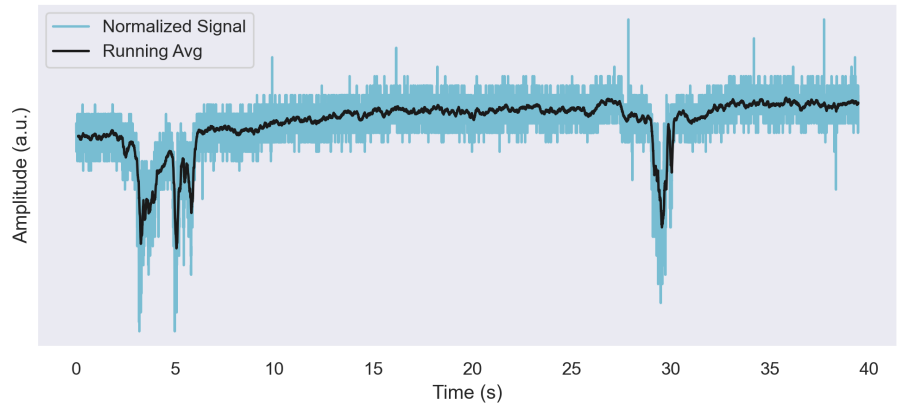

Figure 4.1: Example of transmitted signal (blue) recorded during a transient trapping event. A running average (black) is added to improve readability of the high-frequency oscillations. The signal shows short-lived transmission dips, which were confirmed by live microscopy to correspond to a bacterium approaching the cavity and escaping shortly after. The data were acquired on a photonic chip equipped with a static pool.

Close approach without trapping. Another recurrent observation among strains considered trappable concerns the lack of reproducibility of trapping events. Certain cells approach very close to the trapping region yet do not interact with the trap. In some cases, cells reach what appears to be the effective interaction range of the optical field, where most trappable cells typically begin to interact, as monitored through the live spatial visualization system. Nevertheless, they exhibit no trapping signature in the transmitted signal, not even a short transient trapped-detrapped event. The occurrence of this behaviour is not uniform across strains. While it was not prominent in the strains initially investigated, it became increasingly evident as additional strains were tested. Across multiple experimental runs, some strains consistently exhibited a higher incidence of near-surface non-interaction than others. Although this tendency was not quantified through a dedicated statistical study, its repeated observation suggests that spatial proximity alone is insufficient for capture and that strain-specific properties influence the efficiency of interaction with the optical field. Possible contributors include preferred cell orientations, variations in refractive index distribution, or short-range physicochemical interactions with the SOI surface.

Osmotic pressure. A further complication arises from the suspension conditions used during the early stages of this project. Because bacteria were suspended in pure water rather than in an isotonic buffer, an osmotic pressure difference developed across the cell envelope. This originates from the contrast between the very low ionic concentration of the external medium and the naturally higher solute concentration within the cytoplasm. This imbalance results in water influx into the cytoplasm, which leads to progressive swelling over time, until a mechanical equilibrium is reached. Such changes can alter both the effective volume and the internal composition of the cells, thereby influencing their effective refractive index and optical response. The refractive index contrast between the bacterium and the surrounding medium is already small is the order of $\Delta n \approx 0.05$, since n(*E. coli*)$\simeq$ 1.38 as reported in literature [203] and n(water)$\simeq$ 1.33 [77]. Such modest variations may reduce the magnitude of the optical forces and make trapping more sensitive to experimental conditions. In addition, the extent of osmotic adjustment cannot be precisely controlled and may not affect all cells equally. It therefore becomes difficult to ensure that cells being compared are in comparable physiological states, introducing a potential bias in the interpretation of strain-dependent behaviour.

It remains unclear whether these specific inconsistencies were encountered by previous members of the project working under similar experimental conditions, or to what extent, as such behaviours were not systematically documented. The absence of explicit reporting does not imply their absence in practice. For this reason, the present chapter aims to formalize and quantify these observations and to investigate their possible origins by examining mechanisms that extend beyond purely optical considerations. This constitutes an essential step toward addressing experimental inconsistencies and establishing a reproducible trapping protocol.

Taken together, these observations indicate that optical forces alone are insufficient to account for the full range of behaviours observed experimentally. The strain-dependent differences, the transient escape events, and the near-surface non-interaction phenomena suggest that the equilibrium position of a bacterium near the SOI surface results from a balance between multiple interactions. A systematic analysis of the forces acting at the SOI-bacteria interface is therefore required. In parallel, the influence of the suspension medium on this balance will also be examined later in this chapter.

4.3 Force Analysis at the SOI-Bacteria Interface

4.3.1 Decomposition

In order to identify which mechanisms may govern the interactions between bacterial cells and the surface of the SOI photonic structures, we decompose the problem into the forces that may contribute to the observed behaviours. The objective is not to provide an exhaustive theoretical treatment of each contribution, but rather to determine which forces could realistically account for the untrappability or unstable trapping of bacteria, and which of them can be experimentally modified to test their role.

We therefore consider a bacterium located in the immediate vicinity of the SOI surface, immersed in the suspension medium and exposed to the evanescent part of the resonant optical field. The analysis focuses on this reference cell while accounting for its interaction with the surrounding fluid, the solid interface, and neighbouring cells when relevant.

At the scale of the reduced-volume system considered here, the forces acting on the bacterium can be grouped into three main categories: mechanical forces associated with motion in a fluid environment, optical forces generated by the resonant electromagnetic field, and intermolecular forces arising from physicochemical interactions at the interface between the bacterial envelope and the SOI surface.

The full inventory of forces is summarized below:

- **Mechanical forces:** net gravity (including buoyancy), Brownian fluctuations, hydrodynamic drag, active motility due to flagella, and short-range steric interactions with neighbouring bacteria. The chip surface additionally acts as an impenetrable boundary that limits the spatial degrees of freedom of the cell.
- **Optical forces:** gradient force associated with the evanescent field of the resonant cavity and, in principle, radiation pressure.
- **Intermolecular forces:** van der Waals attraction and electrostatic (double-layer) interactions between the bacterial envelope and the SOI surface.

4.3.2 Analysis

To assess which interactions may realistically influence bacterial trapping near the SOI surface, we examine each force identified in the previous section in light of our experimental conditions. The goal is not to establish a complete quantitative hierarchy of all contributions, but rather to determine which mechanisms can be reasonably excluded, which are unlikely to explain the observed discrepancies, and which remain both physically plausible and experimentally accessible.

(A) Mechanical Forces

Net gravity. Both cellular gravity and buoyancy are small for an *E. coli* bacterium of 1–2 μm in size. The relevant quantity is the buoyant mass, which refers to the apparent weight of an object when it is submerged in a fluid, as described by Archimedes' principle. Experimental measurements report buoyant masses (m_b) in the range 100–200 fg (i.e. $10^{-16} - 2 \times 10^{-16}$ kg) for live *E. coli* cells [204]. This corresponds to an effective gravitational force of order:

$$F_{net} \sim m_b \cdot g \approx 10^{-15}\,\mathrm{N}$$

Since trapping occurs in a sub-micrometre region near the surface, gravity adds a negligeable vertical bias and cannot explain strain-dependent behaviour. Gravity therefore does not contribute in any significant manner to the equilibrium position of the cell and can be safely neglected.

Brownian motion. Brownian fluctuations provide a background positional noise that is directly visible on the transmitted optical signatures. Even when spatially confined within the evanescent field, bacteria continue to undergo thermal agitation due to collisions with surrounding molecules. A characteristic force scale can be estimated from thermal energy considerations as:

$$F_{\text{Brownian}} \sim \frac{3}{2}\frac{k_B T}{r}$$

where k_B is the Boltzmann constant and r denotes a characteristic bacterial radius. For a characteristic size of order $1-2\,\mu m$ and the temperature $T \approx 300\,\text{K}$, this yields a force scale of a few 10^{-15} to $10^{-14}\,\text{N}$, comparable to the effective gravitational force estimated above. Brownian motion is therefore a universal stochastic contribution, present in all runs, and can neither justify the strain-dependent behaviour nor the cell-to-cell differences observed.

Flagellar motility. Structurally, many *E. coli* strains contain flagella (*cf.* fig. 3.2) that propel the cell in liquid media and give rise to active motility. This self-generated motion may oppose optical confinement, particularly in situations where trapping appears weak or transient. Measurements of flagellar motors in *E. coli* report torques of order $4600\,\text{pN}\cdot\text{nm}$ and corresponding propulsion forces on the order of $1\,\text{pN}$ ($10^{-12}\,\text{N}$) [205].

Such forces are therefore several orders of magnitude larger than both gravitational and Brownian contributions, and may in principle compete with optical trapping forces. Since flagellar activity depends on the physiological state of the cell and may vary between strains, it could contribute to the strain-dependent behaviours reported earlier.

However, isolating this contribution would require a dedicated experimental comparison, for instance using non-motile or genetically modified strains to remove or add functional flagella. Such controls were not implemented in the present work for lack of resources and technical expertise. Consequently, while flagellar motility remains a plausible factor in the overall force balance, its specific contribution cannot be assessed here and is not further pursued in this study. It nonetheless represents a relevant direction for future investigations aimed at clarifying strain-dependent phenomena.

Hydrodynamic forces. In fluid dynamics, the Reynolds number ($\text{Re} = \rho v L/\eta$) is a dimensionless quantity that compares inertial to viscous forces to predict the type of flow. A low Reynolds number indicates laminar flow, while a high number indicates turbulent flow. Bacterial motion occurs at very low Reynolds number, typically $\text{Re} \lesssim 10^{-4}$, where viscous forces dominate over inertial effects [206]. In this regime, fluid motion is overdamped and any imposed flow directly translates into viscous drag on the cells. Hydrodynamic drag is therefore only relevant in the case of optofluidic chips that contain a circuit within which the flow of bacteria can be controlled by an external pump system, as described earlier in this manuscript. Indeed, if the pressure within the circuit is very high, a trapped bacterium can be dragged out of the evanescent field both by the force of drag and by being pushed by the flow of other bacteria. However, trapping events are probed at stopped flows (pressure sat at $0-3$ mbar), corresponding to quasi-static conditions. More importantly, the anomalous strain-specific and cell-specific behaviours were also observed in fully static PDMS pools, where no imposed flow is present. Bulk hydrodynamics therefore cannot account for the observed discrepancies.

Contact forces. Steric interactions resulting from collisions with neighbouring bacteria may transiently perturb the position of a cell near the surface. Such events are inherently stochastic and their probability scales with bacterial concentration. In practice, no systematic correlation was observed between concentration variations and the persistence of the anomalous behaviours. Moreover, collision-induced displacements would affect all strains similarly and would not produce

strain-dependent trends as described earlier. Therefore, contact forces are unlikely to constitute the primary mechanism underlying untrappability or unstable trapping.

(B) Optical Forces

Optical gradient forces constitute the trapping mechanism by design in our photonic setup. Their magnitude depends sensitively on the particle polarizability, which in this context refers to the effective dipolar response of the particle to the optical field (as introduced in the gradient force formalism, *cf.* equation (1.4)), and scales approximately with r^3, as well as on the refractive index contrast between the bacterium and its surrounding medium. Consequently, variations in cell size or in suspension composition directly modify the effective trapping potential. This dependence is particularly relevant in pure water, where osmotic effects may alter both cell morphology and optical contrast over time.

Experimental estimates done within our research group, obtained on similar photonic structures, report trapping forces on the order of 1 pN, based on drag-induced detrapment measurements and viscous force calculations [207]. This places optical forces in the same range as flagellar propulsion forces, and several orders of magnitude above gravitational and Brownian contributions.

Radiation pressure forces, in contrast, are negligible in the present configuration. Although the cavity is excited via a propagating mode in the access waveguide, the optical field within the CMT3 cavity itself is strongly localized and forms a resonant distribution with no preferred propagation direction. As a result, the net momentum transfer to a trapped particle remains very limited, and scattering-induced radiation pressure is negligible. The trapping mechanism is therefore dominated by the gradient force.

(C) Intermolecular Forces

When the bacterium approaches the SOI surface down to nanometre separations, interfacial interactions become decisive. At this stage, the equilibrium position of the cell is no longer governed solely by optical confinement but also by forces acting across the thin liquid layer separating the two surfaces. These interactions are commonly described within the DLVO framework, which accounts for van der Waals and electrostatic (double-layer) contributions, and its extended version (xDLVO), which additionally includes specific interactions such as steric or hydrophobic effects [208, 209].

Within this framework, the dominant interactions depend strongly on the separation distance between the two surfaces. At distances larger than ~ 50 nm, van der Waals forces dominate. In the intermediate regime ($\sim 10-20$ nm), both van der Waals and electrostatic interactions contribute. At very short separations (below $\sim 1-2$ nm), additional specific interactions become significant [210].

Van der Waals interactions originate from fluctuating dipoles and are inherently attractive. Their magnitude increases rapidly as the separation distance decreases. The Hamaker constant, A_{H}, is an effective material parameter that quantifies the strength of these interactions across a medium. For a bacterium interacting with a silica surface in water, A_{H} is typically on the order of 6.5×10^{-21} J [208], which is consistent with van der Waals contributions becoming relevant over several tens of nanometres. As mentioned priorly, previous studies have shown that, for stable optical trapping, the trapped object should ideally be located about $80-110$ nm above the CMT resonator surface [76]. Van der Waals interactions are therefore always present in this setup. Despite this, these interactions are not easily tunable experimentally without modifying the material properties of either the substrate or the cell.

On the other hand, electrostatic interactions arise from charges around the surfaces of the bacterial membrane and the SOI interface. In aqueous environments, these charges generate electrical double layers (EDLs), which are interfacial regions where mobile ions in the liquid reorganize to screen the surface charge. The interaction between the EDL of the chip surface and that of an approaching bacterium leads to either attraction or repulsion depending on their respective signs. The characteristic decay length of this interaction is given by the Debye length ℓ_D, which represents the distance over which electrostatic potentials are screened in the medium. It is defined as

$$\ell_D = \sqrt{\frac{\varepsilon_r \varepsilon_0 k_B T}{2 N_A e^2 I}},$$

where ε_r is the relative permittivity of the solution, ε_0 is the vacuum permittivity, k_B is the Boltzmann constant, T is the absolute temperature, N_A is Avogadro's number, e is the elementary charge, and I is the ionic strength of the solution.

This length scale is highly sensitive to the composition of the suspension medium. In low ionic-strength ultra-pure water ($I \sim 10^{-5}$ M), ℓ_D is on the order of 1 μm, whereas in physiological conditions (e.g. 158 mM *NaCl*), it decreases to below 1nm [211]. As a result, electrostatic interactions constitute one of the few contributions that can be either long-range and repulsive or strongly screened depending on experimental conditions. This also makes them readily tunable by adjusting the ionic strength or by modifying surface chemistry.

4.3.3 Summary

Taken together, the analysis shows that several forces can be reasonably excluded as primary drivers of the observed behaviours under our experimental conditions. In particular, gravity, Brownian motion and hydrodynamic effects either remain too weak or do not display the required variability to account for the strain-dependent or stochastic trapping outcomes.

In contrast, optical forces and flagellar motility both lie in the piconewton range and may therefore compete directly. While flagellar activity constitutes a plausible contributor to unstable or transient trapping, its role cannot be isolated within the present experimental framework.

Intermolecular interactions, although acting at shorter range, introduce additional mechanisms that are both sensitive to bacterial surface properties and experimentally tunable. Among them, electrostatic interactions are of particular interest, as their strength and range can be directly controlled through the ionic composition of the surrounding medium.

For clarity, the different forces considered in this analysis and their characteristic features are summarized in table 4.2.

Finally, given that the anomalous trapping behaviours reported earlier display strain dependence, and considering that surface charge properties may vary between bacterial strains, electrostatic interactions emerge as a particularly relevant candidate mechanism to be analysed. This hypothesis motivates the following sections, which focus on characterizing surface charge via zeta-potential measurements and on probing the effect of charge screening and surface passivation on trapping stability.

4.4 Surface Charges

In order to investigate electrostatic interactions at the SOI–bacteria interface, we need to understand the nature of surface charge density of both the bacterial envelope and the SOI surface

Table 4.2: Summary of the forces considered in the present analysis, together with their characteristic scale, range and relevance to the observed trapping behaviour.

Category	**Force**	**Characteristic scale / range**	**Main features / relevance**
Mechanical	Net gravity	$\sim 10^{-15}$ N	Weak constant bias; not strain dependent
Mechanical	Brownian motion	$\sim 10^{-15} - 10^{-14}$ N	Universal stochastic fluctuations
Mechanical	Flagellar motility	~ 1 pN	Active force; potentially strain dependent (not easily controllable)
Mechanical	Hydrodynamic drag	$\mathrm{Re} \lesssim 10^{-4}$	Relevant only under imposed flow (controlled via pressure)
Mechanical	Contact / steric collisions	Short-range	Concentration dependent; stochastic
Optical	Gradient force	~ 1 pN; evanescent decay (< 100 nm)	Primary trapping mechanism (tunable via optical power and design)
Optical	Radiation pressure	Negligible	Inexistent in CMT3 cavity design
Intermolecular	van der Waals	$\lesssim$ 10–50 nm	Always attractive; weakly tunable (material-dependent)
Intermolecular	Electrostatic (double layer)	ℓ_D from < 1 nm to ~ 1 μm	Tunable via ionic strength; strain-dependent candidate

under the aqueous conditions used for trapping. However, direct measurement of the absolute values of these charges in situ is not straightforward, particularly for living cells and microstructured substrates immersed in liquid. Instead, the closest experimentally accessible quantity is the zeta potential, which provides rather an indirect estimate of the effective surface charge through electrokinetic measurements and allows for relative comparison between samples.

In this section, we first introduce the theoretical principles underlying zeta potential measurements and detail the experimental protocol implemented for both bacterial suspensions and SOI samples. We then present and analyse the measured values, before discussing their implications for electrostatic interactions at the SOI-bacterium interface.

4.4.1 Zeta Potential: Theory

When a solid object is placed in an aqueous electrolyte, its surface does not remain electrostatically isolated. Instead, interfacial equilibrium processes between the material and the surrounding solution establish a net surface charge around the object. This surface charge mainly arises from acid–base reactions of surface functional groups (e.g. carboxylic acids for bacterial cells, silanol groups for SOI surfaces) and from the adsorption of ions from the surrounding medium [211]. The presence of this surface charge generates an electric field that extends into the adjacent liquid. In response, mobile ions redistribute: counter-ions accumulate near the interface, while co-ions are partially depleted. This redistribution of charge in the liquid gives rise to what is referred to as the electrical double layer (EDL) that surrounds the object.

This interfacial structure is not characterized by a sharp boundary. Instead, the electrostatic potential decays progressively from the surface into the bulk solution over a characteristic screening length determined primarily by the ionic strength of the medium, as illustrated in fig. 4.2. Close to the surface, a compact region of specifically adsorbed ions, referred to as the Stern layer, is formed. Beyond this layer, the ion distribution becomes diffuse and extends into the bulk liquid.

It is within this diffuse region that a conceptual boundary known as the slipping plane is defined. When the particle is subjected to an external electric field, the liquid beyond this plane moves relative to the particle, whereas the inner region remains effectively associated with it. As a result, the electrostatic potential effectively probed in electrokinetic measurements is lower than the actual surface potential, as illustrated in fig. 4.2.

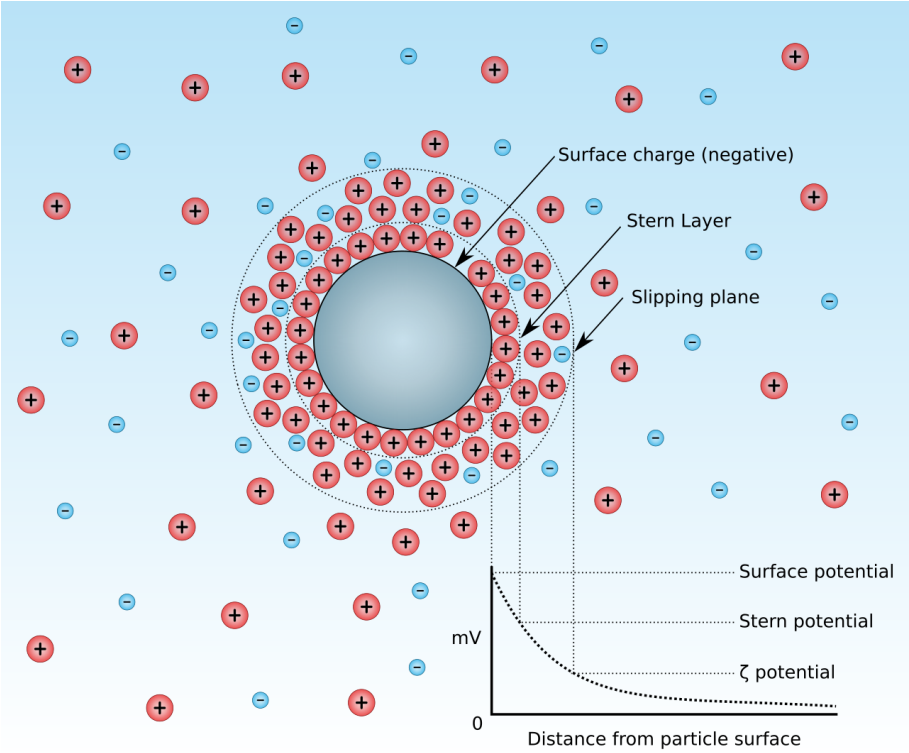

Figure 4.2: Schematic representation of how ionic concentration and electrostatic potential vary with distance from the surface of a charged particle immersed in a dispersion medium. The diagram shows the charged surface, the distribution of counter-ions near it, and how the potential decays as one moves away from the interface. (Source: Modified by Mjones1984 from original work by Larryisgood, 2012, Creative Commons license: CC BY-SA 3.0)

The zeta potential is defined as the electric potential at this slipping plane rather than directly at the surface itself. Importantly, it is not measured directly. The experimentally accessible quantity is the electrophoretic mobility μ_e, from which the zeta potential is inferred using an electrokinetic model [211].

For colloidal particles, an external electric field (typically on the order of a few tens of volts) is applied through an electrode to induce motion of charged objects toward another oppositely charged electrode. The electrophoretic mobility is defined as the steady-state velocity of the particle divided by the applied electric field [212, 213].

For macroscopic solid surfaces such as SOI substrates, the approach is reversed. Instead of inducing motion through an electric field, a pressure-driven flow is imposed along the surface, which generates an electrical potential difference known as the streaming potential. This potential results from the displacement of ions within the electrical double layer by the flowing liquid [213, 214].

In both cases, the zeta potential is then obtained from the measured mobility through the equation:

$$\zeta = \frac{4\pi\eta}{\varepsilon} \cdot f(\kappa\alpha) \cdot \mu_e \tag{4.1}$$

where η is the viscosity of the medium, ε its dielectric permittivity, μ_e the electrophoretic mobility, and $f(\kappa\alpha)$ the Henry function. This function accounts for the ratio between the particle size α and the Debye screening length κ^{-1}, and therefore describes the influence of double-layer thickness on electrokinetic behaviour. Depending on the relative thickness of the electrical double layer compared to the particle size, different limiting approximations can be used (e.g. Hückel or Smoluchowski limits). In practice, the appropriate model is selected during data processing.

Zeta potential is therefore not a direct measurement of the absolute surface charge density. Rather, it is derived from mobility measurements and provides an electrokinetic descriptor of the interfacial state under specific solution conditions, primarily determined by pH and ionic strength. In practice, it allows determination of the sign of the charge and enables relative comparison between samples.

In the present study, this comparative information is considered sufficient to assess the potential role of electrostatic interactions at the SOI-bacteria interface.

4.4.2 Zeta Potential: Experimental Protocol

General Setting

All zeta potential measurements presented in this work were performed using a Zetasizer instrument (Malvern Panalytical [215]) equipped with a transparent capillary cell specifically designed for electrophoretic measurements, both presented in fig. 4.3. The cell consists of a narrow capillary channel into which the liquid sample is introduced. Electrodes positioned at both ends of the capillary allow the application of a controlled electric field across the suspension.

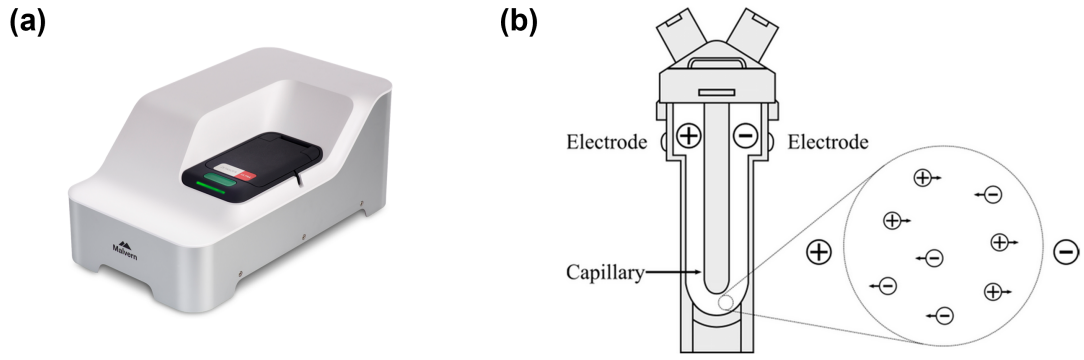

Figure 4.3: Zeta potential measurement setup. (a) Zetasizer instrument (Malvern Panalytical) used for all electrokinetic measurements in this work. Reprinted from [215]. (b) Schematic representation of the zeta capillary cell. Reprinted from [216].

In practice, the measurement consists of applying an alternating electric field in successive cycles of positive and negative polarity. Charged particles suspended in the liquid respond to this field by moving first in one direction and then in the opposite one. The velocity of this motion is measured through electrophoretic light scattering, based on laser Doppler velocimetry: a laser beam passing through the capillary detects the frequency shift of the scattered light induced by particle motion. Additionally, the size distribution can be determined during the same measurement sequence via dynamic light scattering.

From the measured Doppler shift, the electrophoretic mobility is extracted. This relation arises from the balance between the electrical force $F_{\text{elec}} = qE$ acting on the particle (radius R) and the viscous drag force, typically expressed as $F_{\text{drag}} = 6\pi\eta Rv$ at steady state. In practice, the instrument software then converts this mobility into a zeta potential using the conversion expressed

in equation (4.1). For this step, the appropriate approximation of Henry's equation is automatically selected by the software according to the measured particle size and the experimental parameters entered by the user. In the limiting case where the particle size is large compared to the Debye length ($\kappa\alpha \gg 1$), the Smoluchowski approximation applies and simplifies the relation to $\zeta = \mu_e \eta / \varepsilon$. These parameters describe both the suspension medium and the dispersed objects. They include the viscosity and refractive index of the medium, as well as the refractive index and approximate size of the particles. They are either selected from the internal database of the instrument or manually entered to match the experimental conditions used in this study.

It is important to note that more elaborate models have been developed to account for so-called «soft particles», such as bacteria, which possess an ion-permeable outer layer rather than a sharp interface. In these models, the slipping plane is located within this permeable layer, and additional parameters such as electrophoretic softness are introduced to describe fluid penetration [101]. However, these refined descriptions require additional parameters, including the thickness and permeability of the outer layer as well as its internal charge distribution, which are not directly accessible in the present experiments. In this work, the classical framework is therefore used, as it provides a robust and widely adopted basis for comparative analysis between samples.

Bacterial Suspensions Preparation

Zeta potential measurements of bacterial samples were performed on cultures grown 16 to 24 hours prior to the experiment. This growth window ensures that cells are in a comparable physiological state and have reached a stable morphology, consistent with the conditions used during optical trapping experiments.

Furthermore, for each strain, isolated colonies were collected from the Petri dish and resuspended in ultrapure water in order to reproduce the suspension conditions under which the trapping inconsistencies were initially observed. In practice, $3-4$ colonies were used to prepare each sample, which typically corresponds to bacterial concentrations on the order of $10^7 - 10^8$ cells/mL. The suspensions were prepared immediately before measurement to minimise osmotic swelling effects, which could progressively alter cell size and potentially affect both electrophoretic mobility and light scattering signals. This preparation protocol is consistent with commonly reported procedures for electrokinetic characterization of bacterial suspensions, where cells are harvested from agar plates and resuspended in controlled media prior to measurement [101, 208, 213].

Prior to zeta potential acquisition, the instrument was programmed to perform size measurements to verify the homogeneity of the bacterial population. This provides an internal consistency check: aggregates or debris would significantly distort electrophoretic mobility measurements and bias the extracted values.

For each sample, six independent zeta potential runs were performed consecutively. Each run internally consists of multiple measurements of particle velocity under alternating electric field cycles, from which an average electrophoretic mobility is computed by the instrument. The reported value corresponds to the average of these six runs. This averaging procedure reduces the impact of instrumental fluctuations, which can become significant, particularly for values close to zero where the signal-to-noise ratio decreases.

In total, each sample undergoes one size measurement followed by six zeta potential runs. This sequence requires approximately 25 minutes due to multiple stabilisation cycles during which the instrument equilibrates temperature and particle motion. This duration is in addition to the time required for culture preparation and sample handling. Even with partial parallelisation of tasks, the systematic characterisation of all 15 bacterial strains therefore required an experimental campaign spanning several days.

Model System for the SOI Surface

The photonic structures used in this work are fabricated on silicon-on-insulator (SOI) substrates. Although the guiding layer consists of crystalline silicon (Si), exposure to ambient air during fabrication and handling leads to the spontaneous formation of a thin native oxide layer at the surface. This oxide, typically a few nanometres thick, is composed of silicon dioxide (SiO_2). As a result, the interface that is effectively in contact with the bacterial suspension is silica rather than bare silicon.

Zeta potential measurements, however, require dispersed objects in suspension and cannot be directly performed on fixed planar substrates using the present setup. To approximate the electrokinetic behaviour of the SOI surface under our experimental conditions, a model system was therefore introduced.

Commercially available silica (SiO_2) beads of nominal diameter 1 μm (supplier: Cospheric, purity: $> 99.9\%$ [217]) were used as a representative model for the oxidised chip surface. This size was independently confirmed by the DLS measurements performed prior to the zeta potential acquisition. These particles provide a dispersed silica interface compatible with electrophoretic measurements, allowing estimation of the effective surface charge state in the same aqueous environment as the bacterial samples. While this approach does not reproduce the exact surface roughness or fabrication history of the chips, it captures the chemical nature of the interface governing electrostatic interactions in the present study. The use of silica particles as model systems for oxidised silicon surfaces is widely reported in the literature for electrokinetic and interfacial studies, as it captures the dominant surface chemistry governing interactions in aqueous environments [208, 218, 219].

4.4.3 Bacterial Surface Charges

Zeta potential measurements were performed for 15 *E. coli* strains included in the optical trapping study. The averaged values obtained under identical suspension conditions are presented in fig. 4.4.

The most immediate observation is that all strains exhibit a negative zeta potential in freshly prepared deionized water, confirming that the bacterial envelope carries a net negative electrokinetic signature under the tested conditions. Most values fall within a relatively narrow interval from approximately -37 mV to -49 mV, with EC225 standing out as the smallest magnitude among all strains. The dispersion observed across consecutive measurements remains limited, typically within a few millivolts, indicating stable electrophoretic behaviour for each strain.

However, no clear trends seperate bacteria according to their trappability as shown by the markers in fig. 4.4. The non-trappable strains (EC10, EC21, EC207, Eco0122, Eco0125 and Eco0123) display zeta potentials in an interval that substantially overlaps with that of the trappable strains. Therefore, they are not distinguishable based on this metric alone. These results indicate that, within the explored experimental conditions, the absolute magnitude of the zeta potential alone does not provide a predictive criterion for trappability. While all bacteria are negatively charged, there is no obvious separation between trappable and non-trappable strains based solely on this electrokinetic measurement.

This does not imply that electrostatic interactions are irrelevant, as it doesn't exclude them from contributing to the overall interaction landscape at the SOI-bacteria interface, especially the non-strain-dependant behaviours. To further investigate these observations, the next step is to compare them with the measured zeta potential of the silica model surface.

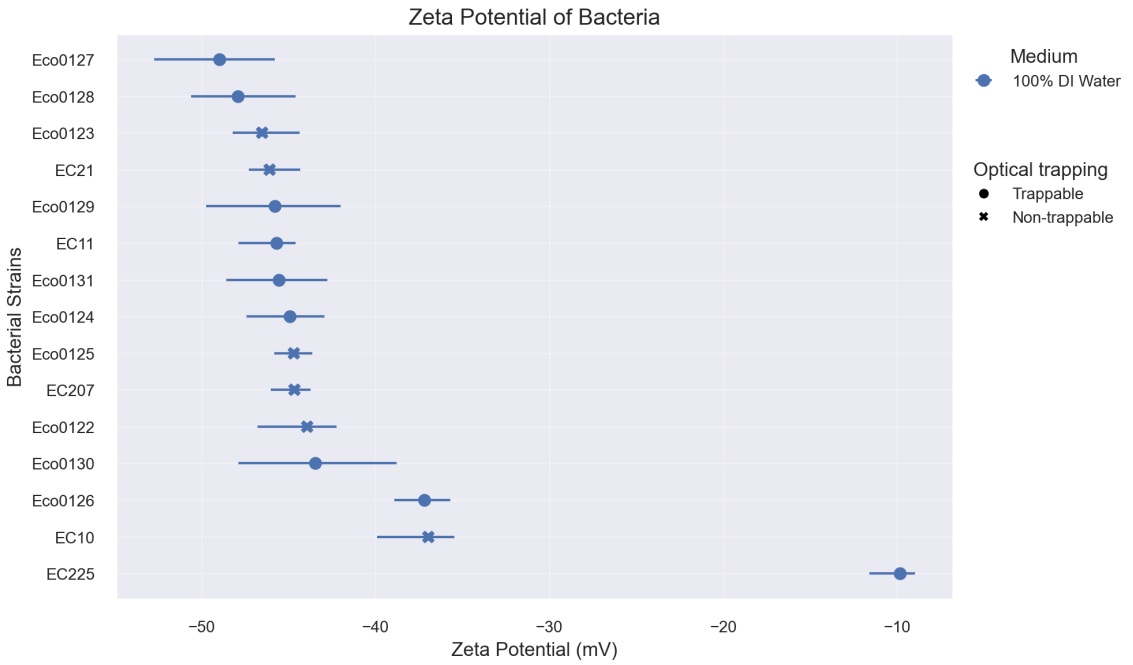

Figure 4.4: Zeta potential measurements for bacterial cells in deionized water. Marker shape indicates optical trappability for each strain, also summarized in table 4.1. Error bars represent the full range (min/max) of consecutive measurements used to compute the averages.

4.4.4 SOI Surface Charges

Zeta potential measurements performed on the silica bead model (Cospheric, diameter 1 μm [217]) in deionized water resulted in an average value of approximately -60 mV. The six consecutive measurements ranged from -62.47 mV to -56.56 mV. The limited variation across runs indicates stable electrokinetic behaviour and good measurement reproducibility under the same suspension conditions used for optical trapping experiments.

This value is consistent with reported zeta potentials for silica interfaces in aqueous environments. For instance, silica nanoparticles have been reported to exhibit zeta potentials around -55 mV at neutral *pH* [220], while planar silica surfaces typically range from -30 mV at *pH* 5 to -65 mV at *pH* 7 depending on ionic strength [221]. The measured value therefore falls within the expected range for negatively charged silica surfaces.

While the silica beads do not reproduce the exact morphology or fabrication history of the planar SOI surface, they provide a chemically representative model of the oxidised silicon dioxide interface that forms at the chip surface. The measured value should therefore be interpreted as an estimate of the effective electrokinetic behaviour under identical aqueous conditions rather than as an exact quantitative equivalent.

4.4.5 Electrostatic Interaction at the SOI–Bacteria Interface

When considered together with the bacterial measurements presented above, these results show that both the oxidised SOI surface and all tested *E. coli* strains carry net negative electrokinetic potentials in deionized water. Electrostatic interactions during bacterial approach to the resonator surface are therefore expected to be repulsive, especially in deionized water where the Debye length ($\approx 1\mu$m) is much larger than the range of the evanescent field [211].

A rough estimate of the electrostatic repulsion between a bacterium and the SOI surface can be obtained using a simplified DLVO-like expression:

$$F_{\text{elec}}(d) \approx 2\pi\varepsilon_0\varepsilon_r R_{\text{eff}}\,\zeta_{\text{bact}}\,\zeta_{\text{surface}}\,\frac{1}{\ell_D}\,e^{-d/\ell_D}, \tag{4.2}$$

where R_{eff} is the effective bacterial radius ($\sim 0.5\ \mu$m), ζ_{bact} and ζ_{surface} are the measured zeta potentials of the bacterium and surface (used here as a proxy for direct surface potentials), ℓ_D is the Debye length in deionized water, and d is the separation distance relevant to surface trapping. Taking $d \approx 80-110$ nm, consistent with the expected trapping height above the resonator surface in pure water [76], and using $\zeta_{\text{surface}} \sim -60$ mV and $\zeta_{\text{bact}} \sim -37$ to -49 mV (for most strains, with the exception of EC225 at -10 mV), the resulting electrostatic force is on the order of $10-50$ fN, corresponding to a repulsive (positive sign) interaction.

In comparison, the optical gradient forces generated in our setup, as measured via drag-induced detrapment experiments and viscous force calculations [207], are on the order of 1 pN. Therefore, the optical forces exceed electrostatic repulsion by at least an order of magnitude, allowing stable confinement of single bacterial cells at the resonator surface.

Two important conclusions follow.

First, the experimental observation of stable optical trapping of single bacterial cells in deionized water demonstrates that the optical forces generated by the evanescent field are sufficient to overcome the repulsive electrostatic contribution at the relevant separation distances. Electrostatic repulsion therefore does not prevent trapping in principle and cannot account, on its own, for the untrappability of certain bacterial strains, since all strains are negatively charged within a comparable range.

Second, this does not exclude electrostatic interactions from contributing to the single-cell inconsistent behaviours reported during trapping experiments. In fact, the zeta potential value obtained for each strain corresponds to an average across multiple measurement rounds, each itself averaging over many bacterial cells. Therefore, it represents a global electrokinetic parameter across the sample and does not resolve possible variations in surface charge heterogeneity, outer membrane composition, or local charge distribution between individual bacteria. Such differences may influence the effective interaction potential during approach, modulating separation distance, confinement stability, or the optical power required to achieve trapping. Electrostatic repulsion may therefore act as a background interaction common to all bacteria-surface pairs, affecting trapping dynamics without constituting the primary discriminating parameter.

To evaluate whether these electrostatic contributions play a role in the observed inconsistencies, charge screening strategies were implemented. Surface treatments were applied to both the bacterial suspensions and the photonic structures in order to reduce or modify the effective surface charges. The methodology and resulting trapping behaviour under screened conditions are presented in the following section.

4.5 SOI Surface Treatment

Optical trapping occurs within the evanescent field at the immediate vicinity of the resonator surface, so the properties of the chip interface directly influence the interactions experienced by approaching bacteria. The native top layer of the SOI chip is oxidised to form silicon dioxide, which carries a net negative charge in deionized water. Modifying this interface provides a controlled way to reduce electrostatic repulsion and probe its role in the observed trapping behaviour.

4.5.1 SOI Surface Treatment: Methods

Bovine serum albumin (BSA) was selected as a coating agent because it readily adsorbs onto silica surfaces and forms a stable, hydrated protein layer. Structurally, BSA is a globular protein with an overall negative charge at neutral pH. When adsorbed onto silica, it forms a hydrated layer that modifies the interfacial charge distribution and effectively screens the underlying surface charge. This screening does not rely on charge inversion but rather on the spatial separation introduced between the surface and the solution, as well as on local charge heterogeneity within the protein layer [211, 222]. As a result, the effective electrostatic interaction experienced by approaching bacteria is reduced without introducing strong attractive interactions that could lead to irreversible adhesion.

In fact, bovine serum albumin is widely used as a blocking agent in surface functionalization, particularly for biosensors and microfluidic devices, because it forms a stable, hydrated protein layer that reduces nonspecific adsorption while minimally perturbing underlying surface properties [223, 224]. Its reliability and well-characterized behaviour on silica and silicon dioxide surfaces make it a convenient choice for blocking surfaces and reducing nonspecific adsorption in optical trapping experiments.

In practice, we prepared BSA solutions by dissolving commercial BSA crystals (Merck) in deionized water to obtain a concentration of 10 mg per 3 mL, corresponding to approximately $50\mu M$. This concentration was selected by previous EPFL colleagues as the highest at which the optical characteristics of the resonator (resonance wavelength and quality factor) remain unaffected. Dissolving the protein generates numerous air bubbles in the solution, which were first reduced by filtration through a 0.2 μm syringe filter and then by allowing the solution to rest overnight before use. Each batch was used for a maximum of one week and stored in the refrigerator between uses to preserve protein integrity and reduce the impact of potential contamination during handling.

Surface treatment was performed by injecting the BSA solution into the integrated fluidic channels of the photonic chip and allowing it to incubate for several hours prior to optical trapping experiments. Between successive experimental runs, the channels were flushed with BSA solution to resaturate the surface. A complete description of these manipulations within the full optical trapping protocol is provided in the next chapter.

To estimate the order of magnitude of the thickness of the adsorbed BSA layer, two $2 \times 2\ cm^2$ pieces of silicon wafer were prepared: one as a reference and one incubated in BSA solution for 20 minutes. Ellipsometry measurements revealed a relative layer thickness between the two samples of $5 - 10\ nm$, corresponding to the BSA layer. This measurement was not straightforward, as multiple fitting models had to be considered due to the porous and heterogeneous nature of the BSA layer, whereas ellipsometry is best suited for smooth, planar surfaces. However, the measured values were consistently within this mentionned range despite the limited precision of the measurement, and remain consistent with values reported in the literature [225, 226]. The treated wafer was then rinsed by manually swirling it in a container filled with deionized water for one minute, after which the measured thickness decreased to roughly one-third to two-thirds of the initial value. This partial depletion is consistent with the fact that adsorbed protein layers such as BSA do not form perfectly rigid coatings, but rather soft and dynamically rearrangeable interfacial structures [227].

This ellipsometry procedure does not reproduce the conditions of the microfluidic channels, as volume, flow, and dynamic interactions differ. Additionally, the measurement represents an average over a large surface area and does not capture potential local variations. It is therefore used, in this context, only as a qualitative demonstration that partial depletion of the BSA surface functionalization of the chip may occur, which justifies the need for regular resaturation of this layer to maintain reproducible interfacial conditions during experiments.

Finally, the impact of this surface modification on the electrokinetic properties of the interface was subsequently evaluated through zeta potential measurements, presented later in the next section.

4.5.2 SOI Surface Treatment: Results

The impact of BSA adsorption on the electrokinetic properties of silica surfaces was assessed through zeta potential measurements performed on treated and untreated silica beads suspended in deionized water.

The measurement on treated silica was prepared by suspending the beads in aqueous solution of BSA (3.33 mg/mL) and allowing them to incubate overnight in order to promote surface saturation. This was followed by centrifugation and resuspension in fresh deionized water, to better simulate experimental results and to isolate the effect of the adsorbed protein layer from any contribution of the incubation medium. The measurement was conducted following the same acquisition protocol presented previously: six consecutive runs were performed during which multiple beads were probed, and the mean values of these runs were retrieved. In these conditions, the treated beads displayed a mean zeta potential of $-34.15\,\mathrm{mV}$, with measured values between $-38\,\mathrm{mV}$ and $-31\,\mathrm{mV}$.

This presents a significant change from the untreated beads in water where they exhibited a mean zeta potential of $-59.85\,\mathrm{mV}$. The magnitude of the surface charge was therefore reduced by approximately $25\,\mathrm{mV}$ following protein adsorption.

Additionally to recording the zeta potential, the size of the silica beads was also independently verified by dynamic light scattering prior to measurement, yielding a mean hydrodynamic diameter of approximately 1 μm. At this size scale, DLS measurements typically exhibit uncertainties on the order of a few percent, corresponding to several tens of nanometres [215]. The thickness of the adsorbed BSA layer, estimated to be in the range of $5-10$ nm, is therefore too small to produce a measurable shift in the apparent particle diameter or to be reliably resolved by DLS

Consequently, while the thickness of the adsorbed BSA layer and the exact zeta potential values may differ between these beads and planar SOI surfaces, this significant shift toward less negative values can reasonably be expected to follow the same qualitative trend for our SOI photonic chips. Although silica beads do not reproduce the exact topography of the nanostructured resonators, they provide a chemically comparable oxidised surface and therefore a relevant model for assessing electrokinetic modification.

In fact, this shift towards less negative values indicates that BSA adsorption effectively screens or partially masks the native oxidation layer responsible for the negative surface charge of SOI. Additionally, the fact that the beads were resuspended in fresh deionized water prior to measurement confirms that this reduction does not arise from ionic screening but from the presence of the adsorbed protein layer itself.

Qualitatively, the introduction of BSA surface treatment led to a noticeable change in trapping behaviour across all the tested trappable strains. In untreated conditions, decribed earlier in the chapter, many bacteria approached the resonator surface without producing any detectable perturbation of the transmitted signal, indicating that they remained effectively outside the interaction range of the evanescent field. After BSA treatment, such approaches were more frequently accompanied by measurable transmission perturbations, suggesting that bacteria were able to reach closer proximity to the surface and interact with the optical field.

However, these interactions remained predominantly transient, as shown in fig. 4.5. The observed perturbations were typically of low amplitude and short duration, with the signal rapidly returning to its baseline value, indicating that stable trapping was still not consistently achieved.

In addition, the few bacteria that were trapped exhibited improved stability, with fewer instances of spontaneous detrapping while the optical field was maintained. These observations collectively suggest that BSA treatment reduces, but does not eliminate, the electrostatic barrier at the SOI-bacteria interface.

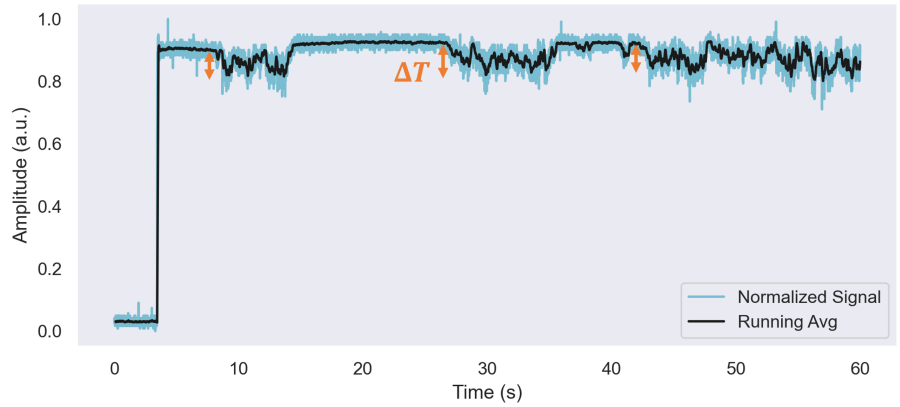

Figure 4.5: Representative example of a normalized transmitted signal (blue) recorded on a BSA-treated resonant photonic chip with E. coli EC11 suspended in deionized water. A running average (black) is added to improve readability of the high-frequency oscillations. The trace shows several short-lived transmission perturbations corresponding to bacteria approaching the evanescent field and briefly affecting the cavity resonance. The perturbations remain weak, with ΔT values below about 10% of the signal maximum, and the signal returns to its baseline within a few seconds, indicating transient and unstable trapping.

This interpretation is consistent with the electrokinetic measurements. Using the expression introduced in equation (4.2), the electrostatic repulsive force can be re-estimated by replacing the surface zeta potential of untreated silica (~ -60 mV) with that measured for BSA-treated silica (~ -34 mV). Since the force scales with the product $\zeta_{\text{bact}}\zeta_{\text{surface}}$, this corresponds to a reduction of the electrostatic repulsion by approximately $40-45\%$. For the range of bacterial zeta potentials measured in this study, this yields a repulsive force on the order of $6-30$ fN at relevant trapping distances.

Although this reduced interaction remains significantly smaller in magnitude than the optical forces (~ 1 pN), it is sufficient to modulate the effective approach distance and interaction time within the evanescent field. This provides a consistent explanation for the increased frequency of detectable interactions and the partial improvement in trapping stability observed experimentally.

Taken together, ellipsometry and zeta potential measurements confirm that BSA forms a partially stable adsorbed layer on oxidised silicon surfaces and significantly reduces their effective negative surface charge in aqueous conditions. However, this modification alone is not sufficient to ensure consistent trapping across all strains. These observations therefore motivated the implementation of additional strategies, in particular modification of the suspension medium, which are discussed in the following section. As a result, the present findings should be interpreted as indicative of a partial mitigation of electrostatic repulsion rather than a complete suppression of the underlying mechanism.

4.5.3 Limitations of BSA functionalization.

Despite its effectiveness in reducing surface charge, the use of BSA introduces practical constraints arising both from its physicochemical nature and its biological origin. Being a naturally derived protein, BSA may exhibit inherent variability depending on properties that are usually not

fully disclosed by suppliers including its source, extraction, purification, and storage. As a result, different BSA batches may behave differently.

Because the coating relies on adsorption of a protein solution prepared by the user, the final surface state also depends on solution quality and handling conditions. Small variations in concentration, incomplete dissolution, or ageing of the solution may influence the degree of surface coverage. For this reason, solutions were prepared according to a standardized protocol, stored for limited durations, and replaced regularly. While these precautions minimise variability, they cannot completely eliminate it.

In addition, dissolution and injection of protein solutions can introduce small air bubbles. In confined microfluidic geometries, such bubbles may persist if not fully removed prior to experiments. Although filtration and resting of the solution reduce this effect, careful inspection of the channels remained necessary. While the visualisation system in our optical bench can be moved to inspect different regions of the chip, its range of motion is limited and does not cover the entire fluidic channel, preventing a thorough inspection.

Finally, the introduction of an adsorbed protein layer modifies the chemical composition of the channel walls. Once BSA is adsorbed, the surface is no longer in its pristine state; restoring the original electrostatic and chemical conditions may be challenging even after extensive cleaning. These long-term aspects, including potential impacts on surface charge and reproducibility over multiple experimental cycles, are discussed further in the next chapter.

4.6 Modification of the Suspension Medium

In addition to modifying the properties of the chip interface, the physicochemical environment of the bacteria themselves was adjusted. Whereas surface functionalization acts locally at the solid-liquid boundary, changing the suspension medium directly alters the electrostatic and osmotic conditions experienced by the cells before and during their approach to the resonator. This provides a complementary means of tuning interaction forces without modifying the photonic structure.

4.6.1 Choice of Suspension Medium

Tests of medium composition presented here were evaluated based on their effect on the quality of the trapping conditions and were first performed on unfunctionalized chips in order to isolate the effect of ionic conditions from that of the surface coating. Only once the influence of the suspension medium had been characterised independently were combined conditions evaluated. The modification of the suspension medium was motivated by two main considerations.

First, the initially used medium was deionized water, which has an ionic strength on the order of 10^{-7} M and therefore provides negligible counter-ions to screen surface charges. In such low-ionic environments, the electric double layer surrounding each bacterium can extend over distances on the order of ~ 1 μm, causing electrostatic repulsion between the negatively charged bacterial envelope and the negatively charged silicon dioxide surface to act over comparably large distances during near-surface approach.

Second, as mentionned earlier in the chapter, suspending bacteria in pure water imposes a strong imbalance between the ionic content inside the cytoplasm and that of the external medium,

which increases internal pressure and modifies membrane tension and envelope structure. Therefore, reducing the contrast in ionic concentration between the interior and the exterior of the cell is expected to reduce these effects.

In this sense, initial trials were conducted using Lysogeny Broth (LB Miller, containing 10 g/L NaCl), a nutrient-rich culture medium with peptides, yeast extract, and sodium chloride. Bacteria were grown on solid agar plates but resuspended in liquid LB prior to introduction into the optofluidic chip. The underlying hypothesis was that LB could simultaneously provide ionic strength through its salt content and physiological support through its nutrients, potentially extending the viable experimental time window.

To prepare this medium, commercial LB powder was dissolved in deionized water according to supplier specifications and then autoclaved to ensure sterility. This results in an NaCl concentration of approximately 170 mM in the undiluted broth. As an additional precaution, the solution was stored at room temperature, allowing any potential contaminants to grow and thus facilitating their visual detection before use; in which case the solution was discarded and re-prepared. For trapping experiments, a portion of sterile LB solution was mixed with deionized water to progressively decrease nutrient concentration while monitoring bacterial behaviour. Specifically, fractions of 10% and 20% LB (corresponding to approximately 17 mM and 34 mM NaCl, respectively) did not produce a noticeable improvement in trapping stability, as evaluated by the frequency of successful near-field trapping events across multiple trials, relative to pure water conditions.

However, when testing higher LB concentrations, a different undesired behaviour started emerging. When suspended in LB fractions $\gtrsim 30\%$ ($\approx 51mM$ of $NaCl$), bacteria frequently non-specifically adhered to the surface of unfunctionalized chips in random locations, including the vicinity of the resonating cavity, preventing controlled near-field trapping. This sticking occurred even in the absence of intentional SOI surface functionalization.

This behaviour can be explained by the composition of LB, which contains peptides and other organic molecules, many of which are partially hydrophobic and therefore amphiphilic. These species can readily adsorb onto silica surfaces and form a passivating layer, effectively acting as blocking agents and modifying the surface chemistry of the SOI interface. As a result, both ionic screening and surface modification may occur simultaneously, and their respective effects cannot be evaluated independently. It was therefore not possible to attribute this behaviour to a specific constituent.

Moreover, while the NaCl concentration in LB is well defined for a given formulation, peptide and yeast extract components can vary in composition and concentration between manufacturers and batches, reducing the overall reproducibility of experiments that rely on this complex medium. For these reasons, and because the primary motivation was to tune ionic conditions rather than provide nutrient support, the use of LB was deemed unsuitable for controlled electrostatic studies, and subsequent trials were conducted with a simpler, chemically defined ionic solution.

To test a simplified medium, we opted for phosphate-buffered saline (PBS), which is a water-based salt solution containing defined concentrations of sodium chloride (137 mM), phosphate salts ($\sim$ 11.9 mM total), and potassium chloride (2.7 mM), which is widely used in microbiology to maintain isotonic conditions (osmolarity $\approx$ 315 mM) and to limit osmotic stress associated with abrupt changes in external ion concentration [228]. Its defined composition and commercial availability as a sterile stock solution reduce handling steps and improve reproducibility relative to complex nutrient media.

In our experiments, commercially available PBS at nominal $1\times$ concentration (ionic strength $\approx$ 175 mM when accounting for all ionic species) was diluted by 50% in deionized water (obtaining an ionic strength of $\approx$ 88 mM). This intermediate ionic strength lies in the same order of magnitude as the highest LB dilutions previously explored, enabling direct comparison while

providing a chemically defined environment. Preliminary tests indicated that this 50% PBS mixture was sufficient to suppress the undesired behaviours observed in pure water and at moderate LB fractions, and therefore additional PBS concentrations were not systematically investigated. All suspensions were freshly prepared in this 50% PBS mixture immediately prior to trapping experiments.

In contrast to LB-based suspensions, no non-specific adhesion of bacteria to SOI surfaces was observed in this buffered medium, for either normal or BSA-functionalized chips. This indicates that the sticking previously encountered is likely associated with the organic components of LB rather than with its salt content. The 50% PBS mixture was therefore retained for all subsequent experiments. The impact of this medium change on both trapping behaviour and bacterial surface charge is quantified in the following subsection.

4.6.2 Effects of Suspension Medium Change

In order to quantify the electrical screening provided by the 50% PBS on bacteria, we measured their zeta potential in these conditions to compare them with the prior values measured in water. This comparison is provided in fig. 4.6.

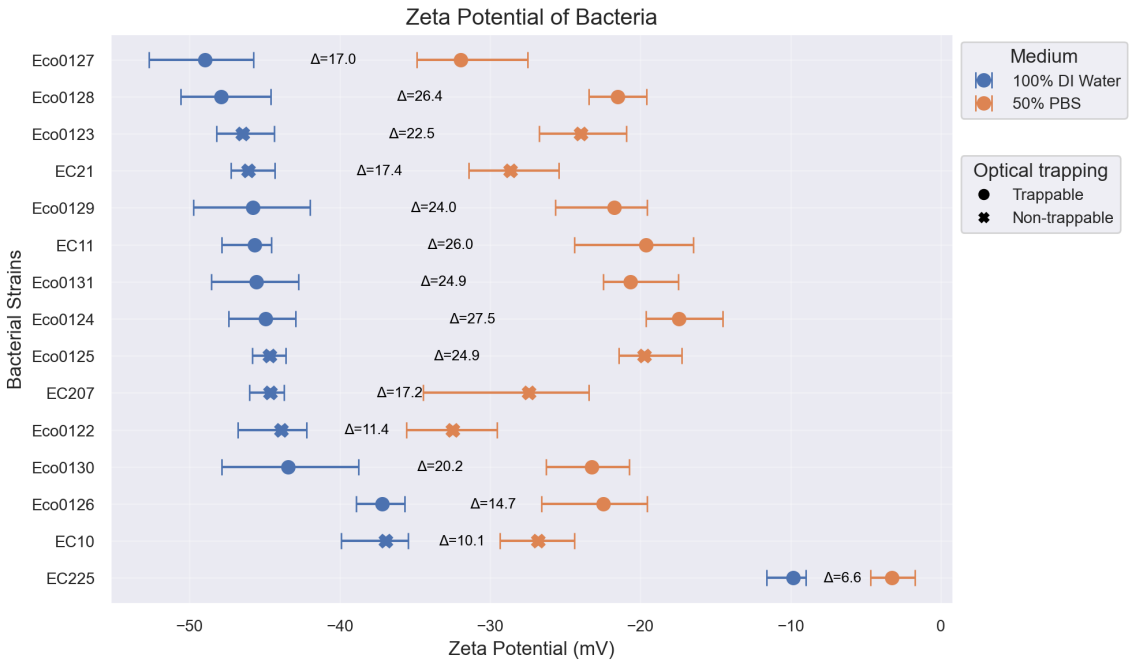

Figure 4.6: Zeta potential measurements for bacterial cells in deionized water (blue) and in 50% DIW 50% PBS mixture (orange). Marker shape indicates optical trappability for each strain, also summarized in table 4.1. Error bars represent the full range (min/max) of consecutive measurements used to compute the averages. Δ values indicate, for each strain, the potential difference between the measurement in both solutions.

Zeta potential measurements performed in the 50% PBS medium show a systematic reduction in the magnitude of the negative charge for all strains tested. This reduction ranged from about +6.6 mV to +27.5 mV, with a mean change of approximately +19.4 mV. In other words, every strain became measurably less negative in the buffered medium. This indicates a significant electrostatic screening effect, which is expected to reduce repulsive interactions with the SOI surface, especially when combined with the BSA-induced reduction of the surface charge.

This effect can be quantified using the expression introduced in equation (4.2). In the PBS medium, the bacterial zeta potentials are typically shifted toward values closer to -20 to -30 mV. When combined with the untreated SOI surface (~ -60 mV), this already reduces the electrostatic repulsion by roughly a factor of 2 compared to the situation in deionized water. When considering instead a BSA-treated surface (~ -34 mV), the product $\zeta_{\text{bact}}\zeta_{\text{surface}}$ is further reduced, leading overall to a decrease of the electrostatic force by approximately a factor of 3 to 4 compared to untreated conditions.

In addition, the presence of ions in the PBS solution drastically reduces the Debye length, bringing it from the micrometric range in deionized water down to a few nanometres. As a result, the exponential term in equation (4.2) strongly suppresses the interaction at the typical trapping distances (~ 100 nm). Altogether, these combined effects reduce the electrostatic repulsion from the $10-50$ fN range in deionized water to sub-femtonewton values (below 10^{-1} fN), rendering it negligible compared to the optical forces (~ 1 pN) in the vicinity of the resonator surface.

Indeed, we experimentally observed a major improvement in trapping reproducibility. The frequency of the inconsistent behaviours described earlier decreased noticeably when using the 50% PBS medium, and inconsistencies became rare when the PBS medium was combined with the BSA surface treatment. In contrast to the weak and transient perturbations observed with BSA alone, stable trapping events were now consistently observed across repeated experiments, as illustrated in fig. 4.7. In these conditions, the transmitted signal exhibits large and sustained shifts, with ΔT reaching approximately 50% of the baseline signal with trapping events persisting over the full duration of the recorded signals (up to ~ 90 s in fig. 4.7), and experimentally maintained for several minutes in practice until voluntary release by manually turning the laser off. Therefore, these factors indicate strong and persistent interaction with the evanescent field.

In addition, live monitoring suggested that the onset of osmotic effects, as judged by changes in cavity signal associated with cell swelling, occurred substantially later for samples in the buffered medium than for those in pure deionized water. This delay was variable and depended on experimental details, but it was typically on the order of $20-30$ minutes, which provided a significantly larger time window for stable trapping.

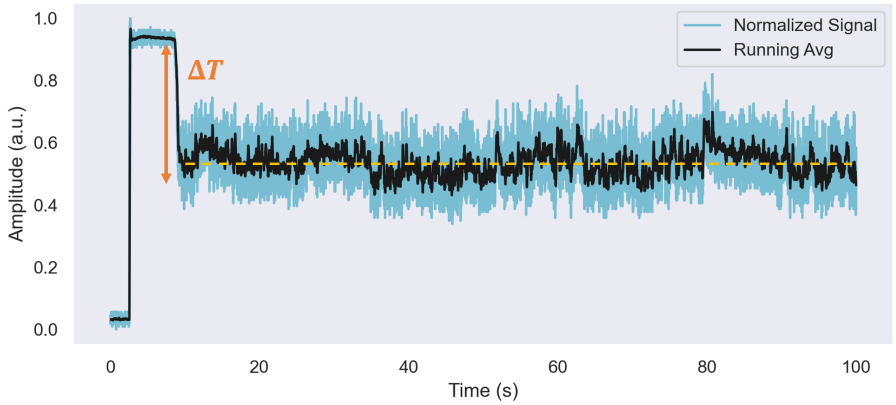

Figure 4.7: Representative example of a normalized transmitted signal (blue) recorded on a BSA-treated resonant photonic chip with E. coli EC11 suspended in a mix of 50% deionized water and 50% PBS. A running average (black) is added to improve readability of the high-frequency oscillations. The trace shows a typical stable trapping event, characterized by a sustained transmission shift with $\Delta T_{EC11} \approx 50\%$ of the baseline signal for this species, and small fluctuations around the average amplitude (yellow line)associated with the motion of the trapped bacterium.

Nevertheless, the change in zeta potential following this medium change did not produce a clear trend seperating bacterial strains according to trappability. It did not either change experi-

mental trappability of strains classified as untrappable (*cf. table 4.1*), further confirming that the origin of this device sensitivity is independant of electrokinetic interactions alone.

Lastly, it is important to note that the refractive index of this 50% PBS solution was measured using an Abbe refractometer, resulting in a value ($\sim$ 1.3345 at 24°C) that is almost identical with water ($\sim$ 1.3325 at 25°C), indicating that there would be no effect on the optical performance of the device. This was confirmed by the optical characterization of resonating cavities both in 100% water and in 50% PBS, before and after surface functionalization, and the impact on the values of the resonance wavelength λ_0 and the quality factor Q were very negligeable.

Taken together, these observations support the conclusion that introducing a controlled ionic background is an efficient means to improve trapping reproducibility. This improvement arises both from electrostatic screening of surface charges, which reduces repulsive interactions, and from a delayed onset of osmotic effects, which extends the time window for optical trapping experiments.

4.7 Conclusions and Perspectives

This chapter addressed the inconsistent interactions observed between bacterial cells and the SOI photonic resonator during the early stages of this PhD. Because optical trapping occurs within the evanescent field at nanometric distances from the chip surface, the forces experienced by approaching bacteria play a central role in determining whether confinement is achieved. In particular, we examined the contribution of interfacial electrostatics through the electrical state of both the SOI interface and the surrounding suspension medium.

This study revealed that both the oxidised SOI surface and the investigated *E. coli* strains carry a negative surface charge in deionized water, resulting in electrostatic repulsion in the range of $10-50$ fN during near-surface approach. The extent of this interaction was reduced by screening the charges on either side. This was achieved by coating the SOI surface with bovine serum albumin on one hand, and by modifying the bacterial suspension medium to a phosphate-buffered saline solution on the other. These changes, implemented separately and especially in combination, led to a measurable decrease in the repulsion force to sub-femtonewton levels. This progressive reduction of the electrostatic barrier correlates directly with the observed improvement in trapping stability. They were therefore adopted as the default working conditions for the main optical trapping experiments presented in the remainder of this work.

However, neither modification alone nor combined eliminated strain-dependent differences in trapping behaviour. This indicates that while electrostatic repulsion constitutes a significant but not limiting barrier to near-surface confinement under low ionic strength conditions, it is not the sole parameter governing trappability. Hydrodynamic effects within the fluidic circuit, steric interactions between particles, intrinsic mechanical properties of bacterial envelopes, and active mechanisms such as flagellar motility may also contribute to the observed variability.

Several limitations remain. BSA adsorption provides a convenient and reversible means of modifying the interface, but it does not constitute a permanent or molecularly defined functionalization. Likewise, changes in ionic strength simultaneously affect surface charge, bacterial charge, and osmotic conditions, making it difficult to isolate individual contributions. A more systematic and quantitative exploration of ionic environments, combined with modelling of electrostatic and optical forces, would enable a more complete description of the trapping landscape.

Future work could also investigate bacterial properties that are intrinsic and independent of interfacial electrostatics, yet may influence mobility within the microfluidic channel and inter-

fere with close approach to the resonator surface. In particular, flagellar motility may oppose optical confinement at short distances. More generally, studying mechanical or structural differences between strains could reveal biological characteristics that account for the strain-dependent untrappability not resolved by the electrokinetic analysis conducted here. Such complementary approaches would help disentangle purely optical effects from interfacial and mechanical contributions.

The following chapter builds upon these controlled conditions to evaluate the reproducibility of the optical traps and to assess their viability as an intra- and inter-strain differentiation tool.

5 Optical Signals Analysis

In this chapter, we discuss the results regarding the trapping measurements, covering the experimental protocol from sample preparation to signal acquisition, as well as the computational methods used for signal treatment and their interpretation.

Contents

5.1 Introduction . . . 111
5.2 Data Collection . . . 111
5.2.1 Experimental Protocol . . . 111
5.2.2 Technical Considerations & Limitations . . . 113
5.2.3 Cavity State Changes . . . 113
5.2.4 Optofluidic Chip Cleaning . . . 115
5.3 Signal Pre-Processing Methodology . . . 119
5.4 Data Analysis: Methods . . . 123
5.4.1 Statistical Representation . . . 123
5.4.2 Reproducibility Scores . . . 125
5.4.3 Supervised Classification Framework . . . 127
5.5 Signal Analysis: Results . . . 128
5.5.1 Intra-Strain Variability . . . 128
5.5.2 Inter-Strain Discrimination . . . 132
5.6 Optical Determination of Strain Refractive Index . . . 135
5.7 Genomic Correlation . . . 140
5.8 Conclusions and Perspectives . . . 141

5.1 Introduction

Following the investigation of bacterial surface behaviour presented in the previous chapter, we established experimental conditions that enable the reliable and repeatable trapping of selected *E. coli* strains using 1D photonic crystal cavity optofluidic chips. Achieving this level of control was a necessary step, as it provides a stable framework in which sources of variability unrelated to the trapping process itself are minimised. With reproducible capture now ensured, we extend the scope of this study to another aspect of reproducibility, namely the interpretation of the signals produced by individual trapped bacteria.

Although the trapping conditions discussed previously, including surface treatment and suspension medium, were kept identical across experiments, each bacterium generates its own optical response while confined within the trap. This raises the question of how consistent these single-cell signals are when measured across individuals originating from the same bacterial strain and grown under identical conditions. In this chapter, we further detail the experimental protocol used for the collection of these signals and compare the responses obtained from different individuals belonging to the same strain in order to characterise potential variations between them. In addition, the optical signatures recorded during trapping are analysed to extract quantitative information about the trapped cells, including an estimate of their effective refractive index. By analysing these single-cell signals, we assess the reproducibility of the optofluidic chips as a sensing platform and discuss possible interpretations of any observed differences.

In parallel, the outcome of the trapping experiments provides a qualitative classification of bacterial strains as trappable or untrappable, independent of the subsequent signal analysis. This classification is then used in a comparative genomic study to explore which bacterial properties may govern the selectivity of the device. By relating trappability to genomic features across strains, this approach aims to identify common biological or physical characteristics shared by trappable bacteria and absent in those that cannot be trapped, thereby offering a complementary perspective on the origins of the observed selectivity of our chips.

5.2 Data Collection

5.2.1 Experimental Protocol

For all the data that will be presented in this chapter, the trapping measurements were conducted using the same optofluidic chip and followed the same experimental procedure. Typically, the protocol starts several hours before the measurement. Bacterial cultures were grown on Tryptic Soy Agar (TSA) plates and incubated at 37°C for approximately $16-20$ hours prior to the experiment. Cells were then collected directly from these plates. This approach was chosen to ensure reproducible physiological conditions during the trapping measurements, while avoiding additional variability introduced by liquid culture conditions.

Another step of the protocol initiated hours before the measurement is surface treatment of the SOI cavity with bovine serum albumin (BSA). As explained in the previous chapter, the optical resonator is coated with BSA to minimise repulsive interactions with bacterial cells. This is achieved by filling the fluidic channel with BSA for multiple hours, i.e., overnight or for 3 to 4 hours prior to experiments performed in the morning or afternoon respectively. This ensures that the surface remains saturated with BSA.

Each data collection round starts by flushing the BSA solution from the fluidic channel with deionised water (DIW), in order to remove excess protein in solution while preserving the ad-

sorbed layer on the surface. During this rinsing step, the resonator transmission spectrum is measured to retrieve its characteristic values, namely the resonance wavelength λ_0 and quality factor Q. Because the refractive index of DIW is comparable to that of the working suspension medium (50% DIW / 50% PBS), this measurement provides an accurate reference for subsequent trapping conditions. The importance of redoing this characterisation for each experiment, despite all measurements being taken on the same cavity, will be discussed in the following section along with other important conditions and limitations of this protocol. Once the resonance is determined, the input excitation laser is tuned to λ_0 and operated at its maximum optical power of 20mW.

Next, bacteria are retrieved from the incubator. A few colonies (3 to 8) are collected from the Petri dish and suspended in a vial containing 1 mL of the suspension mix presented in the previous chapter, consisting of 50% DIW and 50% phosphate-buffered saline (PBS) by volume. After thorough mixing to disperse the cells originating from each colony in the solution, the resulting suspension roughly corresponds to a bacterial concentration on the order of $10^7 - 10^8$ cells$\cdot$mL^{-1}, although this value remains an order-of-magnitude estimate based on the number of colonies resuspended and was not independently quantified. The vial is then directly connected to the tubing of the fluidic circuit attached to the chip to inject the bacteria. During the input vial change, a small air bubble can be manually introduced into the tubing, by gently tapping its outer opening, to create a visual marker, similar to a wave front, for the advance of the new fluid. Injection pressure is adjusted to the cross-sectional dimensions of the fluidic channel to ensure filling in an appropriate time. For example, the chip used here has a fluidic canal whose cross-section dimensions are $15 \times 750\,\mu m^2$, and the bacterial suspension was injected with a pressure of $150 - 250\,mbar$ using a pressure-based flow controller (Fluigent system; *cf.* Chapter 2 for details on the fluidic setup).

After a few minutes, when the air bubble marker exits the optofluidic chip at the output connector, indicating that the fluidic channel above the chip is completely filled with the bacterial suspension, the applied pressure is set to zero, resulting in a rapid stop of the flow. This allows suspended bacteria located within a few micrometres of the resonator to interact with the optical field. If the flow is maintained, hydrodynamic drag can hinder the stablity of optical capture. This can be verified experimentally by reapplying pressure values (> 30 mbar) during a trapping event, which results in a progressive displacement of the bacterium downstream while it remains partially confined near the cavity. At higher pressures (> 100 mbar), the hydrodynamic drag overcomes the optical trapping force, leading to the forced detachment and downstream transport of the bacterium.

Once a bacterium is trapped, the cavity's transmitted signal is recorded on the oscilloscope for approximately 60 seconds. After the recording is saved, the bacterium is released by turning off the input laser, thereby deactivating the trap as the cavity is no longer optically excited. A small pressure of $5 - 10$mbar is then reapplied for $10 - 20$ seconds to slightly advect the fluid, ensuring that new cells are brought into the vicinity of the cavity so that different individuals are probed. When the pressure is returned to zero and the laser is re-activated, the trap-record-release cycle is repeated until a sufficient number of cells have been measured. In this work, 20 to 30 individual cell traces were collected for each *E. coli* strain studied. This corresponds to an experiment duration of approximately 90 to 120 minutes per strain, including preparation and handling steps.

Once measurements with a given strain are complete, the fluidic canal is flushed at high pressure with deionised water for 5 to 10 minutes. This step is critical to remove residual cells, debris, or small air bubbles from the channel that could locally obstruct or perturb the flow near the cavity in subsequent measurements or cause cross-contamination between strains. A brief flush with BSA solution (3.33 mg/mL) is then performed as a precautionary step to replenish the surface coating, which may be partially depleted during prolonged measurements. This ensures that comparable surface conditions are maintained between experiments before reapplying the procedure described above with a different strain.

As mentioned throughout the manuscript, the main challenge of this project is that certain strains of bacteria are untrappable under the conditions described here. This is determined experimentally by following the same procedure. If no trapping event is detected on the transmitted optical signal after one hour, despite visually observing on camera that multiple cells repeatedly approach the cavity without exhibiting any interaction signatures, such as changes in trajectory, speed, or residence time near the resonator, the strain is deemed untrappable under these experimental conditions. This criterion is applied while keeping the optical power, flow conditions, and alignment identical to those used for successfully trapped strains, ensuring that the absence of trapping reflects an intrinsic limitation rather than an experimental artefact. In case of any experimental ambiguities, such as sparse weak transmission signal changes, the experiment is repeated on another day with a different culture of the same strain to clarify whether such weak signatures originate from biological interactions or from measurement noise.

This experimental protocol is schematically summarised in the illustration in fig. 5.1. The dataset analysed in this chapter was collected using a single optical resonator from the same optofluidic chip over a period of approximately one month. During this time, all bacterial strains were tested to determine their trappability under the conditions described above. When applicable, a database of trapping signals was built for subsequent analysis.

The duration of the overall experimental campaign could be extended to take into consideration the several optofluidic chips were fabricated and tested, and the number of technical issues and experimental setbacks that were encountered. These difficulties exposed practical limitations of the setup and protocol: some informed subsequent refinements of the experimental procedure, while others remain unresolved. These limitations are discussed in detail in the following section.

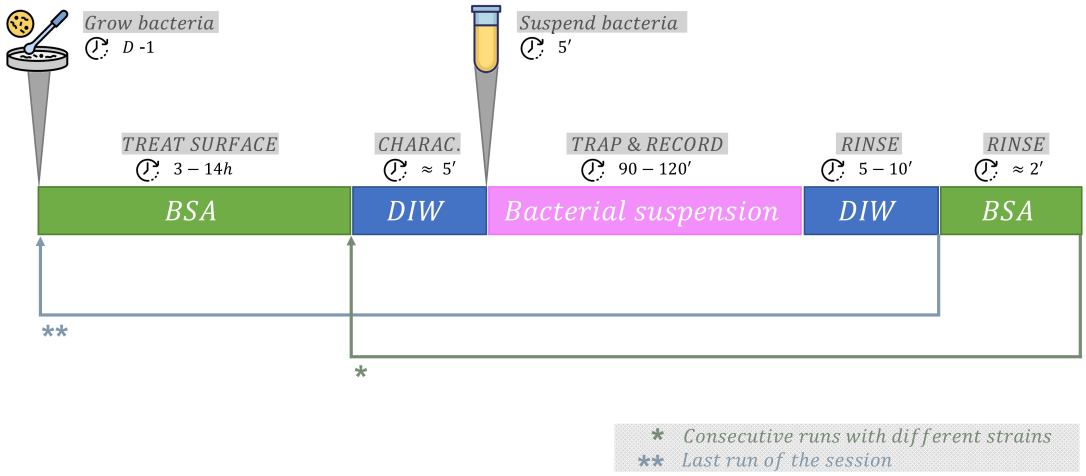

Figure 5.1: Schematic illustration of the experimental protocol used for optical trapping measurements. The protocol is organized around the contents of the fluidic circuit (central bar), with step names and durations shown above.

5.2.2 Technical Considerations & Limitations

5.2.3 Cavity State Changes

Although all measurements were performed on the same photonic chip, a systematic re-characterization of the cavity resonance was required prior to each experiment, as described in the experimental protocol. This precaution was motivated by the consistent observation of small but

non-negligible shifts in the cavity resonance wavelength, typically on the order of a few nanometers. These shifts are significantly larger than the resonance linewidth (full width at half-maximum, FWHM), which is approximately 0.45 to 0.5 nm, making them substantial relative to the cavity response. Variations were also observed in the quality factor. Such changes directly impact the optical conditions under which trapping experiments are performed and therefore must be accounted for to ensure consistent experimental conditions.

Figure 5.2 shows the evolution of the characteristic values λ_0 and Q of the resonating cavity used for the data collection of the database studied in this chapter across different experimental runs. The observed variations do not follow a monotonic or systematic evolution. Instead, they indicate run-to-run fluctuations of the cavity state, suggesting that the optical properties of the cavity are sensitive to experimental conditions that vary between measurements rather than to a gradual or irreversible drift of the device.

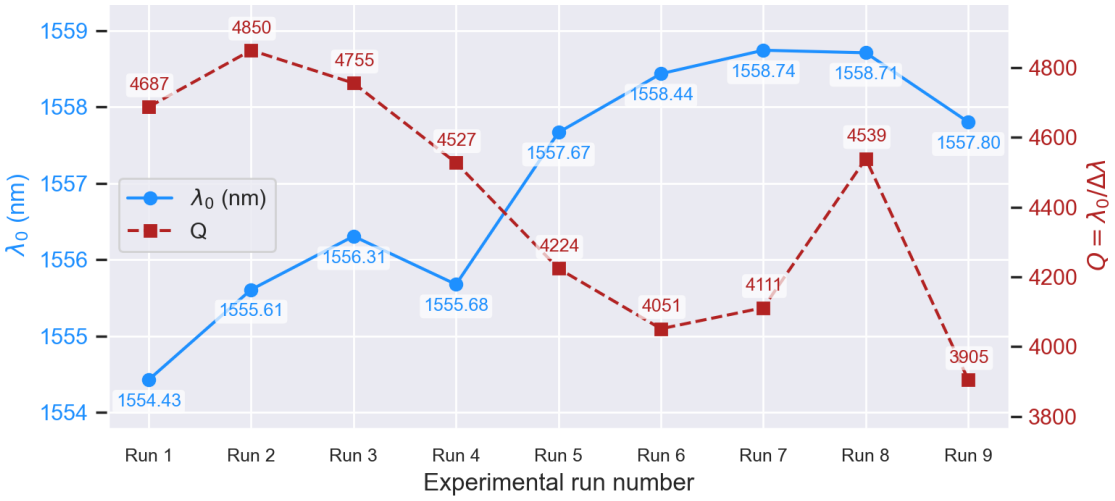

Figure 5.2: Evolution of the characteristic values of the CMT3 resonating cavity used for all trapping experiments over consecutive experimental runs, including runs performed on the same day as well as others acquired on different days.

These variations are most likely related to subtle variations in the optical coupling conditions between the fiber and the on-chip waveguide. Although the chip itself was not repositioned, the input fiber was occasionally retracted and re-approached between experimental runs in order to prevent damage to the tapered tip. As a result, small variations in the fiber-to-waveguide distance, typically on the order of few micrometers ($5-15\mu$m, *cf.* fig. 2.13), are expected.

Such changes modify the coupling strength between the waveguide and the cavity, and therefore the rate at which energy is exchanged with the cavity mode. This is commonly described by the external quality factor Q_{ext}, which accounts for losses due to coupling to the waveguide. The total quality factor Q_{total} measured experimentally from fitting the resonance linewidth results from the combination of intrinsic losses within the cavity and coupling losses, and is expressed as:

$$\frac{1}{Q_{\text{total}}} = \frac{1}{Q_{\text{int}}} + \frac{1}{Q_{\text{ext}}} \tag{5.1}$$

Here, Q_{int} represents the intrinsic quality factor of the cavity, determined by material absorption, scattering, and radiation losses, while Q_{ext} depends on the coupling conditions [229]. Variations in coupling can thus lead to measurable changes in the resonance linewidth and depth, therefoe changing the Q value obtained from spectrum fitting. In addition, slight modifications of the resonance lineshape may result in small apparent shifts in the fitted resonance wavelength.

Another plausible explanation concerns the evolution of the BSA adsorption layer over time and across repeated fluidic cycles involving different solution flushes through the channel. Under these conditions, the protein layer may undergo partial desorption or rearrangement, which could locally alter the effective refractive index in the vicinity of the cavity [227]. Protein adsorption is also known to modify surface wettability, which may influence liquid infiltration and wetting within nanoscale structures [227]. These effects are difficult to quantify and were not directly monitored during the experiments, as no measurement of the protein layer thickness or homogeneity under flow could be performed within the sealed fluidic cell.

Additional factors may contribute to the observed variability. These include small temperature variations, which were not actively controlled, as well as residual contamination effects, which are discussed later. Given the strong sensitivity of the cavity resonance to its local dielectric environment, the combined influence of all these factors justifies the need for a full cavity characterization prior to each data collection round.

This evolution of the cavity optical properties was taken into account when comparing data acquired across different experimental runs. The recorded signals were adjusted during post-processing to reflect the state of the cavity at the time of acquisition. The corresponding correction procedure is described in detail in the signal processing section.

5.2.4 Optofluidic Chip Cleaning

Previous Cleaning Methods

Since the same optofluidic chip is used over extended periods spanning several weeks to months, maintaining a consistent surface state is essential to ensure reproducible and comparable measurements over time. This consistency is partially preserved by regularly reapplying the BSA surface coating in order to maintain identical surface functionalization conditions. However, prior to any coating step, the chip surface itself must also be cleaned periodically to prevent the accumulation of biological cells or molecular residues originating from the suspension medium.

In earlier experiments performed with the previous fluidic design based on a removable static fluidic pool, surface cleaning was routinely performed by rinsing the entire chip with water and diluted detergent solutions containing SDS. In more severe cases, a piranha solution, typically composed of concentrated sulfuric acid (H_2SO_4) and hydrogen peroxide (H_2O_2) in a volumetric ratio of approximately 2:1, was used for approximately five minutes to remove persistent organic residues. This approach is no longer applicable for the present integrated optofluidic chip design for several reasons.

First, the current chip was specifically designed to remain permanently installed on the optical bench in order to minimize optical misalignment. As a result, removing the chip to take it to a chemical laboratory where the use of piranha solution is authorized is strongly discouraged. Moreover, performing piranha cleaning in situ would require disconnecting and relocating the entire fluidic circuitry, including tubing and pumps, to allow safe injection of the solution into the channel. In addition to increasing the risk of mechanical damage and misalignment, this configuration would be incompatible with the significant gas releases associated with piranha reactions, which requires operation in an open and well-controlled environment.

In addition, piranha solution slowly etches silicon-on-insulator substrates under prolonged exposure. While this etching can be reasonably controlled for simple photonic chips that are directly immersed in the solution and subsequently subjected to a rapid and abundant water rinse, achieving precise control over the effective exposure time within an enclosed and integrated fluidic channel would be considerably more difficult. Factors such as dead volumes, diffusion-limited exchange, and uncertainty regarding complete removal of the solution make it challenging to ensure uniform

exposure and full removal of the reactive mixture. This increases the risk of unintended substrate degradation or structural damage to the chip.

More importantly, piranha cleaning is fundamentally incompatible with the materials used in the new optofluidic chip. Although the fully crosslinked SU-8 photoresist employed to define the fluidic channel exhibits partial resistance to piranha solution, extended exposure has been reported to induce oxidation, microcracking, and eventual delamination from the underlying substrate [230]. The consequences are even more critical for other components of the system. The epoxy-based UV-curable adhesive used to bond the glass coverslip that seals the fluidic channel is particularly susceptible to chemical attack and would rapidly degrade under exposure. The silicone tubing used for fluid delivery is comparatively more chemically robust, but prolonged or repeated exposure to such highly oxidative solutions could nevertheless lead to gradual degradation of the material [231]. While the tubing could in principle be replaced, unsealing the glass coverslip would irreversibly compromise the integrity of the chip.

During fabrication, we observed that when the UV-curable adhesive is only partially cured and the glass coverslip detaches, residual glue remains unevenly distributed on the SU-8 surface. This results in a rough and chemically heterogeneous interface that prevents reliable resealing, even when fresh adhesive is fully cured. We therefore anticipate that dissolving the adhesive using piranha solution would lead to a similar failure mode, rendering the chip unusable.

Current Cleaning Methods

Taking all of these constraints into account, and given the limited time available to systematically investigate alternative cleaning strategies and their effects on both the fluidic and photonic structures, a conservative approach was adopted. A comprehensive evaluation would have required the fabrication of a large number of dedicated chips to independently assess chemical compatibility, optical performance degradation, and long-term structural integrity, which was not feasible within the scope of this work. For this reason, the cleaning strategy was intentionally limited in complexity and relied primarily on fluidic rinsing rather than chemical treatments.

The baseline protocol consisted of abundantly flushing the fluidic channel with deionized water between experimental runs. The goal was not to fully sterilize the system, but to remove residual particles, cells, and loosely bound biological material before they could accumulate or reorganize into more stable structures.

This protocol was later complemented by additional operational precautions aimed at preserving the integrity of the fluidic channel during extended periods of use. In particular, the channel was never left stagnant when the chip was not actively used. Instead, a continuous flow at very low pressure, approximately 10 mbar, was maintained in order to ensure constant renewal of the liquid inside the cavity. Depending on the experimental schedule, this consisted of flowing BSA solution overnight prior to a day of measurements, or flowing deionized water between successive runs and during longer periods of inactivity such as weekends.

This continuous rinsing strategy served two main purposes. First, it was expected to reduce the accumulation of debris, cells, or macromolecular aggregates that could otherwise become trapped in dead volumes of the fluidic channel, at channel corners, or in close proximity to the surface. Even at low flow rates, sustained fluid renewal promotes slow but persistent mass transport, which limits the residence time of suspended contaminants and reduces their probability of irreversible adsorption or sedimentation onto the channel walls.

Second, and more critically, continuous rinsing was implemented to prevent drying of the fluidic channel. In earlier experimental protocols using a previous optofluidic chip, the channel was briefly rinsed with deionized water after each run for a few minutes, but the flow was stopped overnight. On one occasion, despite these short rinse, residual phosphate-buffered saline (PBS)

from the suspension medium remained trapped in the channel. As the liquid evaporated, dissolved salts crystallized on the SOI surface and formed large aggregates, as shown in fig. 5.3. In addition to blocking liquid flow within the fluidic canal, the crystallized residues accumulated directly above the optical cavity used for trapping, preventing spatial access to the photonic structure and rendering the chip unusable.

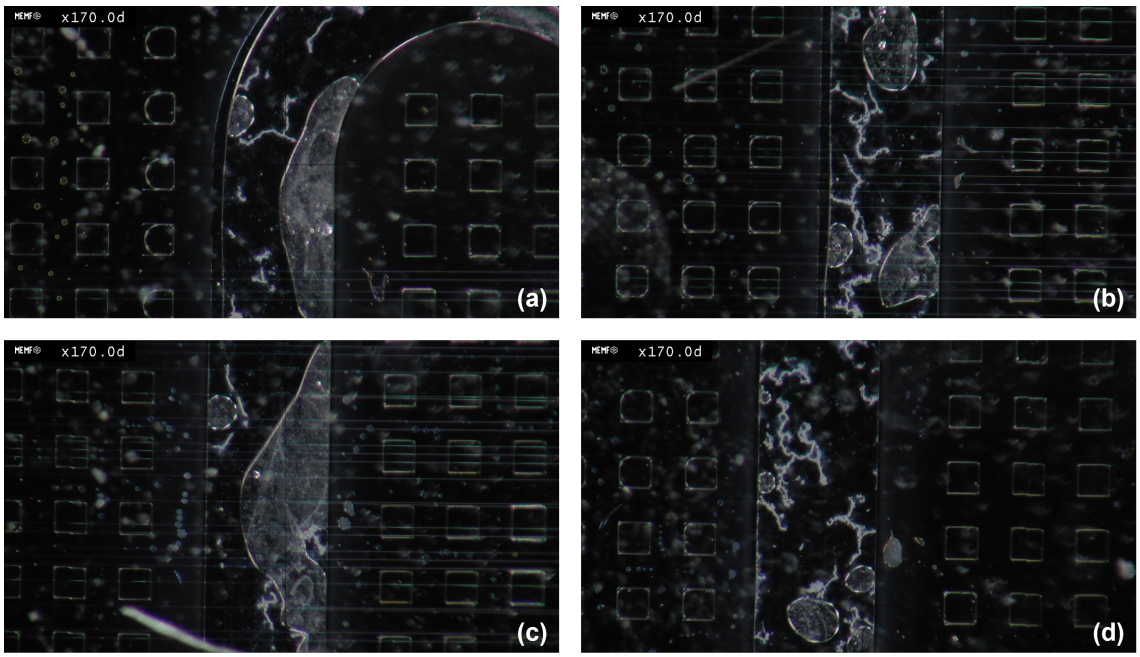

Figure 5.3: Microscope images of different regions of the fluidic canal after phosphate-buffered saline (PBS) residues dried and crystallized inside the canal on the photonic chip surface. Panels (a-d) correspond to distinct locations along the same fluidic channel, illustrating the stochastic spatial distribution of crystallized residues. These residues block liquid flow at different positions within the canal and obstruct the photonic structures, rendering the chip unusable. Stains visible outside the canal regions originate from deposits on the outer surface of the glass coverslip sealing the chip. They result from rinsing steps performed either during chip fabrication or during subsequent cleaning attempts.

Once formed, these crystalline deposits could not be removed by chemical cleaning, as the blockage prevented any effective circulation of cleaning solutions within the canal. Thermal removal of the dried PBS crystals would require temperatures exceeding 800°C due to the high melting point of the constituent salts (*NaCl*, *KCl*, phosphates), far above the thermal limits of SU-8 channels and UV-cured adhesives [231, 232], and was therefore not pursued. Following this failure, the protocol was modified to ensure that the channel is never allowed to dry. For subsequent chips, and as described in the experimental protocol, water was continuously circulated within the chip whenever it was not in use, in order to prevent drying of the fluidic canal.

Despite these precautions, this cleaning strategy eventually proved to be insufficient for long-term operation. The chip used for the data collection presented in this chapter, which was actively used for approximately one month (4 days per week, 8 hours per day) with bacterial suspensions, progressively accumulated large bacterial aggregates on the chip surface along the fluidic channel. These bacterial clumps altered the flow dynamics, particularly in the vicinity of the optical cavity used for trapping. Ultimately, a dense clump that adhered directly to this cavity effectively terminated the usability of the chip.

A sequence of cleaning attempts was carried out in an effort to recover the chip. Initial efforts focused on gentle methods intended to dislodge loosely attached material without introducing

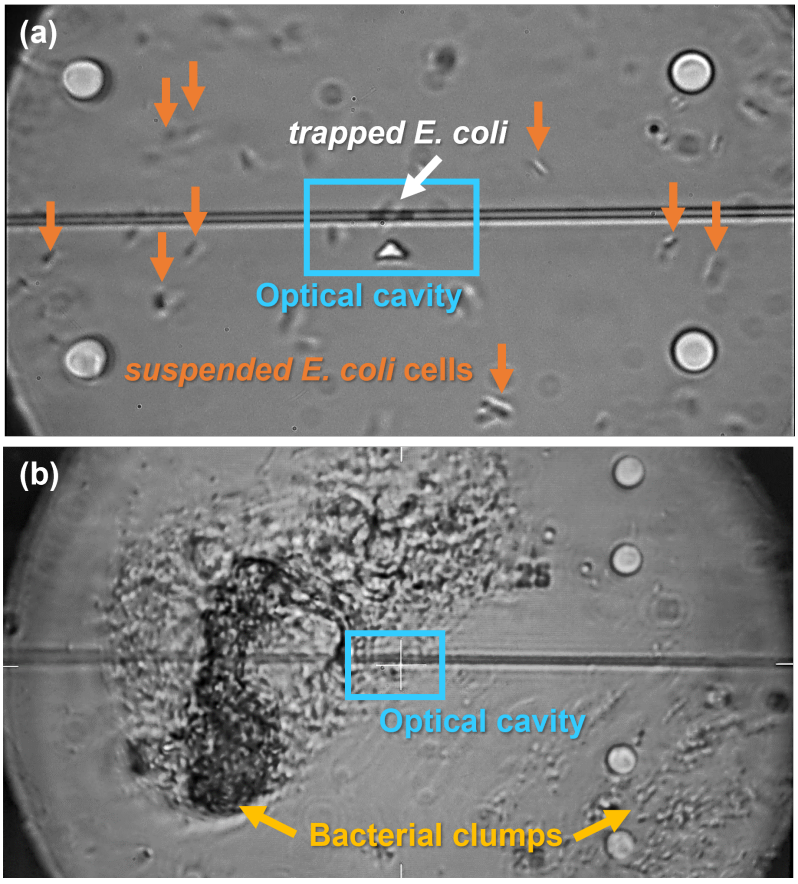

Figure 5.4: Comparison of the area surrounding the same optical cavity (a) before and (b) after the accumulation of bacterial clumps around and above it. In (a), a bacterium is trapped by the optical cavity, while other bacterial cells remain suspended in the liquid medium. The system is at pressure = 0 in the fluidic circuit, and upon a change in pressure, these cells would flow downstream. In (b), bacterial clumps of various sizes and densities accumulate on the chip surface and remain attached despite changes in pressure, particularly over the optical cavity, covering the evanescent field and rendering the cavity unusable.

chemical or mechanical damage. These included flushing in both flow directions at elevated pressures to increase shear stress on the deposits, rinsing with SDS-based detergent solutions as well as high-concentration ethanol rinses were also tested. Additionally, diluted sodium hypochlorite solutions at concentrations below 1% were also tested for rinsing, following established practice by our project collaborators from EPFL, but did not result in noticeable clumps removal.

Once these approaches failed, more aggressive treatments were explored. At this stage, as we have already accumulated almost all the data we needed, preserving the optical performance of the chip was no longer a priority. Therefore, the same sodium hypochlorite solution previously used for short rinses was therefore left inside the channel over multiple nights in order to increase exposure time. This treatment did not result in noticeable biofilm removal.

Further increases in hypochlorite concentration were not immediately pursued as it is a strong oxidizing agent that could degrade other components such as SU-8 structures and UV-curable adhesive. Avoiding such damage was necessary to ensure the possibility of further cleaning tests on this chip.

A final exploratory treatment was tested that included flushing with a concentrated suspension of *E. coli*-specific bacteriophages, kindly provided by our colleague Brunelle ARCHAMBEAUD from CEA/DTIS. Bacteriophages are viruses that specifically infect and replicate within bacteria,

ultimately leading to host cell lysis. Given their high host specificity, this approach was considered a low-probability, last-resort test, aimed at probing whether the aggregates contained viable *E. coli* cells accessible to infection. However, this treatment did not result in any visible changes in the adhered clumps on the channel surface.

Taken together with the failure of the mechanical and chemical cleaning strategies described above, this absence of effect suggests that once established, these persistent aggregates were either largely composed of non-viable bacterial material, such as dead cells or cellular debris, or organized into mechanically stable structures that limited the accessibility of viable bacteria to external treatments.

To conclude, the formation and persistence of such bacterial aggregates ultimately limits the operational lifetime of the chips and introduces variability that cannot be mitigated by simple rinsing protocols as applied throughout this work. This highlights a key limitation of both the current optofluidic platform in handling long-term bacterial accumulation and biofilm formation, and of the cleaning protocol to prevent, reduce or eliminate this accumulation.

These aspects represent an important direction for future work, both to extend chip longevity and to improve the robustness of long-term optofluidic experiments. Within the scope of the present thesis, however, the primary focus remains the analysis of the experimental data acquired using this system. In practice, irreversible bacterial accumulation manifested only at a late stage of the data collection campaign, after 15 bacterial strains had been evaluated for trappability and signals had been successfully recorded for 10 strains. For each of these reliably trappable strains, approximately 20 to 30 one-minute recordings were obtained, forming the dataset used for the signal processing and analysis described in the next sections.

5.3 Signal Pre-Processing Methodology

Typical Trapping Signal

A typical trapping signal of a single bacterium trapped on a CMT3 cavity is shown in fig. 5.5. At the beginning of the acquisition, the transmitted intensity is zero since the probe laser is off, although this part is not always included in the recording. Once the laser is switched on and the cavity is probed using its resonance wavelength in water, the signal enters a regime of stable, high transmission corresponding to the empty cavity, i.e. with no trapped object. Upon trapping of a bacterium, a distinct and abrupt decrease in transmitted intensity is observed. This drop results from the local refractive index contrast introduced by the cell, which modifies the cavity response at the fixed probe wavelength. After trapping, the signal remains centred around a lower transmission level while exhibiting temporal amplitude fluctuations, attributed to the residual motion of the bacterium within the confining optical potential.

Signal Normalization

This typical signal presented in fig. 5.5 is in fact normalised such that the transmission level at resonance prior to trapping was set to unity. This normalisation is performed using `Python` by dividing the entire trace by the value of the transmitted signal's maximum (level before trapping). Therefore, the intensity values are only rescaled by this process, which conserves the relative transmission amplitude shift ΔT induced by the optical trapping of an object within the cavity.

This normalisation translates the signal into a dimensionless scale while referencing it to a common and physically well-defined state, namely the response of the empty cavity at resonance.

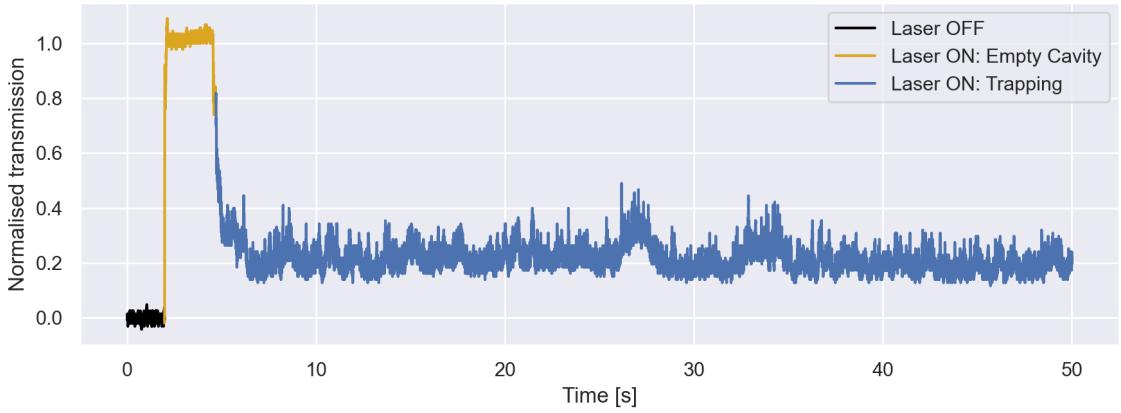

Figure 5.5: Example of a typical transmission signal of a CMT3 optical cavity showing successive phases corresponding to a non-excited cavity in aqueous medium (laser OFF), an empty resonating cavity (laser ON, $\lambda_{in} = \lambda_0$), and the trapping of a single bacterium (laser ON, $\lambda_{in} = \lambda_0$).

By doing so, it compensates for extrinsic experimental factors that are unrelated to the interaction between the bacterium and the cavity and would otherwise interfere with direct comparison between measurements. Such factors include fluctuations in coupling efficiency or drifts in the optical fibre polarisation state. Expressing all signals relative to the empty-cavity baseline therefore enables quantitative comparison across different runs, bacterial strains, and experimental days, while preserving the magnitude and temporal characteristics of the trapping-induced transmission changes. This approach ensures that the subsequent analysis focuses on the effects of bacterial trapping and post-trapping dynamics rather than on experimental artefacts.

Drop Index Determination

To focus the analysis on the effects of bacterial trapping, we restricted attention to the portion of each transmission signal corresponding to the cavity response to the trapped bacterium. The initial parts of the traces, corresponding to the laser-off interval and to the empty-cavity resonance, were excluded from subsequent analysis.

The beginning of trapping was identified using the temporal derivative of a numerically filtered version of the transmission signal. The raw signals, sampled at $f_s = 20$ kHz by the oscilloscope, were low-pass filtered to suppress high-frequency fluctuations while preserving the slower variations associated with transitions between signal phases. The cutoff frequency was empirically set to 3 kHz, but in a small number of cases, when visual inspection such as presented in fig. 5.6(a) showed that the automatically detected transition did not align with the expected phase change, it was manually adjusted within the $2-7$ kHz range. This filtering step is used solely as a numerical tool for phase segmentation: all quantitative analyses are performed on the raw transmission signals once the relevant indices have been determined. The cutoff was chosen empirically to balance suppression of irrelevant high-frequency fluctuations against accurate identification of phase boundaries, and does not correspond to a physical frequency scale in the trapping process.

The derivative of the filtered signal highlights rapid variations in transmission, which appear as prominent peaks. The indices associated with these peaks were extracted and subsequently used to isolate the post-trapping regime of each trace. Figure 5.6 illustrates this procedure, with the peak locations overlaid on the raw signal to visually confirm that the transitions were correctly identified.

Once suitable parameters and drop indices were determined for each trace, all information was consolidated into a structured database in CSV format. This database records the main attributes

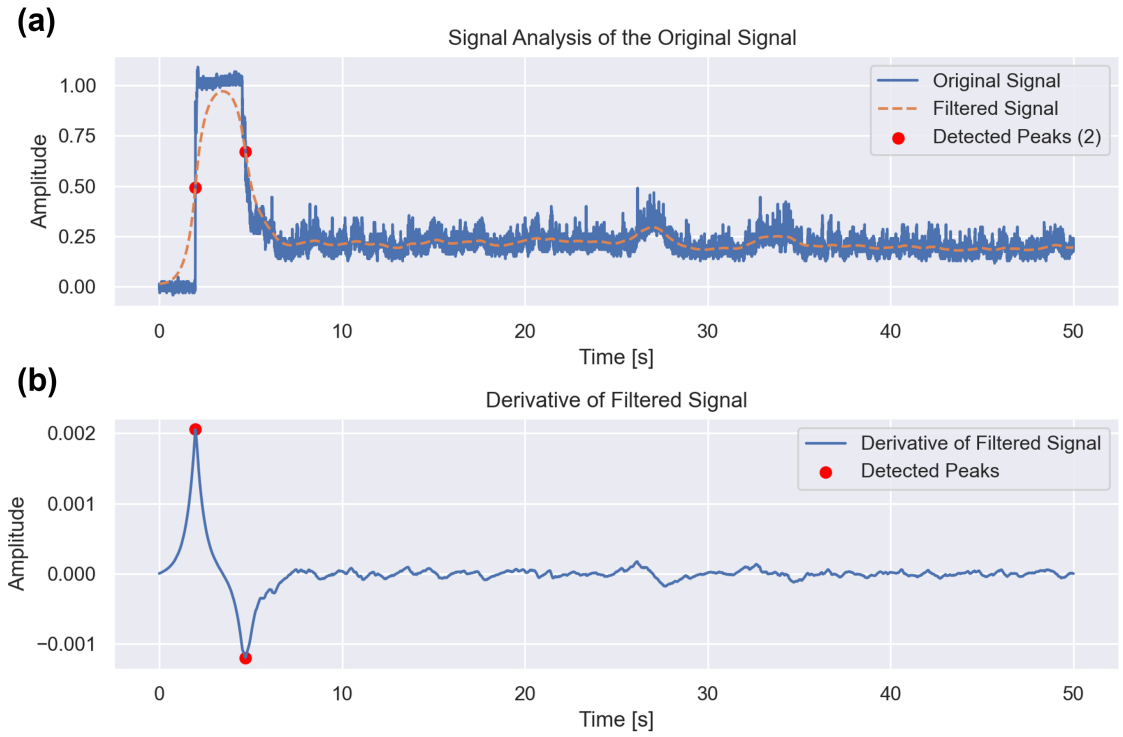

Figure 5.6: Example of the drop-detection procedure applied to a trapping signal. (a) Raw normalized transmission trace (blue) together with the corresponding low-pass filtered signal (orange). (b) Temporal derivative of the filtered signal, where prominent peaks are identified (red markers). The same peak locations are reported in (a) to visually assess whether the transitions between signal phases were correctly identified, and therefore whether the chosen filtering parameters were appropriate.

of each signal, including the file path, bacterial strain, and experimental run, together with the filtering parameters used for drop detection and the computed drop indices. Centralizing this information enabled systematic and automated reuse of the detection results in subsequent analyses.

Expression of the Signal as Resonance Wavelength Shifts

While signal normalization compensates for global amplitude variations by referencing each trace to the empty-cavity transmission level, the transmitted intensity remains an indirect observable of the cavity-object interaction. In fact, the amplitude of signal intensity depends on a variety of experimental factors that are not intrinsically related to the trapping process itself. Such factors include fluctuations of the optical fibre polarisation state, which modify the coupling efficiency between the fibre and the waveguide, as well as variations in injection and collection losses at both ends of the waveguide.

From a physical standpoint, the primary effect of a trapped bacterium is to modify the local refractive index in the vicinity of the cavity, thereby inducing a detuning of the cavity resonance with respect to the fixed probe wavelength. To focus the analysis on this intrinsic interaction and reduce sensitivity to extrinsic amplitude-related effects, the trapping signals are therefore reformulated in terms of effective resonance wavelength shifts rather than transmitted intensity.

This reformulation is performed by mapping the temporal transmission signal $I(t)$ onto the independently characterized cavity transmission spectrum $I(\Delta\lambda)$, expressed as a function of wavelength detuning relative to the resonance. For each time point, the measured intensity value is associated with the corresponding detuning $\Delta\lambda(t)$ on the fitted resonance curve, where $\Delta\lambda = 0$

denotes the empty-cavity resonance wavelength λ_0. As a result, the trapping signal is expressed as a temporal evolution of the effective resonance shift induced by the trapped object. An example of this mapping procedure is illustrated step-by-step in fig. 5.7.

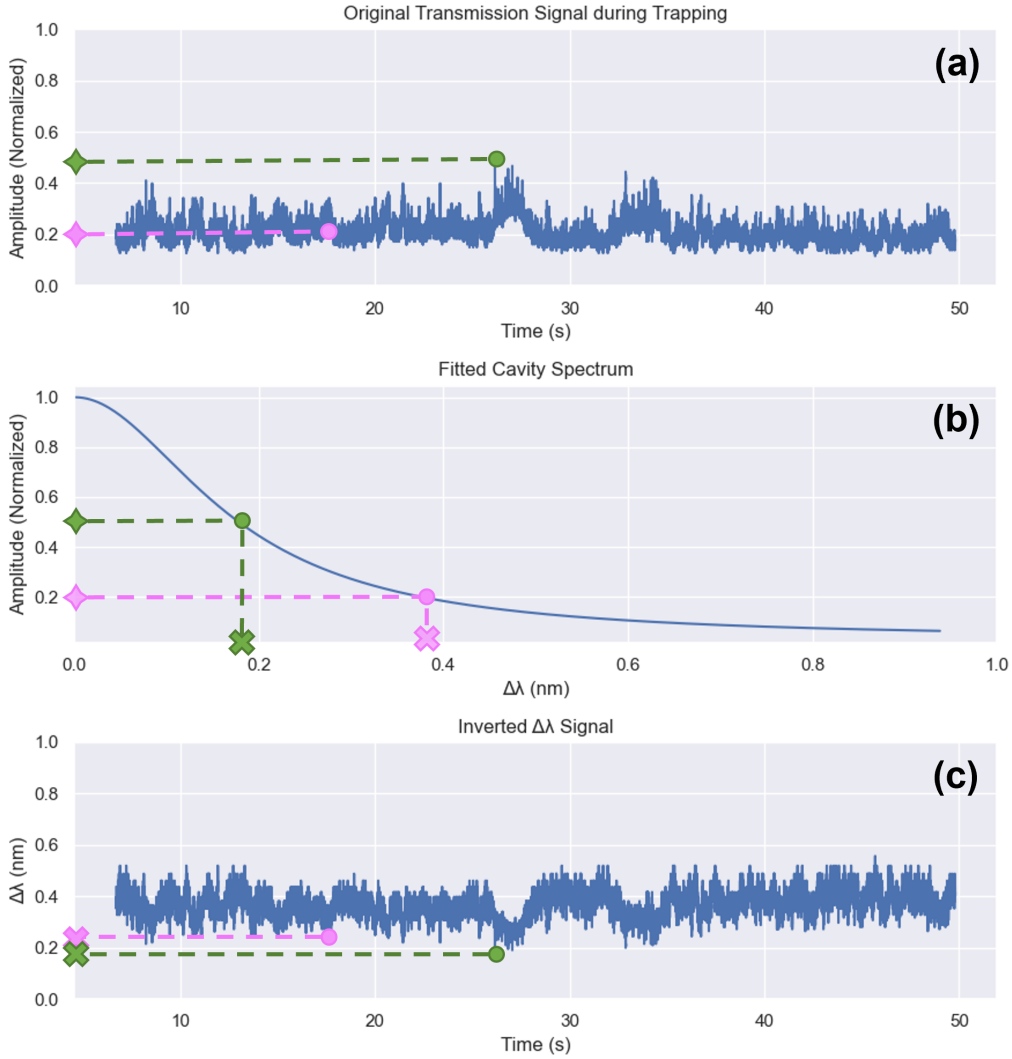

Figure 5.7: Example of the mapping of the transmission signal induced by the trapping of a single bacterium to express it as resonance wavelength shifts. The mapping procedure is illustrated for two points of the signal, highlighted in green and pink and followed throughout the three steps. Circle markers indicate the corresponding point being carried over from the preceding step.
(a) A point is selected from the $I(t)$ signal, and its amplitude is retrieved on the y-axis (star marker).
(b) The corresponding amplitude is marked on the y-axis of the centered cavity spectrum $I(\Delta\lambda)$ and projected onto the fitted resonance curve. The resulting point is indicated by a cross marker, whose abscissa gives the wavelength shift associated with this amplitude.
(c) The determined resonance wavelength shift replaces the amplitude of the initially selected point, thereby converting the signal from $I(t)$ to $\Delta\lambda(t)$.

In this procedure, the mapping computation relies on a fitted version of the cavity spectrum rather than the raw experimental one to avoid artefacts arising from internal reflections within the waveguide. Additionally, only one side of the resonance peak is considered in the conversion, as the fitted Lorentzian curve is symmetric and a given transmission value could otherwise correspond to two distinct detuning values. The selected branch corresponds to the direction of the

expected resonance shift upon trapping, which in the present configuration is towards longer wavelengths. This choice is consistent with the fact that bacterial cells typically possess a refractive index higher than that of the surrounding aqueous medium.In the literature, the refractive index of *E. coli* has been reported to be around 1.388 when measured at a wavelength of 514*nm* using optofluidic immersion refractometry in an on-chip configuration [203]. For comparison, we measured the refractive index of the suspension medium used in our experiments (50% deionized water / 50% phosphate-buffered saline) to be 1.334 using an Abbe refractometer ($\lambda \simeq 589$nm) at the LMGP laboratory at approximately 23°C. Although these values correspond to measurements performed in the visible spectral range, the analysis presented here assumes that the refractive-index contrast between bacterial cells and the surrounding medium remains positive in the infrared spectral range ($n_{bacteria} > n_{water}$) where our cavity operatess. Under this assumption, the wavelength shifts induced by trapping can be related to the effective refractive index of the trapped object, allowing an estimation of the refractive index for each bacterial strain from the measured trapping signals, as presented later in the Results section.

Moreover, the spectral response of the CMT3 cavity used for all the data collection in this work was observed to fluctuate between experimental runs, as discussed earlier in this chapter (section 5.2.3). Therefore, each signal was reformulated with respect to the spectrum recorded at the start of the corresponding experimental run. This highlights the importance of this regular probing step not only in our experimental protocol, but in long-term experimental scenarios in general.

This reformulation completes the signal processing pipeline by transforming the raw transmission traces into a representation that is physically related to the cavity-object interaction and is robust to run-to-run variations in the optical setup. The resulting wavelength-shift signals form the basis of all subsequent quantitative analyses.

5.4 Data Analysis: Methods

In this section, we describe how the collected and pre-treated data are further processed to extract statistically robust descriptors. The objective of this analysis stage is twofold. First, to reduce the high-dimensional temporal signals to a small set of physically meaningful parameters. Second, to assess the reproducibility of these parameters within a given bacterial strain as well as the potential for strain-level classification of the trapped bacteria.

5.4.1 Statistical Representation

The processing procedure described previously yields the temporal evolution of the wavelength shifts induced by each trapped cell. However, in the present study, these signals are not analysed as time-resolved trajectories. Instead, each recording, acquired over a fixed window of approximately 45s to 50s, is treated as a statistical ensemble of optical perturbations sampled during an individual trapping event. This choice reflects the fact that the quantities of interest are not the detailed temporal dynamics of a single event, but rather the characteristic magnitude and variability of the cavity response associated with a given cell or strain.

Accordingly, the first step of the analysis consists in transforming each time series into a statistical representation. For every recording, the distribution of $\Delta\lambda$ values is represented as a histogram. This representation captures the statistical distribution of cavity perturbations while discarding the temporal ordering of the events. In doing so, it isolates the typical amplitude and

spread of the optical response independently of the specific sequence in which fluctuations occur. The resulting histograms are fitted with skew-normal probability density functions, which extend the Gaussian model to allow slight asymmetries while remaining unimodal. A skew-normal distribution reduces to a Gaussian when the asymmetry parameter is zero. An example of a fitted histogram representing a trapping experiment is shown in fig. 5.8.

Each fit yields three parameters: the mean value μ, the standard deviation (SD) σ, and the skewness parameter α. The parameter μ characterizes the central tendency of the wavelength-shift distribution and therefore represents the most probable optical response associated with a trapped bacterium. In other words, μ corresponds to the position where the bacterium spends most of its time within the evanescent field of the cavity mode. Physically, this perturbation arises from the portion of the cell that lies within the evanescent field, namely the cell envelope and any surface appendages that extend close enough to interact with the mode. It depends on cellular properties such as size, refractive index contrast, and average spatial overlap with the cavity field. As such, μ provides a compact descriptor of the typical optical signature of a given cell under trapping conditions.

The parameter σ quantifies the width of the wavelength-shift distribution and captures the magnitude of fluctuations around the typical response. These fluctuations originate primarily from rotational and translational motion of the bacterium within the trap and from residual measurement noise. The parameter σ therefore reflects both the stability of the trapped object and changes in its spatial overlap with the cavity field during trapping.

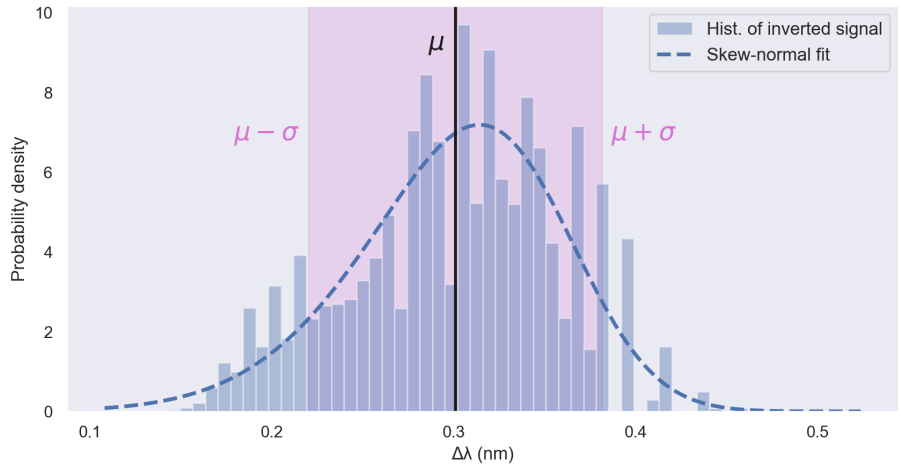

Figure 5.8: Example of a histogram fitted with a skew-normal distribution. The bins represent the distribution of wavelength shifts extracted from an inverted trapping signal. The black vertical line marks the mean of the fitted distribution, and the purple region illustrates the typical spread of values around this mean, corresponding to the interval $\mu \pm \sigma$.

In addition to these descriptors, the skewness parameter α characterizes the asymmetry of the wavelength-shift distribution. A non-zero value of α indicates that the sampled cavity perturbations exhibit a preferential tail toward larger wavelength shifts, corresponding to positions closer to the cavity than the most probable one. This asymmetry naturally arises because the evanescent field decays exponentially away from the silicon slab: configurations closer to the field produce stronger shifts than more distant ones. For the rod-shaped bacterium *E. coli*, orientations parallel to the surface generally produce a larger optical response than perpendicular ones, which can further contribute to asymmetry. Other cell morphologies could show different patterns, but in this study we focus on *E. coli*. Additional effects, such as preferred orientations or electrostatic interactions with the chip interface discussed in Chapter 4, may also influence the instantaneous overlap with the cavity field.

Although α may contain additional information regarding the trapping configuration, its physical interpretation is less direct than that of μ and σ. Several distinct mechanisms can produce similar skewness values, making it difficult to attribute variations in α to a specific underlying process without a dedicated dynamical model. For this reason, the present study focuses primarily on the parameters μ and σ as robust and physically interpretable descriptors of the trapping-induced cavity response. Their values are compared within and across strains to assess reproducibility and strain-dependent differences.

5.4.2 Reproducibility Scores

To quantitatively assess reproducibility, we analyze how the fitted parameters μ and σ vary across repeated single-cell trapping experiments belonging to the same bacterial strain. The statistical metrics introduced below address three complementary aspects: the intrinsic spread of individual measurements, the precision with which the strain-averaged values are determined, and the relative magnitude of variability across strains.

For each given bacterial strain, let $\{\mu_i\}_{i=1}^N$ and $\{\sigma_i\}_{i=1}^N$ denote the parameters extracted from N independent single-cell trapping events. Each pair (μ_i, σ_i) corresponds to one single-cell experiment. The sample mean values

$$\overline{\mu} = \frac{1}{N}\sum_{i=1}^{N}\mu_i, \qquad \overline{\sigma} = \frac{1}{N}\sum_{i=1}^{N}\sigma_i \tag{5.2}$$

define the strain-averaged optical signature and the typical fluctuation amplitude. These quantities serve as reference values around which individual-cell measurements are distributed within a strain.

The dispersion of individual measurements around these strain-specific mean values is quantified by the sample standard deviations,

$$s_\mu = \sqrt{\frac{1}{N-1}\sum_{i=1}^{N}(\mu_i-\overline{\mu})^2}, \qquad s_\sigma = \sqrt{\frac{1}{N-1}\sum_{i=1}^{N}(\sigma_i-\overline{\sigma})^2}. \tag{5.3}$$

where the quantities s_μ and s_σ are properties of the individual measurements that quantifies the run-to-run variability of the extracted parameters across individual cells of the same strain. In these equations, the factor $N-1$ is a statistical correction that accounts for the fact that the mean is estimated from the same dataset, which reduces the effective number of independent degrees of freedom by one. In practice, this tells us how much the optical response of individual cells fluctuates around the typical strain-specific signature.

Additionally, in order to compare intra-strain reproducibility across strains exhibiting different absolute wavelength-shift amplitudes, a normalized measure of dispersion is introduced through the coefficient of variation,

$$\mathrm{CV}_\mu = \frac{s_\mu}{\overline{\mu}}, \qquad \mathrm{CV}_\sigma = \frac{s_\sigma}{\overline{\sigma}}. \tag{5.4}$$

These dimensionless quantities express variability relative to the signal magnitude itself, enabling reproducibility to be compared on equal footing across strains. A smaller CV indicates that the strain behaves more reproducibly relative to its typical optical signature.

To extend this analysis to the joint behavior of μ and σ, a multivariate representation is then introduced, in which the paired measurements (μ_i, σ_i) are characterized through their sample covariance matrix, defined as:

$$\mathbf{\Sigma} = \begin{pmatrix} s_\mu^2 & \mathrm{Cov}(\mu,\sigma) \\ \mathrm{Cov}(\mu,\sigma) & s_\sigma^2 \end{pmatrix} \tag{5.5}$$

with

$$\mathrm{Cov}(\mu,\sigma) = \frac{1}{N-1}\sum_{i=1}^{N}(\mu_i - \overline{\mu})(\sigma_i - \overline{\sigma}). \tag{5.6}$$

To visualize these covariance parameters for each strain, we overlay the distribution of (μ_i, σ_i) values in the (μ,σ) plane, as will be seen later in fig. 5.9, with a 95% confidence ellipse constructed from the corresponding covariance matrix. This ellipse provides a compact geometric representation of intra-strain heterogeneity. Its center is given by the strain-averaged values $(\overline{\mu},\overline{\sigma})$, its tilt is determined by the covariance term $\mathrm{Cov}(\mu,\sigma)$, and its principal diameters reflect the variances along the main directions of spread in the joint parameter space.

The confidence ellipse is constructed to provide a visual boundary that contains most of the observed (μ,σ) points for a given strain. By convention, we choose a 95% probability, meaning that under a normal approximation, roughly 95% of individual observations are expected to lie within this ellipse. This value is standard in statistics because it balances two competing needs: capturing the majority of the data while avoiding an overly large ellipse that would be dominated by extreme outliers. Choosing 100% would make the ellipse excessively large and sensitive to rare events, whereas a smaller value, such as 85%, would exclude a substantial fraction of typical observations.

Mathematically, the ellipse is defined as the set of points (x,y) that satisfy

$$\begin{bmatrix} x-\overline{\mu} \\ y-\overline{\sigma} \end{bmatrix}^T \Sigma^{-1} \begin{bmatrix} x-\overline{\mu} \\ y-\overline{\sigma} \end{bmatrix} = \chi^2_{2,0.95}, \tag{5.7}$$

where Σ is the 2×2 covariance matrix of (μ,σ) and $\chi^2_{2,0.95}$ is the threshold from the chi-squared distribution corresponding to the 95% confidence level.

In addition to the confidence ellipse providing a visual representation of the joint behaviour of μ and σ, it is possible to quantify their degree of association to monitor whether they vary following common underlying mechanisms or independent ones. This is characterized through correlation factors, defined as:

$$\rho_{\mu\sigma} = \frac{Cov(\mu,\sigma)}{s_\mu s_\sigma} \tag{5.8}$$

By definition, $\rho_{\mu\sigma}$ takes values between -1 and 1. A value close to 1 indicates that higher mean wavelength shifts tend to coincide with larger fluctuations, whereas a value near 0 implies that μ and σ vary independently. Graphically, the correlation coefficient is reflected in the tilt and elongation of the ellipse: a highly tilted and elongated ellipse corresponds to a strong positive or negative correlation, while a more circular ellipse indicates weak correlation. In the present work, these tools serve primarily to describe intra-strain variability and to compare trends across strains rather than as formal statistical tests.

Altogether, these statistical descriptors provide a structured framework for quantifying reproducibility at both the single-parameter and joint-parameter levels. The standard deviations and coefficients of variation capture intra-strain variability and relative reproducibility, while the covariance-based representation summarizes how the mean and spread vary together across individual cells. Together, these measures form the quantitative basis for the comparative analyses presented later in the results section.

5.4.3 Supervised Classification Framework

Beyond the characterization of intra-strain variability, we wanted to evaluate whether the optical signatures collected with our device contain sufficient information to enable inter-strain discrimination. In other words, can the cavity response measured during trapping events be used to identify the bacterial strain from which it originates. To address this question in a quantitative manner, we introduced a supervised machine learning framework as an evaluation tool.

Supervised classification consists in constructing an algorithm that learns, from labeled examples, how to associate a set of measured features with a given class. In the present case, each trapping experiment is represented by statistical descriptors extracted from the wavelength-shift distributions, and each experiment is labeled by the corresponding bacterial strain. The objective of the algorithm is therefore to learn how these descriptors are distributed across strains, and to infer decision rules capable of assigning the correct strain label to previously unseen data.

This procedure involves two complementary roles: parameter estimation, where the prediction model is trained to fit to the given data, and performance evaluation, where the prediction results are controlled; thus the name supervised. It is essential to distinguish between these two steps, which are performed at multiple successive iterations. Furthermore, if the same data are used both to train the prediction model's parameters and to assess its predictive performance, the resulting accuracy would be optimistically biased and does not reflect true generalization capability. For this reason, the data used for evaluation must be strictly separated from those used for training.

For the model training, we employ a supervised classification architecture known as quadratic discriminant analysis. The method proceeds by statistically modeling each strain separately based on chosen features. The obtained metrics, which characterize how the features vary and how they are correlated, determine the shape of the decision boundaries that separate the data according to strain identity. In quadratic discriminant analysis, these boundaries can be curved rather than linear, reflecting differences in feature covariances between strains. These computations are done automatically and, beyond the choice of the architecture itself, without direct intervention of the user. Under such conditions, quadratic discriminant analysis provides flexible and analytically interpretable decision rules, directly derived from the data's distribution, with limited model complexity. This reduces the risk of overfitting in moderate-sized datasets, making it well suited for a preliminary assessment of class discrimination.

When it comes to data separation, it is implemented through a stratified 5-fold cross-validation procedure. The dataset is divided into five approximately equal subsets that preserve the class distribution. At each iteration, four folds, corresponding to approximately 80% of the data, are used to train the prediction model, while the remaining fold, corresponding to approximately 20%, is reserved exclusively for performance evaluation. Performance evaluation here refers to using the trained model to predict the strain identity of the held-out subset, which was entirely excluded from the training phase, and then comparing these predictions with the true strain labels. More importantly, the evaluation fold is rotated across iterations so that every experiment serves once as test data. This approach reduces sensitivity to the particular composition of a single split and provides a statistically robust estimate of predictive performance. The final reported results correspond to performance metrics averaged over all cross-validation folds. Given the modest size of the dataset, with approximately 20 to 30 signals per strain, this choice ensures sufficient training data for stable parameter estimation while maintaining an unbiased assessment of generalization capability.

It is important to emphasize that the objective here is not the development of a highly optimized predictive model. Rather, this step is introduced as a controlled and interpretable test of class separability. If the optical signatures associated with different strains occupy distinct regions in the chosen representation space, then even a simple classification architecture should be able to

identify consistent decision boundaries. Conversely, poor performance would indicate that the extracted features do not contain sufficient discriminative information.

5.5 Signal Analysis: Results

5.5.1 Intra-Strain Variability

To analyse the results obtained from our optical trapping measurements, we were first interested in quantifying the reproducibility of the device, i.e. the variability in performance of the same optical cavity when presented multiple times with similar objects. In order to do so, we examine the joint distribution of the fitted parameters μ and σ for each bacterial strain, as shown in fig. 5.9. Each point corresponds to a single-cell trapping event, allowing the dispersion of optical responses within a strain to be directly visualized. For improved readability, the individual subplots are reproduced at full size in the appendix (chapter B). Beyond this visual representation, the associated quantitative metrics are summarized in table 5.1.

Table 5.1: Intra-strain reproducibility metrics extracted from the fitted parameters of optical trapping signals. N represents the number of individual signals per strain.

Strain	N	$\bar{\mu}$ (nm)	s_μ (nm)	CV_μ (%)	$\bar{\sigma}$ (nm)	s_σ (nm)	CV_σ (%)	$\mathrm{Cov}(\mu,\sigma)$ (nm^2)	ρ
EC11	26	0.3007	0.0235	7.8	0.0335	0.0045	13.4	8.0×10^{-5}	0.76
EC225	21	0.1687	0.0332	19.7	0.0279	0.0054	19.4	7.0×10^{-5}	0.38
EcB	34	0.3281	0.0576	17.5	0.0414	0.0165	39.9	4.9×10^{-4}	0.52
Eco0124	24	0.2250	0.0245	10.9	0.0281	0.0034	12.1	6.0×10^{-5}	0.72
Eco0126	26	0.3587	0.0497	13.8	0.0620	0.0151	24.3	4.2×10^{-4}	0.56
Eco0127	22	0.3182	0.0544	17.1	0.0517	0.0172	33.4	6.8×10^{-4}	0.73
Eco0128	23	0.3554	0.0411	11.6	0.0640	0.0143	22.3	3.5×10^{-4}	0.60
Eco0129	25	0.3161	0.0389	12.3	0.0431	0.0112	26.0	3.5×10^{-4}	0.80
Eco0130	32	0.2991	0.0268	8.9	0.0302	0.0105	34.8	6.0×10^{-5}	0.21
Eco0131	25	0.2899	0.0288	9.9	0.0395	0.0087	22.2	3.0×10^{-5}	0.10

Resonance Shifts

Across all strains, the mean resonance shifts μ remain below 0.5 nm. These small amplitudes are consistent with the weak refractive index contrast between biological cells, whose composition is largely water ($n \simeq 1.388$ for *E. coli*), and the surrounding aqueous medium ($n \simeq 1.334$ for the 50% DIW / 50% PBS suspension). Since the cavity is initially resonant in water, trapping a bacterium introduces only a small perturbation of the effective refractive index, resulting in a limited spectral displacement.

This signal amplitude demonstrates, on one hand, the sensitivity of the CMT3 cavity to modest refractive index contrasts, and on the other hand, the importance of the signal analysis methods

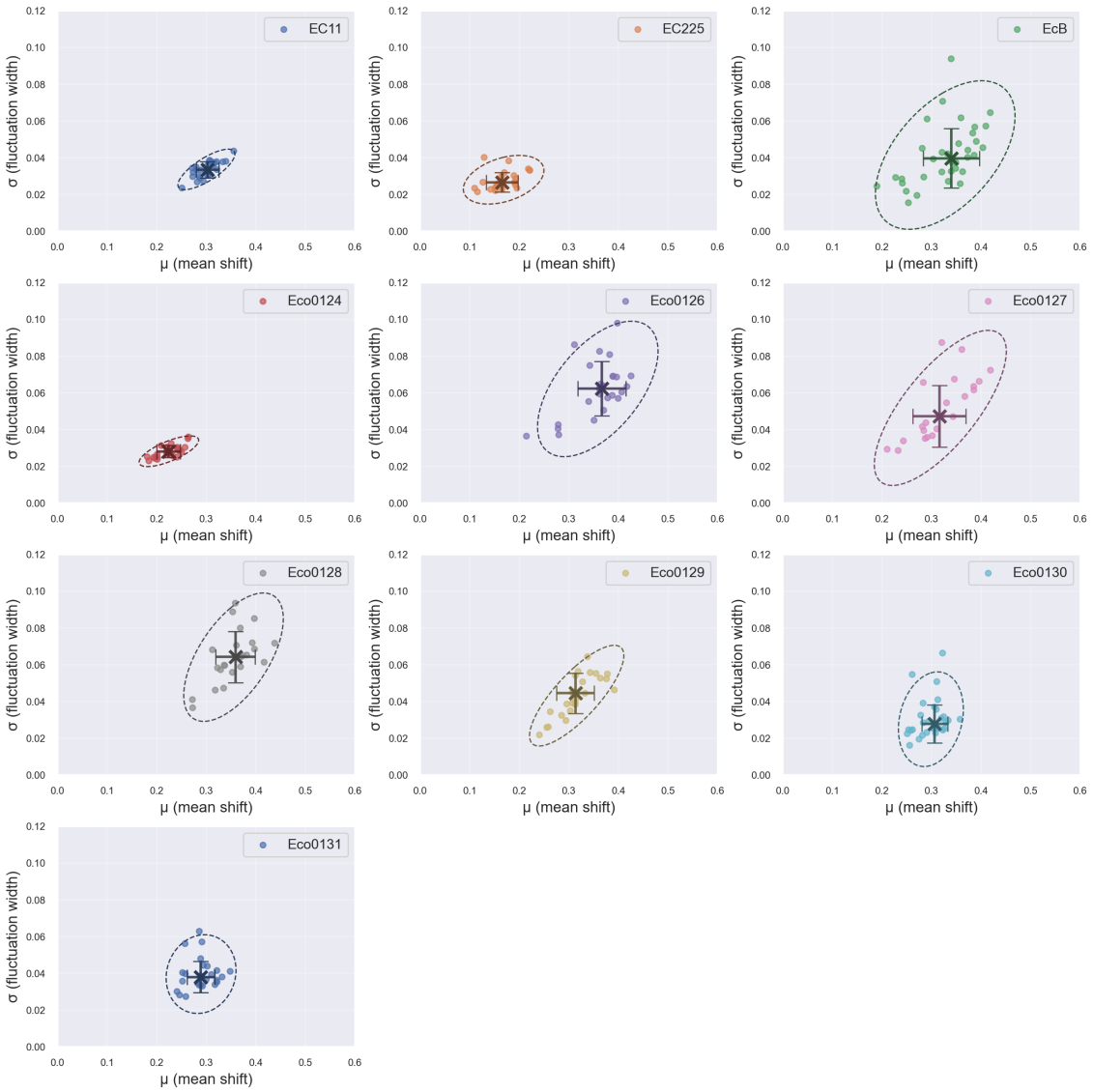

Figure 5.9: $(\mu\text{-}\sigma)$ parameter distributions for all trapped bacterial strains. In each subplot, individual points correspond to single-cell fits. The X marker denotes the strain-averaged values $(\bar{\mu}, \bar{\sigma})$, with error bars representing one standard deviation (s_μ, s_σ). The dotted ellipses indicate the 95% covariance region, providing a visual summary of intra-strain variability and $\mu\text{-}\sigma$ correlation.

applied in this work to reliably quantify such perturbations. In theory, shifts induced by a trapped object could be estimated through direct tuning of the injected laser wavelength until the amplitude of the transmitted signal is back to its maximal value, corresponding to the the injection of the exact resonance wavelength in the current cavity environment as induced by the presence of the bacterium. This tuning could be done either manually, or through complicated feedback loops. The first option would be timecostly and imprecise, while the second would increase the experimental complexity. Moreover, this approach would be very prone to mechanical drift, noise and resolution limitation. Therefore, the signal-processing approach used here enables a more precise, time-efficient and robust extraction of resonance shifts under realistic experimental conditions.

Reproducibility of Resonance Shifts

The dispersion of μ within each strain is quantified by the standard deviation s_μ and the coefficient of variation CV_μ. As presented in table 5.1 and in fig. 5.10, the CV_μ values range approximately from 8% to 20% depending on the strain. For several strains (e.g., EC11, Eco0130, Eco0131), CV_μ remains below 10%, indicating tightly clustered resonance shifts across independent trapping events, consistent with the compact distributions observed in fig. 5.9.

At the single-cell level, variability on the order of $10-15\%$ can reasonably be considered indicative of good experimental reproducibility, particularly for biological systems where intrinsic heterogeneity cannot be fully eliminated. Since the studied populations are assumed to be genetically homogeneous, larger CV_μ values may reflect increased morphological or phenotypic variability within each strain, subtle differences in cell positioning relative to the cavity field maximum, or residual instrumental fluctuations. Overall, the fact that most strains remain within a moderate dispersion range supports the interpretation of μ as a robust strain-dependent optical descriptor rather than a purely stochastic measurement outcome.

Resonance Shift Fluctuations

The parameter σ, which characterizes the width of the signal fluctuations during trapping, remains systematically smaller in absolute magnitude than μ. This hierarchy is expected as it reflects the physical conditions required for stable optical trapping.

In fact, while μ reflects the static optical perturbation induced by the presence of a cell, σ captures dynamic effects occurring during confinement within the optical field. These dynamic contributions include residual Brownian motion, rotational degrees of freedom, and local fluctuations of the electromagnetic field distribution. Brownian motion, in particular, is intrinsically stochastic and cannot be fully suppressed, even under stable trapping conditions.

If dynamic fluctuations were to be comparable to or dominate over the static shift, this would translate into $\sigma \gtrsim \mu$, and would suggest that the optical forces are insufficient to maintain stable confinement. In such a regime, trapping would be unreliable or not observable at all. The systematic observation that $\sigma < \mu$ therefore confirms that optical forces dominate over stochastic motion in the present configuration, ensuring stable trapping while still allowing measurable dynamic fluctuations, providing an internal physical consistency check of the trapping regime.

Reproducibility of Resonance Shift Fluctuations

The reproducibility of σ is quantified through s_σ and CV_σ. As shown in table 5.1 and fig. 5.10, CV_σ values are generally larger than CV_μ, exceding 30% for some strains.

This larger dispersion does not contradict trapping stability. Rather, it reflects the fundamentally different nature of σ and μ. Both these factors originate from the same refractive index perturbation induced by the trapped cell. However, μ reflects the time-averaged optical interaction, whereas σ quantifies the temporal variability of this interaction as the cell undergoes residual motion and reorientation within the trap. In other words, cell motion continuously modifies the effective refractive index "seen" by the cavity, and σ captures the magnitude of these fluctuations around the mean shift. Because such dynamic processes are inherently stochastic, greater dispersion in σ is physically expected.

Thus, the observed hierarchy $CV_\sigma > CV_\mu$ mirrors the distinction between a predominantly static optical perturbation and a dynamically modulated response. The two parameters probe different physical aspects of the trapping interaction, which justifies treating them separately in the analysis.



Figure 5.10: Coefficient of variance for μ (full bars) and σ (dotted bars) per strain. CV_μ quantifies the relative dispersion of the mean resonance shift, while CV_σ reflects the relative variability of fluctuation amplitudes.

Coupled Behavior of μ and σ

While CV scores reflect individual variability of the resonance shifts and their fluctuations, the covariance and correlation coefficient $\rho(\mu,\sigma)$ provide insight into their joint behaviour. As reported in table 5.1, all strains exhibit positive covariance and thus positive correlation coefficients.

This systematic positivity indicates that cells inducing larger resonance shifts also tend to display larger fluctuation amplitudes. However, the strength of this $\mu-\sigma$ coupling varies across strains, with ρ ranging from weak ($\sim 0.1-0.2$) to strong ($\sim 0.7-0.8$). Graphically, the correlation is represented by the tilted covariance ellipses in the (μ,σ) plane. The tilt direction reflects the sign of the correlation (positive in all cases), while the degree of elongation (axis diameters) reflects its strength. Strongly correlated strains display elongated ellipses aligned along a diagonal axis, indicating that static and dynamic responses scale together. In contrast, nearly isotropic ellipses correspond to weak coupling between the two parameters.

Physically, this positive correlation suggests that both μ and σ are influenced by common underlying factors, such as effective interaction volume, cell size, or refractive index contrast. A cell producing a stronger static perturbation may experience modified optical forces or explore a slightly larger portion of the field distribution, thereby increasing fluctuation amplitude. The (μ,σ) pair therefore captures a coupled optical response rather than two fully independent observables.

Device Performance & Perspectives

The consistency of the observed trends across strains demonstrates that the optical cavity provides a reproducible and strain-dependent optical signatures at the single-cell level. The moderate dispersion for μ indicate stable extraction of the mean resonance shift across independent trapping events, while the systematic positive correlation between μ and σ reveals an intrinsic coupling between static optical perturbation and dynamic behavior fluctuation. The joint (μ,σ) parameter space therefore constitutes a tow-dimensional fingerprint of trapped cells.

In principle, such reproducible strain-specific signatures could enable the identification of atypical responses within an otherwise homogeneous population, suggesting potential applications in detecting outliers that express phenotypic variations, mutations, or contamination events at the single-cell scale. In practice, however, translating this concept into a practical diagnostic framework would require larger datasets and systematic validation to establish statistically robust reference distributions.

Strain Classification Based on Statistical Metrics

Although intra-strain variability remains relatively controlled, the inter-strain distributions show substantial overlap, as illustrated in fig. 5.11. The clouds of individual (μ_i, σ_i) points from different strains are largely interlaced, and their corresponding confidence ellipses overlap significantly. This overlap indicates that simple threshold-based separation in the (μ, σ) plane is insufficient for reliable strain discrimination. While mean values differ slightly between strains, the degree of dispersion prevents robust classification based solely on these two scalar parameters.

Consequently, strain identification requires more advanced comparison and classification analysis approaches, which will be discussed in the following section.

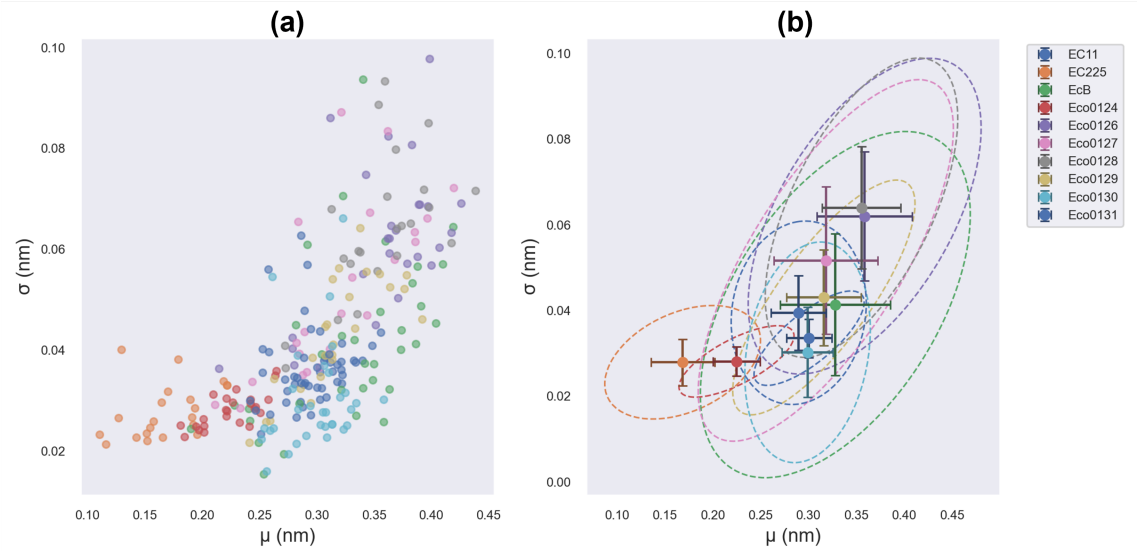

Figure 5.11: Distribution of fitting parameters for all strains. (a) Combined cloud of individual (μ_i, σ_i) points for all bacteria from all strains. (b) Strain-averaged values and their corresponding standard deviation errorbars and confidence ellipses, plotted in the same (μ, σ) plane. Significant overlap between strains highlights the limits of low-dimensional statistical separation.

5.5.2 Inter-Strain Discrimination

To determine whether the optical trapping responses can be used to distinguish between bacterial strains, we performed a supervised classification analysis. The objective of this approach was to test whether the recorded signals contain sufficient strain-specific information to enable automated discrimination.

The classification procedure was applied to two representations of the data. First, we considered the inverted trapping signals $\Delta\lambda(t)$ directly as input features, thereby preserving the full temporal structure of the optical response. Second, we evaluated the classification using the reduced

representation based on the histogram-derived statistical descriptors (μ, σ). Performance was estimated using 5-fold cross-validation, and the reported metrics correspond to averages across folds.

Overall Classification Performance

In the context of machine learning, classification performance is commonly evaluated through accuracy scores and confusion matrices. The accuracy corresponds to the proportion of correctly classified observations relative to the total number of samples, providing a global measure of predictive performance. The confusion matrix complements this metric by detailing how each true strain is reassigned across predicted classes, thereby revealing the structure of classification errors.

Applying quadratic discriminant analysis to the dataset yielded overall cross-validated accuracies of 40.3% when using the full inverted signals and 43.4% when using the reduced (μ, σ) representation. In an ideal situation where the optical signatures of the ten strains produce clearly distinct response distributions, a quadratic classifier would assign the vast majority of events to their correct class, resulting in accuracies approaching unity and a confusion matrix dominated by its diagonal entries, that is, by high proportions of correctly classified strains.

The present results therefore indicate partial rather than complete separability, as shown in fig. 5.12. This outcome is physically consistent with the nature of the dataset: all investigated samples belong to the same bacterial species and are expected to share substantial structural and compositional similarities. Under such conditions, perfect discrimination is not a realistic expectation. Importantly, no absolute threshold can define what constitutes a "good" accuracy in this context, since achievable separability is intrinsically constrained by the biological proximity of the strains under investigation. For this reason, the confusion matrices provide a more informative perspective than the global accuracy alone, as they reveal how similarities are distributed across specific strain pairs.

Comparison of the Data Representation Modes

Using the full inverted signals as input features preserves the entire temporal evolution of the trapping response. In principle, this representation contains more detailed information than the two-parameter summary (μ, σ). However, the comparable and slightly lower accuracy obtained with the full signals suggests that the additional temporal complexity does not substantially improve class separability under the present experimental conditions.

Furthermore, the confusion matrices associated with both representations, shown in fig. 5.12, display highly similar global structures. The reduced (μ, σ) representation achieves a slightly higher overall accuracy and reproduces most of the dominant confusion patterns observed with the full signals. This indicates that a significant fraction of the strain-discriminative information contained in $\Delta\lambda(t)$ is already captured by these two statistical descriptors. In other words, the main separability between strains appears to be governed primarily by differences in mean optical shift and fluctuation amplitude, while temporal features contribute only marginally in this dataset.

This observation reinforces the validity of relying on (μ, σ) as compact and physically meaningful descriptors in the intra-strain variability analysis presented previously. The reduced representation does not only simplify the data; it retains the dominant discriminatory structure relevant to inter-strain comparison.

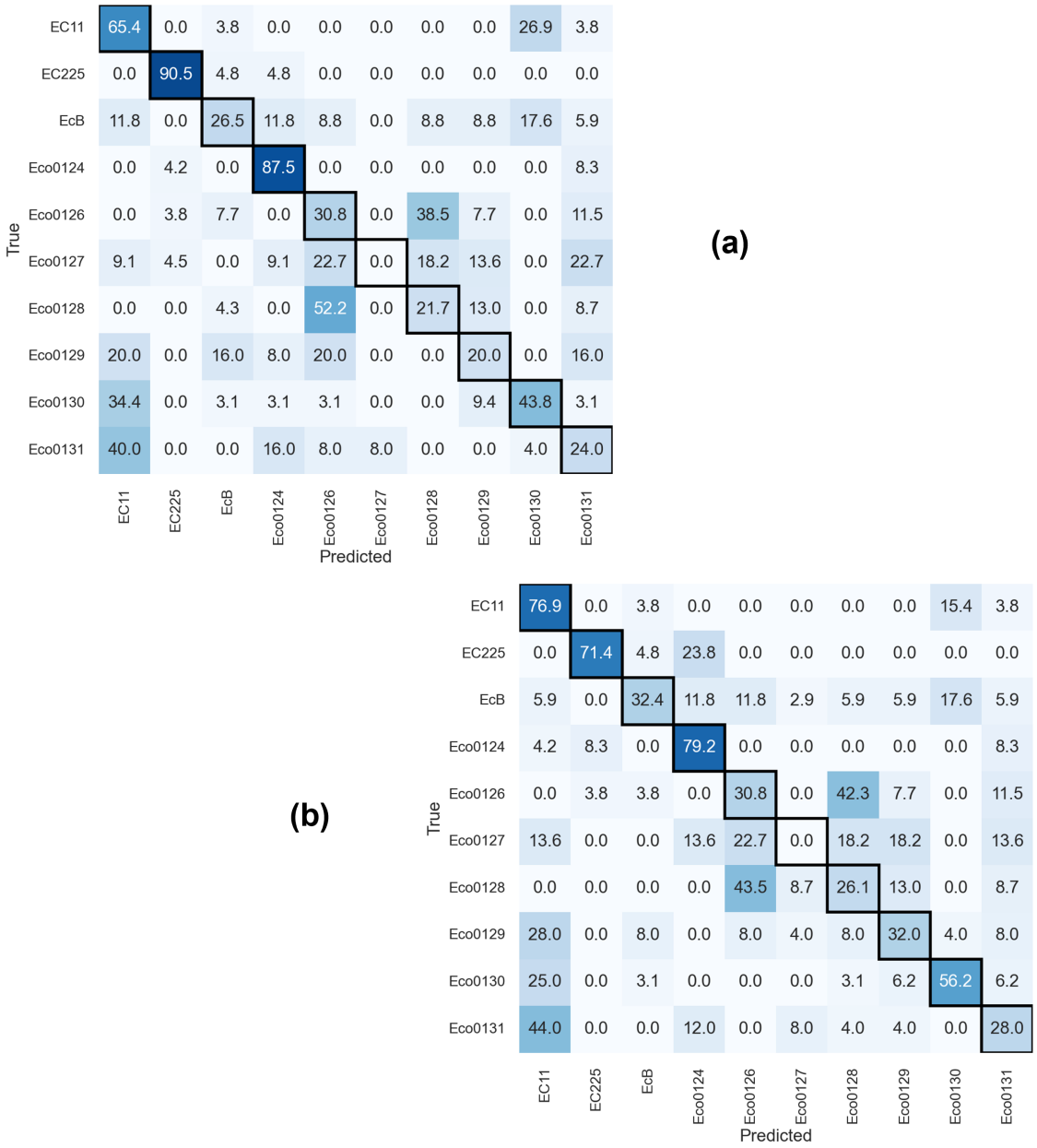

Figure 5.12: Confusion matrices of the bacterial strain predictions. (a) Results based on the classification of inverted trapping signals describing the temporal evolution of resonance perturbations $\Delta\lambda(t)$. (b) Results based on the classification of statistical descriptors (μ_i, σ_i) extracted from the inverted signals. The numbers displayed represent the proportion (in %) of predicted labels relative to the true labels. The framed diagonal cells indicate the ratio of true positive predictions for each class.

Interpretation of Confusion Patterns

The confusion matrices reveal several consistent trends of missclassification patterns. Certain strains, such as EC225 and Eco0124, exhibit high recall values across both data representations, indicating that a large fraction of their signals are consistently assigned to the correct class. This suggests that these strains generate optical responses that remain consistently distinguishable under the present experimental conditions.

In contrast, other strains including Eco0126, Eco0128, and Eco0131 display lower recall val-

ues and are frequently reassigned to a restricted subset of other strains. Importantly, these errors are not randomly distributed across all classes. Instead, specific pairs or small groups of strains are repeatedly confused with one another. For example, Eco0126 is predominantly reassigned to Eco0128, while Eco0131 shows recurrent reassignment toward EC11. Such directional confusion patterns indicate partial overlap in the measured optical responses, but in a structured and reproducible manner rather than randomly across all strains.

Particularly, Eco0127 is notably never recovered as a predicted class. This observation can be interpreted in two complementary ways. First, Eco0127 shows relatively high intra-strain variability (second only to EC225, *cf.* table 5.1), which can cause its measured responses to blur across multiple other strains, thus resulting in a reduced classification confidence. Second, this strain may possess structural or compositional features to which the cavity is comparatively insensitive. This might include factors such as subtle membrane chemistry or surface charge repartitions that influence positioning above the cavity for example.

Overall, when compared to the earlier visual inspection of the (μ, σ) scatter distributions (*cf.* fig. 5.11), the classification analysis provides additional resolution. While the scatter plots revealed extended clusters, the classifier forces each event to be assigned to a single strain, making it possible to identify which strains are repeatedly confused with specific others rather than misclassified randomly. The confusion matrix therefore does more than confirm the presence of overlap: it clarifies the structure of that overlap by showing which strains consistently produce similar optical responses and which strains concentrate a large fraction of ambiguous events.

The structured nature of these overlaps supports a physically meaningful interpretation. Strains that are repeatedly confused may share common morphological traits, membrane compositions, or surface refractive index contrasts that produce comparable effective perturbations of the cavity field. The classifier therefore reveals groups of optical proximity rather than arbitrary classification failures.

Finally, the present results should thus be interpreted not as a diagnostic limitation, but as a quantitative mapping of similarity relationships within the strain panel. The observed confusion clusters provide concrete hypotheses for future investigations. In particular, targeted genomic or phenotypic analyses of recurrently overlapping strain pairs could help identify the structural determinants to which the optical cavity is most sensitive. In parallel, the physical origin of the measured optical response can be further examined by quantifying the refractive-index contrast between the bacterial cell and the surrounding medium. Since the resonance shifts induced during trapping are governed by this contrast, the present dataset also enables an estimation of the effective refractive index associated with each strain under the infrared operating conditions of the cavity. In this sense, the classification framework functions as an exploratory tool that highlights both physical and biological directions for follow-up studies.

5.6 Optical Determination of Strain Refractive Index

While the previous analyses focused on the statistical properties of these wavelength-shift signals, the same measurements can also be interpreted in terms of an effective refractive index associated with the trapped object. In this section, we therefore use the recorded trapping signals to derive refractive-index estimates for the different trapable bacterial strains investigated in this work under the infrared operating conditions of the cavity.

In order to establish a quantitative relationship between refractive index variations and resonance shifts in the present cavity geometry, we first performed numerical simulations using the

finite-difference time-domain (FDTD) solver implemented in the `Lumerical` software suite. In these simulations, the refractive index of the medium surrounding the optical resonator was varied while monitoring the corresponding resonance wavelength of the cavity mode.

Strictly speaking, this configuration does not reproduce the exact physical situation encountered during bacterial trapping. In the experiments, the bacterium introduces a local perturbation of the refractive index in the vicinity of the cavity, whereas the simulation modifies the refractive index of the entire surrounding medium. Nevertheless, this approach provides a useful first-order calibration of the sensitivity of the cavity resonance to refractive-index variations in the external environment.

Numerical Calibration of Resonance Shift vs. Refractive Index

The simulation was performed by sweeping the refractive index of the surrounding medium from $n = 1.30$ to $n = 1.40$ and recording the corresponding resonance wavelength λ_0 of the cavity. The results are represented in fig. 5.13.

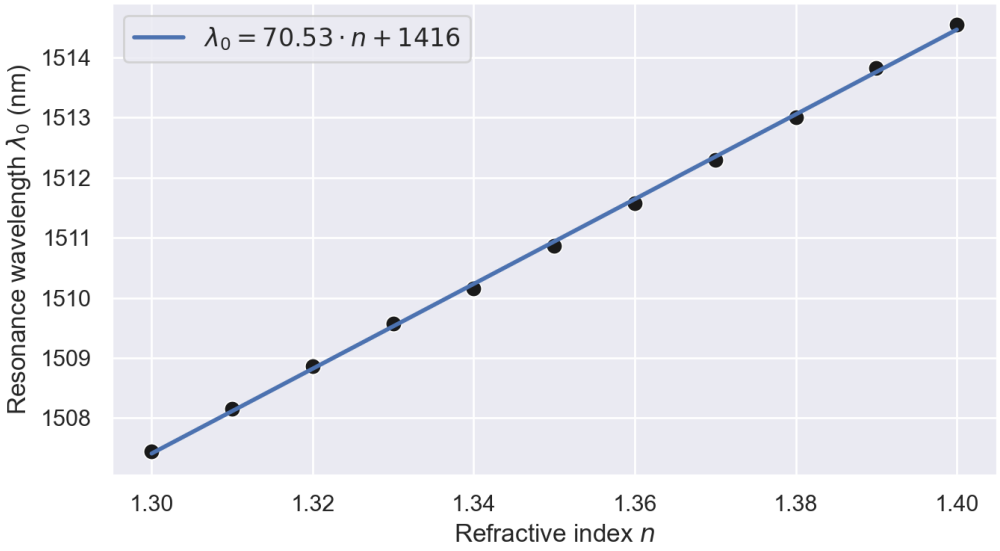

Figure 5.13: Resonance wavelength obtained from FDTD simulations as a function of the refractive index of the cavity's surrounding medium

The simulated resonance wavelength evolves approximately linearly with the refractive index of the surrounding medium. A linear regression of the data yields the relation

$$\lambda_0 \simeq 70.5 \cdot n + 1415 \ (nm) \tag{5.9}$$

This result provides an estimate of the sensitivity of the cavity resonance to refractive-index variations in its environment.

Consistency with Experimental Observations

The magnitude of this simulated sensitivity is consistent with the cavity characterization measurements. While all experimental characterizations of cavity spectra presented in this manuscript were conducted in water, additional characterizations were performed during this work to investigate the general behaviour of our structures. In particular, measurements revealed a resonance shift of approximately $20nm$ when the surrounding medium is changed from air to water.

Using the linear relation obtained above, the expected shift between air ($n = 1.000$) and water ($n \simeq 1.318$ in infrared) can be estimated as

$$\Delta\lambda(water - air) = 70.5 \times (1.318 - 1.000) \simeq 22.4\,\text{nm} \tag{5.10}$$

which is coherent with the experimentally observed shift of approximately $18 - 24\,\text{nm}$, as illustrated by the representative spectra shown in fig. 5.14. This agreement indicates that the numerical calibration captures the dominant physical mechanism governing the resonance response of the cavity to variations of the surrounding RI.

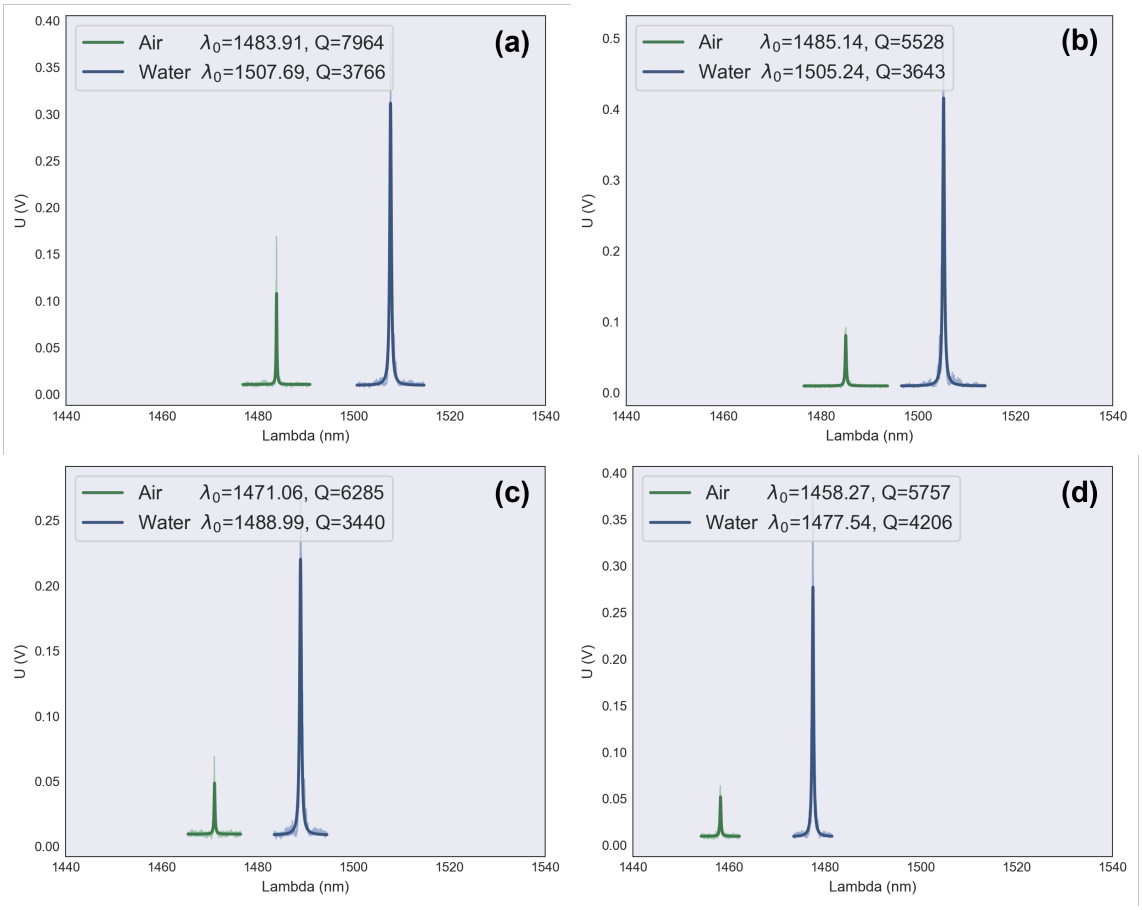

Figure 5.14: Examples of resonance spectra of different CMT3 cavities recorded in air (green) and in deionized water (blue). The structures (a), (b), (c) and (d) have different dimensions, which explains the differences in their resonance wavelengths. The respective wavelength shifts $\Delta\lambda$ between air and water are 23.78 nm, 20.1 nm, 17.93 nm and 19.27 nm.

Field Overlap Correction

In practice, the RI perturbation experienced by the cavity mode during a trapping experiment does not correspond directly to the global refractive index of the bacterium. Instead, the bacterium occupies only a small fraction of the optical mode volume and therefore perturbs the effective index of the mode only partially. Moreover, the cavity probes primarily the membrane region through its evanescent field extending roughly 100 nm above the chip surface.

To account for this effect, we introduce a field-overlap factor F describing the fraction of the optical mode energy that effectively interacts with the bacterial membrane through the evanescent field. The effective RI perturbation perceived by the cavity mode can therefore be written as

$$\Delta n_{eff} = F\,|n_{membrane} - n_{water}| \tag{5.11}$$

where Δn_{eff} denotes the effective refractive-index perturbation experienced by the cavity mode as a result of the presence of the bacterium, while $n_{membrane}$ and n_{water} correspond to the intrinsic refractive indices of the bacterial membrane and of the surrounding aqueous medium, respectively.

From the numerical calibration obtained earlier, the effective RI variation associated with a wavelength shift $\Delta\lambda$ can be expressed as

$$\Delta n_{eff} = \frac{\Delta\lambda}{70.5} \tag{5.12}$$

The trapping experiments presented earlier in this chapter yielded mean wavelength shifts ranging from approximately 0.16 nm to 0.35 nm (*cf.* table 5.1) depending on the bacterial strain. Using the relation above, this corresponds to effective refractive-index perturbations in the range

$$\Delta n_{eff} \simeq 2.27 \times 10^{-3} \; - \; 4.96 \times 10^{-3} \tag{5.13}$$

To estimate the corresponding overlap factor, we first consider typical global RI values reported in the literature for *E. coli*. Measurements performed at visible wavelengths indicate a whole-cell refractive index of approximately $n_{bacteria} \simeq 1.388$ at 514 nm [203], while the surrounding aqueous medium has $n_{water} \simeq 1.335$ at similar wavelengths. Assuming that the RI contrast remains of the same order at infrared wavelengths, the characteristic index difference can be approximated as

$$\Delta n_{bacteria} = |n_{bacteria} - n_{water}| \simeq 0.053 \tag{5.14}$$

This estimate relies on three main assumptions: (i) the global RI measured for *E. coli* at visible wavelengths is representative of the RI in the membrane region probed by the cavity evanescent field, which is likely an underestimate since most of the biomass is concentrated in the membrane, implying that the true membrane index is probably higher; (ii) the RI contrast does not vary significantly between the visible and infrared wavelengths; and (iii) the RI is assumed to be similar across all strains of the *E. coli* species, despite known strain-dependent variations in optical properties. This assumption is supported by literature values such as [203], which report a global species RI, although the specific strain investigated in that study is not explicitly specified. Overall, these assumptions are introduced solely to obtain an order-of-magnitude estimate of the overlap factor F, and do not imply that the refractive index is uniform across strains or within the bacterial cell. This approach can be interpreted as an inverse estimation problem, where the overlap factor is first calibrated using literature values, and subsequently used to infer local refractive indices from measured optical responses. The subsequent analysis relaxes these assumptions by basing the refractive indices estimations on the strain-dependent optical signatures presented earlier.

This yields an estimated range for the field-overlap factor

$$F = \frac{\Delta n_{eff}}{\Delta n_{bacteria}} \simeq 0.04 \; - \; 0.09 \tag{5.15}$$

This corresponds to an overlap between 4% and 9% of the cavity mode interacting effectively with the bacterial cell. Given that the calculation is based on the global RI rather than the local membrane index, the actual overlap with the evanescent field is likely closer to the lower bound. Therefore, we adopt $F = 4\%$ as a conservative representative value for subsequent calculations.

Estimation of Bacterial Membrane RI

Using the mean wavelength shifts obtained for each strain, the effective refractive-index perturbation can be used to estimate the local membrane RI:

$$\begin{aligned} n_{membrane} &= n_{water} + \frac{\Delta n_{eff}}{F} \\ &= n_{water} + \frac{\Delta\lambda_{bacteria}}{70.5 \times F} \end{aligned} \tag{5.16}$$

assuming $n_{water} \simeq 1.318$ in the infrared and a field overlap factor $F = 4\%$. The resulting values are summarized in table 5.2.

Strain	μ (nm)	Δn_{eff}	$n_{membrane}$
EC11	0.3007	4.27×10^{-3}	1.424
EC225	0.1687	2.39×10^{-3}	1.381
EcB	0.3281	4.65×10^{-3}	1.430
Eco0124	0.2250	3.19×10^{-3}	1.398
Eco0126	0.3587	5.09×10^{-3}	1.440
Eco0127	0.3182	4.51×10^{-3}	1.428
Eco0128	0.3554	5.04×10^{-3}	1.439
Eco0129	0.3161	4.48×10^{-3}	1.427
Eco0130	0.2991	4.24×10^{-3}	1.422
Eco0131	0.2899	4.11×10^{-3}	1.417

Table 5.2: Estimated refractive indices of the bacterial membranes derived from the measured wavelength shifts using a conservative overlap factor $F = 4\%$.

Because the overlap factor F is itself an estimate, the absolute RI values reported here should be interpreted as approximate. Propagating the uncertainty in F leads to variations of roughly $\pm(0.03 - 0.04)$ in the membrane refractive indices listed in table 5.2. The values obtained here ($n_{membrane} \simeq 1.38 - 1.44$) are thus in close agreement with reported whole-cell *E. coli* refractive indices around $n \simeq 1.38$ [203]. The systematically higher values observed here are consistent with the fact that the measurement probes a localized, biomolecule-rich region of the cell. More generally, while current literature does not report the precise RI of the *E. coli* membrane itself, dense cellular structures are known to exhibit higher refractive indices than bulk averages due to their increased biomolecular content [233–235]. Therefore, the present results provide strain-resolved estimates of the effective refractive index in the probed membrane region, highlighting a level of variation that is not captured by bulk whole-cell measurements reported in the literature.

These observations motivate a deeper investigation of the structural and biochemical determinants that may influence the optical response of the cavity. In particular, variations in membrane composition, intracellular density, or cell envelope structure may affect the effective refractive index of the cell and thereby modify the optical perturbation experienced by the cavity mode. Establishing these links requires combining the optical measurements with genomic information about the investigated strains, which is the focus of the following section.

5.7 Genomic Correlation

The trapping campaign described in this chapter led to two observations that are particularly relevant for understanding the sensitivity criteria of the CMT3 optical cavity. First, we established a clear partition among the tested *E. coli* strains: some could be optically trapped in a stable and reproducible manner, whereas others could not. This partition is presented in table 4.1. Second, within the subset of successfully trapped strains, the supervised classification revealed recurrent confusion patterns between specific pairs or small groups of strains. These confusions were not randomly distributed but appeared consistently across cross-validation folds.

Taken together, these observations suggest that the device is sensitive to spatially and structurally complex variations of refractive index. If the cavity response were governed solely by bulk refractive index contrast, one would expect relatively uniform trapping behavior within a single bacterial species. Instead, the selective trapping capability and the inter-strain confusions indicate sensitivity to more specific cellular properties. These may include subtle differences in morphology, membrane composition, surface proteins, mechanical stiffness, or intracellular organization. All of these properties are ultimately encoded at the genomic level in the DNA of each strain.

Motivated by this hypothesis, a preliminary investigation was initiated to explore whether the observed optical behavior could be related to genomic differences between strains. The objective was to determine whether strains that behave similarly in the cavity, either by not being trapped or by producing mutually confusable signatures, also share identifiable genetic features. This work was started toward the end of the PhD in collaboration with a post-doctoral colleague, Louis GIVELET. Although it directly originates from the experimental results presented here, the genomic interpretation extends beyond the initial scope of this thesis and requires specific bioinformatics expertise, currently being conducted by GIVELET. For this reason, and due to time limitations, the analysis remains ongoing.

The approach used here consists of constructing a database containing the full DNA sequences of the 16 strains considered in this study, including 10 trapped and 6 non-trapped strains, and performing systematic comparative analyses. For perspective, a typical *E. coli* genome contains on the order of 4 to 5×10^6 base pairs, organised into approximately 4000-5000 genes [236]. A large fraction of these genes belong to the core genome shared by all strains of the species, but the exact number depends on the number of strains included in the comparison. For example, approximately 2200 core genes were identified in the 20-strain dataset analysed by Touchon et al. [236]. The differences between strains are therefore encoded in a more limited subset of variable genes, commonly referred to as the accessory genome. Although smaller than the core genome, this variable fraction still represents several hundreds of genes, which makes direct interpretation non-trivial. Therefore, identifying meaningful correlations requires isolating relatively subtle variations within a largely common genetic background.

Consequently, the comparison cannot be reduced to a simple pairwise alignment. Instead, the analysis combines automated sequence comparison with specifically defined logical operations tailored to the hypotheses under investigation, for example the presence or absence of gene families related to membrane structure, metabolic pathways, or surface-associated proteins. This procedure is both technically demanding and time-consuming. Furthermore, given the limited number of strains included in the present study, the statistical robustness remains constrained. Several candidate correlations have been identified, but additional refinement and validation are required before drawing firm conclusions.

At this stage, the analysis should therefore be regarded as exploratory. Nevertheless, it constitutes a first step toward determining whether the optical trapping selectivity observed in this work can be linked, even indirectly, to genomic-level determinants of bacterial phenotype.

Preliminary observations from this ongoing work suggest that some of the candidate correlations may involve genetic elements related to cell envelope composition, in particular lipopolysaccharide (LPS) structure, as well as motility-associated features such as flagellar components. While these indications remain to be confirmed and are not yet sufficient to establish a direct causal link, they point toward biologically meaningful parameters that could underlie the sensitivity of our photonic chip.

5.8 Conclusions and Perspectives

In this chapter, we discussed the development of an experimental protocol for optical trapping of bacterial cells, focused particularly on extended data collection campaigns using a photonic chip with an integrated fluidic system developed during this PhD (*cf.* Chapter 2).

The measurements obtained throughout these campaigns were shown to be reliable, notably through the intra-strain variability analysis, which demonstrated high reproducibility metrics. In this sense, the device can be expected to exhibit a consistent optical response, reflected in its transmitted signal, when interacting with similar objects. Consequently, this result suggests that the CMT3 cavity may serve as a tool to probe heterogeneities within populations that are assumed to be homogeneous. Such an application would, however, require further optimisation and partial automatisation of the experimental sequence, so that trapping, probing, and release cycles could be performed on individual cells with limited, or ideally no manual intervention as is the case for our current protocol. This upgrade would enable faster screening of larger populations and increase the likelihood of detecting rare or atypical events.

Furthermore, we showed that the optical response of the cavity can be used to derive approximate refractive index estimates for individual bacterial strains from the wavelength shifts induced during trapping under the infrared operating conditions of the cavity. The resulting values are consistent with literature reports for *E. coli* and provide an additional physical interpretation of the optical signatures observed across strains.

At the same time, the relatively narrow range of refractive indices extracted for the different strains provides a plausible explanation for the partial overlaps observed in the classification analysis. Because the optical perturbation induced by the bacterium is largely governed by refractive-index contrast within the evanescent field region of the cavity mode, strains with similar refractive indices are expected to generate comparable optical responses. The classification results may therefore reflect groups of optical similarity rather than purely stochastic misclassification events. Clarifying the precise cellular features that determine these optical similarities remains an open question and constitutes an important direction for future investigations.

The classification analysis presented here relied on a single classifier and on statistical descriptors derived from the distribution of the transmitted signal, without explicitly accounting for its temporal structure. While this approach provides a robust representation of the overall cavity perturbation, it neglects potential dynamical information contained in the time evolution of the signal. Incorporating temporal features could therefore provide additional insight into cell-cavity interactions. In particular, a frequency-domain analysis of the transmittance signal (e.g., via Fourier transform or related spectral methods) may reveal characteristic signatures associated with short- or long-timescale evolution of dynamics such as cell motion, fluctuations, or trapping stability. Such approaches could complement the current descriptors and improve the discriminative power of classification models.

Improving our understanding of the device response will also require larger datasets, including a higher number of signals per strain, as well as the extension of the study to additional bacterial strains and other species exhibiting a broader diversity of structural and morphological features. Such extensions would make it possible to probe how variations in cell envelope composition, size, or motility-related structures influence the optical response of the cavity. Expanding the dataset would also enable testing of more advanced classification approaches, potentially revealing finer inter-strain or inter-species separability within the optical response.

Such extended data campaigns would, however, rely on the availability of stable and durable optofluidic chips. In particular, improvements in the robustness of the fluidic system and in the development of reliable cleaning protocols are necessary to prevent the degradation issues described earlier in this manuscript, which currently limit chip lifetime to a few weeks of operation. This practical constraint represented a significant challenge during this PhD and constitutes an important direction for future work aimed at increasing the longevity and usability of integrated optofluidic platforms.

Overall, this chapter demonstrates that integrated photonic cavities can reproducibly trap bacterial cells and probe their optical properties at the single-cell level. In addition to strain-level classification analyses, the results establish a methodological framework for estimating the effective refractive index of bacterial cells from their optical interaction with a confined cavity mode. Together, these findings highlight the potential of integrated photonic cavities as sensitive probes of biological matter and provide a methodological and experimental basis upon which more systematic, larger-scale, and application-driven investigations can be built.

Conclusion

This thesis was motivated by a simple but challenging question: can an integrated photonic structure be used not only to trap individual bacterial cells, but also to probe their behaviour in a controlled and, especially, reproducible way? To address this question, we developed and characterized an optofluidic platform based on one-dimensional photonic crystal resonators, and we used it to study bacterial trapping at the single-cell level. The work brought together optical trapping, microfluidic handling, surface chemistry, and bacterial electrokinetics in a single experimental framework.

At the physics level, this manuscript first established the principles underlying optical trapping and the reasons why integrated photonic structures are particularly well suited for this task. Compared with free-space setups, on-chip photonic resonators provide a compact and stable means of concentrating the optical field close to the sample. This makes them attractive not only for manipulation, but also for sensing, since the same confined field that enables trapping can also be used to detect small perturbations induced by nearby cells. In this sense, the photonic crystal cavity developed in this work is best viewed as a dual-purpose device, combining optical confinement and optical readout in the same structure.

The technical development of the chip to upgrade the pre-existing framework within the research group was a central part of the work. The introduction of inverted tapers combined with SU-8 mode adapters significantly improved the optical coupling efficiency, while the integration of the fluidic circuit made it possible to bring bacterial suspensions into controlled contact with the resonator surface. These developments were essential for turning a photonic structure into an experimental platform. They also made the measurements more controllable, which was a necessary condition for the single-cell studies carried out later in the thesis. Several practical limitations remain, particularly regarding fluidic robustness, chip lifetime, and long-term packaging, but the platform already demonstrates that integrated photonics can be adapted to bacterial trapping experiments in a reliable way.

A second major component of the thesis was the biological characterization of the system. Because the goal was to trap and probe bacteria rather than inert particles, it was necessary to understand the organisms themselves and how they react with the experimental tools used to study them. Bacteria are not simple hard spheres: their size, envelope structure, membrane composition, motility, and surface charge all influence how they interact with light and with the SOI chip surface. This is particularly important for optical trapping near a solid interface, where the evanescent field does not interact with an idealized object, but with a living cell whose properties can vary from strain to strain and from one physiological state to another.

This becomes particularly important when considering electrostatic interactions at the interface between the bacteria and the SOI surface. One of the key results of this work is that these interactions significantly influence the trapping landscape. In deionized water, both the oxidised SOI surface and the investigated *Escherichia coli* strains carry a negative electrokinetic signature, leading to a repulsive interaction at the distances relevant for trapping. This repulsion is not the dominant force in the system, since optical gradient forces remain much larger, but it is sufficient to affect the approach of cells to the resonator surface and therefore to influence trapping stability.

In other words, electrostatics does not prevent trapping in principle, but it modulates how easily the optical trap can be accessed.

The work on surface treatment and suspension medium change showed that this electrostatic barrier can be partially controlled. Coating the resonator with bovine serum albumin (BSA) reduced the effective negative charge oh the chip surface, while changing the bacterial suspension to a buffered medium (PBS) further screened the charges surrounding the bacterial membranes. These two modifications had a clear effect on the experimental behaviour: stable trapping became more frequent, transient perturbations were reduced, and the interactions with the resonator became easier to reproduce. Quantitatively, the electrostatic repulsion was reduced from the tens of femtonewtons range in deionized water to sub-femtonewton levels under the combined BSA and PBS conditions. This result shows that the interface can be tuned in a controlled way, even though the changes in electrostatic conditions alone do not fully explain the strain-dependent behaviour observed later.

Indeed, one of the most interesting outcomes of this thesis is that strain dependence did not disappear when the electrostatic environment was modified. Some strains remained impossible to trap, while others could be confined more reliably, even under similar external conditions. This indicates that trappability is not governed by a single parameter. Electrostatic interactions are important, but they are only one part of a more complex balance involving hydrodynamic conditions, membrane structure, surface heterogeneity, and possibly flagellar motility. This is an important result because it suggests that the optical response of bacteria is not only a function of the chip, but also of intrinsic biological differences between strains that the device is sensitive to, and which likely govern the observed differences in trappability. Identifying this parameter remains an open question and is currently being investigated through complementary genomic approaches within the research group.

Once the interface and operating conditions were stabilized, the optical signals of the trappable *E. coli* strains could be analysed more systematically. The trapping measurements presented in the last chapter showed that the device can operate reproducibly within a given strain, and that the transmitted optical signal contains information that can be used to compare strains. The analysis also suggested that the optical signatures are related to intrinsic cellular properties, including an estimate of the effective refractive index of the bacteria in the infrared range, a parameter that is rarely accessible at the single-cell level. While the separation between strains is still incomplete, the results indicate that the cavity response is sensitive enough to probe cell-to-cell differences at the single-cell level. This is a promising result, because it means that the same device used for trapping can also serve as a physical probe of bacterial heterogeneity.

At the same time, the limits of the current approach are clear. The analysis of the signals shows partial overlaps between strains, which means that the present descriptors are not yet sufficient to produce a robust biological classification tool at the strain level. Improving this aspect will likely require larger datasets, additional strains, and a more systematic analysis of the temporal structure of the signal. While the integration of the fluidic circuit greatly enhanced the throughput of the experiment, the current protocol is still limited by various manual steps. Further automation of the trap-record-release cycle would be a natural next step if the device is to be used for larger-scale screening.

Several practical limitations also remain on the engineering side. BSA adsorption is effective, but it is not a permanent or molecularly defined surface functionalization. In addition, changes in ionic strength alter several parameters at once, including electrostatic screening and osmotic conditions, which makes the interpretation of some results less direct. Chip lifetime and fluidic robustness also remain important constraints, especially for long experimental campaigns. These limitations do not invalidate the results of the present work; rather, they define the conditions

under which the platform can currently be used and point to the directions in which it should be improved.

Overall, this thesis shows that integrated photonic cavities can be used to trap bacterial cells and to extract meaningful physical information from the optical signals they generate. It demonstrates that the device response is not determined by optical confinement alone, but by a balance between photonic, electrostatic, hydrodynamic, and biological factors. It also shows that these factors can be controlled to some extent, making it possible to improve trapping stability and to gain access to the physical properties of individual cells.

The next steps are now clear. On the experimental side, future work should focus on improving the robustness and automation of the platform, increasing the number of recorded events, and extending the study to additional strains and species to further understand the device specificity. On the analytical side, more refined signal descriptors and temporal analyses could improve strain discrimination and help identify the specific features of the optical response that are most informative. More broadly, the results of this thesis open a route toward integrated optical tools for probing bacteria at the single-cell level, with potential applications in microbiology, biosensing, and the study of heterogeneity in microbial populations.

Bibliography

[1] M. I. Hutchings, A. W. Truman, and B. Wilkinson, "Antibiotics: Past, present and future," en, *Current Opinion in Microbiology*, vol. 51, pp. 72–80, Oct. 2019, ISSN: 13695274. DOI: 10.1016/j.mib.2019.10.008

[2] World Health Organization, *New report calls for urgent action to avert antimicrobial resistance crisis*, https://www.who.int/news/item/29-04-2019-new-report-calls-for-urgent-action-to-avert-antimicrobial-resistance-crisis, 2019.

[3] L. Novotny and B. Hecht, *Principles of Nano-Optics*, 2nd ed. Cambridge University Press, Sep. 2012, ISBN: 978-1-107-00546-4 978-0-511-79419-3. DOI: 10.1017/CBO9780511794193

[4] A. Ashkin, "Acceleration and Trapping of Particles by Radiation Pressure," en, *Physical Review Letters*, vol. 24, no. 4, pp. 156–159, Jan. 1970, ISSN: 0031-9007. DOI: 10.1103/PhysRevLett.24.156

[5] A. Ashkin, J. M. Dziedzic, and T. Yamane, "Optical trapping and manipulation of single cells using infrared laser beams," en, *Nature*, vol. 330, no. 6150, pp. 769–771, Dec. 1987, ISSN: 0028-0836, 1476-4687. DOI: 10.1038/330769a0

[6] P. M. Bendix, L. Jauffred, K. Norregaard, and L. B. Oddershede, "Optical trapping of nanoparticles and quantum dots," *IEEE Journal of Selected Topics in Quantum Electronics*, vol. 20, no. 3, pp. 15–26, 2014. DOI: 10.1109/JSTQE.2013.2287094

[7] S. E. S. Spesyvtseva and K. Dholakia, "Trapping in a Material World," en, *ACS Photonics*, vol. 3, no. 5, pp. 719–736, May 2016, ISSN: 2330-4022, 2330-4022. DOI: 10.1021/acsphotonics.6b00023

[8] L. Hartung, M. Seubert, S. Welte, E. Distante, and G. Rempe, "A quantum-network register assembled with optical tweezers in an optical cavity," en, *Science*, vol. 385, no. 6705, pp. 179–183, Jul. 2024, arXiv:2407.09109 [quant-ph], ISSN: 0036-8075, 1095-9203. DOI: 10.1126/science.ado6471

[9] O. M. Maragò, P. H. Jones, P. G. Gucciardi, G. Volpe, and A. C. Ferrari, "Optical trapping and manipulation of nanostructures," en, *Nature Nanotechnology*, vol. 8, no. 11, pp. 807–819, Nov. 2013, ISSN: 1748-3387, 1748-3395. DOI: 10.1038/nnano.2013.208

[10] U. M. S. Andrade, A. M. Garcia, and M. S. Rocha, "Bessel beam optical tweezers for manipulating superparamagnetic beads," en, *Applied Optics*, vol. 60, no. 12, p. 3422, Apr. 2021, ISSN: 1559-128X, 2155-3165. DOI: 10.1364/AO.420600

[11] W. H. Campos et al., "Germanium microparticles as optically induced oscillators in optical tweezers," en, *Physical Review Research*, vol. 1, no. 3, p. 033 119, Nov. 2019, ISSN: 2643-1564. DOI: 10.1103/PhysRevResearch.1.033119

[12] T. Moura, U. Andrade, J. Mendes, and M. Rocha, "Modulating the trapping and manipulation of semiconductor particles using Bessel beam optical tweezers," en, *Optics and Lasers in Engineering*, vol. 170, p. 107 778, Nov. 2023, ISSN: 01438166. DOI: 10.1016/j.optlaseng.2023.107778

[13] S. C. Chapin, V. Germain, and E. R. Dufresne, "Automated trapping, assembly, and sorting with holographic optical tweezers," en, *Optics Express*, vol. 14, no. 26, p. 13 095, Dec. 2006, ISSN: 1094-4087. DOI: 10.1364/OE.14.013095

[14] L. Lin et al., "Opto-thermophoretic assembly of colloidal matter," en, *Science Advances*, vol. 3, no. 9, e1700458, Sep. 2017, ISSN: 2375-2548. DOI: 10.1126/sciadv.1700458

[15] D. G. Grier and Y. Roichman, "Holographic optical trapping," en, *Applied Optics*, vol. 45, no. 5, p. 880, Feb. 2006, ISSN: 0003-6935, 1539-4522. DOI: 10.1364/AO.45.000880

[16] M. M. Burns, J.-M. Fournier, and J. A. Golovchenko, "Optical binding," en, *Physical Review Letters*, vol. 63, no. 12, pp. 1233–1236, Sep. 1989, ISSN: 0031-9007. DOI: 10.1103/PhysRevLett.63.1233

[17] A. Ashkin, J. M. Dziedzic, J. E. Bjorkholm, and S. Chu, "Observation of a single-beam gradient force optical trap for dielectric particles," *Opt. Lett.*, vol. 11, no. 5, pp. 288–290, May 1986, Publisher: Optica Publishing Group. DOI: 10.1364/OL.11.000288

[18] S. Chu, J. E. Bjorkholm, A. Ashkin, and A. Cable, "Experimental Observation of Optically Trapped Atoms," en, *Physical Review Letters*, vol. 57, no. 3, pp. 314–317, Jul. 1986, ISSN: 0031-9007. DOI: 10.1103/PhysRevLett.57.314

[19] A. Ashkin and J. M. Dziedzic, "Optical trapping and manipulation of viruses and bacteria," *Science*, vol. 235, no. 4795, pp. 1517–1520, 1987. DOI: 10.1126/science.3547653

[20] N. B. Viana, M. S. Rocha, O. N. Mesquita, A. Mazolli, P. A. M. Neto, and H. M. Nussenzveig, "Towards absolute calibration of optical tweezers," en, *Applied Physics Letters*, vol. 88, no. 13, p. 131 110, Mar. 2006, arXiv:physics/0612252, ISSN: 0003-6951, 1077-3118. DOI: 10.1063/1.2189148

[21] K. C. Neuman and S. M. Block, "Optical trapping," en, *Review of Scientific Instruments*, vol. 75, no. 9, pp. 2787–2809, Sep. 2004, ISSN: 0034-6748, 1089-7623. DOI: 10.1063/1.1785844

[22] E. Fällman and O. Axner, "Design for fully steerable dual-trap optical tweezers," en, *Applied Optics*, vol. 36, no. 10, p. 2107, Apr. 1997, ISSN: 0003-6935, 1539-4522. DOI: 10.1364/AO.36.002107

[23] I. A. Favre-Bulle et al., "Sound generation in zebrafish with Bio-Opto-Acoustics," en, *Nature Communications*, vol. 11, no. 1, p. 6120, Nov. 2020, ISSN: 2041-1723. DOI: 10.1038/s41467-020-19982-5

[24] K. Visscher, G. J. Brakenhoff, and J. J. Krol, "Micromanipulation by "multiple" optical traps created by a single fast scanning trap integrated with the bilateral confocal scanning laser microscope," en, *Cytometry*, vol. 14, no. 2, pp. 105–114, Jan. 1993, ISSN: 0196-4763, 1097-0320. DOI: 10.1002/cyto.990140202

[25] D. G. Grier, "A revolution in optical manipulation," en, *Nature*, vol. 424, no. 6950, pp. 810–816, Aug. 2003, ISSN: 0028-0836, 1476-4687. DOI: 10.1038/nature01935

[26] Y. Pang, H. Song, J. H. Kim, X. Hou, and W. Cheng, "Optical trapping of individual human immunodeficiency viruses in culture fluid reveals heterogeneity with single-molecule resolution," en, *Nature Nanotechnology*, vol. 9, no. 8, pp. 624–630, Aug. 2014, ISSN: 1748-3387, 1748-3395. DOI: 10.1038/nnano.2014.140

[27] A. A.-B. N'guessan, P. Yale, E. J. M. Konin, M. A. Kouacou, and Z. T. Jérémie, "Characterization of red blood cells infected by Plasmodium falciparum using optical tweezers," en, *Scientific African*, vol. 27, e02553, Mar. 2025, ISSN: 24682276. DOI: 10.1016/j.sciaf.2025.e02553

[28] X. Liu, Q. Gao, Y. Zhang, Y. Li, and B. Li, "In Vivo Optofluidic Switch for Controlling Blood Microflow," en, *Advanced Science*, vol. 7, no. 14, p. 2 001 414, Jul. 2020, ISSN: 2198-3844, 2198-3844. DOI: 10.1002/advs.202001414

[29] M.-C. Zhong, X.-B. Wei, J.-H. Zhou, Z.-Q. Wang, and Y.-M. Li, "Trapping red blood cells in living animals using optical tweezers," en, *Nature Communications*, vol. 4, no. 1, p. 1768, Apr. 2013, ISSN: 2041-1723. DOI: 10.1038/ncomms2786

[30] H.-C. Chen and C.-J. Cheng, "Holographic Optical Tweezers: Techniques and Biomedical Applications," en, *Applied Sciences*, vol. 12, no. 20, p. 10 244, Oct. 2022, ISSN: 2076-3417. DOI: 10.3390/app122010244

[31] D. S. Yadav and T. Savopol, "Optical tweezers in biomedical research – progress and techniques," en, *Journal of Medicine and Life*, vol. 17, no. 11, pp. 978–993, Nov. 2024, ISSN: 1844-3117. DOI: 10.25122/jml-2024-0316

[32] B. A. Koss and D. G. Grier, "Optical peristalsis," en, *Applied Physics Letters*, vol. 82, no. 22, pp. 3985–3987, Jun. 2003, ISSN: 0003-6951, 1077-3118. DOI: 10.1063/1.1579859

[33] B. Kemper et al., "Towards 3D modelling and imaging of infection scenarios at the single cell level using holographic optical tweezers and digital holographic microscopy," en, *Journal of Biophotonics*, vol. 6, no. 3, pp. 260–266, Mar. 2013, ISSN: 1864-063X, 1864-0648. DOI: 10.1002/jbio.201200057

[34] E. A. Abbondanzieri, W. J. Greenleaf, J. W. Shaevitz, R. Landick, and S. M. Block, "Direct observation of base-pair stepping by RNA polymerase," en, *Nature*, vol. 438, no. 7067, pp. 460–465, Nov. 2005, ISSN: 0028-0836, 1476-4687. DOI: 10.1038/nature04268

[35] I. A. Favre-Bulle, A. B. Stilgoe, E. K. Scott, and H. Rubinsztein-Dunlop, "Optical trapping *in vivo* : Theory, practice, and applications," en, *Nanophotonics*, vol. 8, no. 6, pp. 1023–1040, Jun. 2019, ISSN: 2192-8614, 2192-8606. DOI: 10.1515/nanoph-2019-0055

[36] C. J. Bustamante, Y. R. Chemla, S. Liu, and M. D. Wang, "Optical tweezers in single-molecule biophysics," en, *Nature Reviews Methods Primers*, vol. 1, no. 1, p. 25, Mar. 2021, ISSN: 2662-8449. DOI: 10.1038/s43586-021-00021-6

[37] S. Casabella, P. Scully, N. Goddard, and P. Gardner, "Automated analysis of single cells using Laser Tweezers Raman Spectroscopy," en, *The Analyst*, vol. 141, no. 2, pp. 689–696, 2016, ISSN: 0003-2654, 1364-5528. DOI: 10.1039/C5AN01851J

[38] W. Shuyun et al., "Laser tweezer Raman spectroscopy combined with deep neural networks for identification of liver cancer cells," en, *Talanta*, vol. 264, p. 124 753, Nov. 2023, ISSN: 00399140. DOI: 10.1016/j.talanta.2023.124753

[39] Y. Wang et al., "Visualizing the mechanical activation of Src," en, *Nature*, vol. 434, no. 7036, pp. 1040–1045, Apr. 2005, ISSN: 0028-0836, 1476-4687. DOI: 10.1038/nature03469

[40] F. Svedberg, Z. Li, H. Xu, and M. Käll, "Creating Hot Nanoparticle Pairs for Surface-Enhanced Raman Spectroscopy through Optical Manipulation," en, *Nano Letters*, vol. 6, no. 12, pp. 2639–2641, Dec. 2006, ISSN: 1530-6984, 1530-6992. DOI: 10.1021/nl062101m

[41] A. Blázquez-Castro, "Optical Tweezers: Phototoxicity and Thermal Stress in Cells and Biomolecules," en, *Micromachines*, vol. 10, no. 8, p. 507, Jul. 2019, ISSN: 2072-666X. DOI: 10.3390/mi10080507

[42] K. C. Neuman, E. H. Chadd, G. F. Liou, K. Bergman, and S. M. Block, "Characterization of Photodamage to Escherichia coli in Optical Traps," en, *Biophysical Journal*, vol. 77, no. 5, pp. 2856–2863, Nov. 1999, ISSN: 00063495. DOI: 10.1016/S0006-3495(99)77117-1

[43] M. B. Rasmussen, L. B. Oddershede, and H. Siegumfeldt, "Optical Tweezers Cause Physiological Damage to *Escherichia coli* and *Listeria* Bacteria," en, *Applied and Environmental Microbiology*, vol. 74, no. 8, pp. 2441–2446, Apr. 2008, ISSN: 0099-2240, 1098-5336. DOI: 10.1128/AEM.02265-07

[44] A. Chowdhury, D. Waghmare, R. Dasgupta, and S. K. Majumder, "Red blood cell membrane damage by light-induced thermal gradient under optical trap," en, *Journal of Biophotonics*, vol. 11, no. 8, e201700222, Aug. 2018, ISSN: 1864-063X, 1864-0648. DOI: 10.1002/jbio.201700222

[45] Y. Liu et al., "Microthermometry of laser-heated Chinese hamster ovary cells and sperm cells," en, S. L. Jacques, Ed., San Jose, CA, United States, May 1995, p. 484. DOI: 10.1117/12.209917

[46] P. Praveen Kamath, S. Sil, V. G. Truong, and S. Nic Chormaic, "Particle trapping with optical nanofibers: A review [Invited]," en, *Biomedical Optics Express*, vol. 14, no. 12, p. 6172, Dec. 2023, ISSN: 2156-7085, 2156-7085. DOI: 10.1364/BOE.503146

[47] H. Xin, C. Cheng, and B. Li, "Trapping and delivery of Escherichia coli in a microfluidic channel using an optical nanofiber," en, *Nanoscale*, vol. 5, no. 15, p. 6720, 2013, ISSN: 2040-3364, 2040-3372. DOI: 10.1039/c3nr02088f

[48] E. Faudry and J. Fick, "Optical trapping with nanostructured optical fibers and motility analysis of Pseudomonas aeruginosa," en, *European Biophysics Journal*, vol. 54, no. 5, pp. 277–287, Jul. 2025, ISSN: 0175-7571, 1432-1017. DOI: 10.1007/s00249-025-01775-7

[49] B. S. Schmidt, A. H. J. Yang, D. Erickson, and M. Lipson, "Optofluidic trapping and transport on solid core waveguides within a microfluidic device," en, *Optics Express*, vol. 15, no. 22, p. 14 322, Oct. 2007, ISSN: 1094-4087. DOI: 10.1364/OE.15.014322

[50] V. O. Bessonov, A. D. Rozanov, and A. A. Fedyanin, "Optical Trapping and Moving of Microparticles by the Near Field of Bloch Surface Waves in Polymer Waveguides," en, *JETP Letters*, vol. 119, no. 4, pp. 261–266, Feb. 2024, ISSN: 0021-3640, 1090-6487. DOI: 10.1134/S0021364024600010

[51] E. Rigo et al., "Evanescent-field excitation and collection approach for waveguide based photonic luminescent biosensors," en, *Applied Physics B*, vol. 114, no. 4, pp. 537–544, Mar. 2014, ISSN: 0946-2171, 1432-0649. DOI: 10.1007/s00340-013-5557-4

[52] S. Gaugiran et al., "Optical manipulation of microparticles and cells on silicon nitride waveguides," en, *Optics Express*, vol. 13, no. 18, p. 6956, Sep. 2005, ISSN: 1094-4087. DOI: 10.1364/OPEX.13.006956

[53] W. Bogaerts et al., "Silicon microring resonators," en, *Laser & Photonics Reviews*, vol. 6, no. 1, pp. 47–73, Jan. 2012, ISSN: 1863-8880, 1863-8899. DOI: 10.1002/lpor.201100017

[54] Abul Kalam Ajad, M. J. Islam, M. R. Kaysir, and J. Atai, "Highly sensitive bio sensor based on WGM ring resonator for hemoglobin detection in blood samples," en, *Optik*, vol. 226, p. 166 009, Jan. 2021, ISSN: 00304026. DOI: 10.1016/j.ijleo.2020.166009

[55] L. Ali, Mahmood Uddin Mohammed, M. Khan, A. H. B. Yousuf, and M. H. Chowdhury, "High-Quality Optical Ring Resonator-Based Biosensor for Cancer Detection," en, *IEEE Sensors Journal*, vol. 20, no. 4, pp. 1867–1875, Feb. 2020, ISSN: 1530-437X, 1558-1748, 2379-9153. DOI: 10.1109/JSEN.2019.2950664

[56] Y. Tanaka, S. Kaneda, and K. Sasaki, "Nanostructured Potential of Optical Trapping Using a Plasmonic Nanoblock Pair," en, *Nano Letters*, vol. 13, no. 5, pp. 2146–2150, May 2013, ISSN: 1530-6984, 1530-6992. DOI: 10.1021/nl4005892

[57] K. Wang, E. Schonbrun, P. Steinvurzel, and K. B. Crozier, "Trapping and rotating nanoparticles using a plasmonic nano-tweezer with an integrated heat sink," en, *Nature Communications*, vol. 2, no. 1, p. 469, Sep. 2011, ISSN: 2041-1723. DOI: 10.1038/ncomms1480

[58] S. Jones, D. Andrén, P. Karpinski, and M. Käll, "Photothermal Heating of Plasmonic Nano-antennas: Influence on Trapped Particle Dynamics and Colloid Distribution," en, *ACS Photonics*, DOI: 10.1021/acsphotonics.8b00231

[59] M. Samadi et al., "Plasmonic tweezers: Towards nanoscale manipulation," en, *Optics and Lasers in Engineering*, vol. 154, p. 107 001, Jul. 2022, ISSN: 01438166. DOI: 10.1016/j.optlaseng.2022.107001

[60] J. S. Kee, S. Y. Lim, A. P. Perera, Y. Zhang, and M. K. Park, "Plasmonic nanohole arrays for monitoring growth of bacteria and antibiotic susceptibility test," en, *Sensors and Actuators B: Chemical*, vol. 182, pp. 576–583, Jun. 2013, ISSN: 09254005. DOI: 10.1016/j.snb.2013.03.053

[61] K. Syal et al., "Antimicrobial Susceptibility Test with Plasmonic Imaging and Tracking of Single Bacterial Motions on Nanometer Scale," en, *ACS Nano*, vol. 10, no. 1, pp. 845–852, Jan. 2016, ISSN: 1936-0851, 1936-086X. DOI: 10.1021/acsnano.5b05944

[62] J. Xia, Q. Qiao, G. Zhou, F. S. Chau, and G. Zhou, "Opto-Mechanical Photonic Crystal Cavities for Sensing Application," en, *Applied Sciences*, vol. 10, no. 20, p. 7080, Oct. 2020, ISSN: 2076-3417. DOI: 10.3390/app10207080

[63] M. Tardif et al., "On-Chip Optical Nano-Tweezers for Culture-Less Fast Bacterial Viability Assessment," en, *Small*, vol. 18, no. 4, p. 2 103 765, Jan. 2022, ISSN: 1613-6810, 1613-6829. DOI: 10.1002/smll.202103765

[64] E. Tartari et al., "Monitoring of Single-Cell Bacterial Lysis by Phages Within Integrated Optical Traps," en, *Advanced Optical Materials*, vol. 13, no. 6, p. 2 402 586, Feb. 2025, ISSN: 2195-1071, 2195-1071. DOI: 10.1002/adom.202402586

[65] M. Soltani et al., "Nanophotonic trapping for precise manipulation of biomolecular arrays," en, *Nature Nanotechnology*, vol. 9, no. 6, pp. 448–452, Jun. 2014, ISSN: 1748-3387, 1748-3395. DOI: 10.1038/nnano.2014.79

[66] A. Rizzo et al., "Fabrication-robust silicon photonic devices in standard sub-micron silicon-on-insulator processes," en, *Optics Letters*, vol. 48, no. 2, p. 215, Jan. 2023, ISSN: 0146-9592, 1539-4794. DOI: 10.1364/OL.476873

[67] H. Jayatilleka et al., "Post-Fabrication Trimming of Silicon Photonic Ring Resonators at Wafer-Scale," en, *Journal of Lightwave Technology*, vol. 39, no. 15, pp. 5083–5088, Aug. 2021, ISSN: 0733-8724, 1558-2213. DOI: 10.1109/JLT.2021.3079801

[68] H. S. Sözüer and K. Sevim, "Robustness of one-dimensional photonic band gaps under random variations of geometrical parameters," en, *Physical Review B*, vol. 72, no. 19, p. 195 101, Nov. 2005, ISSN: 1098-0121, 1550-235X. DOI: 10.1103/PhysRevB.72.195101

[69] K. Foubert, "Etude en champ proche optique de structures nanophotoniques couplées," Ph.D. dissertation, Agence Bibliographique de l'Enseignement Supérieur. DOI: 10.70675/86886103z63d9z4e80zaeddzc5052ee8c5a0

[70] J. B. Herzog, M. W. Knight, and D. Natelson, "Thermoplasmonics: Quantifying Plasmonic Heating in Single Nanowires," en, *Nano Letters*, vol. 14, no. 2, pp. 499–503, Feb. 2014, ISSN: 1530-6984, 1530-6992. DOI: 10.1021/nl403510u

[71] S. Jones, D. Andrén, P. Karpinski, and M. Käll, "Photothermal Heating of Plasmonic Nano-antennas: Influence on Trapped Particle Dynamics and Colloid Distribution," en, *ACS Photonics*,

[72] A. I. Kuznetsov, A. E. Miroshnichenko, M. L. Brongersma, Y. S. Kivshar, and B. Luk'yanchuk, "Optically resonant dielectric nanostructures," en, *Science*, vol. 354, no. 6314, aag2472, Nov. 2016, ISSN: 0036-8075, 1095-9203. DOI: 10.1126/science.aag2472

[73] C. Sauvan, G. Lecamp, P. Lalanne, and J. P. Hugonin, "Modal-reflectivity enhancement by geometry tuning in Photonic Crystal microcavities," en, *Optics Express*, vol. 13, no. 1, p. 245, 2005, ISSN: 1094-4087. DOI: 10.1364/OPEX.13.000245

[74] P. Lalanne, C. Sauvan, and J. Hugonin, "Photon confinement in photonic crystal nanocavities," en, *Laser & Photonics Reviews*, vol. 2, no. 6, pp. 514–526, Dec. 2008, ISSN: 1863-8880, 1863-8899. DOI: 10.1002/lpor.200810018

[75] K. Reiner. "Catalase test protocol. "[Online]. Available: https://asm.org/protocols/catalase-test-protocol

[76] M. Tardif, "Piégeage et caractérisation de bactéries par cristaux photoniques," PhD Thesis Manuscript, Université Grenoble Alpes, Nov. 2018.

[77] M. N. Polyanskiy, "Refractiveindex.info database of optical constants," en, *Scientific Data*, vol. 11, no. 1, p. 94, Jan. 2024, ISSN: 2052-4463. DOI: 10.1038/s41597-023-02898-2

[78] P.-T. Lin, T.-W. Lu, and P.-T. Lee, "Photonic crystal waveguide cavity with waist design for efficient trapping and detection of nanoparticles," en, *Optics Express*, vol. 22, no. 6, p. 6791, Mar. 2014, ISSN: 1094-4087. DOI: 10.1364/OE.22.006791

[79] "Smart Print UV datasheet." en, Accessed: Sep. 24, 2025. [Online]. Available: https://www.microlight3d.com/our-products/smartprint-uv

[80] Z. Chen and J.-B. Lee, "Biocompatibility of SU-8 and Its Biomedical Device Applications," en, *Micromachines*, vol. 12, no. 7, p. 794, Jul. 2021, ISSN: 2072-666X. DOI: 10.3390/mi12070794

[81] M. T. Madigan, K. S. Bender, D. H. Buckley, W. M. Sattley, D. A. Stahl, and T. D. Brock, *Brock biology of microorganisms*, eng, Fifteenth edition, global edition. New York, NY: Pearson, 2019, ISBN: 978-1-292-23510-3 978-1-292-23519-6.

[82] S. Baron and T. Albrecht, Eds., *Medical microbiology*, eng, 4th ed. Galveston, Tex: University of Texas Medical Branch at Galveston, Dept. of Microbiology & Immunology, 1996, ISBN: 978-0-9631172-1-2.

[83] P. A. Levin and E. R. Angert, "Small but Mighty: Cell Size and Bacteria," en, *Cold Spring Harbor Perspectives in Biology*, vol. 7, no. 7, a019216, Jul. 2015, ISSN: 1943-0264. DOI: 10.1101/cshperspect.a019216

[84] P. G. Falkowski, T. Fenchel, and E. F. Delong, "The Microbial Engines That Drive Earth's Biogeochemical Cycles," en, *Science*, vol. 320, no. 5879, pp. 1034–1039, May 2008, ISSN: 0036-8075, 1095-9203. DOI: 10.1126/science.1153213

[85] G. T. Macfarlane and S. Macfarlane, "Bacteria, Colonic Fermentation, and Gastrointestinal Health," en, *Journal of AOAC INTERNATIONAL*, vol. 95, no. 1, pp. 50–60, Jan. 2012, ISSN: 1060-3271, 1944-7922. DOI: 10.5740/jaoacint.SGE_Macfarlane

[86] Y.-J. Zhang, S. Li, R.-Y. Gan, T. Zhou, D.-P. Xu, and H.-B. Li, "Impacts of Gut Bacteria on Human Health and Diseases," en, *International Journal of Molecular Sciences*, vol. 16, no. 4, pp. 7493–7519, Apr. 2015, ISSN: 1422-0067. DOI: 10.3390/ijms16047493

[87] M. Nanda, V. Kumar, and D. Sharma, "Multimetal tolerance mechanisms in bacteria: The resistance strategies acquired by bacteria that can be exploited to 'clean-up' heavy metal contaminants from water," en, *Aquatic Toxicology*, vol. 212, pp. 1–10, Jul. 2019, ISSN: 0166445X. DOI: 10.1016/j.aquatox.2019.04.011

[88] V. H. T. Pham, J. Kim, S. Chang, and W. Chung, "Bacterial Biosorbents, an Efficient Heavy Metals Green Clean-Up Strategy: Prospects, Challenges, and Opportunities," en, *Microorganisms*, vol. 10, no. 3, p. 610, Mar. 2022, ISSN: 2076-2607. DOI: 10.3390/microorganisms10030610

[89] H. Shi, F. An, H. Lin, M. Li, J. Wu, and R. Wu, "Advances in fermented foods revealed by multi-omics: A new direction toward precisely clarifying the roles of microorganisms," en, *Frontiers in Microbiology*, vol. 13, p. 1 044 820, Dec. 2022, ISSN: 1664-302X. DOI: 10.3389/fmicb.2022.1044820

[90] F. Leroy and L. De Vuyst, "Lactic acid bacteria as functional starter cultures for the food fermentation industry," en, *Trends in Food Science & Technology*, vol. 15, no. 2, pp. 67–78, Feb. 2004, ISSN: 09242244. DOI: 10.1016/j.tifs.2003.09.004

[91] M. Diard and W.-D. Hardt, "Evolution of bacterial virulence," en, *FEMS Microbiology Reviews*, vol. 41, no. 5, pp. 679–697, Sep. 2017, ISSN: 1574-6976. DOI: 10.1093/femsre/fux023

[92] M. Kelly Cowan and H. S. (teacher), "Microbiology fundamentals: A clinical approach," en, in 2025, ch. 11, ISBN: 9781264585557.

[93] A. Van Belkum, C.-A. D. Burnham, J. W. A. Rossen, F. Mallard, O. Rochas, and W. M. Dunne, "Innovative and rapid antimicrobial susceptibility testing systems," en, *Nature Reviews Microbiology*, vol. 18, no. 5, pp. 299–311, May 2020, ISSN: 1740-1526, 1740-1534. DOI: 10.1038/s41579-020-0327-x

[94] C. McGoverin, C. Steed, A. Esan, J. Robertson, S. Swift, and F. Vanholsbeeck, "Optical methods for bacterial detection and characterization," en, *APL Photonics*, vol. 6, no. 8, p. 080 903, Aug. 2021, ISSN: 2378-0967. DOI: 10.1063/5.0057787

[95] D. H. Parks et al., "A standardized bacterial taxonomy based on genome phylogeny substantially revises the tree of life," en, *Nature Biotechnology*, vol. 36, no. 10, pp. 996–1004, Oct. 2018, ISSN: 1087-0156, 1546-1696. DOI: 10.1038/nbt.4229

[96] D. C. Yang, K. M. Blair, and N. R. Salama, "Staying in Shape: The Impact of Cell Shape on Bacterial Survival in Diverse Environments," en, *Microbiology and Molecular Biology Reviews*, vol. 80, no. 1, pp. 187–203, Mar. 2016, ISSN: 1092-2172, 1098-5557. DOI: 10.1128/MMBR.00031-15

[97] K. J. Ryan, C. G. Ray, and J. C. Sherris, Eds., *Sherris medical microbiology: an introduction to infectious diseases*, eng, 4th ed. New York: McGraw-Hill, 2004, ISBN: 978-0-8385-8529-0 978-0-07-121245-8.

[98] Q. Lu, J. Wang, A. Faghihnejad, H. Zeng, and Y. Liu, "Understanding the molecular interactions of lipopolysaccharides during E. coli initial adhesion with a surface forces apparatus," en, *Soft Matter*, vol. 7, no. 19, p. 9366, 2011, ISSN: 1744-683X, 1744-6848. DOI: 10.1039/c1sm05554b

[99] S. Micciulla, Y. Gerelli, and E. Schneck, "Structure and Conformation of Wild-Type Bacterial Lipopolysaccharide Layers at Air-Water Interfaces," en, *Biophysical Journal*, vol. 116, no. 7, pp. 1259–1269, Apr. 2019, ISSN: 00063495. DOI: 10.1016/j.bpj.2019.02.020

[100] S. Knutton, P. H. Williams, D. R. Lloyd, D. C. Candy, and A. S. McNeish, "Ultrastructural study of adherence to and penetration of cultured cells by two invasive Escherichia coli strains isolated from infants with enteritis," en, *Infection and Immunity*, vol. 44, no. 3, pp. 599–608, Jun. 1984, ISSN: 0019-9567, 1098-5522. DOI: 10.1128/iai.44.3.599-608.1984

[101] A. T. Poortinga, R. Bos, W. Norde, and H. J. Busscher, "Electric double layer interactions in bacterial adhesion to surfaces," en, *Surface Science Reports*, vol. 47, no. 1, pp. 1–32, Jun. 2002, ISSN: 01675729. DOI: 10.1016/S0167-5729(02)00032-8

[102] R. Coico, "Gram Staining," en, *Current Protocols in Microbiology*, vol. 00, no. 1, Feb. 2006, ISSN: 1934-8525, 1934-8533. DOI: 10.1002/9780471729259.mca03cs00

[103] G. Ohji et al., "Comparison of Automated Point-of-Care Gram Stainer (PoCGS®) and Manual Staining," en, *Diagnostics*, vol. 15, no. 9, p. 1137, Apr. 2025, ISSN: 2075-4418. DOI: 10.3390/diagnostics15091137

[104] L. Boyanova, "Direct Gram staining and its various benefits in the diagnosis of bacterial infections," en, *Postgraduate Medicine*, vol. 130, no. 1, pp. 105–110, Jan. 2018, ISSN: 0032-5481, 1941-9260. DOI: 10.1080/00325481.2018.1398049

[105] Biomérieux. "Api ®product presentation. "[Online]. Available: https://www.biomerieux.com/us/en/our-offer/clinical-products/api.html?anchor=accordion-683661eadc-item-cc39052d73/

[106] S. Aryal. "Api (analytical profile index) 20e test – procedure, uses and interpretation. "[Online]. Available: https://microbiologyinfo.com/api-20e-test/

[107] E. Crowley et al., "Evaluation of the VITEK 2 Gram-Negative (GN) Microbial Identification Test Card: Collaborative Study," en, *Journal of AOAC INTERNATIONAL*, vol. 95, no. 3, pp. 778–785, May 2012, ISSN: 1060-3271, 1944-7922. DOI: 10.5740/jaoacint.CS2011_17

[108] D. S. Katz. "Bacterial agglutination protocol. "[Online]. Available: https://asm.org/protocols/bacterial-agglutination-protocol

[109] Y. H. Huang, H. C. Chang, and T. C. Chang, "Development of a Latex Agglutination Test for Rapid Identification of Escherichia coli," en,

[110] H.-C. Slotved, M. Kaltoft, I. C. Skovsted, M. B. Kerrn, and F. Espersen, "Simple, Rapid Latex Agglutination Test for Serotyping of Pneumococci (Pneumotest-Latex)," en, *Journal of Clinical Microbiology*, vol. 42, no. 6, pp. 2518–2522, Jun. 2004, ISSN: 0095-1137, 1098-660X. DOI: 10.1128/JCM.42.6.2518-2522.2004

[111] B. Yang et al., "Self-made Salmonella Pullorum agglutination antigen development and its potential practical application," en, *Poultry Science*, vol. 98, no. 12, pp. 6326–6332, Dec. 2019, ISSN: 00325791. DOI: 10.3382/ps/pez453

[112] T.-F. Wu et al., "A Rapid and Low-Cost Pathogen Detection Platform by Using a Molecular Agglutination Assay," en, *ACS Central Science*, vol. 4, no. 11, pp. 1485–1494, Nov. 2018, ISSN: 2374-7943, 2374-7951. DOI: 10.1021/acscentsci.8b00447

[113] A. Zorgani and H. Ziglam, "Typhoid fever: Misuse of Widal test in Libya," en, *The Journal of Infection in Developing Countries*, vol. 8, no. 06, pp. 680–687, Jun. 2014, ISSN: 1972-2680. DOI: 10.3855/jidc.3700

[114] "Sandwich elisa protocol - methods and principles from our scientific staff." en, Accessed: Mar. 24, 2026. [Online]. Available: https://www.leinco.com/sandwich-elisa-protocol/

[115] J. Verma, S. Saxena, and S. G. Babu, "ELISA-Based Identification and Detection of Microbes," en, in *Analyzing Microbes*, D. K. Arora, S. Das, and M. Sukumar, Eds., Series Title: Springer Protocols Handbooks, Berlin, Heidelberg: Springer Berlin Heidelberg, 2013, pp. 169–186, ISBN: 978-3-642-34409-1 978-3-642-34410-7. DOI: 10.1007/978-3-642-34410-7_13

[116] N. V. Hegde et al., "Detection of the Top Six Non-O157 Shiga Toxin–Producing *Escherichia coli* O Groups by ELISA," en, *Foodborne Pathogens and Disease*, vol. 9, no. 11, pp. 1044–1048, Nov. 2012, ISSN: 1535-3141, 1556-7125. DOI: 10.1089/fpd.2012.1231

[117] M. O. Peplow, M. Correa-Prisant, M. E. Stebbins, F. Jones, and P. Davies, "Sensitivity, Specificity, and Predictive Values of Three *Salmonella* Rapid Detection Kits Using Fresh and Frozen Poultry Environmental Samples versus Those of Standard Plating," en, *Applied and Environmental Microbiology*, vol. 65, no. 3, pp. 1055–1060, Mar. 1999, ISSN: 0099-2240, 1098-5336. DOI: 10.1128/AEM.65.3.1055-1060.1999

[118] C. H. Chen, H. C. Ding, and T. C. Chang, "Rapid Identification of Bacillus cereus Based on the Detection of a 28.5-Kilodalton Cell Surface Antigen," en, *Journal of Food Protection*, vol. 64, no. 3, pp. 348–354, Mar. 2001, ISSN: 0362028X. DOI: 10.4315/0362-028X-64.3.348

[119] B. K. Kumar et al., "Development of monoclonal antibody based sandwich ELISA for the rapid detection of pathogenic Vibrio parahaemolyticus in seafood," en, *International Journal of Food Microbiology*, vol. 145, no. 1, pp. 244–249, Jan. 2011, ISSN: 01681605. DOI: 10.1016/j.ijfoodmicro.2010.12.030

[120] B. Gustafsson, "Monoclonal antibody-based enzyme-linked immunosorbent assays for identification and serotyping of Vibrio cholerae O1," en, *Journal of Clinical Microbiology*, vol. 20, no. 6, pp. 1180–1185, Dec. 1984, ISSN: 0095-1137, 1098-660X. DOI: 10.1128/jcm.20.6.1180-1185.1984

[121] P. M. Fratamico, C. DebRoy, Y. Liu, D. S. Needleman, G. M. Baranzoni, and P. Feng, "Advances in Molecular Serotyping and Subtyping of Escherichia coli†," en, *Frontiers in Microbiology*, vol. 7, May 2016, ISSN: 1664-302X. DOI: 10.3389/fmicb.2016.00644

[122] A. B. Ludi et al., "Cross-Serotype Reactivity of ELISAs Used to Detect Antibodies to the Structural Proteins of Foot-and-Mouth Disease Virus," en, *Viruses*, vol. 14, no. 7, p. 1495, Jul. 2022, ISSN: 1999-4915. DOI: 10.3390/v14071495

[123] D. W. Lacher, J. Gangiredla, S. A. Jackson, C. A. Elkins, and P. C. H. Feng, "Novel Microarray Design for Molecular Serotyping of Shiga Toxin-Producing Escherichia coli Strains Isolated from Fresh Produce," en, *Applied and Environmental Microbiology*, vol. 80, no. 15, D. W. Schaffner, Ed., pp. 4677–4682, Aug. 2014, ISSN: 0099-2240, 1098-5336. DOI: 10.1128/AEM.01049-14

[124] A. Dreyfus et al., "Comparison of the Serion IgM ELISA and Microscopic Agglutination Test for diagnosis of Leptospira spp. infections in sera from different geographical origins and estimation of Leptospira seroprevalence in the Wiwa indigenous population from Colombia," en, *PLOS Neglected Tropical Diseases*, vol. 16, no. 6, E. Wunder, Ed., e0009876, Jun. 2022, ISSN: 1935-2735. DOI: 10.1371/journal.pntd.0009876

[125] M. Alamro et al., "Phase Variation Mediates Reductions in Expression of Surface Proteins during Persistent Meningococcal Carriage," en, *Infection and Immunity*, vol. 82, no. 6, A. Camilli, Ed., pp. 2472–2484, Jun. 2014, ISSN: 0019-9567, 1098-5522. DOI: 10.1128/IAI.01521-14

[126] P. C. Feng and S. P. Reddy, "Prevalence and Diversity of Enterotoxigenic Escherichia coliStrains in Fresh Produce," en, *Journal of Food Protection*, vol. 77, no. 5, pp. 820–823, May 2014, ISSN: 0362028X. DOI: 10.4315/0362-028X.JFP-13-412

[127] EFSA Panel on Biological Hazards (EFSA BIOHAZ Panel) et al., "Whole genome sequencing and metagenomics for outbreak investigation, source attribution and risk assessment of food-borne microorganisms," en, *EFSA Journal*, vol. 17, no. 12, Dec. 2019, ISSN: 18314732, 18314732. DOI: 10.2903/j.efsa.2019.5898

[128] L. Váradi et al., "Methods for the detection and identification of pathogenic bacteria: Past, present, and future," en, *Chemical Society Reviews*, vol. 46, no. 16, pp. 4818–4832, 2017, ISSN: 0306-0012, 1460-4744. DOI: 10.1039/C6CS00693K

[129] S. Quainoo et al., "Whole-Genome Sequencing of Bacterial Pathogens: The Future of Nosocomial Outbreak Analysis," en, *Clinical Microbiology Reviews*, vol. 30, no. 4, pp. 1015–1063, Oct. 2017, ISSN: 0893-8512, 1098-6618. DOI: 10.1128/CMR.00016-17

[130] W. Gu et al., "Rapid pathogen detection by metagenomic next-generation sequencing of infected body fluids," en, *Nature Medicine*, vol. 27, no. 1, pp. 115–124, Jan. 2021, ISSN: 1078-8956, 1546-170X. DOI: 10.1038/s41591-020-1105-z

[131] M. Doll, A. L. Bryson, and T. N. Palmore, "Whole Genome Sequencing Applications in Hospital Epidemiology and Infection Prevention," en, *Current Infectious Disease Reports*, vol. 26, no. 4, pp. 115–121, Apr. 2024, ISSN: 1523-3847, 1534-3146. DOI: 10.1007/s11908-024-00836-w

[132] E. Suchman. "Polymerase chain reaction protocol. "[Online]. Available: https://asm.org/protocols/polymerase-chain-reaction-protocol

[133] M. Loeffelholz and J. Dong, "PCR and Its Variations," en, in *Advanced Techniques in Diagnostic Microbiology*, Y.-W. Tang and C. W. Stratton, Eds., Boston, MA: Springer US, 2013, pp. 273–291, ISBN: 978-1-4614-3969-1 978-1-4614-3970-7. DOI: 10.1007/978-1-4614-3970-7_15

[134] M. Kubista et al., "The real-time polymerase chain reaction," en, *Molecular Aspects of Medicine*, vol. 27, no. 2-3, pp. 95–125, Apr. 2006, ISSN: 00982997. DOI: 10.1016/j.mam.2005.12.007

[135] E. M. Elnifro, A. M. Ashshi, R. J. Cooper, and P. E. Klapper, "Multiplex PCR: Optimization and Application in Diagnostic Virology," en, *Clinical Microbiology Reviews*, vol. 13, no. 4, pp. 559–570, Oct. 2000, ISSN: 0893-8512, 1098-6618. DOI: 10.1128/CMR.13.4.559

[136] B. Vogelstein and K. W. Kinzler, "Digital PCR," en, *Proceedings of the National Academy of Sciences*, vol. 96, no. 16, pp. 9236–9241, Aug. 1999, ISSN: 0027-8424, 1091-6490. DOI: 10.1073/pnas.96.16.9236

[137] P. Kralik and M. Ricchi, "A Basic Guide to Real Time PCR in Microbial Diagnostics: Definitions, Parameters, and Everything," en, *Frontiers in Microbiology*, vol. 8, Feb. 2017, ISSN: 1664-302X. DOI: 10.3389/fmicb.2017.00108

[138] M. C. J. Maiden et al., "Multilocus sequence typing: A portable approach to the identification of clones within populations of pathogenic microorganisms," en, *Proceedings of the National Academy of Sciences*, vol. 95, no. 6, pp. 3140–3145, Mar. 1998, ISSN: 0027-8424, 1091-6490. DOI: 10.1073/pnas.95.6.3140

[139] A. A. Ramadan, "Bacterial typing methods from past to present: A comprehensive overview," en, *Gene Reports*, vol. 29, p. 101 675, Dec. 2022, ISSN: 24520144. DOI: 10.1016/j.genrep.2022.101675

[140] S. Yang and R. E. Rothman, "PCR-based diagnostics for infectious diseases: Uses, limitations, and future applications in acute-care settings," en, *The Lancet Infectious Diseases*, vol. 4, no. 6, pp. 337–348, Jun. 2004, ISSN: 14733099. DOI: 10.1016/S1473-3099(04)01044-8

[141] A. Freiwald and S. Sauer, "Phylogenetic classification and identification of bacteria by mass spectrometry," en, *Nature Protocols*, vol. 4, no. 5, pp. 732–742, May 2009, ISSN: 1754-2189, 1750-2799. DOI: 10.1038/nprot.2009.37

[142] A. Sloan, G. Wang, and K. Cheng, "Traditional approaches versus mass spectrometry in bacterial identification and typing," en, *Clinica Chimica Acta*, vol. 473, pp. 180–185, Oct. 2017, ISSN: 00098981. DOI: 10.1016/j.cca.2017.08.035

[143] R. Patel, "MALDI-TOF MS for the Diagnosis of Infectious Diseases," en, *Clinical Chemistry*, vol. 61, no. 1, pp. 100–111, Jan. 2015, ISSN: 0009-9147, 1530-8561. DOI: 10.1373/clinchem.2014.221770

[144] E. Carbonnelle et al., "MALDI-TOF mass spectrometry tools for bacterial identification in clinical microbiology laboratory," en, *Clinical Biochemistry*, vol. 44, no. 1, pp. 104–109, Jan. 2011, ISSN: 00099120. DOI: 10.1016/j.clinbiochem.2010.06.017

[145] S. Sauer et al., "Classification and Identification of Bacteria by Mass Spectrometry and Computational Analysis," en, *PLoS ONE*, vol. 3, no. 7, C.-H. Yang, Ed., e2843, Jul. 2008, ISSN: 1932-6203. DOI: 10.1371/journal.pone.0002843

[146] J. Rychert, "Benefits and Limitations of MALDI-TOF Mass Spectrometry for the Identification of Microorganisms," en, *Journal of Infectiology*, vol. 2, no. 4, pp. 1–5, Jul. 2019, ISSN: 26899981. DOI: 10.29245/2689-9981/2019/4.1142

[147] A. E. Clark, E. J. Kaleta, A. Arora, and D. M. Wolk, "Matrix-Assisted Laser Desorption Ionization–Time of Flight Mass Spectrometry: A Fundamental Shift in the Routine Practice of Clinical Microbiology," en, *Clinical Microbiology Reviews*, vol. 26, no. 3, pp. 547–603, Jul. 2013, ISSN: 0893-8512, 1098-6618. DOI: 10.1128/CMR.00072-12

[148] A. Elbehiry and A. Abalkhail, "Spectral Precision: Recent Advances in Matrix-Assisted Laser Desorption/Ionization Time-of-Flight Mass Spectrometry for Pathogen Detection and Resistance Profiling," en, *Microorganisms*, vol. 13, no. 7, p. 1473, Jun. 2025, ISSN: 2076-2607. DOI: 10.3390/microorganisms13071473

[149] C. Weis, C. Jutzeler, and K. Borgwardt, "Machine learning for microbial identification and antimicrobial susceptibility testing on MALDI-TOF mass spectra: A systematic review," en, *Clinical Microbiology and Infection*, vol. 26, no. 10, pp. 1310–1317, Oct. 2020, ISSN: 1198743X. DOI: 10.1016/j.cmi.2020.03.014

[150] R. E. Jabbour et al., "Double-Blind Characterization of Non-Genome-Sequenced Bacteria by Mass Spectrometry-Based Proteomics," en, *Applied and Environmental Microbiology*, vol. 76, no. 11, pp. 3637–3644, Jun. 2010, ISSN: 0099-2240, 1098-5336. DOI: 10.1128/AEM.00055-10

[151] P. Lasch, A. Schneider, C. Blumenscheit, and J. Doellinger, "Identification of Microorganisms by Liquid Chromatography-Mass Spectrometry (LC-MS1) and in Silico Peptide Mass Libraries," en, *Molecular & Cellular Proteomics*, vol. 19, no. 12, pp. 2125–2139, Dec. 2020, ISSN: 15359476. DOI: 10.1074/mcp.TIR120.002061

[152] Q. Zhang et al., "Accurate determination for lipidomics based on LC-tandem-MS parameters modeling, prediction, and database: Monitoring the progression of hepatocellular carcinoma," en, *Journal of Pharmaceutical and Biomedical Analysis*, vol. 223, p. 115 126, Jan. 2023, ISSN: 07317085. DOI: 10.1016/j.jpba.2022.115126

[153] S. Angeletti, "Matrix assisted laser desorption time of flight mass spectrometry (MALDI-TOF MS) in clinical microbiology," en, *Journal of Microbiological Methods*, vol. 138, pp. 20–29, Jul. 2017, ISSN: 01677012. DOI: 10.1016/j.mimet.2016.09.003

[154] Y.-P. Ho and P. M. Reddy, "Identification of Pathogens by Mass Spectrometry," en, *Clinical Chemistry*, vol. 56, no. 4, pp. 525–536, Apr. 2010, ISSN: 0009-9147, 1530-8561. DOI: 10.1373/clinchem.2009.138867

[155] C. McGoverin, C. Steed, A. Esan, J. Robertson, S. Swift, and F. Vanholsbeeck, "Optical methods for bacterial detection and characterization," en, *APL Photonics*, vol. 6, no. 8, p. 080 903, Aug. 2021, ISSN: 2378-0967. DOI: 10.1063/5.0057787

[156] A. Cambré and A. Aertsen, "Bacterial Vivisection: How Fluorescence-Based Imaging Techniques Shed a Light on the Inner Workings of Bacteria," en, *Microbiology and Molecular Biology Reviews*, vol. 84, no. 4, e00008–20, Nov. 2020, ISSN: 1092-2172, 1098-5557. DOI: 10.1128/MMBR.00008-20

[157] T. S. Gunasekera, P. V. Attfield, and D. A. Veal, "A Flow Cytometry Method for Rapid Detection and Enumeration of Total Bacteria in Milk," en, *Applied and Environmental Microbiology*, vol. 66, no. 3, pp. 1228–1232, Mar. 2000, ISSN: 0099-2240, 1098-5336. DOI: 10.1128/AEM.66.3.1228-1232.2000

[158] D. Veal, D. Deere, B. Ferrari, J. Piper, and P. Attfield, "Fluorescence staining and flow cytometry for monitoring microbial cells," en, *Journal of Immunological Methods*, vol. 243, no. 1-2, pp. 191–210, Sep. 2000, ISSN: 00221759. DOI: 10.1016/S0022-1759(00)00234-9

[159] K. M. McKinnon, "Flow Cytometry: An Overview," en, *Current Protocols in Immunology*, vol. 120, no. 1, Jan. 2018, ISSN: 1934-3671, 1934-368X. DOI: 10.1002/cpim.40

[160] H. B. Steen, "Flow cytometry of bacteria: Glimpses from the past with a view to the future," en, *Journal of Microbiological Methods*, vol. 42, no. 1, pp. 65–74, Sep. 2000, ISSN: 01677012. DOI: 10.1016/S0167-7012(00)00177-9

[161] R. G. Ashcroft and P. A. Lopez, "Commercial high speed machines open new opportunities in high throughput flow cytometry (HTFC)," en, *Journal of Immunological Methods*, vol. 243, no. 1-2, pp. 13–24, Sep. 2000, ISSN: 00221759. DOI: 10.1016/S0022-1759(00)00219-2

[162] V. Ambriz-Aviña, J. A. Contreras-Garduño, and M. Pedraza-Reyes, "Applications of Flow Cytometry to Characterize Bacterial Physiological Responses," en, *BioMed Research International*, vol. 2014, pp. 1–14, 2014, ISSN: 2314-6133, 2314-6141. DOI: 10.1155/2014/461941

[163] S. Servain-Viel et al., "A flow cytometry method for safe detection of bacterial viability," en, *Cytometry Part A*, vol. 105, no. 2, pp. 146–156, Feb. 2024, ISSN: 1552-4922, 1552-4930. DOI: 10.1002/cyto.a.24794

[164] *Flow Cytometry in Microbiology: Technology and Applications*, en. Caister Academic Press, 2015, ISBN: 978-1-910190-11-1 978-1-910190-12-8. DOI: 10.21775/9781910190111

[165] L. G. Marutescu, "Current and Future Flow Cytometry Applications Contributing to Antimicrobial Resistance Control," en, *Microorganisms*, vol. 11, no. 5, p. 1300, May 2023, ISSN: 2076-2607. DOI: 10.3390/microorganisms11051300

[166] J. Zhou et al., "Imaging flow cytometry with a real-time throughput beyond 1,000,000 events per second," en, *Light: Science & Applications*, vol. 14, no. 1, p. 76, Feb. 2025, ISSN: 2047-7538. DOI: 10.1038/s41377-025-01754-9

[167] Z. Gitai, "New fluorescence microscopy methods for microbiology: Sharper, faster, and quantitative," en, *Current Opinion in Microbiology*, vol. 12, no. 3, pp. 341–346, Jun. 2009, ISSN: 13695274. DOI: 10.1016/j.mib.2009.03.001

[168] I. Smolina, C. Lee, and M. Frank-Kamenetskii, "Detection of Low-Copy-Number Genomic DNA Sequences in Individual Bacterial Cells by Using Peptide Nucleic Acid-Assisted Rolling-Circle Amplification and Fluorescence In Situ Hybridization," en, *Applied and Environmental Microbiology*, vol. 73, no. 7, pp. 2324–2328, Apr. 2007, ISSN: 0099-2240, 1098-5336. DOI: 10.1128/AEM.02038-06

[169] C. Coltharp and J. Xiao, "Superresolution microscopy for microbiology: Superresolution microscopy for microbiology," en, *Cellular Microbiology*, vol. 14, no. 12, pp. 1808–1818, Dec. 2012, ISSN: 14625814. DOI: 10.1111/cmi.12024

[170] M. Woźniak, D. Połap, L. Kośmider, and T. Clapa, "Automated fluorescence microscopy image analysis of Pseudomonas aeruginosa bacteria in alive and dead stadium," en, *Engineering Applications of Artificial Intelligence*, vol. 67, pp. 100–110, Jan. 2018, ISSN: 09521976. DOI: 10.1016/j.engappai.2017.09.003

[171] B. Balakrishnan, S. Barizuddin, T. Wuliji, and M. El-Dweik, "A rapid and highly specific immunofluorescence method to detect Escherichia coli O157:H7 in infected meat samples," en, *International Journal of Food Microbiology*, vol. 231, pp. 54–62, Aug. 2016, ISSN: 01681605. DOI: 10.1016/j.ijfoodmicro.2016.05.017

[172] L. C. Ong, L. Y. Ang, S. Alonso, and Y. Zhang, "Bacterial imaging with photostable upconversion fluorescent nanoparticles," en, *Biomaterials*, vol. 35, no. 9, pp. 2987–2998, Mar. 2014, ISSN: 01429612. DOI: 10.1016/j.biomaterials.2013.12.060

[173] H. Jayan, H. Pu, and D.-W. Sun, "Recent developments in Raman spectral analysis of microbial single cells: Techniques and applications," en, *Critical Reviews in Food Science and Nutrition*, vol. 62, no. 16, pp. 4294–4308, Jun. 2022, ISSN: 1040-8398, 1549-7852. DOI: 10.1080/10408398.2021.1945534

[174] U. Neugebauer, P. Rösch, and J. Popp, "Raman spectroscopy towards clinical application: Drug monitoring and pathogen identification," en, *International Journal of Antimicrobial Agents*, vol. 46, S35–S39, Dec. 2015, ISSN: 09248579. DOI: 10.1016/j.ijantimicag.2015.10.014

[175] S. A. Strola et al., "Single bacteria identification by Raman spectroscopy," en, *Journal of Biomedical Optics*, vol. 19, no. 11, p. 111 610, Jul. 2014, ISSN: 1083-3668. DOI: 10.1117/1.JBO.19.11.111610

[176] J. Sun, L. Gong, W. Wang, Z. Gong, D. Wang, and M. Fan, "Surface-enhanced Raman spectroscopy for on-site analysis: A review of recent developments," en, *Luminescence*, vol. 35, no. 6, pp. 808–820, Sep. 2020, ISSN: 1522-7235, 1522-7243. DOI: 10.1002/bio.3796

[177] I. W. Schie and T. Huser, "Methods and Applications of Raman Microspectroscopy to Single-Cell Analysis," en, *Applied Spectroscopy*, vol. 67, no. 8, pp. 813–828, Aug. 2013, ISSN: 0003-7028, 1943-3530. DOI: 10.1366/12-06971

[178] J. De Gelder, K. De Gussem, P. Vandenabeele, and L. Moens, "Reference database of Raman spectra of biological molecules," en, *Journal of Raman Spectroscopy*, vol. 38, no. 9, pp. 1133–1147, Sep. 2007, ISSN: 0377-0486, 1097-4555. DOI: 10.1002/jrs.1734

[179] B. Sharma, R. R. Frontiera, A.-I. Henry, E. Ringe, and R. P. Van Duyne, "SERS: Materials, applications, and the future," en, *Materials Today*, vol. 15, no. 1-2, pp. 16–25, Jan. 2012, ISSN: 13697021. DOI: 10.1016/S1369-7021(12)70017-2

[180] K. Gaus et al., "Classification of lactic acid bacteria with UV-resonance Raman spectroscopy," en, *Biopolymers*, vol. 82, no. 4, pp. 286–290, Jul. 2006, ISSN: 0006-3525, 1097-0282. DOI: 10.1002/bip.20448

[181] Y. Qi et al., "Recent Progresses in Machine Learning Assisted Raman Spectroscopy," *Advanced Optical Materials*, vol. 11, no. 14, p. 2 203 104, Jul. 2023, ISSN: 2195-1071, 2195-1071. DOI: 10.1002/adom.202203104

[182] K. Eberhardt, C. Stiebing, C. Matthäus, M. Schmitt, and J. Popp, "Advantages and limitations of Raman spectroscopy for molecular diagnostics: An update," en, *Expert Review of Molecular Diagnostics*, vol. 15, no. 6, pp. 773–787, Jun. 2015, ISSN: 1473-7159, 1744-8352. DOI: 10.1586/14737159.2015.1036744

[183] H. J. Butler et al., "Using Raman spectroscopy to characterize biological materials," en, *Nature Protocols*, vol. 11, no. 4, pp. 664–687, Apr. 2016, ISSN: 1754-2189, 1750-2799. DOI: 10.1038/nprot.2016.036

[184] V. Erukhimovitch, V. Pavlov, M. Talyshinsky, Y. Souprun, and M. Huleihel, "FTIR microscopy as a method for identification of bacterial and fungal infections," en, *Journal of Pharmaceutical and Biomedical Analysis*, vol. 37, no. 5, pp. 1105–1108, Apr. 2005, ISSN: 07317085. DOI: 10.1016/j.jpba.2004.08.010

[185] B. Dziuba, A. Babuchowski, D. Nałęcz, and M. Niklewicz, "Identification of lactic acid bacteria using FTIR spectroscopy and cluster analysis," en, *International Dairy Journal*, vol. 17, no. 3, pp. 183–189, Mar. 2007, ISSN: 09586946. DOI: 10.1016/j.idairyj.2006.02.013

[186] H. Yang et al., "Protocol for bacterial typing using Fourier transform infrared spectroscopy," en, *STAR Protocols*, vol. 4, no. 2, p. 102 223, Jun. 2023, ISSN: 26661667. DOI: 10.1016/j.xpro.2023.102223

[187] P. I. C. Richardson, M. J. Horsburgh, and R. Goodacre, "Benchmarking classification abilities of novel optical photothermal IR spectroscopy at the single-cell level with bulk FTIR measurements," en, *Analytical Methods*, vol. 16, no. 31, pp. 5419–5425, 2024, ISSN: 1759-9660, 1759-9679. DOI: 10.1039/D4AY00810C

[188] D. Martak et al., "Fourier-Transform InfraRed Spectroscopy Can Quickly Type Gram-Negative Bacilli Responsible for Hospital Outbreaks," en, *Frontiers in Microbiology*, vol. 10, p. 1440, Jun. 2019, ISSN: 1664-302X. DOI: 10.3389/fmicb.2019.01440

[189] Â. Novais et al., "Development and validation of a quick, automated, and reproducible ATR FT-IR spectroscopy machine-learning model for *Klebsiella pneumoniae* typing," en, *Journal of Clinical Microbiology*, vol. 62, no. 2, P. J. Simner, Ed., e01211–23, Feb. 2024, ISSN: 0095-1137, 1098-660X. DOI: 10.1128/jcm.01211-23

[190] S. Shams et al., "Application of infrared spectroscopy to study carbon-deuterium kinetics and isotopic spectral shifts at the single-cell level," en, *Spectrochimica Acta Part A: Molecular and Biomolecular Spectroscopy*, vol. 327, p. 125 374, Feb. 2025, ISSN: 13861425. DOI: 10.1016/j.saa.2024.125374

[191] C. B. Prater, K. J. Kjoller, A. P. D. Stuart, D. A. Grigg, R. 'Limurn, and K. M. Gough, "Widefield super-resolution infrared spectroscopy and imaging of autofluorescent biological materials and photosynthetic microorganisms using fluorescence detected photothermal infrared (FL-PTIR)," en, *Appl. Spectrosc.*, vol. 78, no. 11, pp. 1208–1219, Nov. 2024.

[192] M. Zelsmann et al., "Seventy-fold enhancement of light extraction from a defectless photonic crystal made on silicon-on-insulator," en, *Appl. Phys. Lett.*, vol. 83, no. 13, pp. 2542–2544, Sep. 2003.

[193] B. Cluzel et al., "Experimental demonstration of bloch mode parity change in photonic crystal waveguide," *Applied Physics Letters*, vol. 85, no. 14, pp. 2682–2684, Oct. 2004, ISSN: 1077-3118. DOI: 10.1063/1.1795370

[194] P. Velha et al., "Ultra-high q/v fabry-perot microcavity on soi substrate," *Optics Express*, vol. 15, no. 24, p. 16 090, 2007, ISSN: 1094-4087. DOI: 10.1364/oe.15.016090

[195] B. Cluzel et al., "Addressable subwavelength grids of confined light in a multislotted nanoresonator," en, *Applied Physics Letters*, vol. 98, no. 8, p. 081 101, Feb. 2011, ISSN: 0003-6951, 1077-3118. DOI: 10.1063/1.3555489

[196] K. Foubert et al., "An air-slotted nanoresonator relying on coupled high q small v fabry–perot nanocavities," *Applied Physics Letters*, vol. 94, no. 25, Jun. 2009, ISSN: 1077-3118. DOI: 10.1063/1.3159820

[197] C. Renaut et al., "Assembly of microparticles by optical trapping with a photonic crystal nanocavity," *Applied Physics Letters*, vol. 100, no. 10, p. 101 103, Mar. 2012, ISSN: 1077-3118. DOI: 10.1063/1.3692104

[198] C. Pin et al., "Optical tweezing using tunable optical lattices along a few-mode silicon waveguide," *Lab on a Chip*, vol. 18, no. 12, pp. 1750–1757, 2018, ISSN: 1473-0189. DOI: 10.1039/c8lc00298c

[199] M. Tardif et al., "Single-cell bacterium identification with a SOI optical microcavity," en, *Applied Physics Letters*, vol. 109, no. 13, p. 133 510, Sep. 2016, ISSN: 0003-6951, 1077-3118. DOI: 10.1063/1.4963070

[200] R. Therisod et al., "Gram-type differentiation of bacteria with 2D hollow photonic crystal cavities," en, *Applied Physics Letters*, vol. 113, no. 11, p. 111 101, Sep. 2018, ISSN: 0003-6951, 1077-3118. DOI: 10.1063/1.5037849

[201] M. H. Adams, *Bacteriophages*. English. New York (& London): Inter-science Publishers., 1959, xviii + 592 pp.

[202] T. A. Zangle and M. A. Teitell, "Live-cell mass profiling: An emerging approach in quantitative biophysics," en, *Nature Methods*, vol. 11, no. 12, pp. 1221–1228, Dec. 2014, ISSN: 1548-7091, 1548-7105. DOI: 10.1038/nmeth.3175

[203] P. Y. Liu et al., "An optofluidic imaging system to measure the biophysical signature of single waterborne bacteria," en, *Lab Chip*, vol. 14, no. 21, pp. 4237–4243, 2014, ISSN: 1473-0197, 1473-0189. DOI: 10.1039/C4LC00783B

[204] C. L. Lewis, C. C. Craig, and A. G. Senecal, "Mass and Density Measurements of Live and Dead Gram-Negative and Gram-Positive Bacterial Populations," en, *Applied and Environmental Microbiology*, vol. 80, no. 12, J. Björkroth, Ed., pp. 3622–3631, Jun. 2014, ISSN: 0099-2240, 1098-5336. DOI: 10.1128/AEM.00117-14

[205] N. C. Darnton, L. Turner, S. Rojevsky, and H. C. Berg, "On Torque and Tumbling in Swimming *Escherichia coli*," en, *Journal of Bacteriology*, vol. 189, no. 5, pp. 1756–1764, Mar. 2007, ISSN: 0021-9193, 1098-5530. DOI: 10.1128/JB.01501-06

[206] E. M. Purcell, "The efficiency of propulsion by a rotating flagellum," en, *Proceedings of the National Academy of Sciences*, vol. 94, no. 21, pp. 11 307–11 311, Oct. 1997, ISSN: 0027-8424, 1091-6490. DOI: 10.1073/pnas.94.21.11307

[207] C. Pin, "Piégeage et manipulation d'objets colloïdaux à l'aide de structures photoniques en silicium intégrées dans des puces optofluidiques," Theses, Université de Bourgogne, Jun. 2016.

[208] A. J. De Kerchove and M. Elimelech, "Relevance of Electrokinetic Theory for "Soft" Particles to Bacterial Cells: Implications for Bacterial Adhesion," en, *Langmuir*, vol. 21, no. 14, pp. 6462–6472, Jul. 2005, ISSN: 0743-7463, 1520-5827. DOI: 10.1021/la047049t

[209] S. Perni, E. C. Preedy, and P. Prokopovich, "Success and failure of colloidal approaches in adhesion of microorganisms to surfaces," en, *Advances in Colloid and Interface Science*, vol. 206, pp. 265–274, Apr. 2014, ISSN: 00018686. DOI: 10.1016/j.cis.2013.11.008

[210] H. J. Busscher and A. H. Weerkamp, "Specific and non-specific interactions in bacterial adhesion to solid substrata," en, *FEMS Microbiology Letters*, vol. 46, no. 2, pp. 165–173, Jun. 1987, ISSN: 03781097, 15746968. DOI: 10.1111/j.1574-6968.1987.tb02457.x

[211] J. N. Israelachvili, *Intermolecular and Surface Forces*, en. Elsevier, 2011, ISBN: 9780123751829. DOI: 10.1016/c2009-0-21560-1

[212] M. J. Vold, "Zeta potential in colloid science. Principles and applications," en, *Journal of Colloid and Interface Science*, vol. 88, no. 2, p. 608, Aug. 1982, ISSN: 00219797. DOI: 10.1016/0021-9797(82)90296-X

[213] T. Luxbacher, *The zeta potential for solid surface analysis: a practical guide to streaming potential measurement*. Anton Paar GmbH, 2014.

[214] C. Werner, H. Körber, R. Zimmermann, S. Dukhin, and H.-J. Jacobasch, "Extended Electrokinetic Characterization of Flat Solid Surfaces," en, *Journal of Colloid and Interface Science*, vol. 208, no. 1, pp. 329–346, Dec. 1998, ISSN: 00219797. DOI: 10.1006/jcis.1998.5787

[215] "Zetasizer ultra - product page." nl, Accessed: Jan. 20, 2026. [Online]. Available: https://www.sysmex.nl/producten/products-detail/malvern-zetasizer-ultra/

[216] A. Lázaro García, *Nano-silica production at low temperatures from the dissolution of olovine: synthesis, tailoring and modelling* (Bouwstenen 195), en. Eindhoven: Univ. Press, 2014, ISBN: 978-90-386-3640-5.

[217] "Monodisperse silica microspheres - product page." en, Accessed: Jan. 20, 2026. [Online]. Available: https://www.cospheric.com/SiO2MS_monodisperse_silica_spheres_beads_nm_microns.htm

[218] G. V. Franks, "Zeta Potentials and Yield Stresses of Silica Suspensions in Concentrated Monovalent Electrolytes: Isoelectric Point Shift and Additional Attraction," en, *Journal of Colloid and Interface Science*, vol. 249, no. 1, pp. 44–51, May 2002, ISSN: 00219797. DOI: 10.1006/jcis.2002.8250

[219] J. Kim, "Characteristics of Zeta Potential Distribution in Silica Particles," en, *Bulletin of the Korean Chemical Society*, vol. 26, no. 7, pp. 1083–1089, Jul. 2005. DOI: 10.5012/BKCS.2005.26.7.1083

[220] D. Lee, D. Omolade, R. E. Cohen, and M. F. Rubner, "pH-Dependent Structure and Properties of TiO_2 /SiO_2 Nanoparticle Multilayer Thin Films," en, *Chemistry of Materials*, vol. 19, no. 6, pp. 1427–1433, Mar. 2007, ISSN: 0897-4756, 1520-5002. DOI: 10.1021/cm070111y

[221] L. Bousse, S. Mostarshed, B. V. D. Shoot, N. F. d. Rooij, P. Gimmel, and W. Göpel, "Zeta potential measurements of Ta2O5 and SiO2 thin films," *Journal of Colloid and Interface Science*, vol. 147, no. 1, pp. 22–32, 1991, ISSN: 0021-9797. DOI: https://doi.org/10.1016/0021-9797(91)90130-Z

[222] M. Rabe, D. Verdes, and S. Seeger, "Understanding protein adsorption phenomena at solid surfaces," en, *Advances in Colloid and Interface Science*, vol. 162, no. 1-2, pp. 87–106, Feb. 2011, ISSN: 00018686. DOI: 10.1016/j.cis.2010.12.007

[223] S. Sarkar and S. Kundu, "Structure and morphology of adsorbed protein (BSA) layer on hydrophilic silicon surface in presence of mono-, di- and tri-valent ions," en, *JCIS Open*, vol. 3, p. 100 016, Oct. 2021, ISSN: 2666934X. DOI: 10.1016/j.jciso.2021.100016

[224] A. Chiadò et al., "Optimization and characterization of a homogeneous carboxylic surface functionalization for silicon-based biosensing," en, *Colloids and Surfaces B: Biointerfaces*, vol. 143, pp. 252–259, Jul. 2016, ISSN: 09277765. DOI: 10.1016/j.colsurfb.2016.03.048

[225] A. Scarangella et al., "Adsorption properties of BSA and DsRed proteins deposited on thin SiO_2 layers: Optically non-absorbing versus absorbing proteins," en, *Nanotechnology*, vol. 29, no. 11, p. 115 101, Mar. 2018, ISSN: 0957-4484, 1361-6528. DOI: 10.1088/1361-6528/aaa68b

[226] B. Jachimska and A. Pajor, "Physico-chemical characterization of bovine serum albumin in solution and as deposited on surfaces," en, *Bioelectrochemistry*, vol. 87, pp. 138–146, Oct. 2012, ISSN: 15675394. DOI: 10.1016/j.bioelechem.2011.09.004

[227] W. Norde, "My voyage of discovery to proteins in flatland ... and beyond," en, *Colloids and Surfaces B: Biointerfaces*, vol. 61, no. 1, pp. 1–9, Jan. 2008, ISSN: 09277765. DOI: 10.1016/j.colsurfb.2007.09.029

[228] B. Alberts et al., *Molecular Biology of the Cell*, 6th. Garland Science, 2015.

[229] J. D. Joannopoulos, J. N. Winn, and S. G. Johnson, *Photonic Crystals: Molding the Flow of Light - Second Edition*, en. Princeton, NJ: Princeton University Press, 2011, ISBN: 978-0-691-12456-8 978-1-4008-2824-1. DOI: 10.1515/9781400828241

[230] M. Holmes, J. Keeley, K. Hurd, H. Schmidt, and A. Hawkins, "Optimized piranha etching process for SU8-based MEMS and MOEMS construction," en, *Journal of Micromechanics and Microengineering*, vol. 20, no. 11, p. 115 008, Nov. 2010, ISSN: 0960-1317, 1361-6439. DOI: 10.1088/0960-1317/20/11/115008

[231] G. Wypych, *Handbook of material weathering*, en, 5th edition. Toronto: ChemTec Publishing, 2013, ISBN: 978-1-895198-62-1.

[232] A. D. Campo and C. Greiner, "SU-8: A photoresist for high-aspect-ratio and 3D submicron lithography," en, *Journal of Micromechanics and Microengineering*, vol. 17, no. 6, R81–R95, Jun. 2007, ISSN: 0960-1317, 1361-6439. DOI: 10.1088/0960-1317/17/6/R01

[233] B. Gul, S. Ashraf, S. Khan, H. Nisar, and I. Ahmad, "Cell refractive index: Models, insights, applications and future perspectives," en, *Photodiagnosis and Photodynamic Therapy*, vol. 33, p. 102 096, Mar. 2021, ISSN: 15721000. DOI: 10.1016/j.pdpdt.2020.102096

[234] R. E. Marquis, "Immersion Refractometry of Isolated Bacterial Cell Walls," en, *Journal of Bacteriology*, vol. 116, no. 3, pp. 1273–1279, Dec. 1973, ISSN: 0021-9193, 1098-5530. DOI: 10.1128/jb.116.3.1273-1279.1973

[235] J. A. Welsh, J. Kepley, A. Rosner, P. Horak, J. A. Berzofsky, and J. C. Jones, "Prospective Use of High-Refractive Index Materials for Single Molecule Detection in Flow Cytometry," en, *Sensors*, vol. 18, no. 8, p. 2461, Aug. 2018, ISSN: 1424-8220. DOI: 10.3390/s18082461

[236] M. Touchon et al., "Organised Genome Dynamics in the Escherichia coli Species Results in Highly Diverse Adaptive Paths," en, *PLoS Genetics*, vol. 5, no. 1, J. Casadesús, Ed., e1000344, Jan. 2009, ISSN: 1553-7404. DOI: 10.1371/journal.pgen.1000344

[237] P. Shields and A. Y. Tsang. "Mannitol salt agar plates protocols. "[Online]. Available: https://asm.org/protocols/mannitol-salt-agar-plates-protocols

[238] M. E. Allen. "Macconkey agar plates protocol. "[Online]. Available: https://asm.org/protocols/macconkey-agar-plates-protocols

[239] E. staff. "Difference between selective and differential media. "[Online]. Available: https://www.labtestsguide.com/difference-between-selective-and-differential-media

[240] P. Shields and L. Cathcart. "Oxidase test protocol. "[Online]. Available: https://asm.org/protocols/oxidase-test-protocol

[241] S. Shanmugavelu, G. Ruzickova, J. Zrustova, and J. Brooker, "A fermentation assay to evaluate the effectiveness of antimicrobial agents on gut microflora," en, *Journal of Microbiological Methods*, vol. 67, no. 1, pp. 93–101, Oct. 2006, ISSN: 01677012. DOI: 10.1016/j.mimet.2006.03.005

[242] M. Hedberg, P. Hasslöf, I. Sjöström, S. Twetman, and C. Stecksén-Blicks, "Sugar fermentation in probiotic bacteria – an *in vitro* study," en, *Oral Microbiology and Immunology*, vol. 23, no. 6, pp. 482–485, Dec. 2008, ISSN: 0902-0055, 1399-302X. DOI: 10.1111/j.1399-302X.2008.00457.x

[243] D. Lehman. "Triple sugar iron agar protocols. "[Online]. Available: https://asm.org/protocols/triple-sugar-iron-agar-protocols

A

Appendix 1 : Additional Microbiology Methods and Practices

This appendix gathers complementary material related to the microbiological aspects introduced in chapter 3. It includes methodological details that, while not central to the main discussion, provide useful context for standard laboratory practices. In particular, additional information on sample preparation, culture conditions, and classical biochemical identification techniques is presented here to support the understanding of experimental workflows and to offer extended background for interested readers.

A.1 Sample Preparation

Bacterial samples used for scientific research must be carefully prepared, stored, and maintained to preserve their viability and genetic stability. In laboratory settings, bacteria are typically grown in or on nutrient-rich media that provide essential sources of carbon, nitrogen, and minerals required for growth. Solid media, such as agar plates in Petri dishes, are used for isolating individual colonies, while liquid cultures in flasks or tubes allow for large-scale growth and experimental manipulation.

Once pure cultures are obtained, bacterial stocks are usually preserved by mixing cells with cryoprotective agents such as glycerol and storing them at $-80°C$, which prevents ice crystal formation and long-term damage to cellular structures. In most research contexts, these purified and frozen samples are purchased from certified suppliers that maintain industrial-scale quality control to ensure purity and consistency. Commercially distributed strains are often registered with the American Type Culture Collection (ATCC) or similar repositories, where each receives a unique identification code to ensure traceability and reproducibility between laboratories (for example, *Staphylococcus aureus* ATCC 25923).

Before experiments, small portions of frozen stock are thawed and cultivated under defined conditions such as optimal incubation temperature, aeration, growth medium composition, and

culture format (solid or liquid), all tailored to the species of interest and the expected duration of cultivation. For short-term storage, working cultures can be refrigerated at 4°C to minimize genetic drift and contamination. Proper sample preparation and storage are fundamental to reproducibility, biosafety, and the reliability of downstream analyses.

A.2 Extended Culture-Based and Biochemical Methods

Overview

In addition to the main identification methods presented in chapter 3, a number of classical culture-based and biochemical techniques have historically played a central role in microbiology. While some of these approaches are now less commonly used in modern high-throughput or single-cell analyses, they remain important for understanding the foundations of bacterial identification. This section provides a brief overview of such methods, including selective and differential media as well as common biochemical assays.

Selective and Differential Media

Culture media are the foundation of bacterial isolation, providing the nutrients and physical support necessary for growth. General-purpose media such as Tryptic Soy Agar (TSA) and Columbia Blood Agar are widely used because they support a broad range of bacterial species. TSA contains enzymatic digests of casein and soybean meal, while Columbia Blood Agar incorporates sheep or horse blood. The choice of medium depends largely on the nutritional requirements of the target bacteria and the diagnostic goal of the experiment, whether it is to recover as many species as possible or to focus on specific groups.

When using these generic media, several colony characteristics can be observed, including size, color, texture, and even odor. These features, while informative, remain very broad. Therefore, when the goal shifts from general cultivation to targeted isolation and identification, selective and differential media are used. These formulations introduce specific biochemical agents into the agar in addition to, or instead of, basic nutrients. Selective media restrict the growth of unwanted organisms, while differential components reveal metabolic properties through color change or distinctive colony morphology. It is also possible to combine both functions within a single formulation, producing media that are simultaneously selective and differential.

Widely used examples of such media are Mannitol Salt Agar (MSA) and MacConkey agar. MSA contains a high sodium chloride (NaCl) concentration, typically between 7.5 % and 10 %, which inhibits the growth of most bacterial genera except *Staphylococcus*, *Enterococcus*, and *Micrococcaceae*. This defines its selectivity. Within the *Staphylococcus* genus, MSA differentiates *S. aureus*, which ferments mannitol and causes the medium to change from red to yellow. [237] These characteristics are illustrated in fig. A.1(a).

Following the same principle, MacConkey agar contains bile salts and crystal violet to suppress Gram-positive bacteria, thereby selecting for Gram-negative ones. This medium also contains lactose, a sugar naturally present in milk, and a neutral red pH indicator that turns pink when lactose is fermented [238]. Fermenters such as *Escherichia coli* therefore produce pink colonies, while non-fermenters like *Salmonella* or *Shigella* remain colorless. These characteristics are shown in fig. A.1(b).

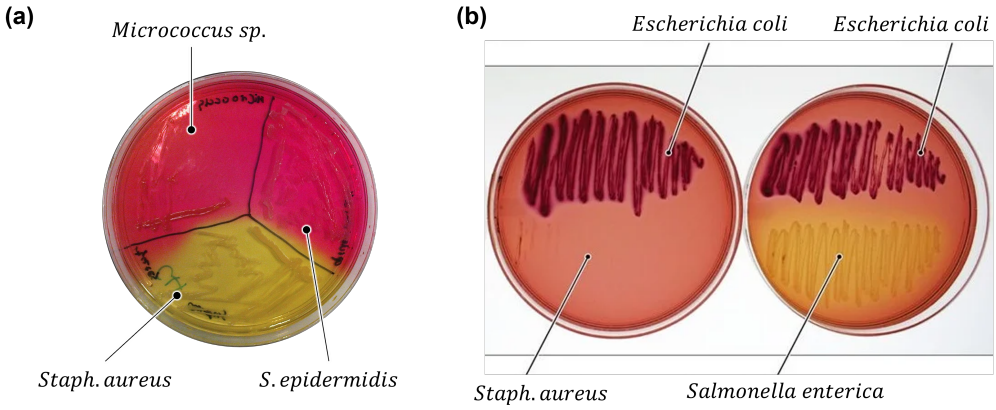

Figure A.1: Examples of differential and selective properties of growth media. ***(a)*** *MSA plate showing the selectivity for Micrococcus sp. and Staphylococcus epidermidis, and the differentiation of Staphylococcus aureus, which changes the medium's color due to mannitol fermentation. (Source: Navaho, 2008, Creative Commons license: CC BY-SA 4.0)* ***(b)*** *MacConkey agar plate demonstrating the respective selection (right) and differentiation (left) of Escherichia coli in comparison to Staphylococcus aureus and Salmonella enterica respectively. (Reprinted and adapted from [239]).*

Biochemical Assays

In typical microbiological workflows, preliminary tests such as staining and examination of growth characteristics provide an initial level of classification. To further refine identification, biochemical assays are employed to probe bacterial metabolic activity through specific enzymatic or fermentation reactions. In this section, we present selected examples of such assays, noting that numerous others exist targeting a wide range of metabolic pathways.

The first tier of biochemical identification often involves simple enzymatic assays that detect characteristic chemical reactions. Among these, the catalase and oxidase tests are fundamental, as they reveal the presence of key enzymes involved in aerobic respiration. The catalase test assesses the ability of bacteria to decompose hydrogen peroxide (H_2O_2) into water and oxygen, evident by the rapid formation of bubbles when drops of hydrogen peroxide are added to a bacterial smear on a flat surface or a suspension in a tube [75]. This test distinguishes, for instance, catalase-positive *Staphylococcus* species from catalase-negative *Streptococcus* species, as shown in fig. A.2(a).

The oxidase test, on the other hand, detects bacteria that make cytochrome c oxidase, an enzyme involved in their energy-producing process known as respiration. This enzyme helps move electrons through a chain of reactions in the cell membrane to release usable energy. The reaction is stimulated by adding tetra-methyl-p-phenylenediamine dihydrochloride, a redox indicator that changes from colorless to dark blue or purple when oxidized by cytochrome c [240]. This test may be conducted directly by introducing an oxidase reagent to bacteria grown on solid or in liquid culture media, or indirectly by using filter paper impregnated with the reagent and smearing colonies on it. Examples of both the liquid and filter-paper methods are shown in fig. A.2(b). These inexpensive enzymatic assays, among others of this type, are valued for their immediacy but offer only limited taxonomic precision. They are therefore typically used as orientation tests to guide the selection of more comprehensive biochemical identification panels.

Another major category of metabolic testing relies on fermentation-based assays to provide another diagnostic dimension. In these tests, bacteria are challenged, using different reagents, to ferment different carbohydrates (sugars), under both aerobic and anaerobic conditions. Fermentation activity is assessed by detecting the resulting acid formation, which lowers the pH, and gas production, which indicates the release of metabolic by-products such as carbon dioxide or

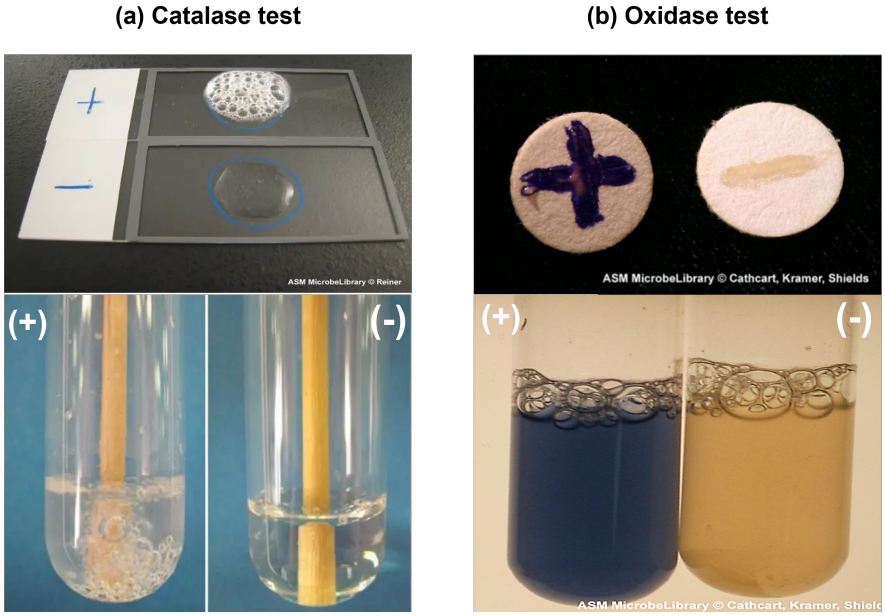

Figure A.2: Examples of enzymatic assays results. ***(a)*** *The catalase-positive reactions showing bubbles in the sample were produced by Staphylococcus aureus, while the negative reactions were produced by Streptococcus pyogenes. Reprinted and adapted from [75].* ***(b)*** *The oxidase-positive reactions showing a colored sample were produced by Pseudomonas aeruginosa (top) and Neisseria sicca (bottom), while the negative reactions were produced by Escherichia coli (top) and Staphylococcus aureus (bottom). Reprinted and adapted from [240].*

hydrogen [241, 242]. These tests can be used independently or in conjunction with differential media assays, most notably the Triple Sugar Iron (TSI) test. The TSI test simultaneously assesses the ability of bacteria to ferment multiple sugars and to produce gas or hydrogen sulfide. It employs an agar-based medium containing glucose, lactose, sucrose, phenol red as a pH indicator, and ferrous sulfate to detect H_2S production. The results are determined based on color shifts and gas bubble formation in the medium [243]. However, this assay is very sensitive as over- or under-incubation can mask subtle reactions.

Taken together, these biochemical reactions form a metabolic fingerprint that characterizes the organism and enables differentiation among genera. Nevertheless, individual assays rarely provide definitive identification, as metabolic expression can vary depending on environmental conditions or strain-specific differences. Despite their simplicity and rapidity, performing multiple tests sequentially can be time-consuming and may introduce variability in the results.

For these reasons, modern microbiology has progressively transitioned over the past decade toward automated and miniaturized systems. This evolution has been driven by several key innovations, including the use of lyophilized reagents, the miniaturization of reaction volumes (typically from several millilitres to a few hundred microlitres), and the introduction of disposable plastic supports, which have greatly simplified handling and improved standardization [93].

B

Appendix 2 : Trapping Signals

In this appendix, we individually present all the plots included in fig. 5.11 to provide a clearer visualisation of the distributions of the $(\mu - \sigma)$ parameters of the optical signatures obtained for each trappable bacterial strain, for a more detailed examination of the variations and patterns within each strain's optical signature.

For each figure, individual signals are represented by a scattered cloud of points whose sizes are proportional to the signal's skewness α. Each cloud is delimited by the 95% covariance ellipse, reflecting the correlation between the mean shift and the fluctuation width. The X marker denotes the median values $(\bar{\mu} - \bar{\sigma})$ for each strain, while the associated error bars represent the standard deviation of the point distribution.

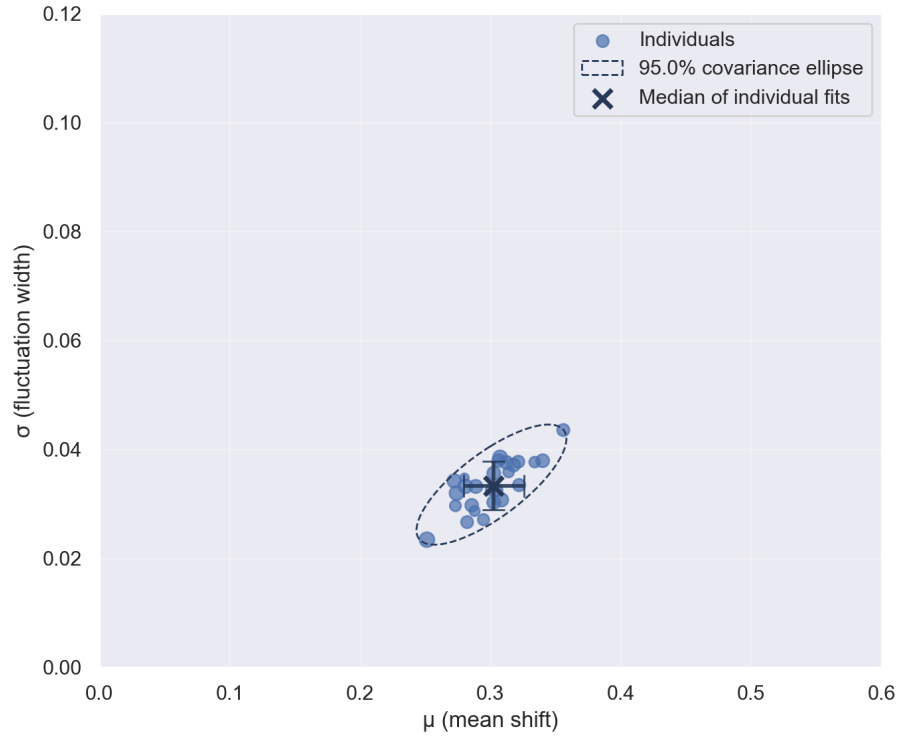

*Figure B.1: Distribution of $(\mu - \sigma)$ parameters for **EC11** optical signatures. The scattered cloud represents individual signals, with point size proportional to the skewness α of the corresponding histogram.*

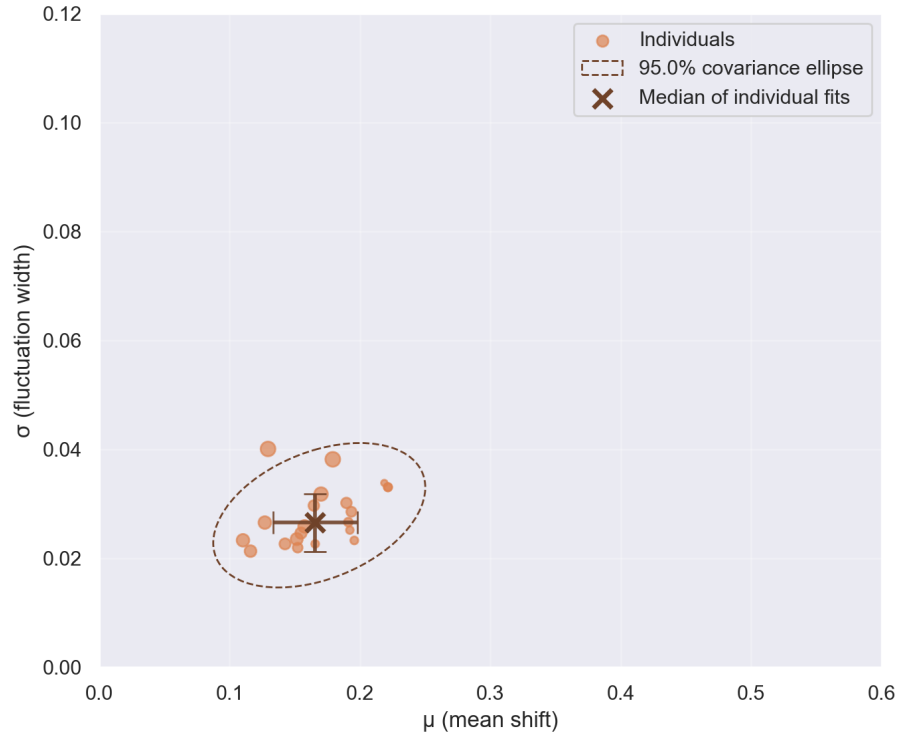

*Figure B.2: Distribution of $(\mu - \sigma)$ parameters for **EC225** optical signatures. The scattered cloud represents individual signals, with point size proportional to the skewness α of the corresponding histogram.*

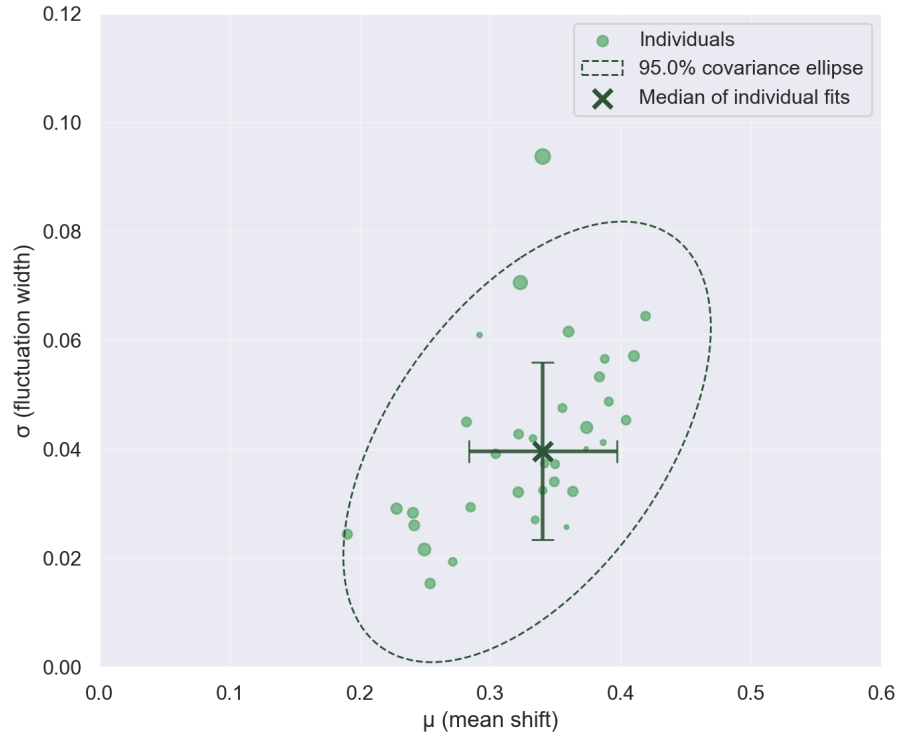

*Figure B.3: Distribution of $(\mu - \sigma)$ parameters for **EcB** optical signatures. The scattered cloud represents individual signals, with point size proportional to the skewness α of the corresponding histogram.*

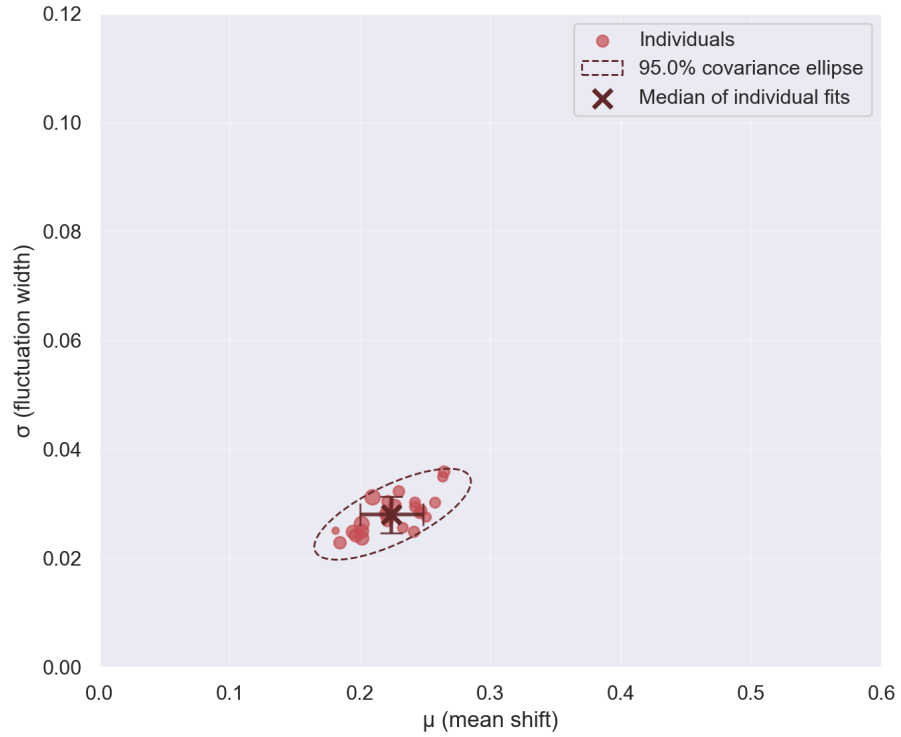

*Figure B.4: Distribution of $(\mu - \sigma)$ parameters for **Eco0124** optical signatures. The scattered cloud represents individual signals, with point size proportional to the skewness α of the corresponding histogram.*

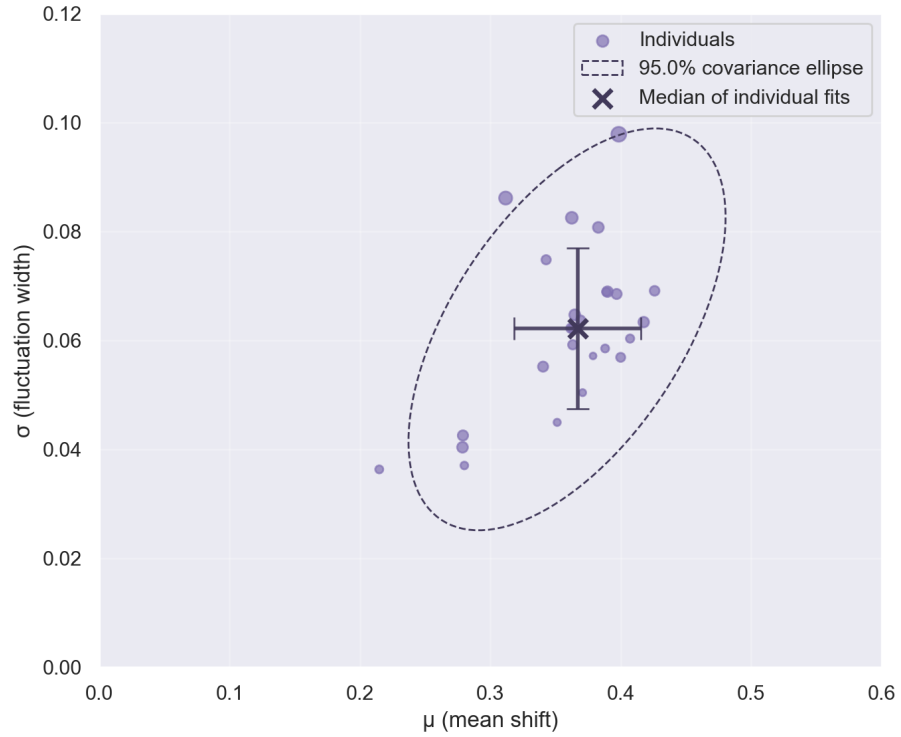

*Figure B.5: Distribution of $(\mu - \sigma)$ parameters for **Eco0126** optical signatures. The scattered cloud represents individual signals, with point size proportional to the skewness α of the corresponding histogram.*

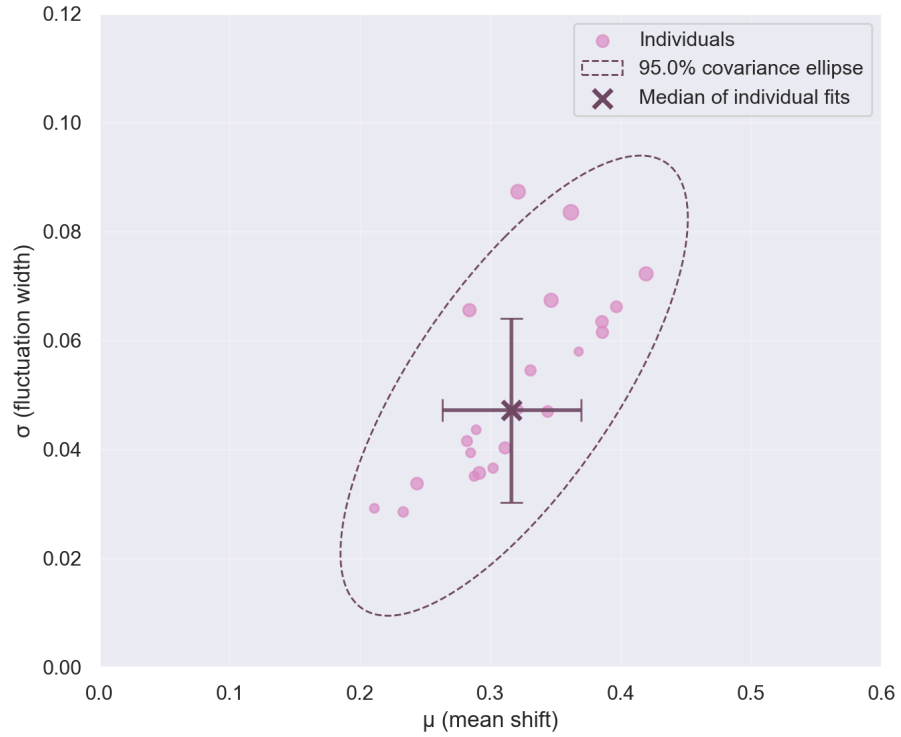

*Figure B.6: Distribution of $(\mu - \sigma)$ parameters for **Eco0127** optical signatures. The scattered cloud represents individual signals, with point size proportional to the skewness α of the corresponding histogram.*

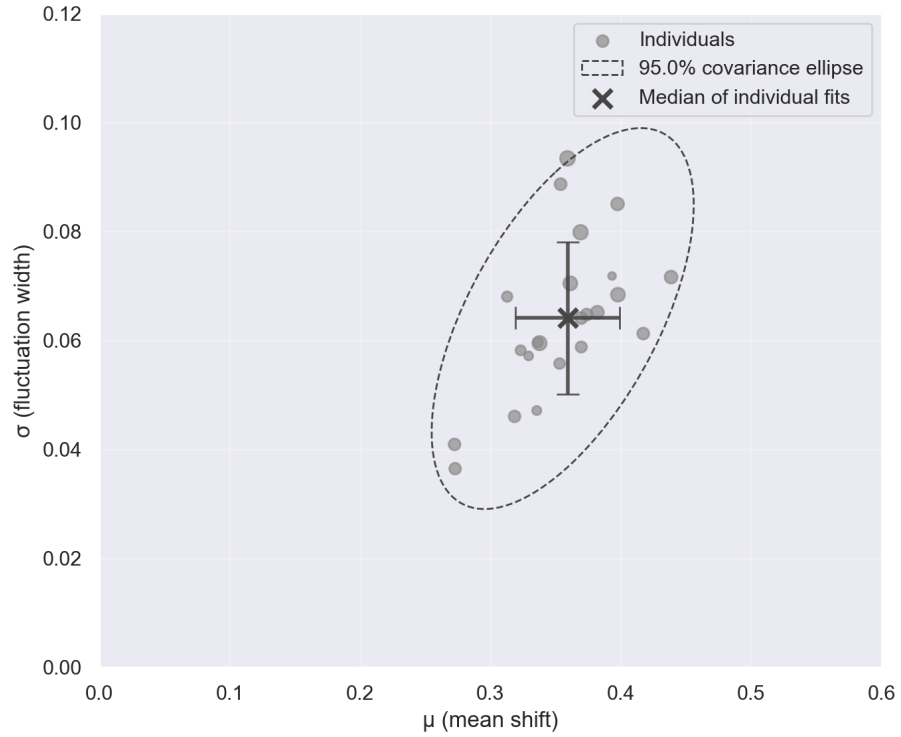

*Figure B.7: Distribution of $(\mu - \sigma)$ parameters for **Eco0128** optical signatures. The scattered cloud represents individual signals, with point size proportional to the skewness α of the corresponding histogram.*

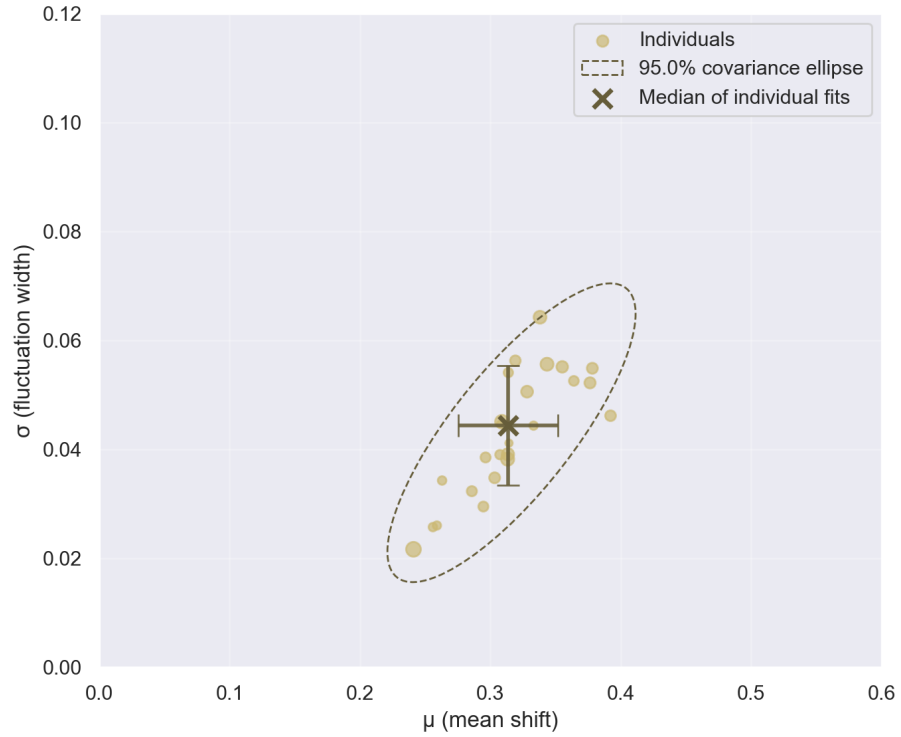

*Figure B.8: Distribution of $(\mu - \sigma)$ parameters for **Eco0129** optical signatures. The scattered cloud represents individual signals, with point size proportional to the skewness α of the corresponding histogram.*

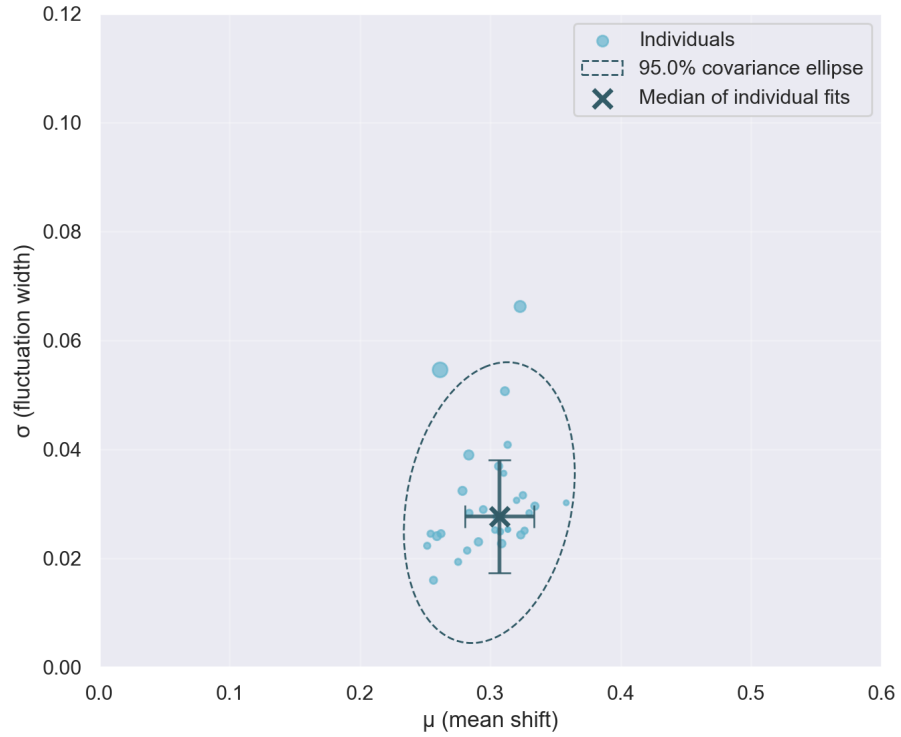

*Figure B.9: Distribution of $(\mu - \sigma)$ parameters for **Eco0130** optical signatures. The scattered cloud represents individual signals, with point size proportional to the skewness α of the corresponding histogram.*

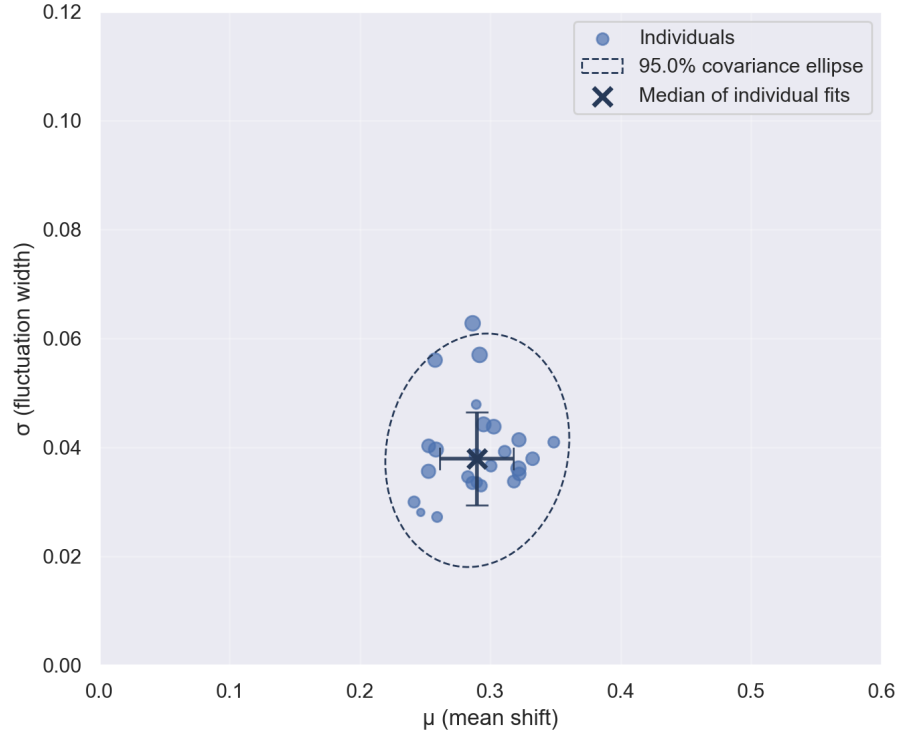

*Figure B.10: Distribution of $(\mu - \sigma)$ parameters for **Eco0131** optical signatures. The scattered cloud represents individual signals, with point size proportional to the skewness α of the corresponding histogram.*

Single-cell optical trapping for the typing of *Escherichia coli* using an optofluidic chip

Typage de l'espèce *Escherichia coli* par piégeage optique de cellule unique sur puce optofluidique

Abstract

The rise of antimicrobial resistance has transformed the treatment of bacterial infections into a race against time, as it is predicted to become a leading cause of mortality worldwide by 2050. This situation is driven in part by the widespread use of broad-spectrum antibiotics, which remain necessary in the absence of precise diagnostic alternatives capable of guiding therapeutic strategies. Addressing this challenge requires a deeper investigation of bacterial populations at the single-cell level, not only to understand their behaviour, but also to anticipate the emergence of phenotypic shifts and resistance-associated changes.

Conventional microbiological methods rely predominantly on population-averaged measurements, which provide robust and standardized information but fail to capture the heterogeneity that may exist within bacterial populations. As a result, rare or transient behaviours expressed by a small fraction of cells may remain undetected, despite their potential role in the development of resistance or in the response to environmental stress. Detecting these early signs requires experimental approaches capable of isolating and probing individual cells with sufficient sensitivity and reproducibility.

Optical methods offer a promising framework to address these limitations. The interaction of light with microscopic objects enables both the manipulation and the characterization of single cells in a non-invasive manner. In particular, photonic structures allow strong confinement of light, enhancing sensitivity to minute variations in cellular properties. When combined with microfluidic systems, these approaches provide precise control over the cellular environment while enabling continuous and non-invasive measurements.

In this manuscript, we present the development of optofluidic chips based on SOI photonic crystal optical resonators for the trapping and analysis of individual *Escherichia coli* bacterial cells. Particular attention was given to the design and integration of the microfluidic circuit, enabling controlled delivery and positioning of cells within the optical structures. These devices integrate optical manipulation and sensitive detection within a microfluidic platform, allowing controlled investigations of cell-surface interactions, and optical responses at the single-cell level.

The results demonstrate the ability of this approach to trap individual bacterial cells and to probe their physical interactions with the surrounding environment, including transient behaviours that were investigated and controlled through adjustments of the experimental conditions. Statistical analysis confirms the reproducibility of the optical measurements and the ability to extract consistent single-cell signatures. These observations highlight the variability of bacterial responses and indicate that discrimination between *Escherichia coli* strains remains challenging under the current experimental conditions. Finally, the measured optical responses were used to estimate the refractive index of each bacterial strain in the infrared.

Overall, this work contributes to the development of optical tools for single-cell microbiology and outlines perspectives for more precise diagnostic approaches.

Keywords : photonic crystals, optical trapping, optofluidics, microfluidics, single-cell analysis, *Escherichia coli*, bacterial typing, cell-surface interactions, measurement reproducibility